N°d'ordre NNT : **2023ISAL0029**

THESE de DOCTORAT DE L'INSA LYON, membre de l'Université de Lyon

Ecole Doctorale MEGA N° ED 162
(Mécanique, Energétique, Génie Civil, Acoustique)

Spécialité / discipline de doctorat :
Génie Mécanique

Soutenue publiquement le 17/04/2023, par :
Thomas Lubrecht

Numerical and Experimental Analysis of the Tribological Performance of a Diamond-Like Carbon Coated Piston Ring Cylinder Liner Contact

---

Devant le jury composé de :

Molinari, J.-F.	Professor and lab. director, EPFL, Lausanne	Président
Tian, Tian	Senior Research Engineer, MIT, Boston	Rapporteur
Fabre, Agnès	Maître de Conférences HDR, ENSAM, Aix-en-Provence	Rapporteur
Dufils, Johnny	Docteur-ingénieur, IREIS (HEF groupe), Saint-Etienne	Encadrant
Biboulet, Nans	Maître de Conférences HDR, INSA-Lyon	Co-directeur de thèse
Lubrecht, A. A.	Professeur des Universités, INSA-Lyon	Directeur de thèse

INSTITUT NATIONAL DES SCIENCES APPLIQUÉES LYON

Département de la Formation par la Recherche et des Études Doctorales (**FEDORA**)

Bâtiment INSA direction, 1er étage
37, av. J. Capelle
69621 Villeurbanne Cédex
fedora@insa-lyon.fr

Référence : TH0959_Thomas LUBRECHT

L'INSA Lyon a mis en place une procédure de contrôle systématique via un outil de détection de similitudes (logiciel Compilatio). Après le dépôt du manuscrit de thèse, celui-ci est analysé par l'outil. Pour tout taux de similarité supérieur à 10%, le manuscrit est vérifié par l'équipe de FEDORA. Il s'agit notamment d'exclure les auto-citations, à condition qu'elles soient correctement référencées avec citation expresse dans le manuscrit.

Par ce document, il est attesté que ce manuscrit, dans la forme communiquée par la personne doctorante à l'INSA Lyon, satisfait aux exigences de l'Etablissement concernant le taux maximal de similitude admissible.

Département FEDORA – INSA Lyon - Ecoles Doctorales

SIGLE	ECOLE DOCTORALE	NOM ET COORDONNEES DU RESPONSABLE
CHIMIE	**CHIMIE DE LYON** **https://www.edchimie-lyon.fr** Sec. : Renée EL MELHEM Bât. Blaise PASCAL, 3e étage secretariat@edchimie-lyon.fr	**M. Stéphane DANIELE** C2P2-CPE LYON-UMR 5265 Bâtiment F308, BP 2077 43 Boulevard du 11 novembre 1918 69616 Villeurbanne **directeur@edchimie-lyon.fr**
E.E.A.	**ÉLECTRONIQUE, ÉLECTROTECHNIQUE, AUTOMATIQUE** **https://edeea.universite-lyon.fr** Sec. : Stéphanie CAUVIN Bâtiment Direction INSA Lyon Tél : 04.72.43.71.70 secretariat.edeea@insa-lyon.fr	**M. Philippe DELACHARTRE** INSA LYON Laboratoire CREATIS Bâtiment Blaise Pascal, 7 avenue Jean Capelle 69621 Villeurbanne CEDEX Tél : 04.72.43.88.63 **philippe.delachartre@insa-lyon.fr**
E2M2	**ÉVOLUTION, ÉCOSYSTÈME, MICROBIOLOGIE, MODÉLISATION** **http://e2m2.universite-lyon.fr** Sec. : Bénédicte LANZA Bât. Atrium, UCB Lyon 1 Tél : 04.72.44.83.62 secretariat.e2m2@univ-lyon1.fr	**Mme Sandrine CHARLES** Université Claude Bernard Lyon 1 UFR Biosciences Bâtiment Mendel 43, boulevard du 11 Novembre 1918 69622 Villeurbanne CEDEX **sandrine.charles@univ-lyon1.fr**
EDISS	**INTERDISCIPLINAIRE SCIENCES-SANTÉ** **http://ediss.universite-lyon.fr** Sec. : Bénédicte LANZA Bât. Atrium, UCB Lyon 1 Tél : 04.72.44.83.62 secretariat.ediss@univ-lyon1.fr	**Mme Sylvie RICARD-BLUM** Institut de Chimie et Biochimie Moléculaires et Supramoléculaires (ICBMS) - UMR 5246 CNRS - Université Lyon 1 Bâtiment Raulin - 2ème étage Nord 43 Boulevard du 11 novembre 1918 69622 Villeurbanne Cedex Tél : +33(0)4 72 44 82 32 **sylvie.ricard-blum@univ-lyon1.fr**
INFOMATHS	**INFORMATIQUE ET MATHÉMATIQUES** **http://edinfomaths.universite-lyon.fr** Sec. : Renée EL MELHEM Bât. Blaise PASCAL, 3e étage Tél : 04.72.43.80.46 infomaths@univ-lyon1.fr	**M. Hamamache KHEDDOUCI** Université Claude Bernard Lyon 1 Bât. Nautibus 43, Boulevard du 11 novembre 1918 69 622 Villeurbanne Cedex France Tél : 04.72.44.83.69 **hamamache.kheddouci@univ-lyon1.fr**
Matériaux	**MATÉRIAUX DE LYON** **http://ed34.universite-lyon.fr** Sec. : Yann DE ORDENANA Tél : 04.72.18.62.44 yann.de-ordenana@ec-lyon.fr	**M. Stéphane BENAYOUN** Ecole Centrale de Lyon Laboratoire LTDS 36 avenue Guy de Collongue 69134 Ecully CEDEX Tél : 04.72.18.64.37 **stephane.benayoun@ec-lyon.fr**
MEGA	**MÉCANIQUE, ÉNERGÉTIQUE, GÉNIE CIVIL, ACOUSTIQUE** **http://edmega.universite-lyon.fr** Sec. : Stéphanie CAUVIN Tél : 04.72.43.71.70 Bâtiment Direction INSA Lyon mega@insa-lyon.fr	**M. Jocelyn BONJOUR** INSA Lyon Laboratoire CETHIL Bâtiment Sadi-Carnot 9, rue de la Physique 69621 Villeurbanne CEDEX **jocelyn.bonjour@insa-lyon.fr**
ScSo	**ScSo*** **https://edsciencessociales.universite-lyon.fr** Sec. : Mélina FAVETON INSA : J.Y. TOUSSAINT Tél : 04.78.69.77.79 melina.faveton@univ-lyon2.fr	**M. Bruno MILLY** Université Lumière Lyon 2 86 Rue Pasteur 69365 Lyon CEDEX 07 **bruno.milly@univ-lyon2.fr**

*ScSo : Histoire, Géographie, Aménagement, Urbanisme, Archéologie, Science politique, Sociologie, Anthropologie

“Life is like riding a bicycle.
To keep your balance you must keep moving.”
Albert Einstein

“Piégé dans notre propre système.
Prisonnier dans une sauvegarde bloquante.”
Orelsan

to Alexia
to my parents

Foreword

March 2019, on a cold winter day, my father and myself went for a small walk to avoid the hustle and bustle of my nephew's first year birthday party. My father grumbled about the recent withdraw of his future PhD student on an industrial contract. Meanwhile, I did not receive the funding for my PhD at the Twente University. Also, I complained about the perfunctory work I was performing as an analysis engineer. A few weeks later, he suggested that I apply to his open PhD offer and a few months later I was hired by the industrial company. Since, I have enjoyed a remarkable, scientific, father and son journey.

A thesis is often seen as a solitary, individual labour. However, the following extensive work could not have been possible without the priceless help of great people that I like to thank.
First of all, I want to express my gratitude to my supervisor Pr. Ton Lubrecht for the opportunity, his help, patience and encouraging talks. Also, I want to thank him for the many lunch walks and interesting talks about tribology, science, politics and future. Overall, I would like to thank him for the scientific curiosity he transmitted. I am also very indebted to Dr Nans Biboulet for his guidance and fruitful advice. They were very precious all along this journey.
I am very grateful to the jury members: Pr. Jean-François Molinari (EPFL, Lausanne) for accepting to preside the jury. Dr Agnès Fabre (ENSAM, Aix-en-Provence) to have cordially animated my thesis defence as well as for accepting to review my work. Last but not least, Dr Tian Tian (MIT, Boston) for reviewing my work, for all his interesting comments/remarks and for the fascinating discussions.
I am thankful to the LaMCoS laboratory and in particular to Jérôme Cavoret and Philippe Sainsot for their help with the experiments and the surface measurements. I am grateful to Sophie de Oliveira and Emmanuel Montero who were very helpful in practical matters.
The thesis journey would not have been so much fun without the other PhD students in the team: Dr Pierre, Dr Valentin, Dr Nicolas, Dr Arif, Dr Lucas, Dr Simona, Gabriel, Aude, Gladys, Aurore, Busra, Marie, Paul, Lucas, Augustin, Gabriel, Julien, Elias, Sebastian, Lionel, Wassim and many more. Thank you for you help and for the great times we spent together. I wish you the best.
I am thankful to the IREIS company and in particular to Dr Christophe Pupier and Dr Philippe Maurin Perrier. I am indebted to Etienne Macron for managing the work and I am particularly thankful to Dr Johnny Dufils for the long hours he spent with me on the test-rig and for all the inspiring scientific discussions we had.
I must not forget my family and extended family for their support. A particular thank you to Alexia, who placed trust in me more than I do, who supported me and often carried me all along the way. I would not have reached this level without you, thank you.
At last, I am grateful to all my friends for their interest and support.

To all, we did it together.

Abstract

Forced by the climate emergency and the recent geopolitical issues, the world industry and transport sectors are initiating a change towards sustainable energies. The automotive industry is mainly relying on the electrical technology to deal with the local emission limitations. However, today this technology is unsuitable to overcome the globalisation challenges. Therefore, Internal Combustion (IC) engines will probably be used for a few more years and improving their efficiency, reliability and sustainability is still of main interest. Surface coatings, such as Diamond-Like Carbon (DLC), may help in this quest since they present excellent tribological properties. Its application to all parts of the crucial Piston-Ring / Cylinder-Liner (PRCL) contact has not been widely studied yet. For this purpose, both an experimental and numerical methods are developed to analysis the tribological performance of the DLC coated PRCL contact.

A semi-analytical, time-dependent, line-contact, mixed lubrication solver is developed. Contrary to the regular stochastic theories, this method relies on deterministic contact mechanics results using measured topographies. To account for the sample macro-geometry, analytical correction coefficients evaluated using the Reynolds equation and the sample macro-geometry are implemented. Thereby, the solver allows for a rapid prediction of the contact different friction forces accounting for oil starvation (geometrical or by lack of lubricant) as well as oil transport. The solver is validated using measurements and fully numerical solutions.

In addition, an experimental "floating-liner" device using real engine parts is improved. By means of an experimental (vibration measurements) and numerical (modal analysis) vibrational investigation, the test-rig signal to noise ratio is enhanced. Furthermore, a strategy to mimic high speeds contact conditions from low speed operating parameters is introduced.

Finally, using both experimental and numerical methods, an excellent tribological performance of a DLC coating compression ring / liner contact is observed. A substantial reduction in friction, as well as an excellent wear endurance for a variety of lubricants is obtained. These results are promising for the efficiency enhancement of future internal combustion engines.

KEYWORDS
Internal Combustion Engine (ICE) - Piston Ring Cylinder Liner (PRCL) - Diamond Like Carbon (DLC) - Mixed Lubrication - Starvation - Floating Liner.

Résumé

Contraints par l'urgence climatique et les enjeux géopolitiques, les secteurs mondiaux de l'industrie et du transport initient une transition vers les énergies durables. L'industrie automobile mise sur les véhicules électriques pour satisfaire les normes locales d'émissions de polluants. Cependant, cette technologie est, en l'état, incapable de répondre aux challenges de la mondialisation. Pour cette raison, les moteurs à combustion interne seront probablement toujours utilisés au cours des prochaines années. Ainsi, améliorer leur efficacité, fiabilité et réduire leurs émissions de polluants est aujourd'hui plus que nécessaire. Les revêtements de surface, tel que le Diamond-Like Carbon (DLC), peuvent par leurs excellentes propriétés tribologiques améliorer le rendement et la durée de vie d'un moteur. La mise en œuvre de revêtement DLC sur toutes les pièces du contact primordial Segment-Piston-Chemise (SPC) a pour le moment peu été étudiée, mais semble cependant être une solution prometteuse. Afin d'évaluer la pertinence d'une telle solution, une étude expérimentale et numérique du contact SPC revêtu DLC est menée.

Dans ce but, un solveur semi-analytique transitoire pour la résolution de contact linéique, lubrifié mixte est développé. Contrairement aux habituelles théories stochastiques, cette méthode repose sur un calcul déterministe du contact entre rugosité à partir du relevé topographique de la surface. Afin de prendre en compte la macro-géométrie des pièces en contact, des coefficients correcteurs évalués analytiquement à partir de l'équation de Reynolds et de la macro-géométrie sont implémentés. Ainsi, le solveur permet l'estimation rapide des différentes forces de frottement du contact tout en considérant les phénomènes de sous-alimentation (géométrique ou par manque de lubrifiant) et de transport d'huile. Le solveur est validé expérimentalement et numériquement.

En parallèle, un moyen d'essai dit à ≪chemise-flottante≫ et équipé de vraies pièces moteur est amélioré. A la suite d'une étude expérimentale (mesures vibratoires) et numérique (analyses modales) du banc d'essai, certaines pièces sont modifiées afin d'obtenir un meilleur ratio signal sur bruit mesuré. En outre, une méthode permettant de reproduire des conditions d'essai à hautes vitesses tout en fonctionnant à basses vitesses est présentée.

Enfin, à partir des méthodes expérimentales et numériques, d'excellentes performances tribologiques sont observées pour le contact segment coupe-feu / chemise revêtu DLC. Une réduction significative du frottement ainsi qu'une excellente résistance à l'usure pour une variété de lubrifiants sont obtenues. Ces résultats sont prometteurs pour l'amélioration du rendement des moteurs à combustion interne futurs.

MOTS-CLÉS:
Moteur à Combustion Interne (MCI) - Segment Piston Chemise (SPC) - Diamond Like Carbon (DLC) - Lubrification Mixte - Sous-alimentation - Chemise Flottante.

Résumé Étendu en Français

Introduction

Le transport est le second secteur mondial à engendrer le plus de gaz à effet de serre derrière la production d'énergie. Il a généré en 2019 environ 8,43 milliards de tonnes d'équivalent CO_2 dont les trois quarts sont émis par les transports routiers (véhicule léger, camion, bus, etc.). Le transport mondial contribue également fortement à la dégradation de la qualité de l'air dans le monde, engendrant la mort prématurée de plusieurs millions de personnes. De nos jours, les véhicules routiers ainsi que les navires sont majoritairement propulsés par des moteurs à combustion interne (MCI). Les carburants utilisés étant essentiellement des hydrocarbures (pétrole, gaz naturel), cette technologie est une source majeure d'émission de CO_2 et de polluants. Poussé par les normes locales anti-pollutions / anti-émissions, les industries automobiles Européenne, Américaine et Chinoise initient une électrification de leur flotte de véhicules. Cependant, en l'état, les véhicules électriques sont limités par plusieurs facteurs. La forte proportion de production d'électricité non renouvelable, le poids et la faible autonomie des batteries ainsi que le prix (économique et environnemental) de l'exploitation et du recyclage des métaux rares en sont les principales limites. Pour ces raisons, la propulsion électrique semble inadaptée aux challenges actuels de la mondialisation. Il est alors évident que les MCI seront toujours utilisés au cours des prochaines dix à vingt années, notamment par l'implémentation de carburants alternatifs (hydrogène, biocarburants, etc.) et par l'extension des technologies hybrides. Ainsi, améliorer l'efficacité, la fiabilité et la durabilité des MCI est de première nécessité.

Dans ce but, les efforts de recherche se focalisent souvent sur le contact segment-piston-chemise (SPC) qui représente 50% des pertes d'énergie du moteur et qui contrôle la majorité de sa consommation en huile. Ce contact a la double fonction (contraire) de seller la chambre de combustion et de lubrifier le piston. Pour cela, il est constitué de trois segments/joints métalliques montés en série dans le piston et qui frotte contre la chemise moteur au cours du mouvement alternatif du piston. Traditionnellement, la chemise moteur est rectifiée par pierrage pour obtenir une cylindricité adéquate. Ce procédé génère une finition de surface texturée avec des ≪plateaux≫ lisses et des stries profondes. Cet état de surface présente des avantages et des inconvénients quant à la lubrification du contact. Récemment, la tendance est à la fabrication de chemises lisses, essentiellement par dépôt de matière, pour réduire le poids des moteurs. Cette finition de surface pourrait permettre une réduction des pertes par frottement du contact. L'étude du contact SPC est relativement complexe de part la variété et la variation des paramètres d'opération tout au long de la course du piston. Ainsi, les segments expérimentent durant leur fonctionnement les trois régimes de lubrification : limite, mixe et hydrodynamique. Pour cette raison et malgré une multitude d'études réalisées sur le sujet, il n'existe aujourd'hui aucune méthode universelle pour l'étude tribologique du contact SPC.

Outre l'état de surface des pièces en contact, les matériaux de celles-ci jouent également un rôle important dans la tribologie de l'interface. Traditionnellement les pièces en contact sont en acier, mais la mise en œuvre de revêtement de surface peut permettre l'amélioration des propriétés tribologiques du contact. Une solution efficace est le dépôt en surface d'un revêtement s'approchant des propriétés mécaniques du diamant, nommé le Diamond-Like Carbon (DLC). Le revêtement DLC est une fine couche (quelques micromètres) de carbone amorphe (a-C) déposé par plasma sous vide et qui présente une excellente résistance à l'usure ainsi qu'un faible coefficient de frottement sous certaines conditions. L'application de revêtement DLC dans les MCI est de plus en plus courante, notamment pour les contacts fortement chargés tels que la distribution ou le segment coupe-feu. Cependant, son application sur l'intégralité des pièces du contact SPC a été peu étudiée et est principalement réservée aux MCI hautes performances, tel qu'en Formule 1. Néanmoins, cette solution semble prometteuse pour la décarbonisation et la dépollution de tous les types de transports routiers. Ainsi, l'objectif principal de cette étude est d'évaluer les performances tribologiques du contact SPC revêtu DLC. Cet objectif peut être décomposé selon les objectifs secondaires suivants :

- Evaluer expérimentalement les propriétés tribologiques en régime de lubrification limite du revêtement DLC sélectionné pour une variété de lubrifiants,
- Développer une méthode numérique de prédiction des pertes par frottement du contact SPC revêtu DLC,
- Valider expérimentalement/numériquement le code développé,
- Développer une méthode expérimentale pour l'évaluation des pertes par frottement du contact SPC.

Résultats

Modèle numérique

Le modèle développé est basé sur la théorie de lubrification en régime mixte élaborée par Christensen. Elle repose sur l'évaluation de l'équilibre des charges du segment afin de prédire l'épaisseur de film générée entre les deux pièces. Les charges agissant sur le segment sont : la charge hydrodynamique générée par le film d'huile et la charge portée par le contact solide entre les rugosités, toutes deux faisant opposition à la tension élastique du segment le poussant contre la chemise. Conformément aux faibles accélérations radiales que subissent le segment, son inertie est ignorée. Compte tenu de l'état de surface lisse et isotrope des pièces étudiées, l'influence de la rugosité sur la charge hydrodynamique est ignorée et le contact est assumé linéique. Egalement, au regard des faibles pressions de contact (de l'ordre de quelques mégapascals hors combustion) le contact est supposé iso-visqueux rigide.
Ainsi, les pressions et charges hydrodynamiques du contact sont calculées en intégrant analytiquement l'équation de Reynolds, 1D, transitoire, lisse et iso-visqueux rigide. Afin de prendre en compte les phénomènes de sous-alimentation et de transport d'huile, deux équations de conservation de la masse en entrée et en sortie du contact sont définies.
Contrairement aux théories stochastiques usuelles, l'évaluation de la charge portée par les aspérités repose sur une résolution déterministe de la mécanique du contact basée notamment sur le relevé topographique 3D des surfaces. Ainsi, aucun paramètre statistique de rugosité n'est utilisé dans le modèle. Pour ne pas altérer la rapidité de calcul du solveur hydrodynamique, la méthode développée repose sur la construction en «off-line» d'une courbe dite «charge-distance» qui décrit, à charge imposée, la distance moyenne entre les surfaces rugueuses déformés élastiquement. Cette courbe est ensuite interpolée en «on-line» au cours du processus itératif de prédiction du film d'huile, créant ainsi un modèle de lubrification mixte.
Le code est développé sous Matlab R2021b, les intégrales analytiques du modèle sont évaluées à l'aide de la *toolbox symbolic* et le système d'équation non linéaire est résolu par la fonction native *fsolve*. Ainsi, le code développé permet l'estimation rapide de l'épaisseur de film et donc des pertes par frottement du contact segment-chemise pour chaque pas de temps et tout en considérant l'aspect transitoire, la sous-alimentation, le transport d'huile et l'interaction entre rugosités du contact.

Moyens Expérimentaux

Afin d'étudier les propriétés tribologiques du revêtement DLC, différents moyens et méthodes d'essais sont utilisés et modifiés. Premièrement, les performances tribologiques du revêtement DLC en régime limite de lubrification sont testées sur deux bancs d'essais bille/plan. Au total, plus de 50 essais sont menés, pour des configurations DLC-DLC, acier-acier et acier-DLC ainsi que pour une variété de lubrifiants (huile moteur de base / avancée, glycérol pure, huile de ricin et eau). Contrairement aux surfaces aciers, peu

ou pas de tribofilm est observé sur les échantillons revêtus DLC. De plus, en l'absence d'additif modificateur de frottement (FM) dans l'huile, le contact DLC-DLC présente un coefficient de frottement limite 15% à 20% plus faible que le contact acier-acier. De façon générale, aucune usure est observée sur les échantillons revêtus DLC. Cependant, pour un contact acier-DLC en présence d'additif FM de type MoDTC (dithiocarbamate de molybdène), une usure tribo-chimique progressive du DLC est observée.
Deuxièmement, dans l'optique d'évaluer la pertinence du modèle, une méthode de mesure du frottement d'un contact linéique est développée. Pour cela, un banc d'essai linéaire alternatif est modifié et un cylindre, poli-miroir, revêtu DLC est frotté contre un plan pour une multitude de conditions de fonctionnement. De plus, certains cylindres sont usinés afin de reproduire l'épaisseur finie (de l'ordre du millimètre) d'un segment moteur afin de valider la modélisation de la sous-alimentation géométrique. Cette méthode expérimentale permet la mesure précise des forces de frottement d'un contact linéique pour tous les régimes de lubrification et pour des conditions de sous-alimentation en huile.
Enfin, un moyen d'essai dit à ≪chemise flottante≫ pour la mesure des pertes par frottement du contact SPC est décrit. Il permet l'évaluation des pertes par frottement de vraies pièces moteur telles que le piston et la segmentation. Le mouvement alternatif linéaire du piston est assuré par un moteur électrique et par un système de bielle-manivelle. La chemise quant à elle est montée dans un support installé sur un capteur d'effort piézo-électrique mesurant les forces générées par le contact SPC. Ce banc d'essai est conçu pour mesurer les performances tribologiques du contact à des vitesses et conditions de lubrification proche d'un MCI. Cependant, le banc souffre d'une instabilité vibratoire qui pollue fortement la mesure à des vitesses de rotations supérieures à 400 tr/min. Au moyen d'une étude vibratoire poussée du banc d'essai, la flexibilité du support de chemise est mise en cause. Par le biais d'une étude modale numérique, des solutions de rigidification du support de chemise sont proposées. De plus, pour utiliser le banc d'essai en l'état, une stratégie établissant un lien entre des conditions d'essais à hautes vitesses / faible viscosité et à faibles vitesses / haute viscosité basé sur l'étude de l'équation de Reynolds est établie.

Validation du Modèle

Lors du développement d'un modèle théorique, il est crucial de vérifier la cohérence des simulations avec d'autres méthodes.
Premièrement, les résultats du modèle théorique développé sont comparés à une solution P-Θ résolue par différence finie. Les résultats en épaisseur de film d'huile et en frottement des deux méthodes de calcul sont proches, avec une différence moyenne inférieure à 3%, confirmant la cohérence du modèle semi-analytique. L'avantage principal du modèle semi-analytique est qu'il nécessite uniquement une discrétisation en temps tandis que le modèle P-Θ nécessite une discrétisation temporelle et spatiale. Le code développé est ainsi plus rapide et plus simple d'utilisation.
Deuxièmement, les résultats du modèle sont comparés aux mesures de frottement linéique décrites dans le chapitre précédent. Dans ce but, les conditions de fonctionnement du banc d'essai, la géométrie des cylindres, la viscosité des lubrifiants testés et la topographie

3D des surfaces sont implémentées dans le modèle. Les simulations montrent que le modèle est incapable de prédire le contact entre les rugosités en considérant uniquement la microrugosité des surfaces. Ainsi, il est démontré que la macro-géométrie / ondulation des cylindres selon la longueur du contact a une influence non-négligeable sur la lubrification du contact. En conséquence, le modèle est modifié pour prendre en compte la macro-géométrie des cylindres. A partir de l'analyse de l'équation de Reynolds et de la géométrie 3D déformée des cylindres, des coefficients correcteurs analytiques traduisant la perte de charge hydrodynamique dus à l'ondulation de la surface sont implémentés. Enfin, les résultats du modèle mis à jour sont en accord avec les mesures de frottement et ce pour des conditions sur- et sous-alimentées en lubrifiant.

Résultats

Au moyen des méthodes expérimentales et numériques développées, les performances tribologiques du contact segment coupe-feu / chemise revêtu DLC sont étudiées. Cette étude permet également l'analyse des performances de chaque méthode employée.
Les essais sont effectués sur le banc d'essai à «chemise-flottante» pour trois tribo-paires : segment non-revêtu / chemise non-revêtue, segment DLC / chemise non-revêtue, segment DLC / chemise DLC. Les essais sont réalisés pour de relativement faibles vitesses de rotation (100-400 RPM) et pour une huile de grade 10W-60 à 50°C. Ces paramètres d'essais sont équivalents à une configuration hautes vitesses (1000-4000 RPMeq) pour une huile de grade 5W-30 à 100°C. Les différents essais ont démontré une réduction de l'ordre de 10% à 30% du frottement aux point-morts haut et bas pour une configuration DLC-DLC, en comparaison à une configuration non-revêtue. A l'inverse, aucun gain n'est observé dans le régime de lubrification hydrodynamique. Sur un cycle moteur complet, une réduction de 5% de la valeur de FMEP est obtenue pour la configuration DLC-DLC. En outre, en comparaison aux surfaces non-revêtues, les surfaces DLC présentent une très faible usure après essais. Néanmoins, il est vraisemblablement nécessaire de reproduire ces essais sur un plus grand nombre d'échantillons afin de vérifier, ou non, les tendances observées.
Numériquement, les géométries des segments testés, la topographie 3D des segments et chemises ainsi que les conditions de fonctionnement du banc d'essai sont implémentées dans le modèle. Similairement au cas cylindre-plan étudié précédemment, le modèle est incapable de prédire le contact entre les rugosités en considérant uniquement la microrugosité des surfaces. Au regard de la complexité de la distorsion segment/chemise, la stratégie analytique présentée pour le cas cylindre-plan n'est pas applicable. Néanmoins, un réglage fin des paramètres de simulation pour correspondre aux frottements mesurés permet d'utiliser le modèle pour optimiser le contact. Ainsi, en sélectionnant le rayon de courbure et l'épaisseur de segment optimums, une réduction de 50% des pertes par frottement du contact SPC est démontré.

Conclusion

Au moyen de nouvelles méthodes expérimentales et numériques les performances tribologiques du contact SPC revêtu DLC sont étudiées.

Numériquement, un solveur hydrodynamique 1D semi-analytique et transitoire existant est étendu avec succès au contact lubrifié mixte. Contrairement aux théories stochastiques usuelles, le contact entre rugosités est établi à partir de calculs déterministes de mécanique des contacts entre aspérités, à partir de la topographie 3D mesurée des surfaces. Un code relativement simple développé sous Matlab R2021b permet la prédiction rapide (de l'ordre de la minute) de l'épaisseur de film d'huile et des pertes par frottement du contact. Les simulations ont été validées numériquement et expérimentalement pour les trois régimes de lubrification ainsi que pour des conditions de sur- et sous-alimentation en lubrifiant.
Il est démontré, par confrontation des simulations aux essais expérimentaux, que la macro-géométrie des pièces en contact i.e. l'ondulation selon la longueur du contact a une influence non-négligeable sur la lubrification à l'interface. Contrairement à une solution théorique lisse, l'existence de creux diminue fortement la charge hydrodynamique générée. Afin de prendre en compte ce phénomène dans le modèle semi-analytique développé, une nouvelle stratégie est présentée. Basés sur l'analyse de l'équation de Reynolds ainsi que sur la géométrie déformée élastique, des coefficients correcteurs hydrodynamiques analytiques variant en fonction de l'épaisseur de film d'huile sont implémentés dans les équations. Cette solution rapide et simple présente d'excellents résultats en comparaison aux essais expérimentaux.
Au moyen de l'amélioration des instabilités vibratoires d'un banc d'essai dit à ≪chemise-flottante≫ , une méthode expérimentale efficace d'évaluation des pertes par frottement du contact SPC est présentée. Cette méthodologie permet l'essai de pièces moteur telles que le piston ou la segmentation pour des conditions de fonctionnement équivalents proches d'un MCI (vitesse, lubrification, charge).
Ainsi, les performances tribologiques d'un segment coupe-feu revêtu DLC contre une chemise polie revêtue DLC sont étudiées. Il est démontré que cette configuration, en comparaison à une configuration polie acier-acier, permet une réduction significative des pertes par frottement dans les régimes mixte et limite de lubrification. Expérimentalement et numériquement, une réduction de l'ordre de 5% des valeurs de FMEP (Friction Mean Effective Pressure) est obtenue pour la configuration DLC-DLC. En outre, il est montré que le revêtement DLC présente une excellente capacité de protection des surfaces et ce pour la variété de lubrifiants testée. Cette amélioration de la robustesse/durabilité du contact peut, in fine, permettre l'augmentation de la pression de combustion dans le cylindre ainsi que permettre une réduction de l'épaisseur de film d'huile globale du contact, tous deux permettant une augmentation de l'efficacité du MCI. Finalement, la bonne compatibilité tribologique du revêtement DLC avec l'eau (faible coefficient de frottement et faible usure) en fait une solution prometteuse pour les futurs MCI à hydrogène.

Toutefois, les travaux illustrés présentent certaines limitations et hypothèses qui peuvent être améliorées. Quelques pistes d'améliorations sont listées ci-dessous :

- Le modèle peut être étendu au calcul d'une segmentation moteur complète. Dans ce but, les équations du modèle doivent être évaluées pour chaque géométrie de segment et les conditions aux limites de lubrification et de pression doivent être adaptées.

- Une solution efficace pour la prise en compte de la distorsion du contact segment/chemise doit être développée afin de prédire avec plus de précision les pertes par frottement du contact. La méthodologie analytique employée pour le contact cylindre plan ne pouvant être étendue à la complexité du contact SPC, une stratégie plus avancée doit être trouvée.

- L'amélioration du ratio signal sur bruit du banc d'essai à ≪chemise-flottante≫ doit être poursuivie afin de permettre des essais à plus hautes vitesses. Ainsi la stratégie d'équivalence mise en œuvre pourra être validée. De plus, les essais effectués au cours de ces travaux doivent être répétés afin de confirmer les tendances observées.

- Cette solution technique devra par la suite être validée pour des essais moteur avec combustion afin de contrôler son efficacité et durabilité. Pour mettre en œuvre cette solution au sein des MCI à hydrogène, il peut être intéressant dans un premier temps d'étudier les performances tribologiques du revêtement dans un mélange huile / résidu de combustion hydrogène.

Contents

List of Figures

List of Tables

Notation

Abbreviations

a-C	Amorphous carbon
a-C:H	Hydrogenated amorphous carbon
AW	Anti-Wear
BDC	Bottom Dead Centre
BMEP	Brake Mean Effective Pressure
CA	Crankshaft Angle
CO_2	Carbon dioxide
EHL	Elastohydrodynamic Lubrication
EU	European Union
EV	Electric Vehicle
FM	Friction-Modifier
FMEP	Friction Mean Effective Pressure
GCI	Gray Cast Iron
GHG	Greenhouse Gases
H	Hydrogen
H_2	Dihydrogen
H_2O	Water
HFRR	High Frequency Reciprocating Rig
HL	Hydrodynamic Lubrication
IC	Internal Combustion
ICE	Internal Combustion Engine
IMEP	Indicative Mean Effective Pressure
IVR	Iso-Viscous Rigid
LCC	Load Carrying Capacity
LIF	Laser-Induced Fluorescence
MoDTC	Molybdenum Dithiocarbamate
MoS_2	Molybdenum disulfide
PECVD	Plasma-Enhanced Chemical Vapour Deposition
PV	Pressure Velocity ratio
PVD	Physical Vapour Deposition
SI	Spark Ignition
STD	Standard Deviation
ta-C	Tetrahedral amorphous carbon

ta-C:H	Tetrahedral hydrogenated amorphous carbon
TDC	Diamond-Like Carbon
TDC	Top Dead Centre
US	United States
WHO	World Health Organization

Greek Symbols

α_f	Hydrodynamic friction correction coefficient
α_w	Hydrodynamic load correction coefficient
Δ_t	Dimensionless time-step
δ_t	Time step [s]
η	Fluid viscosity [Pa.s]
κ	Master parameter $\kappa = Amp\sqrt{\Lambda_{groove}}$
λ	Film thickness ratio $\lambda = h_0/\sigma$
Λ_{groove}	Dimensionless groove wave length
λ_{groove}	Groove wave length [m]
μ_{bound}	Boundary friction coefficient
Ω	Crankshaft rotational speed [rad/s] or [deg/s]
ρ	Fluid density [kg/m^3]
σ_q	Composite root mean square roughness [m]
τ_{hydro}	Viscous shear stress [Pa]
θ	Crankshaft angle [rad] or [deg]

Latin Symbols

$\bar{E}$	Mean energy loss per time unit [W/s]
$\bar{f}_{hydro}$	Mean viscous force [N/m]
$\bar{u}_m$	Reference mean horizontal speed [m/s]
$\bar{w}_h$	Mean hydrodynamic load [N/m]
ℓ	Ring face width [m]
$\tilde{F}_{hydro}$	Dimensionless shifted viscous friction
$\tilde{f}_{hydro}$	Shifted viscous friction force
$\tilde{P}_h$	Dimensionless shifted hydrodynamic pressure
$\tilde{p}_h$	Shifted hydrodynamic pressure [Pa]
$\tilde{W}_h$	Dimensionless shifted hydrodynamic load
$\tilde{w}_h$	Shifted hydrodynamic load [N/m]
A	Real contact area [m^2]
a	Ring vertical acceleration [m/s^2]
A_0	Nominal contact area [m^2]
Amp	Dimensionless groove depth
amp	Groove depth [m]
b	Bore diameter [m]

c	Connecting rod length [m]
d	Ring height [m]
dCA	Crank angle step [deg]
E	Young modulus [Pa]
e	Crankshaft radius [m]
f	Friction force per unit length [N/m]
F_t	Ring pre-tension force [N]
f_{asp}	Asperity friction force per unit length [N/m]
F_{hydro}	Dimensionless viscous friction
f_{hydro}	Viscous friction force per unit length [N/m]
$FMEP$	Friction Mean Effective Pressure [Pa]
g	Ring end gap prior to fitting [m]
H	Dimensionless geometry
h	Geometry height [m]
H^*	Dimensionless integration constant
h^*	Integration constant
H_0	Dimensionless minimum film thickness[-]
h_0	Minimum gap [m]
h_0^{MV}	Moes & Venner minimum film thickness
H_a	Dimensionless film thickness at the inlet point X_a
H_b	Dimensionless film thickness at the outlet point X_b
h_m	Minimum film thickness [m]
h_r	Reference film thickness [m]
h_a	Film thickness at the inlet point x_a [m]
h_b	Film thickness at the outlet point x_b [m]
H_{in}	Dimensionless film thickness upstream
h_{in}	Film thickness upstream [m]
H_{out}	Dimensionless film thickness downstream
h_{out}	Film thickness downstream [m]
I_r	Ring cross section [m^4]
$I_{...}$	First primitive with respect to x
$J_{...}$	Second primitive with respect to x
k	Time index
lvl	Time step refining level
m_l	Ring linear mass [kg/m]
p	Pressure [Pa]
P_h	Dimensionless hydrodynamic pressure
p_h	Hydrodynamic pressure [Pa]
p_r	Reference pressure [Pa]
P_w	Power loss [W]
p_{asp}	Asperity pressure [Pa]
P_{gas}	In-cylinder gas pressure [Pa]
r	Ring face radius [m]

r_i	Groove geometry
RPM	Engine rotational speed [rev/min]
s	Piston displacement from TDC [m]
t	Time [s]
t_r	Reference time [s]
U_m	Dimensionless horizontal mean velocity
u_m	Mean horizontal velocity [m/s]
u_{mean}	Mean reciprocating rig velocity [m/s]
V	Dimensionless vertical velocity
v	Transient term (vertical velocity) [m/s]
V_d	Displaced volume [m^3]
w	Load per unit length [N/m]
W_h	Dimensionless hydrodynamic load
w_r	Reference load [N/m]
w_{asp}	Asperity load carrying capacity [N/m]
w_{hydro}	Hydrodynamic load carrying capacity [N/m]
w_{tot}	Contact normal load [N/m]
X	Dimensionless coordinate in direction of sliding
x	Coordinate in direction of sliding [m]
X_a	Dimensionless inlet point abscissa
x_a	Inlet point abscissa [m]
X_b	Dimensionless outlet point abscissa
x_b	Outlet point abscissa [m]
x_l	Ring edge abscissa [m]
x_r	Reference abscissa [m]
Y	Dimensionless coordinate perpendicular to direction of sliding
y	Coordinate perpendicular to direction of sliding [m]
z	Coordinate in height direction [m]

Chapter 1

Introduction

Contents

1.1 Environmental Issue

In April 2022, an article published in the journal Nature Reviews Earth & Environment indicates that the freshwater planetary boundary is now transgressed [12]. Earlier in 2022, scientist concluded that humanity has exceeded another planetary boundary related to environmental pollutants: plastics [13]. Planetary boundary is a concept highlighting the impact of human action and activities on the Earth system "health". Nine boundaries were set during the research years based on the idea that maintaining the observed resilience of the earth system in the Holocene is a precondition for humanity's pursuit of long-term social development [12–15].
According to these researchers, "transgressing one or more planetary boundaries may be deleterious or even catastrophic due to the risk of crossing thresholds that will trigger non-linear, abrupt environmental changes within the continental- to the planetary-scale system" [16].

Today, six of the nine established planetary boundaries are exceeded as shown in Figure 1.1.

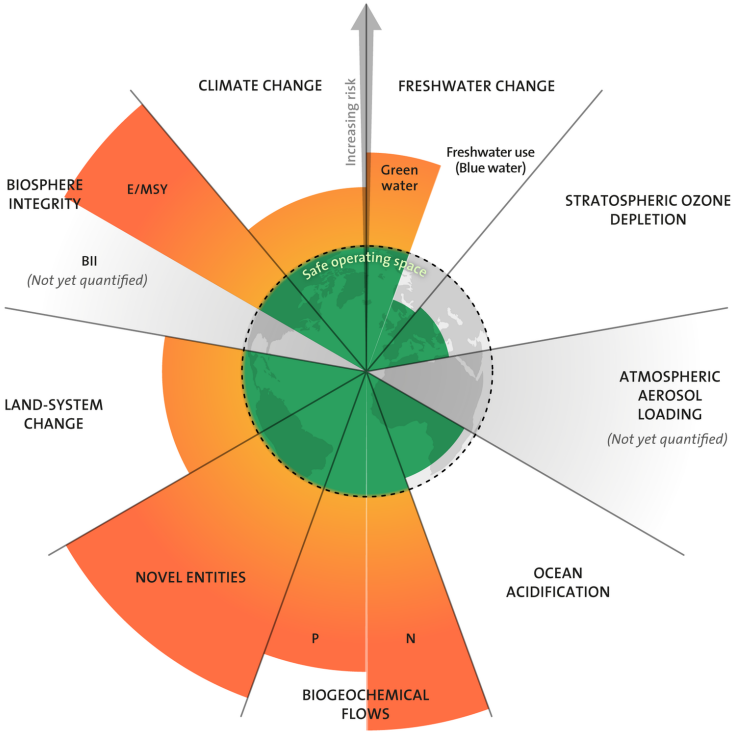

Figure 1.1: Planetary boundaries diagram; orange stands for an "overshoot" of the boundary, green for a "safe" state (from the "Stockholm Resilience Centre")

"Abrupt environmental changes within the continental- to the planetary-scale system" as called by Rockström et al. in 2009 are common these-days. Heat waves and drought are more frequent and severe all around the world affecting the lives of billions of people with food and water scarcity. Today, twice as many trees are burn due to wildfires compared to 20 years ago. Intense storms, floods and in general weather extremes are now common in regions such as Europe. Increased Earth's warming has contributed to melting permafrost, glacial retreat and sea level rise [17].

The main contributor to all these alarming facts is climate change caused by the emission of greenhouse gases (GHG), mostly carbon dioxide (CO_2) and methane (CH_4). GHG increase the Earth's surface temperature by allowing the sunshine to pass through and by stooping the infra-red radiation of the Earth, trapping the heat near the Earth's surface. The World Health Organization (WHO) calls climate change the greatest threat to global health in the 21^{st} century [18].
Our modern/industrialized way of life and consumption habits, relying on the use of fossil i.e. non-renewable energy, have a huge carbon footprint. Such as today, on the fifth of September 2022, the ambient air concentration of CO_2 is equal to 416 ppm [1] (part per million) while the planetary boundary is stated at 350 ppm.

[1] from the "Global Monitoring Laboratory"

As shown in Figure 1.2, in 2020 China is and since 2006 the world largest CO_2 emitter with roughly 30% of the world CO_2 emissions. The United States (US) are second and the European Union (of 27) third with respectively 13% and 7% of the world CO_2 emissions. Figure 1.3 shows the CO_2 emissions per capita of the same six countries including the world's mean value. Reduced to the number of inhabitants per country, oil producing countries with a relatively small population such as Qatar, Bahrain or Saudi Arabia are the ones that emit the most CO_2 per person. More populous countries such as the US, Australia and Canada have a high average per capita footprint, more than three times higher than the global average, mainly due to the country high total emissions. Finally, China with an average footprint of 7.4 tCO_2 per person is the fortieth country in the CO_2 emissions per capita ranking [19, 20]. This contradiction compared to Figure 1.2 can be explained by; first Chinese's large population (roughly 1.4 billion in 2020) and secondly because China is the world's leading net exporter of goods with many of the goods produced using carbon-intensive manufacturing processes (not accounted in the Chinese CO_2 emissions per capita in figure 1.3).

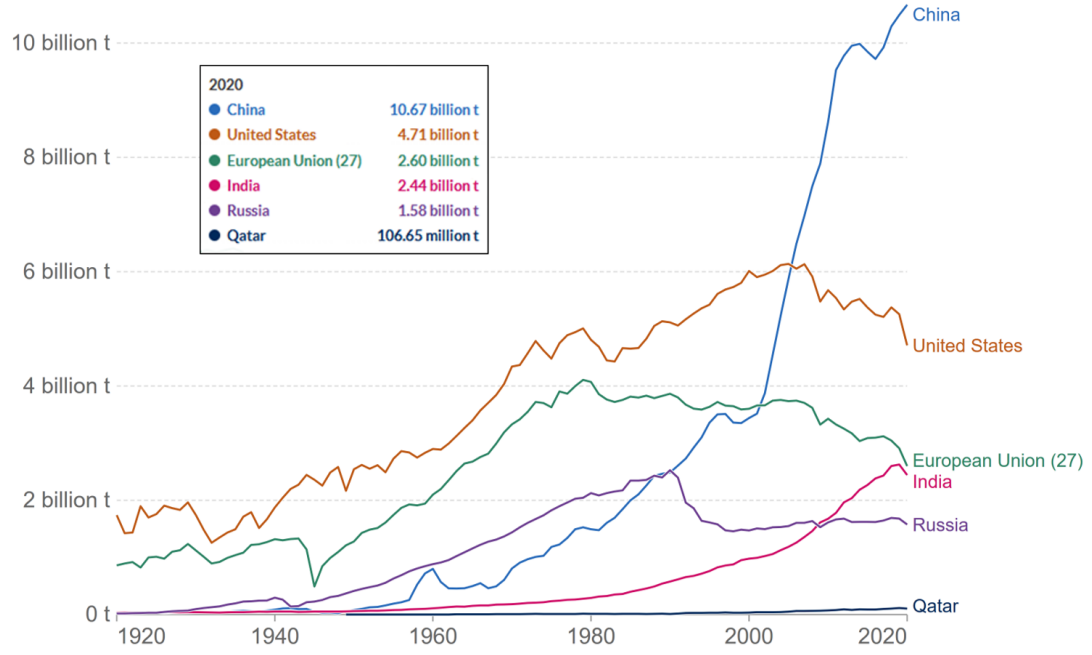

Figure 1.2: Annual CO_2 emissions (from fossil fuels and industry, land use change is not included) of the five world largest emitters plus Qatar [1].

GHG emission is strongly related to the production of energy used for electricity, heating, transportation, manufacturing, etc. and based on the burning of fossil fuels such as coal, oil and gas. Electricity and heat production are the sectors emitting the most GHG approximately 30% of the world global CO_2eq emissions as shown in Figure 1.4(a). This is true in countries relying on coal and gas for the electricity and heat production

such as in Germany or the US. In France, where the majority of electricity is produced using nuclear power, electricity and heat represents only 13% of the country GHG emissions compared to transport being the first with 30%. In the world, the transport sector stands for 17% of the total CO_2eq emissions in which road vehicles accounts for roughly 75%, aviation for 11.6% and shipping 10.6%, as detailed in Figure 1.4(b). This means that road transport accounts for over 13% of the world global GHG emission and plays a substantial part in the "overshooting" of the climate change planetary boundary.

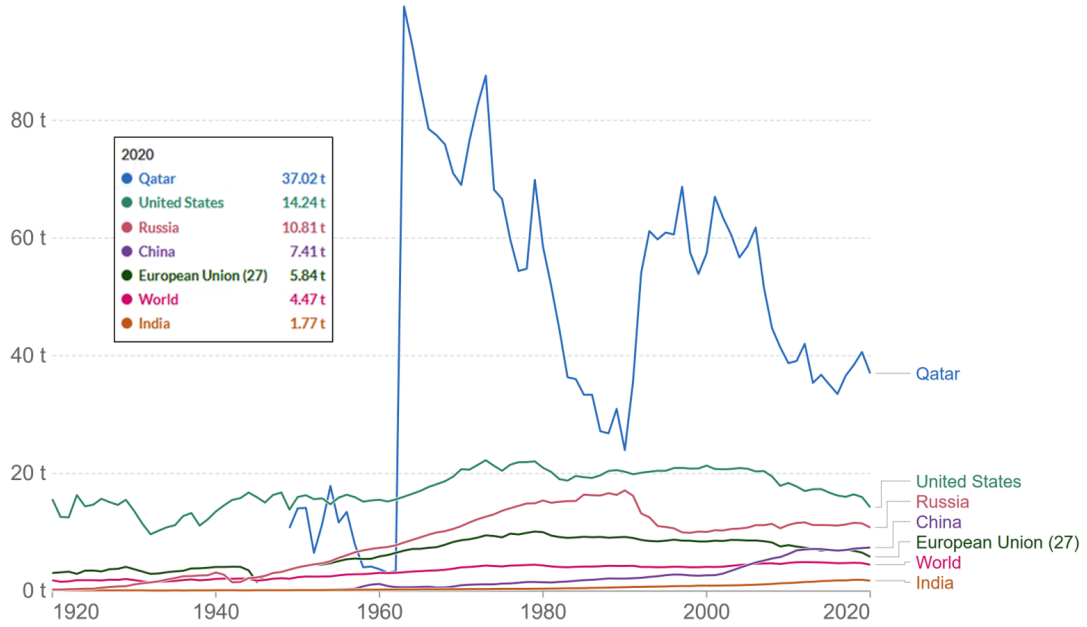

Figure 1.3: CO_2 emissions per capita [1] (from fossil fuels and industry, land use change is not included).

Besides the climate change, air pollution is also a major challenge for the future century. According to the WHO 99% of the global population breathe air that exceeds WHO guidelines limits and contains high level of pollutants. Air pollution is defined by the WHO as "contamination of the indoors or outdoor environment by any chemical, physical or biological agent that modifies the natural characteristics of the atmosphere". The major outdoor pollution sources include residential energy for cooking and heating, vehicles, power generation, agriculture/waste incineration and industry, for most driven by the burning of fossil fuel. Pollutants of major public health concern include particulate matter (PM), carbon monoxide (CO), ozone (O_3), nitrogen dioxide (NO_2) and sulphur dioxide (SO_2), which all result in heart diseases, chronic respiratory diseases and lung cancer.

Figure 1.5(a) highlights the contribution of the transport sector to the total emissions of the main air pollutants in 2017 in Europe while Figure 1.5(b) shows the trends from 1990 to 2017. Progress has been made since 1990 in reducing the emissions of many

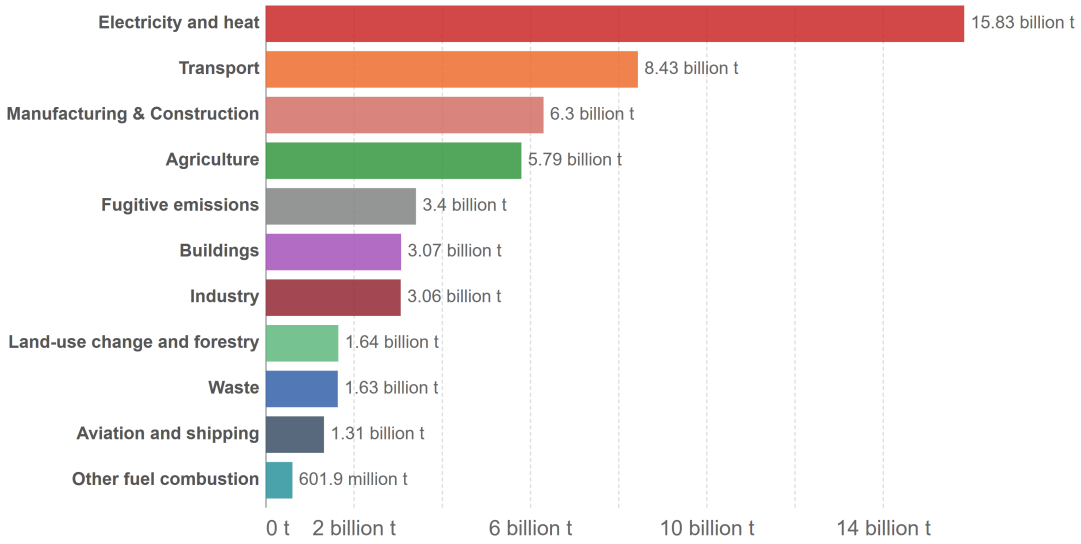

(a) By economical sector (based on 2019 data)

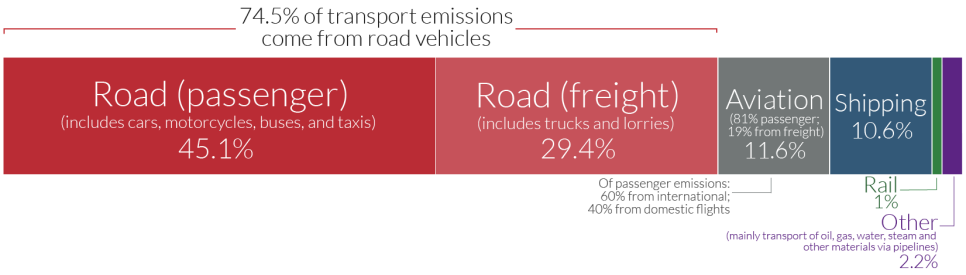

(b) Transport sector (based on 2018 data)

Figure 1.4: Worldwide greenhouse gas emission [1].

air pollutants from the transport sector mainly because of the establishment of European Emission Standards. However, the use of internal combustion (IC) engines as power-train for road transport, international and domestic shipping is still an important contributor to air pollution with 20% of the CO emissions, 48% of the NO_x emissions and roughly 10% of the PM and SO_x emissions.

According to the WHO, outdoor air pollution in both cities and rural areas was estimated to cause at least 4.2 million premature deaths worldwide with 91% of those deaths occurring in low- and middle-income countries. This justifies the "overshooting" of the chemical pollution i.e. novel entities planetary boundary as well as soon the atmospheric aerosol boundary .

1.2 The Automotive Context

The automotive industry is at a turning point in history, leaving the fossil-fuel era to enter the sustainable, zero-emissions era. This change is indeed induced by international organisations on the threat of the climate change and global population health emergency. Over the past few years and still, the automotive industry is facing some challenging times: stringent vehicle fuel-economy regulation and/or emission regulation (e.g. European Union), the COVID crisis and its impact on the production and missing components, the price increase of raw materials, petrol and diesel while the vehicle demand is still increasing. For several decades, researchers and automotive engineers have been working hard to make vehicles more efficient to reach the country's regulation. Lots of efforts have been made into the vehicle efficiency and especially into the IC engine tribology i.e. lifetime and friction loss reduction. Unfortunately, these efforts have often been spoiled by the weight increase of cars related to security, comfort and fashion. Such as today, the use of IC engine as power-train is still the main source of CO_2 and air pollutants.

On June 28, 2022 the European Council of environmental ministers confirmed the IC engine ban in 2035 for new cars and vans. The European Union (EU) council also agreed to raise the target for reducing car CO_2 emissions by 2030 to 55% instead of the previous 50%. In the US, twelve states have already adhered to the California's Zero-Emission Vehicle (ZEV) Program. Asian countries such as China (with the New Energy Vehicle mandate), Japan or South Korea are also proposing bans or implementing 100% sales of zero-emissions vehicles for the ten or twenty future years. For this purpose, worldwide car-makers are already on-track to electrify their fleet. As a result, 2.1 million electric car were sold in 2019 twice the number of 2017, reaching 2.6% of the worldwide market share. China being the world's largest electric car market with over 50% of the global sales (Europe second and US third) [21].

Despite the hype about electric vehicles (EV), EVs are today not the ultimate solution to the automotive industry challenges. Electric technologies have many drawbacks; first, in 2021 only 38% (35% in 2000) of the world electricity production is based on low-carbon technologies (including nuclear energy) [22]. For example, 60% of the US or Chinese electricity production is generated using fossil fuels and is not free from GHG. In addition, today's electricity production plants and transmission network are not capable to handle the everyday everyone car recharge demand. Second, today's batteries are heavy, their autonomy is low and battery lifetime is short and highly affected by the charge cycles, making these electrical solutions poorly adapted for heavy duty transports. Third, precious metal resources to build batteries and electric motors are rare, expensive and their exploitation is toxic for people and Earth. Last but not least, the recycling process of lithium-ion-batteries is still incomplete.

Meanwhile, hydrogen H (or dihydrogen H_2) is studied and seems to be a promising source of energy for the transportation sector. It can rather be used in fuel-cells to

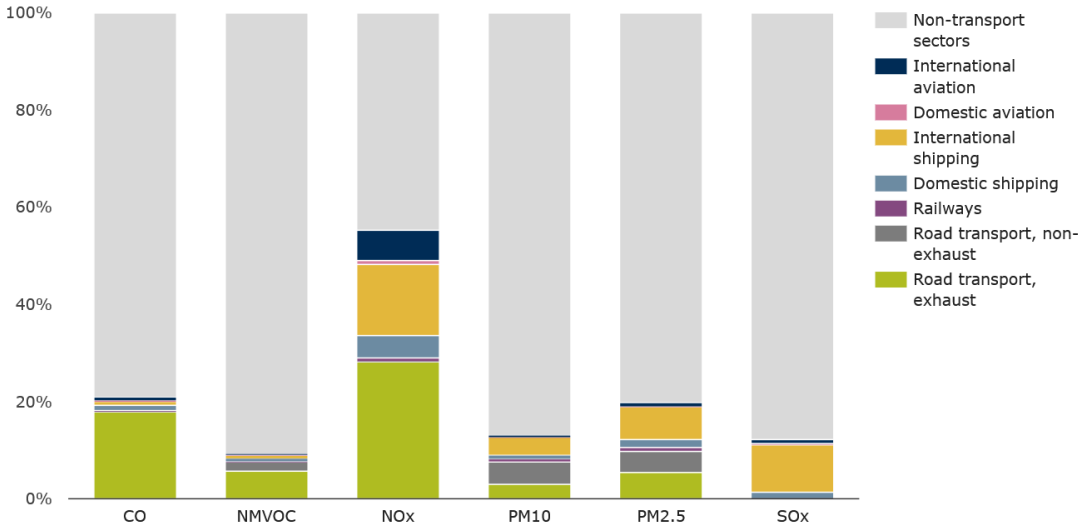

(a) Contribution (based on 2017 data)

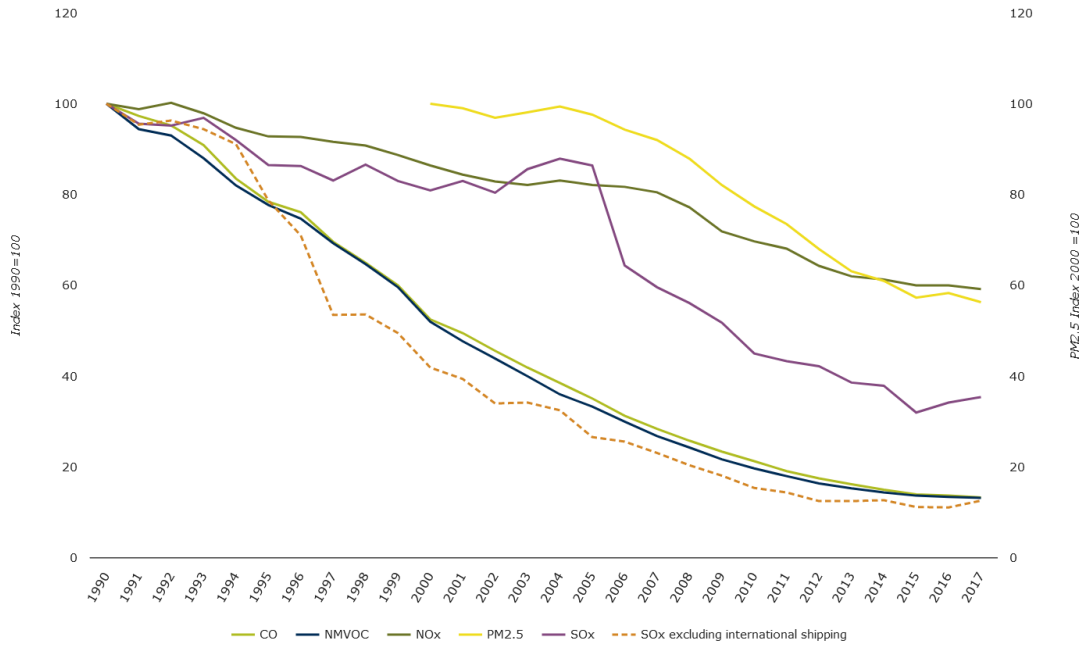

(b) Trend (1990-2017)

Figure 1.5: European transport emission of main air pollutants (from the "European Environment Agency")

generate electricity and power an electric motor or be injected as fuel in a modified IC engine. H is the most abundant chemical substance in the universe and is a non-toxic, highly combustible gas that produces water when burned. However, H (or H_2) is almost always as part of another compound, such as water (H_2O) or methane (CH_4) and must be separated into pure hydrogen to be used as fuel. Today, the majority of the world's hydrogen is produced using the steam methane reforming (SMR) process which releases a huge amount of CO_2. Electrolysis of water is an other, emission-free, industrial process to produce hydrogen, but it requires a large amount of electricity. In both cases, hydrogen industrial production is energy-intensive which is the first difficulty in developing this resource. Secondly, H_2 safety storage is a huge technical challenge because of hydrogen high volatility (i.e. lightest element) and high inflammability. Last but not least, the hydrogen delivery network/system is today non-existent.

These emerging technologies will in the near future play a key role to the automotive industry zero-emissions challenge. However today, these solutions can so far not stand the increasing and harsh demand of worldwide road and overseas transportation. Hybrid power-trains offer an suitable intermediate solution. Combination of an electric motor for slow speeds and an IC engine for high speeds, their technology is based on both the optimisation of the IC engine and the electric batteries. IC engines can also be modified to be used with renewable fuels such as biofuel or hydrogen, to fully exploit a century long optimised technology and to reuse a part of today's fuel distribution network/system.

With these points in mind the European Car Industry Association (ACEA) warns the EU council against banning a specific technology and calls for IC engines fuelled by e-fuels (as bio-diesel or hydrogen) to play a role in the low-carbon transition. It seems clear that traditional IC engine will still be part of the future of transportation and improving their performance remains a major investment for the automotive industry.

1.3 Internal Combustion Engine: Operation and Lubrication

According to Holmberg, Andersson and Erdemir [2], the IC engine friction losses stand for 9% of the total energy losses of a passenger car. Figure 1.6(a) gives the details of an passenger car energy consumption.

An Internal Combustion engine is a machine that partially converts thermo-chemical energy into kinetic energy to provide outstanding drivability and durability. Therefore, a fuel and air mixture is injected into a sealed internal chamber composed of a fixed cylinder and a moving piston. The combustion of the fuel-air mixture is initiated either by an ignition spark-plug (for a gasoline engine) or either by compression of the gas (for a diesel engine). The expanding combustion gas generates a high pressure into the combustion chamber, pushing the piston and rotating the crankshaft through a crank/rod

system. This motion is then transmitted to the vehicle's wheels through a gearbox. The majority of modern IC engines are based on the four stroke cycle shown in Figure 1.7. The cycle includes four distinct "times"; *the intake stroke*: the fuel-air mixture is sucked into the combustion chamber, *the compression stroke*: the mixture is compressed by the piston, *the combustion stroke*: combustion occurs due to ignition, the expansion of the high-temperature / high-pressure gas applies a force on the piston and generates work and *the exhaust stroke*: where the piston (under inertia effect) pushes the burned gases out of the engine. The intake and the exhaust strokes are driven and well timed by the cylinder head and especially the camshaft, cam and valve system.

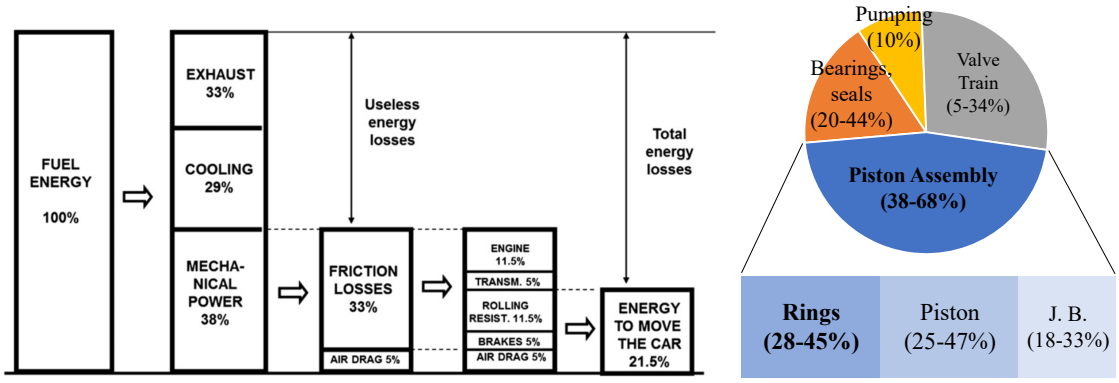

(a) Passenger car (b) IC engine

Figure 1.6: Automotive energy consumption breakdown [2, 3])

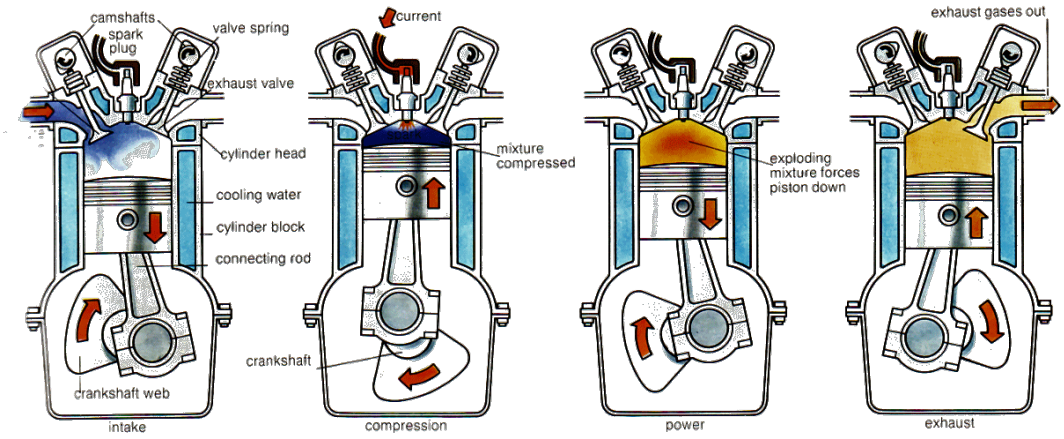

Figure 1.7: Four-stroke cycle for an Spark Ignition (SI) gasoline engine (from "www.gopracticals.com").

Modern vehicles have a durability of several hundred thousand kilometres and so does the IC engine often without any part replacement. Thus, meaning that the piston

assembly endures billions of engine cycles. This remarkable durability would not be possible without lubrication. Otherwise, while an engine component moves with respect to another one under a certain load, friction occurs generating a large amount of heat and causes damage to the solid surfaces leading to wear or in some cases to failure. To avoid this dramatic scenario, a viscous liquid called lubricant is interposed between the two surfaces. Lubricant primary purpose is to minimise wear and friction between the moving parts by avoiding any direct contact. Besides, the lubricant also works as a coolant, removing heat, dust, debris and contaminants from the contact zone. Thanks to a variety of chemical additives it can also avoid corrosion, sludge, and foam formation in the crankcase. As a result of tribological additives such as viscosity modifiers, anti-wear, friction modifiers, in addition to the engine oil viscosity, the lubrication film provides the ability to carry load, absorb shock and vibration in order to avoid wear.

An IC engine requires a large amount of lubricant because of the large number of moving parts. The engine oil has to be supplied to all the contact zones to avoid any failure, therefore the engine has a lubrication network similar to the example shown in Figure 1.8. The cylinder wall and the piston assembly are often lubricated by the oil flung of the con-rod big-end using centrifugal force. Some high-end engines, often for motor-sports, uses several oil jets to enhance the piston assembly lubrication. However, the engine lubrication system is sometimes not sufficient and starved lubrication conditions may occur in some contacts such as for the PRCL. For modern combustion engines, half of the engine mechanical losses is related to the piston assembly system (Figure 1.6(b)). Within this assembly, the PRCL contact is the most important source of friction.

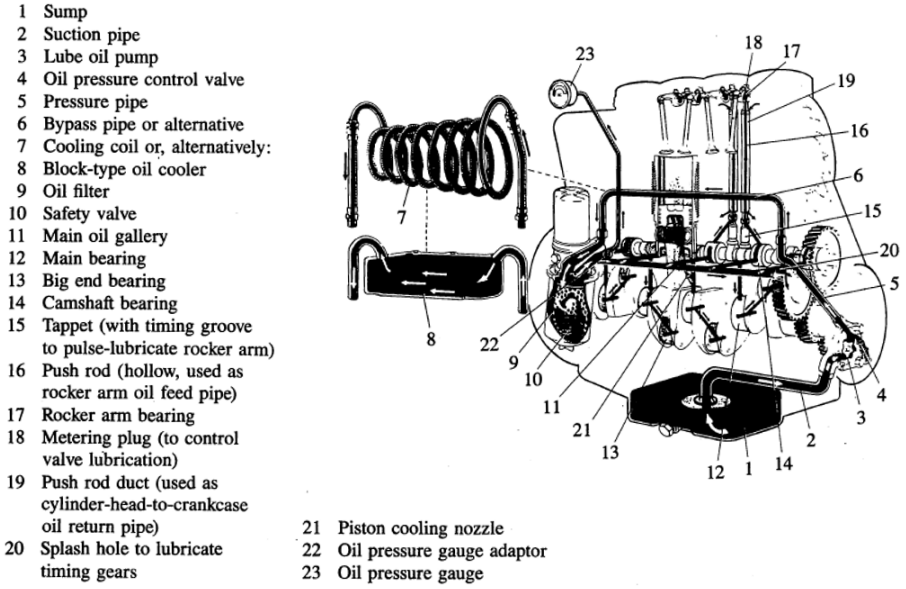

Figure 1.8: Lubrication system layout for an air-cooled diesel engine (*Courtesy Klöckner-Humboldt-Deutz AG* from [4]).

The Stribeck curve describes the different lubrication regimes of a specific contact. It defines the coefficient of friction as a function of the contact kinematic parameters: η the fluid viscosity, u the contact velocity and w the contact normal load per unit length.

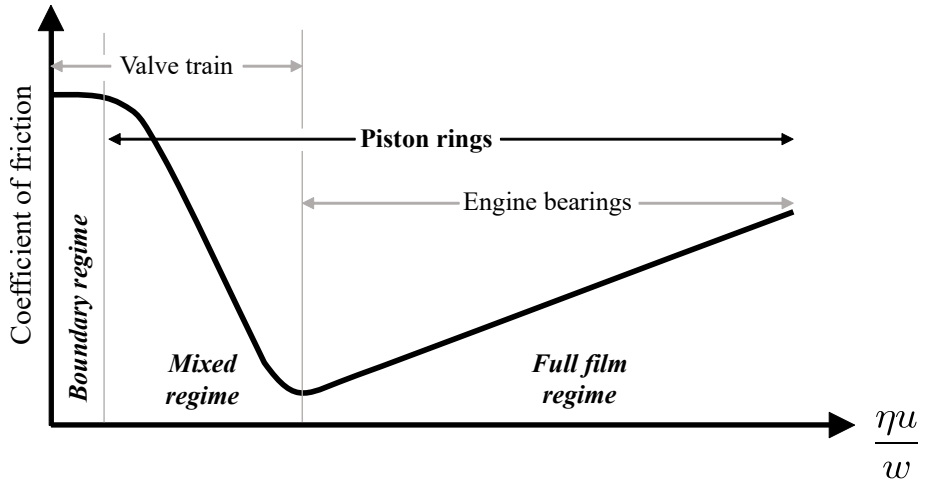

Figure 1.9: A Stribeck curve highlighting the lubrication regimes of different engine components.

Figure 1.9 outlines the lubrication regimes of some engine components. The Stribeck curve is divided in three zones corresponding to the three different lubrication regimes of the contact:

- **The Boundary lubrication regime:** For low speed / low viscosity / high load, the contact is in the boundary regime and friction is constant and as its highest value. The contact normal load is entirely carried by the solid to solid contact (i.e. surface roughness). No load is carried by the fluid which acts solely as a reservoir for additives.
- **The Mixed lubrication regime:** In the mixed lubrication regime, both the surface roughness (i.e. the asperities) and the fluid film carry the contact normal load. Friction can reach a minimum in this regime. The mixed regime is the most complicated lubrication regime to study because of the overlapping of the fluid and solid effects.
- **The Full film lubrication regime:** For high speed / high viscosity / low load, the normal contact load is completely carried by the fluid film. No solid to solid contact occurs and friction is only due to the shearing of the lubricant film thickness. The lubrication can either be Hydrodynamic (HL) for low contact pressures (order of magnitude of Mega Pascals) or Elastohydrodynamic (EHL) for high contact pressures (order of magnitude of Giga Pascals).

1.4 The Piston-Ring / Cylinder-Liner Contact

The piston assembly is composed of the piston, the piston ring pack, the piston pin and the connection rod (con-rod). During the reciprocating motion of the piston assembly inside the cylinder three main types of friction are induced (see Figure 1.6(b)): the piston skirt against the liner, the piston rings against the liner and the journal bearings, more detail can be found in [23]. Figure 1.10(a) gives a general view of the piston assembly and Figure 1.10(b) shows a sketch of the ring-pack liner subsystem.

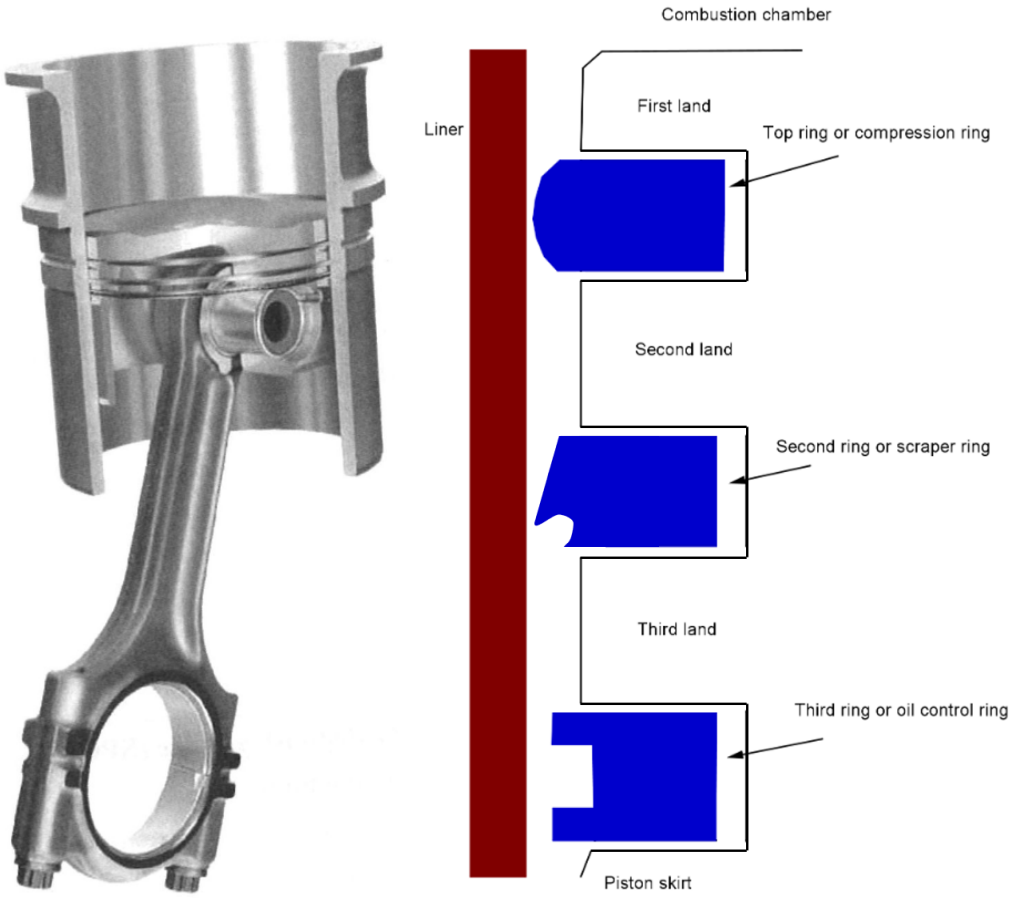

Figure 1.10: Piston pack [5] (left: global view - right: piston rings and liner)

Modern ring packs mainly consist of three rings that have the dual-opposite functions of sealing and lubricating. Sealing the combustion chamber from the crankcase to ensure high combustion pressure and engine efficiency without any lubricant degradation due to fuel leakage. Sealing the crankcase from the combustion chamber to avoid any oil leakage and burning resulting in pollutant emission. On the contrary, lubrication is needed between the rings and the liner to reduce friction and avoid wear. It is a sharp trade-off between lubrication and sealing i.e. performances and emissions.

A piston ring is a metallic elastic ring which fits perfectly inside the cylinder bore by elastic deformation. It is placed on the outer diameter of the piston, into a groove slightly larger than the ring. The ring pre-tension pushes it against the cylinder wall sealing the combustion chamber from the crankcase. To ensure the ring pack functions, each ring has its specific design according to its role:

- **Top ring or compression ring:** It is the closest ring to the combustion chamber and therefore provides the major part of the combustion gas sealing. It has generally a barrel-shaped face and is often chrome, molybdenum or Diamond-Like carbon coated because it has to withstand high loads and high temperatures during combustion. The top ring pre-tension is in general between 5 and 20 N.

- **Second ring or scraper ring:** It has both top ring and third ring functions. It ensures some gas sealing and also scrape down some engine oil from the liner. Therefore it has often a tapered or napier/hook shape. The second ring pre-tension is in general between 5 and 30 N.

- **Third ring or oil control ring (OCR):** It is the closest ring to the crankcase and therefore it controls and regulates the oil distribution on the cylinder liner. Its geometry is more complex than the other rings and can be composed of one, two or three parts. It may have an additional spring to enhanced its pre-tension. The OCR ring pre-tension is in general between 10 and 60 N.

The traditional cylinder liner surface finish is a cross-hatched pattern with deep and continuous grooves and relatively smooth “plateaux” [24] as shown in Figure 1.11(a). This liner finish is generated during the “honing” process by rotating an abrasive grinding stone along the gray cast iron (GCI) cylinder bore to improve it geometric form. This process has been and is still widely used for mass production in IC engines. Other processes such as laser texturing are more flexible but are expensive and are only used for prototype engines. Liner texture acts as a micro-bearing, an oil reservoir and a debris trap and is therefore crucial to avoid the PRCL contact failure. However, the liner texture may act differently with respect to the ring geometry. Bouassida [25] has shown that liner texture, especially deep grooves, can decrease the fluid film load-carrying capacity (LCC) for a convergent shape ring. On the contrary, Ma et al. [26], have shown that the liner texture is essential to flat shape rings to generate hydrodynamic lift and avoid direct contact.

In a search for weight reduction, light aluminium engine blocks are becoming more frequent in passenger cars often with the application of a thermal spray or a physical vapour deposition (PVD) coating on the cylinder wall. Compared to regular cross-hatched liner surface finish, coated bores are significantly smoother with no valleys or grooves. Coated liners have an isotropic very smooth roughness with localised pores due to the deposition process. These liner finishes are usually called “Mirror-Like”, Figure 1.11(b) gives an example of a coated liner topography. Coated bores are recently

studied to improve the PRCL tribological performances such as in [27], as well as to reduce the oil consumption and blow-by. This kind of liner finish is often use in high-end IC engine such as in Formula 1 power-units.

The PRCL contact is one of the most complicated tribological interface to analyse in an IC engine, especially because of the varying operating conditions. The piston linear speed varies along the stroke from zero speed at the dead centres to several meters per second at mid-stroke. The rings normal load varies from several Newtons to hundred Newtons during the combustion phase. Liner temperature varies usually from $80°C$ at bottom-dead-centre (BDC) to $160°C$ at top-dead-centre (TDC) with the peak burned gas temperature in the cylinder of the order of $2000°C$ [4]. This temperature change induces a 80% drop in oil viscosity (for a 5W-30 engine oil) meaning a huge change in the fluid lift capabilities. Furthermore and as shown in Section 1.3, the PRCL lubrication is barely well distributed on the bore's circumference and the rings operates mainly under starved conditions. Over a single stroke, the ring-liner contact may experience boundary, mixed and full film lubrication regime [28] as well as strong transient effects which are all relatively complex to model.

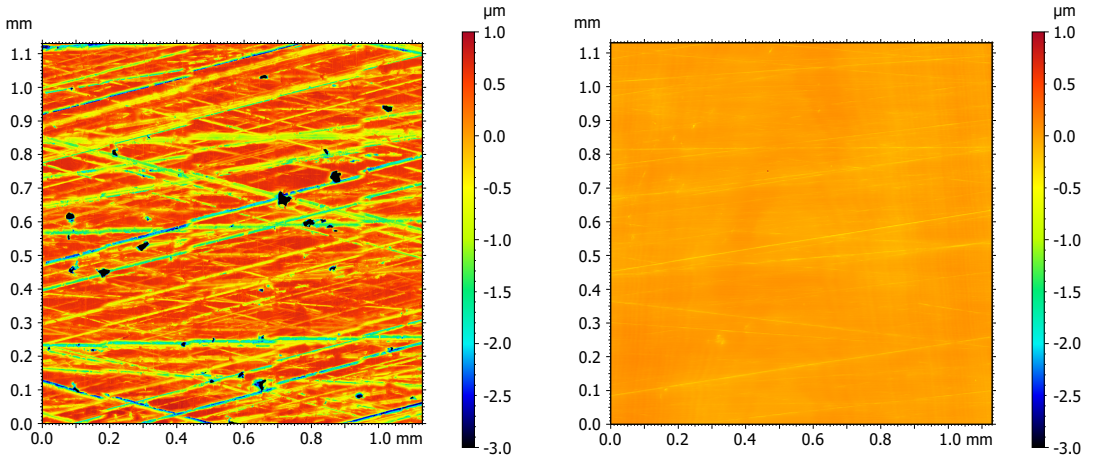

(a) Cross-hatched (b) Mirror-like

Figure 1.11: Liner surface finish.

1.5 Diamond-Like Carbon Coating

One efficient technical solution to reduce friction is to use enhanced coatings such as Diamond-Like Carbon. Diamond is known as a three-dimensional solid with some of the best mechanical properties: highest hardness, highest Young's modulus, etc. However, synthetic diamond is inconvenient as a coating material because its growth temperature

is high. On the contrary, Diamond-Like Carbon (DLC) has the huge advantage of having a reasonable growth temperature, relatively low cost and large-area vacuum deposition methods [29].

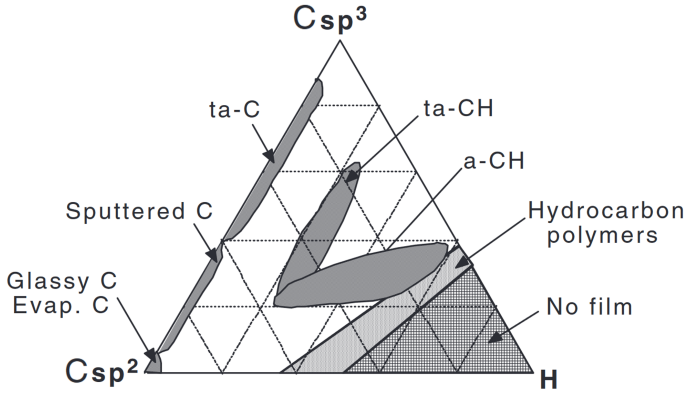

Figure 1.12: Ternary phase diagram for various DLC films (adapted from [6]).

DLC is an amorphous carbon (a-C) thin material with a high fraction of sp^3 carbon hybridisation (i.e. diamond like bounding) and a small fraction of sp^2 carbon hybridisation (i.e. graphite like bounding) [6]. DLC coatings can contain none or a substantial quantity of hydrogen (a-C:H) and their composition is usually described using a ternary phase diagram (proposed by Robertson and Ferrari) and shown in Figure 1.12. DLC films are usually prepared by a deposition process involving energetic ions which produce the sp^3 meta-stable bounding. DLCs are used as protective coating in a lot of areas and can also provide low friction under specific lubricated conditions [29]. To improve their compatibility with engine oil additives, mostly reactive to steel, they can be alloyed with metals such as Ti, W, Fe and Mo [30].

DLC coatings are these days common in the automotive industry and have shown to provide friction reduction and lifetime extension [31]. They are often applied to parts operating under severe boundary lubrication conditions such as the piston compression ring and the valve-train. In the recent years, automotive companies designing motor-sport IC engines are interested in wear resistant DLC coated bores and their potential to reduce friction losses. Only a few reports about the tribological properties of DLC coated liners exist. In 2004, Sato et al. [32] experimentally showed a 10 % reduction in the Friction Mean Effective Pressure (FMEP) and an improvement of the wear resistance studying a DLC coated liner. In 2012, Rejowski et al. [33] studied the friction reduction potential of a DLC coated Heavy-duty cylinder liner in comparison with an uncoated cast iron cylinder. The coating was deposited on top of the classical cross-hatched texture with no additional polishing. They experimentally showed a reduction in friction of roughly 19 % for the DLC coated liner. In 2018, Koszela et al. [34] studied the combined effect of surface texturing and DLC coating of the bore on the efficiency of an motor bike engine. They concluded on 4.8 horsepower increase (5.8 %) provided by both the DLC coating

and the dimple texture. Recently, Dolatabadi et al. [35] studied using numerical tools the effect of the DLC coating liner on the engine fuel economy and emissions. Contrary to the previously cited experimental studies, they found a negative impact of the coating on the PRCL friction. This is caused mainly by low thermal conductivity of the DLC, leading to an increase in the liner temperature, a decrease in the oil viscosity, a thinner oil film thickness and thus an increase in the film shearing and in the amount of boundary friction.
According to the lack of research on the DLC coated liners and despite the use of this technique in Formula 1 power-units, it is nowadays difficult to conclude on its benefit.

1.6 Thesis Objectives

The world industry and transport sectors are initiating a crucial energy transition driven by the climate emergency and the recent geopolitical issues. The automotive industry is mainly focusing on the electrical technology to power passenger cars. However, this technology is today unsuitable to heavy-duty vehicles. Consequently, traditional IC engines will still be produced and used in the ten to twenty future years, mostly paired with an electric motor (hybrid engine) or powered with alternative fuels (bio-diesel, bio-alcohol, hydrogen). Hence, increasing the IC engine efficiency, sustainability and reliability is still a crucial research topic. For this purpose, the effort mostly focuses on the PRCL contact which generates roughly 50% of the engine energy loss and controls the majority of the engine oil consumption. Nevertheless, the PRCL tribology is complex because of the varying operating conditions. Despite a large number of numerical and experimental studies, no straightforward method exists to improve its performance. Recently, the trend is to manufacture smooth liners for weight reasons contrary to typical grey cast iron liners. Nonetheless, this technical solution might also lead to a reduction in friction and oil consumption. In addition, the deposition of hard coatings such as DLC on both the rings and the bore seems to be a promising technical solution for improving the contact tribological performance (wear and friction-wise).
Based on this, the main purpose of this research work is to evaluate the friction reduction of the DLC coated PRCL contact. This main objective comprises the following specific objectives:

- **To experimentally evaluate the tribological compatibility of the DLC coating intended to the PRCL contact with a variety of lubricants.**
- **To develop a numerical method to predict the PRCL friction:** in order to quickly evaluate the friction reduction of the DLC coating and optimise the contact parameters, as well as creating a deep understanding of the contact lubrication.
- **To experimentally validate the numerical method.**
- **To develop an experimental method to evaluate the PRCL friction:** in order to quantify the friction reduction of the DLC coating as well as to confirm the computer simulation predictions.

1.7 Thesis Structure

In order to achieve the multiple objectives detailed in Section 1.6, several tasks were performed. For a better comprehension of the work, the thesis is organised in five chapters:

- **Chapter 2 - Model:** after a brief state of the art about the PRCL friction prediction, the model general assumptions and operating conditions are listed. Then the new line-contact, mixed lubrication model equations and solution methods are outlined.
- **Chapter 3 - Experimental Devices:** after a brief state of the art of the experimental methods to evaluate the PRCL friction, the different tribological test-rigs used in this work are described. The DLC coating / lubricant compatibility results are discussed and the floating liner optimisation is detailed.
- **Chapter 4 - Model Validation:** the model results are compared to a fully numerical solution and to line-contact friction measurements in order to test its relevance. Consequently, the model is upgraded to account for the sample macro-geometry.
- **Chapter 5 - Results:** the lubrication of the piston compression ring is studied by means of the improved PRCL test-rig and the theoretical model. The DLC coating benefits are both experimentally and numerically evaluated. The friction predictions are compared to the measurements, the differences and adjustments are discussed. In addition, the code ability in evaluating the best compression ring parameters are presented.

Chapter 2

Model

Contents

2.1 Introduction

The Piston-Ring / Cylinder-Liner (PRCL) contact operates mainly under full film and mixed lubrication regimes (see Section 1.3). In the mixed lubrication regime, the normal load is carried by both hydrodynamic pressure and the interaction between the surface asperities. Therefore, to predict accurately the PRCL friction one has to model mixed lubrication. Commonly, fluid and asperity Load Carrying Capacities (LCC) are computed separately and are afterwards superimposed to balance the normal load. In

1972, the theory of the first mathematical model of mixed lubrication was presented by Christensen [36]. He generalised his stochastic model of hydrodynamic lubrication to deal with the mixed lubrication conditions. Half a decade later, Lebeck et al. [37] extended Christensen's theory by using a random height distribution to model the surface roughness. Nowadays, this theory is commonly used either relying on deterministic or stochastic models. One well-known example is the Lulea Mixed Lubrication Model (LMLM) developed by Sahlin et al. [38, 39] and used for instance in [40] to predict the PRCL friction.

Our goal is to develop a fast but relevant friction prediction of the Diamond-Like Carbon (DLC) coated PRCL contact. Therefore, Christensen's idea is extended and adapted to our specific contact. Some assumptions related to the contact load and surface topography are made and detailed in the following section.
Existing stochastic and deterministic models for the PRCL lubrication are detailed. On one hand, stochastic theories benefit is to be fast, but they often rely on contact parameters toughly measurable. On the other hand, deterministic theories are the most accurate way to model a physical phenomenon but are often difficult to use and are time-consuming. Deterministic models are thus hardly implemented by industrials compared to stochastic theories.
Hence in this study, the full film lubrication model is based on a fast and simple line-contact, time-dependent, semi-analytical solver developed by Biboulet et al. [9]. The solid-to-solid part of the model relies on a so called "load-distance" curve computed using a measured surface topography as input of a deterministic contact mechanics numerical tool developed by Sainsot [10]. This combination allows for a rapid friction prediction all along the piston stroke accounting for lubricant starvation, lubricant reserve build-up, transient effects, real surface topography, speed, load and viscosity variation.

2.2 State of the Art

The following section is mainly based on Kared Sophia Bastidas Moncayo complete literature review from her recent thesis work called "Experimental and Analytical Study of the Mechanical Friction Losses in the Piston-Cylinder Liner Tribological Pair In Internal Combustion Engines (ICE)" [41].

2.2.1 Full Film Lubrication Model

Existing full film lubrication models are principally based on the Reynolds equation. In 1886, Reynolds [42] described using one equation the hydrodynamic behaviour of thin fluid films. He derived his formula from the Navier-Stokes equations using the following assumptions:

- both inertia and external forces are neglected (laminar viscous flow),

- the narrow gap assumption: the dimension in z direction is much smaller than those in x and y directions,
- the condition of no-slip at the wall boundary,
- the fluid is newtonian and continuous,
- the pressure is constant over the film height,
- the bodies are rigid,

The two-dimensional Reynolds equation reads:

$$\underbrace{\frac{\partial}{\partial x}\left(\frac{\rho h^3}{12\eta}\frac{\partial p}{\partial x}\right)+\frac{\partial}{\partial y}\left(\frac{\rho h^3}{12\eta}\frac{\partial p}{\partial y}\right)}_{\text{Poiseuille}}-\underbrace{\frac{\partial(u_m\rho h)}{\partial x}}_{\text{Couette}}-\underbrace{\frac{\partial(\rho h)}{\partial t}}_{\text{transient}}=0 \tag{2.1}$$

where ρ is the fluid density, η the fluid viscosity, h the film thickness, p the fluid pressure, $u_m=(u_1+u_2)/2$ the mean velocity and x and y the plane coordinates. The first two terms describe the pressure generated by the last two terms. The Couette term (or here wedge term) describes the classical converging gap effect as the transient term describes the film thickness variation as a function of time; the squeeze effect. By solving this equation, one can estimate the fluid pressure distribution, fluid LCC, viscous friction force and fluid flow [43].

The first paper about hydrodynamic lubrication of piston rings was written in 1936 by Castelman [44]. Since then, many different models have been published and two main approaches can be named: the analytical approach and the numerical approach.

On the first hand, PRCL analytical models often assume that the bodies in contact are infinite, with smooth surface and no side flow. Therefore, they are often based on the simplified one-dimensional Reynolds equation:

$$\frac{\partial}{\partial x}\left(\frac{\rho h^3}{12\eta}\frac{\partial p}{\partial x}\right)-\frac{\partial(u_m\rho h)}{\partial x}-\frac{\partial(\rho h)}{\partial t}=0 \tag{2.2}$$

where the force that pushes the ring against the liner wall is balanced by the fluid film LCC.
Furuhama in 1959 [45] was the first to study the piston ring hydrodynamic lubrication analytically by solving the one-dimensional time-dependent Reynolds equation. The studied piston ring profile consisted of a quadratic section followed by a flat section.
Dowson et al. [7, 46] extended Furuhama work to the entire ring pack. The pressure boundary conditions are set equal to the combustion chamber pressure for the up-stroke and equal to the crankcase pressure for the down-stroke. By mean of a forward stepping process, the Reynolds equation is solved for a range of crank angles to obtain h_m as a function of the operating conditions (piston speed, ring load and liner temperature). The

lubrication of the ring pack is governed by flow continuity between the rings (assuming no external oil supply). Thus, meaning that the lubricant film encountered by a ring is that left by the preceding ring allowing for starvation calculations (see Figure 2.1).

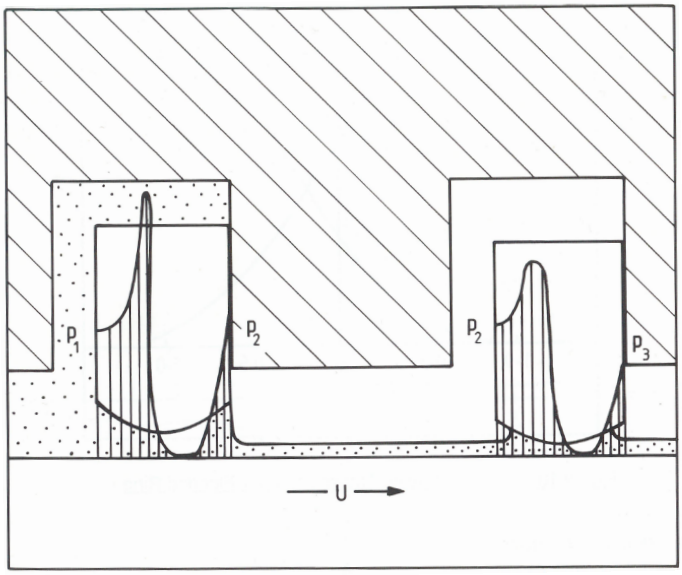

Figure 2.1: Piston ring pack lubrication theory by [7]

Ruddy et al. [47] extended Dowson's work by adding the piston groove profile in the lubrication analysis. The study also includes the angular distortion of the ring, the ring twist and wear of the piston groove. They concluded that the piston groove profile has a big influence on the ring lubrication and oil transport.
In 2000, Sawicki et al. [48] proposed an analytical solution of the piston ring lubrication using a mass conserving cavitation algorithm. They created a system of five non-linear equations based on the one-dimensional Reynolds equation. Both Reynolds cavitation and Jakobsson-Floberg-Olsson (JFO) theories were tested. D'Agostino et al. [49] used an open-end boundary condition allowing them to find the point where the hydrodynamic pressure reaches the fluid saturation pressure.
Perera et al. [50] added viscosity variation due to heat generation in the contact by means of an analytical solution of the energy equation.
Morris et al. [51] presented an average analytical flow model based on the theory developed by Patir and Cheng [52] and also included the surface topography using the approximation of Greenwood and Tripp [53]. They later extended their model by including a thermal model to determine the effective oil temperature in the contact [54]. Gore et al. [55] finally extended the Morris et al. model by adding the oil density variation as a function of pressure and temperature.
Biboulet et al. studied the analytical solution of a starved hydrodynamically lubricated line contact [56, 57]. They later extended this theory to textured PRCL contacts [58]. Recently, Biboulet et al. presented a semi-analytical, simple and fast solver for the

time-dependent iso-viscous-rigid smooth line contact [9]. The solver is based on a system of four non-linear equations and accounts for starvation (geometrical and lack of lubricant), upstream oil reserve build-up and oil transport.

On the other hand, the numerical method to solve the Reynolds equation consists in dividing the contact area into finite subdivision, creating a mesh, and compute approximations of the real solution in each subdivisions. Solutions are then obtained by means of interpolation, three main groups of numerical methods exist: Finite Difference, Finite Element and Finite Volume.
In 1974, Hamilton et al. [59] developed, for one piston ring, an iterative method to solve the time-dependent one-dimensional Reynolds equation. The Reynolds equation is analytically integrated to obtain the pressure distribution in which the variables are replaced by their finite difference equivalent. The pressure distribution is then computed using the over-relaxation method and the film thickness is obtained by numerical differentiation. h_m is finally determined using the ring load balance equation.
Fifteen years later, Miltsios et al. [60] presented a three piston ring model based on the two-dimensional Reynolds equation solved using the Finite Element Method (FEM). The model accounts for bore distortion and ring twist. The piston ring gap is assumed to be small without any oil flow trough it. The Reynolds equation is written dimensionless and is solved using a Newton-Raphson iteration scheme.
In 1996, Ma et al. [61] developed a different numerical approach for the study of the piston ring lubrication known as the flow continuity algorithm. This model is based on Paydas and Smith's [62] work on journal bearings itself based on Elrod's cavitation algorithm [63]. It incorporates a switching function (or cavitation index) that changes depending on the region where the equation is applied (full film region or cavity). Two equations are derived, the pressure distribution applied to the full film region and the degree of lubricant filling applied to the cavitation region. The study was carried out on one piston ring in a distorted bore accounting for ring starvation and considering oil accumulation in front of the ring. Gas blow-by can also be computed using this algorithm.
Liu et al. [64] combined the solution of the two-dimensional Reynolds equation by finite difference with an asperity contact model based on the Greenwood and Tripp [53] approach, creating a mixed lubrication model. Starvation is considered in the model by assuming that the oil available for one ring is equal to the oil left by the preceding ring. The face profile of the ring is a parabola and the half-Sommerfeld boundary condition is applied for cavitation. Later on Liu and Tian [65] made some improvements to Ma et al. [61] flow continuity algorithm. Firstly, the discontinuity in oil flow at the separation point is reduced by adding a transition zone between the fully- and partially-filled regions. The aim was to improve the numerical solution and to represent how the oil gradually attached to the ring. Secondly, a piece-wise linear function is implemented to give a smooth transition between the fully- and partially-filled regions, especially near the point of minimum clearance. The model equations were solved using a finite volume method.

Wannatog et al. [66] presented a three dimensional piston ring motion simulation where the rings could move and twist in the piston groove. Even if the main goal of the model was to study the ring motion and blow-by flow, a one-dimensional piston ring lubrication model was also integrated. The influence of the ring and liner roughness on the hydrodynamic lubrication is accounted for, using flow factors as proposed by Patir and Cheng [52]. Equations are solved by finite difference.

Recently, Taylor [67] studied the squeeze film lubrication in piston rings and reciprocating contacts by means of a simple one-dimension lubrication model. Taylor showed that the oil film thickness close to the piston reversal positions is very sensitive to the ring profile radius of curvature; the "flatter" the piston ring, the greater the oil film thickness. Also, he concluded that cavitation effects disappeared around the bottom dead centres. Due to the squeeze effect, the separation point of the lubricant moved out to the piston ring edge and the piston ring is completely covered in oil.

The effect of the surface roughness on the hydrodynamic lubrication has been firstly analysed and modelled by Patir and Cheng [52, 68] in 1978. The developed model uses "flow factors" included as coefficient in a modified Reynolds equation solve on a smooth global domain. Aside from the fact that the Patir and Cheng (PC) flow factors are based on stochastic parameters, the PC method cannot properly simulate the effects due to anisotropic roughness or roughness having a diagonal layout with respect to the flow direction [38]. To overcome these difficulties, the homogenized method is used to derive a homogenized Reynolds equation that approximate the average effect of random surface roughness as used in Sahlin et al. [38, 39] mixed lubrication model. Also, to overcome the uncertainty of stochastic theories, Noutary et al. [5, 69] created a deterministic robust piston ring lubrication solver. Using multigrid techniques based on Alcouffe's [70] idea they were able to precisely study the influence of measured liner textures on the hydrodynamic lubrication of the PRCL contact. They concluded that groove depth and density are important factors determining the LCC, whereas the groove shape has only a small influence. Also to avoid the use of stochastic parameters, Li, Chen and Tian [71–73] developed a deterministic model to simulate the hydrodynamic pressure and shear stress between a twin land oil control ring and a rough liner. It was later extended by Liu [74] to the top two rings based on Li's [75] multiphase deterministic oil transport model. It was recently used by Liu et al. in [76].

2.2.2 Contact Mechanical Model

Hertz pioneering work published in 1882 [77] studied the frictionless contact between smooth elastic solids with approximated parabolic profiles close to the contact area. This theory predicts that the real contact area A increases non-linearly with the squeezing force F_N as $A \sim F_N^{2/3}$ while experiments for randomly rough surfaces shows that $A \sim F_N$ (for a purely elastic contact). Seventy five years later, Archard [78] showed theoretically that the real area of contact is proportional to the load using a more realistic model. The

roughness is described by an idealised hierarchical model consisting of small spherical bumps on top of a larger spherical bumps and so on, explaining the contact basic physics but this model can not be used to represent real surface roughness.

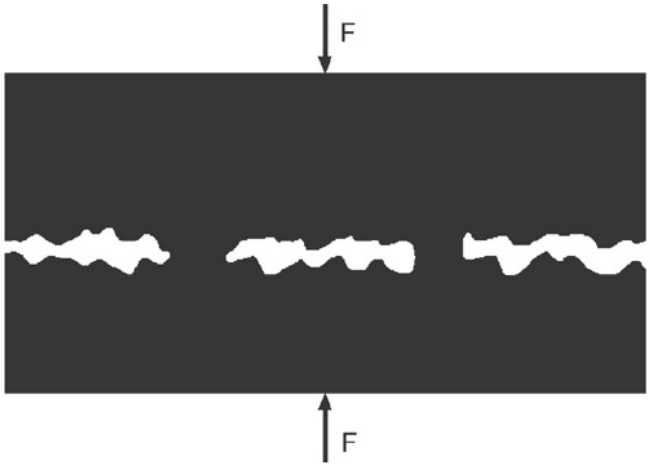

Figure 2.2: Schematic of the contact mechanics problem: how large is the real area of contact when two solids with rough surfaces are pushed into contact ? [8]

In 1966, Grennwood and Williamson [79] presented a more realistic and applicable model. The rough surface is described as a variety of spherical bumps of equal radius of curvature R with a Gaussian distribution of heights as shown in Figure 2.3). The Hertzian theory is then applied to each spherical bump in contact. Using this model, they predicted that the real contact area is nearly proportional to the load.
Four years later, this theory was extended to the contact of two nominally flat rough surfaces by Grennwood and Tripp [53]. In 1976, Bush et al. [80] refined Greenwood and Williamson's theory by approximating the asperities summits with paraboloids.
The above cited contact mechanical models all assume that the area of real contact is very small compared to the nominal contact area and rely on a variety of small Herzian-like contacts leading to three main drawbacks. First, the description of the asperities as spherical bumps or paraboloids with an average radius of curvature R is not physical. Secondly, they neglect the interaction between the squeezed asperities. Thirdly, these theories can only be applied for $A << A_0$.
To overcome these difficulties, Persson [81, 82] has more recently developed a model based on a different approach. The Persson model starts from a near complete contact ($A \simeq A_0$) to move to low squeezing loads. Initially developed to study the tire-road contact, it accounts for the elastic coupling between the deformed asperities and is approximately valid for all squeezing force [8]. The surface roughness power spectrum noted $C(q)$ is the only input related to the roughness and can be easily obtained from the surface height profile [8]. However, the parameter $C(q)$ is strongly affected by the measured surface boundaries cut-off and measurement accuracy.

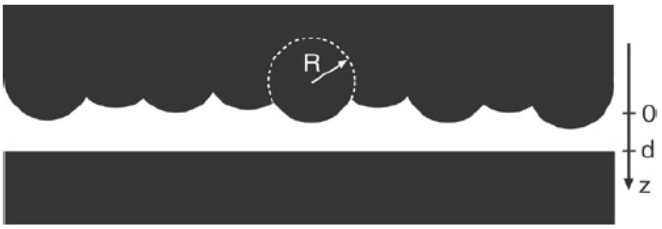

Figure 2.3: Greenwood & Williamson contact theory between a smooth plane and a rough surface. All asperities with height z greater than the separation d make contact [8].

Although the Persson theory is more recent, a great majority of existing tribological models rely on the "old-fashioned" Greenwood and Tripp [53] stochastic theory when it comes to boundary lubrication. And even if the "Greenwood & Tripp" theory relies on an simplified representation of the surface topography and on coarse simplifying assumptions, it is still an industrial standard.

Nevertheless, efficient deterministic contact mechanical models are nowadays more and more affordable given the modern computer performances. Deterministic methods provide an accurate evaluation of the real contact area A as well as the shape of the deformed roughness. One of the main strengths of these models is the opportunity to use 3D measured surface topography as input. Therefore, the surface topography has to be carefully assessed avoiding any measurement artefacts due for example to dust or vibration. In addition, the measurement conditions in terms of step of scanning, size of area as well as the measurement technique have a great influence on the results, as shown by Fabre et al. [83], and has to be accounted for. The larger the measured surface, the better the prediction but also the more time-consuming and memory intensive the calculation will be. For example, 7 Gigabytes of random-access memory (RAM) are required for a surface measurement of 4096×4096 number of points.
Two principal methods can be found in the literature, the multi-level multi-summation (MLMS) method developed by Brandt and Lubrecht [84] and the Fast Fourier Transform (FFT) method initially developed by Ju and Farris [85] as well as Stanley and Kato [86] and lately extended by Wang et al. [87]. More recently, Frérot et al. [88] developed a strategy based on the boundary method element and a Fourier approach to solve the real contact area using the open-source software Tamaas. It is for example used in [89] to study the evolution of micro-contacts for a quasi-static sliding condition. At the crossroads of statistical and deterministic theories, Bigerelle et al. [90] proposed a statistical work-flow method to predict the statistics of contact pressure between rough surfaces. Therewith, they were able to predict the probability of plastic deformation from the analysis of the roughness statistics.

Some of the previously cited methods are paired with an hydrodynamic solver in order to compute the mixed lubrication contact, such as done by Sahlin et al. [38, 39] or by Costagliola et al. [91].

2.2.3 Commercial Software

Several commercial programmes exist to study the piston lubrication. They are either dedicated specifically to the piston assembly lubrication or either dedicated to the whole IC engine lubrication. We can cite AVL EXCITE from the AVL company which is a multi-body dynamics software for power-train analysis. It includes a Piston&Rings module with three-dimensional simulation of the ring allowing to compute the ring displacement, oil film thickness, oil consumption, gas flow, friction and wear. This software is employed by various authors [27, 92] to study the piston ring film thickness and friction. The RICARDO company propose a similar software named RINGPACK and PISDYN used for example in [93, 94]. Other software such as The Virtual Engine by FEV or GT-Suite by the Gamma Technologies company can also be cited.

2.3 Assumption

The specificity of the studied contact allows one to make some simplifying assumptions. Both the rings and the liner are coated with a hydrogenated amorphous carbon (a-C:H) with approximately 20% of hydrogen and a film thickness of $2-4$ µm. For both coating adhesion and tribological (i.e. wear and friction reduction) purposes the DLC film is coated on a "mirror-like" polished surface. The steel liner and piston rings are thus polished by a custom process such that the classical liner's cross-hatched honing pattern is almost completely removed. Figure 2.4 shows the typical surface finish of the piston compression ring and liner DLC coated after polishing, measured using an optical technique. Chart 2.1 gives the roughness parameter of both surfaces.

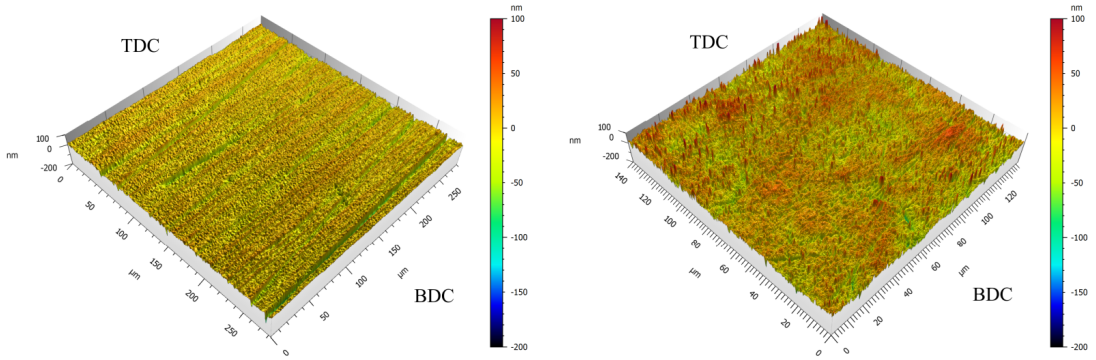

(a) Polished and DLC coated liner (b) Polished and DLC coated compression ring

Figure 2.4: Measured surface topography.

[nm]	Liner	Ring
Sa	9.40	16.3
Sq	15.0	21.4
Sz	233	288
Sk	22.8	36.9
Spk	6.42	19.4
Svk	24.8	27.2

Table 2.1: Polished and DLC coated liner and compression ring roughness parameters.

In view of these observations, the two following simplifying assumptions are made:

- with respect to the surface finish of both the liner and the piston rings, the hydrodynamic contact surfaces are assumed perfectly smooth. Hence, the LCC generated by the roughness is assumed negligible compared to the LCC generated by the ring profile in the case of a non flat ring [26],
- the absence of any texture and the isotropic property of the DLC coating roughness allows one to assume that no side-flow occurs in the contact and thus reduce the model to a one-dimensional line-contact.

As explained in Section 3.5, the PRCL contact load is mainly generated by the elasticity of the ring pushing against the liner. The ring pre-tension (in a range of 10 to 60 Newton) generates an Hertzian contact pressure of $1\,MPa$ to $50\,MPa$. However, during the combustion process and close to TDC the rings contact pressure strongly increases. The high pressure gases resulting from the combustion, flow behind the rings through the piston groove and the ring gap. Acting on the back of the ring, they increase the ring Hertzian contact pressure against the liner from $0.1\,GPa$ to $0.5\,GPa$. Still, on the major part of the stroke, the contact pressures are relatively low and the PRCL mainly operates in the hydrodynamic lubrication regime (in opposition to the Elastohydrodynamic lubrication regime for which the contact pressure is in order of Giga Pascals). Thus, one can assume that the contact pressure is not large enough to generate a lubricant viscosity variation or to deform the bodies. Therefore, the Reynolds equation can be reduced to its simplified Iso-Viscous Rigid (IVR) form.
These three assumptions allow for a drastic simplification of the hydrodynamic equations and the development of an efficient solver as described in the following sections.

2.4 Operating Condition

The mixed lubrication model is based on the ring load balance equation, given below, assuming that the inertia term of the ring is negligible (see Appendix A):

$$\sum \vec{w} = \vec{0} \qquad \Leftrightarrow \qquad \vec{w_{hydro}} + \vec{w_{asp}} + \vec{w_{tot}} = \vec{0} \tag{2.3}$$

where $\vec{w}_{hydro}$ stands for the hydrodynamic LCC, $\vec{w}_{asp}$ the load carried by the solid-to-solid contact (i.e. asperities) and $\vec{w}_{tot}$ the total normal load. $\vec{w}_{tot}$ is a known variable as $\vec{w}_{hydro}$ and $\vec{w}_{asp}$ are unknown functions of the distance i.e. the film thickness between the two surfaces. By solving equation 2.3, one can compute the gap between the ring and the liner, from which the friction losses can be evaluated.

In equation 2.3 the total normal load w_{tot} is equal to the sum of the ring pre-tension and the in-cylinder pressure acting behind the ring:

$$w_{tot} = \frac{2F_t}{b} + \frac{1}{2} P_{gas}\, \ell \tag{2.4}$$

where F_t is the pre-tension force needed to close the ring gap, b the bore diameter, ℓ the ring width and P_{gas} the gas pressure acting behind the ring (in-cylinder or in-between the rings). To approximate the friction losses in the ring-flank / piston-groove contact, only half of the gas pressure is considered in Equation 2.4. P_{gas} is either obtained from in-cylinder gas pressure measurements or from a blow-by model.

In Equation 2.3 w_{hydro} and w_{asp} have to be evaluated using a hydrodynamic and a solid-to-solid contact model for each stroke position of the piston. Therefore, some operating conditions have to be computed as a function of the stroke position or the crankshaft angle, such as the piston speed, the liner temperature and the oil supply.

Figure 2.5 shows an illustration of the piston / connecting-rod / crank mechanism.

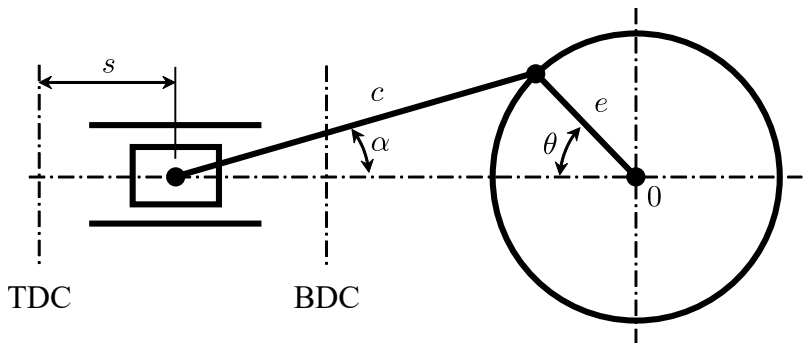

Figure 2.5: Piston / con-rod / crankshaft mechanism.

The piston displacement from top dead centre as a function of the crank angle θ is given by:

$$s = e\,(1-\cos\theta) + c\,(1-\cos\alpha)$$

$$\sin\alpha = \left(\frac{e}{c}\right)\sin\theta \quad \Rightarrow \quad \cos\alpha = \sqrt{1-\sin^2\alpha} = \sqrt{1-\left(\frac{e}{c}\right)^2\sin^2\theta} \tag{2.5}$$

$$s = e(1-\cos\theta) + c(1-\sqrt{1-\left(\frac{e}{c}\right)^2\sin^2\theta}) \tag{2.6}$$

The piston velocity as a function of θ reads:

$$u = \frac{ds}{dt} = \frac{ds}{d\theta}\frac{d\theta}{dt} = \Omega\frac{ds}{d\theta} \qquad \Rightarrow \qquad u = \Omega\left[e\sin\theta + \frac{e^2\sin\theta\cos\theta}{c\sqrt{1-\left(\frac{e}{c}\right)^2\sin^2\theta}}\right] \tag{2.7}$$

with Ω the crankshaft rotational speed.

The oil temperature at each crank angle is assumed to be equal to the surface temperature of the cylinder liner. This statement is obviously wrong as we know that a temperature flux exists from the piston to the coolant (behind the liner) through the PRCL contact. However, this assumption is adequate for an initial analysis. The temperature gradient along the piston stroke can either be obtained from a temperature measurement, a thermodynamic model or by use of a linear / quadratic interpolation of TDC and BDC temperatures.
The oil viscosity is then computed for each stroke position using the empirical viscosity-temperature Walther formula (ASTM D341):

$$\log\log(\eta + 0.7) = A + B\log(T) \tag{2.8}$$

where A and B are fitting parameters related to the oil viscosity and computed using two measured viscosities at two different temperatures (from the lubricant data-sheet).
Vogel's viscosity-temperature has been proven in the literature to be highly accurate [95] and is often used in lubrication models. However, it is a three parameter equation needing three viscosity measurements at three different temperatures. Yet, the great majority of lubricant data-sheets only provide the oil viscosity at $40°C$ and $100°C$. For this reason, it is more convenient to use Walther's formula.

It is assumed that when the piston moves from TDC to BDC, the IC-engine lubrication system has refurnished sufficient oil on the liner so that the OCR operates under fully-flooded conditions. Also, the oil available on the liner for one ring is equal to the oil left by the preceding ring, assuming no external oil supply as modelled by Dowson et al. in [7].

2.5 Hydrodynamic Lubrication Equation

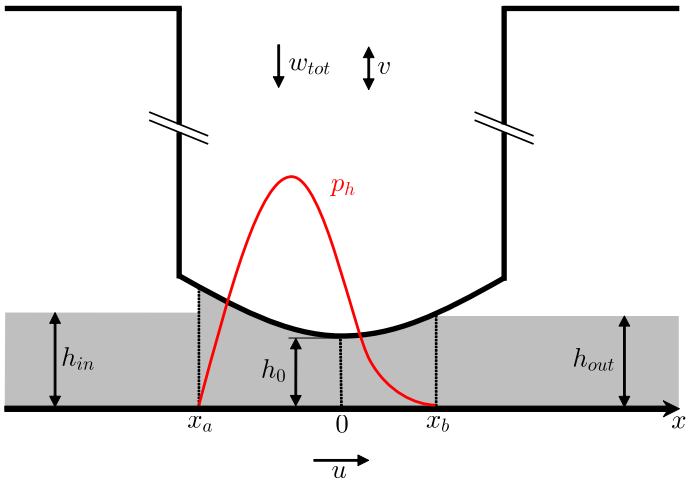

Figure 2.6: Schematic of the hydrodynamic problem to solve.

The hydrodynamic model relies on a line-contact, time-dependent, semi-analytical solver developed by Biboulet et al. [9]. It is a fast and simple solver that boils down to a set of four non-linear equations. It mainly accounts for starvation (geometrical and lack of lubricant), oil reserve upstream build-up, oil transport and non-continuous geometries. Figure 2.6 describes the model main variables. The theory main equations are rewritten in this section.

Equation 2.9 gives the transient Reynolds equation for the smooth IVR line-contact:

$$\frac{\partial}{\partial x}\left(h^3\frac{\partial p_h}{\partial x}\right) = 12\eta\left(u_m\frac{\partial h}{\partial x} + v\right) \tag{2.9}$$

with u_m the mean contact velocity as:

$$u_m = \frac{(u_1 + u_2)}{2} \tag{2.10}$$

and v the transient term as:

$$v^{(k-1/2)} = \frac{h_0^{(k)} - h_0^{(k-1)}}{\delta_t} \tag{2.11}$$

where $(k-1)$ stands for the initial step, (k) the system state after a time step δ_t and $(k-1/2)$ is defined as the average value of step $(k-1)$ and (k).

Equation 2.12 gives the gap geometry for a simple symmetrical parabolic ring profile where h_0 stands for the minimum gap at the ring centre.

$$h = h_0 + \frac{x^2}{2r} \tag{2.12}$$

where r is the ring face radius. The gap geometry can either be more complicated (non-symmetrical, inclined pad, etc.) or either be non-continuous (i.e. piecewise function). However, it is limited to convergent divergent shapes and there must exists an analytical solution to the integrals given in Equations 2.16-2.18, 2.22-2.24, 2.26, 2.35 and 2.36.

Integrating Equation 2.9 once, we obtain the pressure gradient equation:

$$\frac{h^3}{12\eta}\frac{\partial p}{\partial x} = u_m h - \bar{u}_m h^* + vx \tag{2.13}$$

where h^* is an integration constant and $\bar{u}_m$ is introduced as a fixed reference value of u_m in case of zero speed (i.e dead centres).

Integrating Equation 2.9 once more, we obtain the hydrodynamic pressure distribution equation for a smooth IVR line-contact:

$$\tilde{p}_h = 12\eta\left(u_m I_1 - \bar{u}_m h^* I_2 + v I_3\right) \tag{2.14}$$

$$p_h = \tilde{p}_h - \tilde{p}_h(x_b) \tag{2.15}$$

where $\tilde{p}_h$ is an arbitrary shifted pressure and I_1, I_2 and I_3 are four primitives such that:

$$I_1 = \int \frac{1}{h^2}\mathrm{d}x \tag{2.16}$$

$$I_2 = \int \frac{1}{h^3}\mathrm{d}x \tag{2.17}$$

$$I_3 = \int \frac{x}{h^3}\mathrm{d}x \tag{2.18}$$

x_a and x_b are respectively defined as the contact inlet and outlet meniscus positions. The outlet boundary condition is stated by Equation 2.15 as $p_h(x_b) = 0$. The inlet boundary condition is set as follows:

$$p_h(x_a) = 0 \tag{2.19}$$

In-cylinder pressure rising from the combustion process can be considered here in the model by adapting Equations 2.15 and 2.19. For a first approach, the boundary pressure conditions are set to zero.

The hydrodynamic LCC is obtained by integrating the hydrodynamic pressure distribution (Equation 2.14) over the contact domain; x_a to x_b:

$$\tilde{w}_h = 12\eta\left(u_m J_1 - \bar{u}_m h^* J_2 + v J_3\right) \tag{2.20}$$

$$w_h = \tilde{w}_{h_b} - \tilde{w}_{h_a} - (x_b - x_a)\tilde{p}_{h_b} \tag{2.21}$$

with J_1, J_2, J_3 integration primitives such that:

$$J_1 = \iint \frac{1}{h^2} \mathrm{d}x^2 \tag{2.22}$$

$$J_2 = \iint \frac{1}{h^3} \mathrm{d}x^2 \tag{2.23}$$

$$J_3 = \iint \frac{x}{h^3} \mathrm{d}x^2 \tag{2.24}$$

Biboulet et al. [9] managed to write down two semi-analytical mass-conserving equations describing the variation of the inlet and outlet positions: x_a and x_b. By analysing the flow imbalance on a time step δ_t through the dotted vertical lines in Figure 2.7, they established the following development.

In the inlet, the mass-conserving equation can be written as the balance of the light gray area and the Couette/Poiseuille oil flows:

$$\begin{aligned} \delta_t \Bigg(& \overbrace{\underbrace{u_m^{(k-1/2)} \left(h_{in}^{(k-1/2)} - h_a^{(k-1/2)} \right)}_{\text{Couette}} + \underbrace{\frac{\left(h_a^{(k-1/2)} \right)^3}{12\eta^{(k-1/2)}} \left. \frac{\partial p}{\partial x} \right|_{x_a^{(k-1/2)}}}_{\text{Poiseuille}}}^{\text{flow imbalance}} \Bigg) \\ & = \underbrace{I_h(x_a^{(k-1)}) - I_h(x_a^{(k)}) - \left(x_a^{(k-1)} - x_a^{(k)} \right) h_{in}^{(k-1/2)}}_{\text{Inlet light gray arrea}} \end{aligned} \tag{2.25}$$

with $h_a = h(x_a)$ the film thickness at the inlet, $h_{in}^{(k-1/2)}$ the oil film thickness on the liner in front of the ring known from the previous step or from the boundary condition and $u_m^{(k-1/2)}$ is computed using Equations 2.7 and 2.10.

I_h is defined as the primitive of the gap geometry Equation 2.12 and thus describes the amount of oil in the gap:

$$I_h = \int h \, \mathrm{d}x \tag{2.26}$$

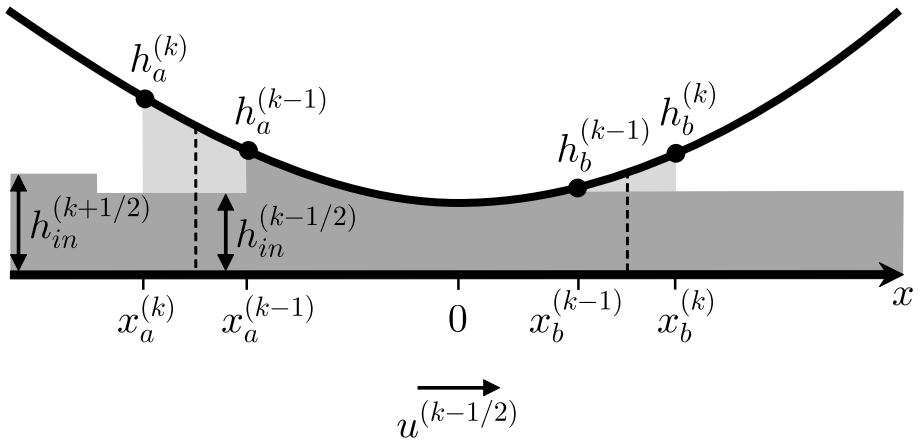

Figure 2.7: Schematic of the inlet and outlet locations variation for a zero vertical velocity [9].

Similarly, the outlet mass-conserving equation can be written as:

$$\begin{aligned}
&\delta_t \left(\overbrace{-\frac{\left(h_b^{(k-1/2)}\right)^3}{12\eta} \left.\frac{\partial p}{\partial x}\right|_{x_b^{(k-1/2)}}}^{Poiseuille} \right) \\
&= I_h(x_b^{(k)}) - I_h(x_b^{(k-1)}) - \left(x_b^{(k)} - x_b^{(k-1)}\right) h_0^{(k-1)} \\
&\qquad \underbrace{- u_m \delta_t \left(h_b^{(k-1)} - h_0^{(k-1)}\right)}_{Couette}
\end{aligned} \tag{2.27}$$

Using Equations 2.11 and 2.13 as well as by replacement of the $(k-1/2)$ terms, Equations 2.25 and 2.27 can be simplified.

The final inlet equation reads:

$$\begin{aligned}
&\delta_t u_m^{(k-1/2)} \left(2h_{in}^{(k-1/2)}\right) - \delta_t \bar{u}_m \left(h^{*(k-1)} + h^{*(k)}\right) \\
&\qquad + \left(h_0^{(k)} - h_0^{(k-1)}\right) \left(x_a^{(k-1)} + x_a^{(k)}\right) \\
&= 2\left(I_h(x_a^{(k-1)}) - I_h(x_a^{(k)}) - \left(x_a^{(k-1)} - x_a^{(k)}\right) h_{in}^{(k-1/2)}\right)
\end{aligned} \tag{2.28}$$

Similarly, the final outlet equation reads:

$$\begin{aligned}\delta_t u_m^{(k-1/2)} \left(-2\frac{I_h(x_b^{(k)}) - I_h(x_b^{(k-1)})}{x_b^{(k)} - x_b^{(k-1)}} \right) + \delta_t \bar{u}_m \left(h^{*(k-1)} + h^{*(k)} \right) \\ - \left(h_0^{(k)} - h_0^{(k-1)} \right) \left(x_b^{(k-1)} + x_b^{(k)} \right) \\ = 2 \left(I_h(x_b^{(k)}) - I_h(x_b^{(k-1)}) - \left(x_b^{(k)} - x_b^{(k-1)} \right) h_0^{(k-1)} \right. \\ \left. - u_m \delta_t \left(h_b^{(k-1)} - h_0^{(k-1)} \right) \right)\end{aligned} \tag{2.29}$$

2.6 Load-Distance curve

First, the surface roughness profile is measured. In this study, a 3D optical profilometer is mainly used as opposed to contact profilometer (AFM). Using a white light interferometer (Sensofar Neox PLu) a 3D map of the surface is recorded with a spatial resolution of 0.28 µm and a vertical resolution below 0.1 nm. Confocal and tactile methods may also be used in this work and are specified if so. The surface 3D patch is then post-treated on the MountainsMap software to correct any measurement artefact, to remove the virtual shape induced by the interferometer lens, to remove the curvature shape of the ring or the liner and to check the data consistency. Figure 2.8 shows for example the measured surface roughness of a DLC coated liner.

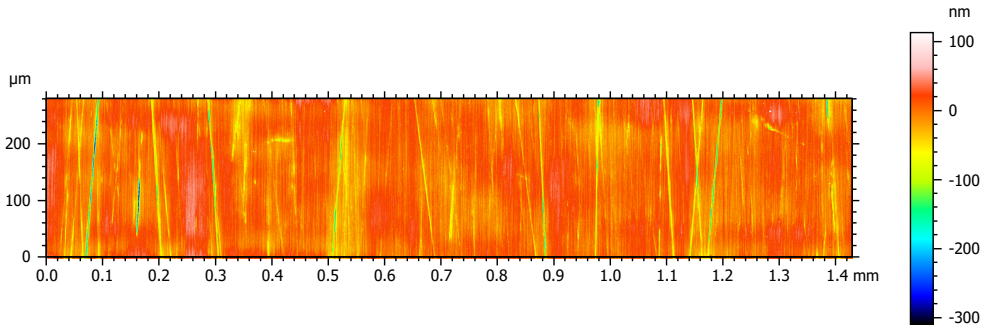

Figure 2.8: DLC coated liner topography measured by white light interferometry.

Once the previous steps are done, the measured surface is ready to be used as input of a deterministic contact mechanics numerical tool developed by Sainsot [10] and based on a Conjugate Gradient Fourier Transform solver. Since the contact mechanics code takes the real surface in consideration, no average asperity parameter has to be characterised in contrary to the popular "Greenwood & Tripp" theory. Also, the surface mechanical properties such as the Young modulus and the Poisson coefficient have to be filled in the code.

From the previous input parameters, the code computes through an iterative process the deformation of the elastic rough surface pushed against a rigid plane at a given load. Once the solver as converged, the distance of each node is averaged to evaluate the mean distance between the deformed rough surface and the rigid plane. The code input and output are outlined in Figure 2.9.

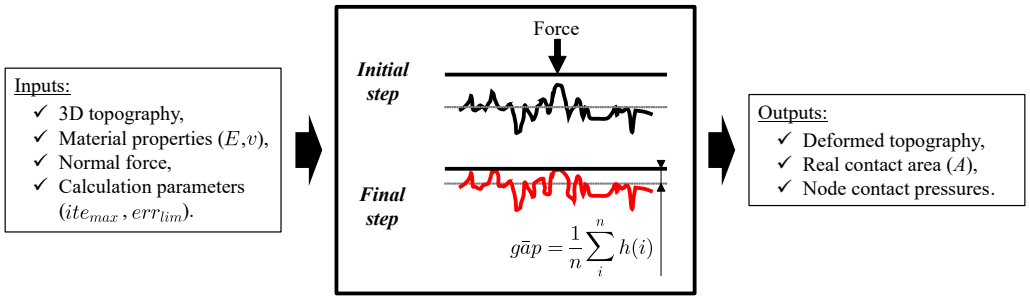

Figure 2.9: 2D scheme of the deterministic rough contact model and model inputs and outputs [10].

The calculation process outlined in Figure 2.9 is repeated for several normal forces in the range of the PRCL contact pressure. Herewith, one can build a curve describing the dry average distance between the deformed rough surfaces as a function of the mean contact pressure. In other words, it allows one to interpolate the mean pressure carried by the asperities at any roughness deformation. This curve can also be seen as the solid-to-solid contact stiffness and is in this study called the "pressure-distance" curve. Figure 2.10(a) gives an example of the pressure-distance curve computed for the topography given in Figure 2.8. Figure 2.10(b) describes the real contact area ratio as a function of the contact mean pressure. For a contact pressure of 1 to 100 MPa (typical of the ring tension) the rough contact area is equal to 0.05% to 5% of the nominal area. Thus, it is assumed that the solid-to-solid contact has a negligible impact on the hydrodynamic calculation described in Section 2.5.

The pressure-distance curve in Figure 2.10(a) describes the solid-to-solid contact behaviour for a flat on flat surface contact. To be used in the PRCL code the flat on flat pressure-distance data has to be converted to ring on flat, line contact data, called the "load-distance" curve. Therefore, the ring geometry described in Equation 2.12 is discretized in small linear flat elements and the asperity load of each element is interpolated on the flat on flat load-distance curve and summed-up. Figure 2.11 summarises this process. Using this method, from a unique flat on flat pressure-distance data, the dry contact behaviour of each piston ring having a different geometry can be rapidly obtained. Finally, the load carried by the asperities w_{asp} in Equation 2.3 is interpolated as a function of the hydrodynamic film thickness h_0 accounting for the dry contact complexity without the drawback of the time-consuming calculations.

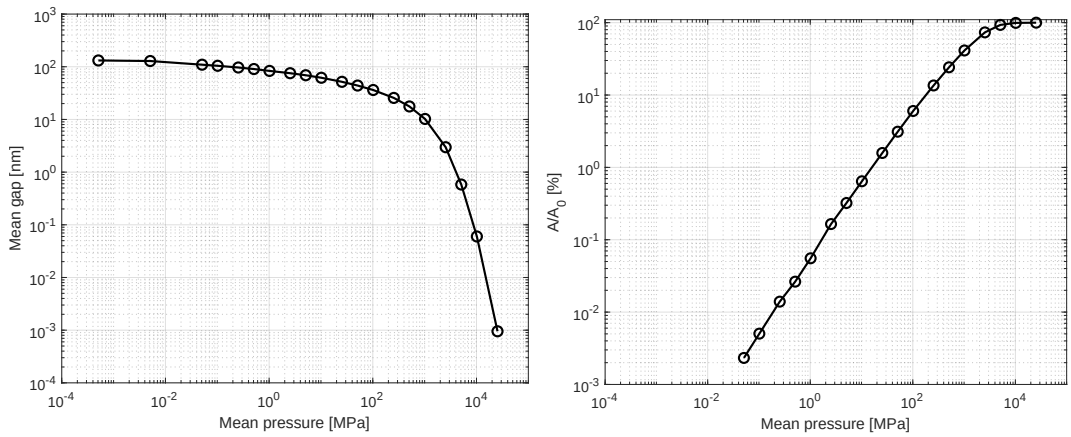

(a) Mean pressure (b) Real contact area ratio

Figure 2.10: Pressure distance curve and real contact area ratio computed for a mirror-polished DLC coated liner.

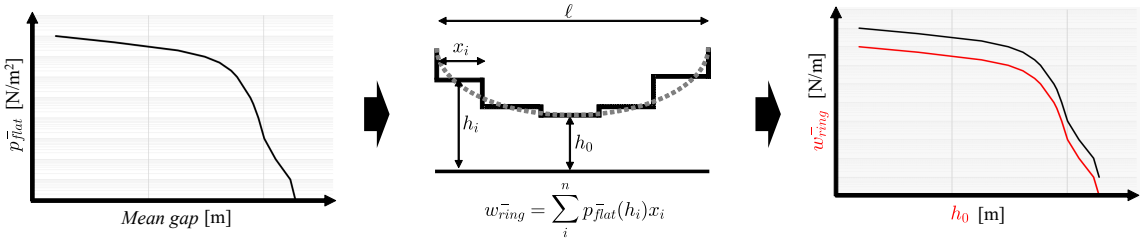

Figure 2.11: Conversion process of a flat on flat pressure-distance curve to a ring on flat load-distance curve (the number of discretised elements is small for illustration issues, normally it is larger than 1E3).

2.7 Friction Equation

The main goal of the mixed lubrication model is the prediction of the contact friction loss. Friction is also measured in experimental studies as it is easier to monitor than film thickness (see Chapter 3). In the mixed lubrication regime, both hydrodynamic and solid phenomena occur (see Section 1.3), thus the total friction loss of the contact can be seen as the sum of both features:

$$f = f_{hydro} + f_{asp} \tag{2.30}$$

The linear viscous friction force noted f_{hydro} is equal to the integral of the viscous friction stress over the contact domain: x_a to x_b. The viscous friction stress is defined as:

$$\tau_{hydro} = \frac{h}{2}\frac{\partial p_h}{\partial x} + \frac{2\,u_m \eta}{h} \tag{2.31}$$

The hydrodynamic pressure gradient can be substituted from Equation 2.13 to obtain:

$$\tau_{hydro} = \frac{8\eta u_m}{h} - \frac{6\eta \bar{u}_m h^*}{h^2} + \frac{6\eta v x}{h^2} \tag{2.32}$$

and:

$$\tilde{f}_{hydro} = \int \tau_{hydro}\, \mathrm{d}x \tag{2.33}$$

$$\tilde{f}_{hydro} = 8\eta u_m I_4 - 6\eta \bar{u}_m h^* I_2 + 6\eta v I_5 \tag{2.34}$$

with:

$$I_4 = \int \frac{1}{h}\, \mathrm{d}x \tag{2.35}$$

$$I_5 = \int \frac{x}{h^2}\, \mathrm{d}x \tag{2.36}$$

Finally, the linear viscous friction force is:

$$f_{hydro} = \tilde{f}_{hydro_b} - \tilde{f}_{hydro_a} \tag{2.37}$$

The linear solid-to-solid contact friction force noted f_{asp} is defined as:

$$f_{asp} = \mu_{bound}\, w_{asp} \tag{2.38}$$

where μ_{bound} is the measured boundary friction coefficient (see Chapter 3) of the tribological pair and lubricant. w_{asp} is the load carried by the asperities.

The linear contact power loss is defined as the product of the friction force and body velocity:

$$P_w = f\, u \tag{2.39}$$

2.8 Amount of Lubricant in the Outlet

No external lubricant supply in between the rings is assumed for this PRCL model, therefore each rings sees the amount of lubricant left by the preceding ring. Hence, one has to compute the amount of lubricant left on the liner behind the ring. Biboulet et al. [9] outlet film thickness equation is used in this model. The $\tilde{u}_m$ notation is introduced to account for the amount of lubricant pushed in front the ring by the squeeze motion at the dead-centres (i.e. $u_m = 0$).

$$h_{out} = \frac{1}{\tilde{u}_m}\left(u_m h_b - \frac{h_b^3}{12\eta}\frac{\partial p}{\partial x}\Big|_{x_b}\right) = \frac{1}{\tilde{u}_m}\left(\bar{u}_m h^* - v x_b\right) \tag{2.40}$$

$$\begin{cases} \tilde{u}_m^{(k-1/2)} = u_m^{(k-1/2)} & \text{if } u_m^{(k-1/2)} > 0 \\ \tilde{u}_m^{(k-1/2)} = u_m^{(k+1/2)} & \text{if } u_m^{(k-1/2)} = 0 \end{cases}$$

2.9 Piston Change in Direction

The piston motion is a back and forth displacement, at the dead-centres (TDC and BDC) the piston ring experiences zero speed as well as a change in direction. This change in direction leads in an inversion of the hydrodynamic pressure distribution as well as an inversion in the boundary conditions. This point has to be considered in the model mass-conserving equations in order to correctly predict the oil transport and thus the oil starvation. Hence, for the time-step following the dead-centre the lubricant flow conditions are inverted such as the previous step inlet becomes the outlet and vice versa:

$$\begin{aligned} &\text{if} \quad u_m^{(k-3/2)} = 0 \\ &\text{then} \begin{cases} x_a^{(k-1)} = -x_b^{(k-1)} \\ x_b^{(k-1)} = -x_a^{(k-1)} \end{cases} \end{aligned} \tag{2.41}$$

2.10 Solution Procedure

The code has been developed on *Matlab R2021b*. First the hydrodynamic primitives I_h, I_1 to I_5 (Equations 2.26, 2.16 to 2.18, 2.35 and 2.36) and double primitives J_1 to J_3 (Equations 2.22 to 2.24) are integrated as a function the gap shape (Equation 2.12) using the *Matlab* symbolic toolbox. For this step, one has to make sure that the different primitives can be analytically integrated twice. From this point, all the model equations are symbolically defined and then converted to *Matlab function handle* in order to be quickly evaluated at each time-step. Although this code step can be time-consuming (depending on the gap geometry complexity and the symbolic toolbox performance), it leads to a substantial reduction in computing time when it comes to the iterating solving process.
Then, by means of a forward stepping process over the crankshaft angle (CA) range (i.e time range), the transient minimum film thickness is computed at each step (k). First, the contact operating conditions are computed for the given piston position. Then, the following time-dependent system of four non-linear equations is created in order to solve the contact unknowns: $x_a^{(k)}$, $x_b^{(k)}$, $h^{*(k)}$ and $h_0^{(k)}$.

$$\begin{cases} \text{Inlet flow conservation} \\ \text{Outlet flow conservation} \\ \text{Inlet boundary condition} \\ \text{Ring load balance} \end{cases} \Rightarrow \begin{cases} x_a^{(k)}\text{: inlet meniscus position} \\ x_b^{(k)}\text{: outlet meniscus position} \\ h^{*(k)}\text{: integration constant} \\ h_0^{(k)}\text{: minimum film thickness} \end{cases} \tag{2.42}$$

Subsequently, system 2.42 is solved using the *Matlab* built-in *fsolve* function. In most cases, fewer than ten iterations are needed to reach a residual below 1E-12. The function *fsolve* is initialised using the solution at the previous step $(k-1)$. In Equation 2.3 of system 2.42, the load carried by the asperities w_{asp} is "on-line" interpolated from the load-distance curve (described in Section 2.6) as the minimum gap distance h_0 is updated.

However, with the previous system of non-linear equations 2.42, the outlet meniscus position x_b can be found such as cavitation occurs between x_a and x_b. In this case, the pressurised zone has to be cut-off. This can be checked by computing the pressure gradient at the outlet meniscus position x_b. If the pressure gradient at x_b is negative or equal to zero (see Figure 2.12(a)) the solution from the system 2.42 is correct. If the pressure gradient at x_b is positive (see Figure 2.12(b)) the following set of non-linear equations is solved to account for the cut-off:

$$\begin{cases} \text{Inlet flow conservation: Equation 2.28} \\ \text{Nil outlet pressure gradient: Equation 2.13} \\ \text{Inlet boundary condition: Equation 2.19} \\ \text{Ring load balance: Equation 2.3} \end{cases} \Rightarrow \begin{cases} x_a^{(k)}\text{: inlet meniscus position} \\ x_b^{(k)}\text{: outlet meniscus position} \\ h^{*(k)}\text{: integration constant} \\ h_0^{(k)}\text{: minimum film thickness} \end{cases} \tag{2.43}$$

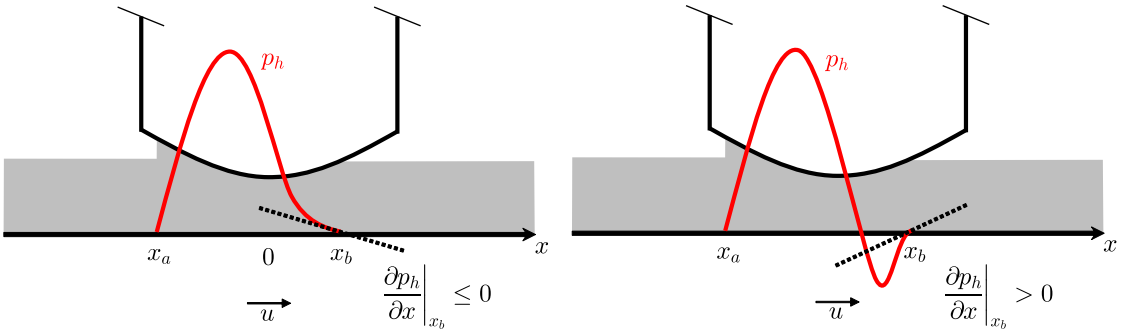

(a) Negative pressure gradient (b) Positive pressure gradient

Figure 2.12: Schematic representation of the cavitation at the contact outlet.

Once the transient solver has converged, the code moves to the next step $(k+1)$ by incrementing the current time with the time step δ_t, until it reaches the end of the time range (i.e CA range). Finally, the contact friction forces are computed using Equations 2.30, 2.37 and 2.38.

The first step of the transient solver is initialised by a steady-state ($v = 0$) and full film regime ($w_{asp} = 0$) step. Therefore, the best initial step is at mid-stroke where the ring radial speed is nearly constant. At least two strokes (360°CA) are pre-computed to avoid any influence of the steady-state initial step on the transient results.

All equations are made dimensionless to improve the calculation efficiency with respect to [9] and are described in Appendix B.

Close to the dead centres, the contact speed drops to zero as the piston reaches the reversal point leading to a rapid decrease in time of the minimum film thickness. The transient squeeze term v increases while the piston speed u decreases and at one point $v >> u$ triggering some divergence. In addition, the change in the piston direction generates a brutal inversion of the hydrodynamic pressure distribution as well as an abrupt change in lubrication conditions (i.e. fully-flooded to starvation). For all these reasons, the transient solver may encounter some stability issues close to the dead centres. One way to tackle these instabilities is by refining the time discretisation. However, changing the over-all time step δ_t is not an efficient solution since a small time step is not needed for most of the time (for $u >> v$). Therefore, a more efficient varying time discretisation is proposed based on the piston speed and reads:

$$lvl^{(k)} = \left\lfloor \frac{\log\left(u_m^{(k-1)}/u_{max}\right)}{\log(2)} \right\rfloor \tag{2.44}$$

with:

$$\text{if} \quad lvl^{(k)} > lvl_{max} \qquad \text{then} \quad lvl^{(k)} = lvl_{max} \tag{2.45}$$

and:

$$\delta_t^{(k)} = 2^{lvl^{(k)}} \delta_t^{(k-1)} \tag{2.46}$$

The model performances are investigated in Chapter 4.

2.11 Reference Solution

For this work, the Moes & Venner line-contact, iso-viscous rigid solution is chosen as a reference to the model film thickness predictions. Appendix C.4 provides a short insight on this solution establishment.
The dimensional, line-contact, iso-viscous rigid, Moes & Venner film thickness solution reads:

$$h_0^{MV} = 4.9 \frac{\eta u_m r}{w} \tag{2.47}$$

2.12 Conclusion

In this chapter, Christensen's mixed lubrication theory is implemented to predict the PRCL friction losses. Using some assumptions regarding the contact roughness and load, the line-contact, iso-viscous-rigid Reynolds equation is integrated following Biboulet's et al. idea [9]. A system of four non-linear equations, comprising of two mass-conserving equations is built allowing one to compute in a forward stepping process the minimum film thickness at each time step. The solid-to-solid part of the contact is solved using a "load-distance" curve describing the dry gap between the deformed surfaces for a load range. The "load-distance" curve is computed using a deterministic contact mechanics numerical tool developed by Sainsot [10] and the measured topography of the ring and liner. Finally, the *Matlab* code solution procedure relying on the built-in *fsolve* function is explained as well as the varying time discretisation to improve the solver stability.

Chapter 3

Experimental Devices

Contents

3.1 Introduction

While developing a computer simulation it is crucial to compare its predictions with measurements. Commonly, tribological testing methods can be divided into three categories:

- **Specimen testing** is designed to simplify the contact as much as possible, using standard test specimens and processes. For example, commercialised ball on plate test-rigs offer a first investigation into the tribo-pair and lubricant tribological properties.
- **Component or sub-system testing** is designed to test the tribological performance of a specific sub-system, running under typical operating conditions and using real engine parts. The aim is to minimise the influence of other elements as much as possible.

- **Full system testing** requires measurement equipment installed onto/into the real engine to investigate the triblogical performance of the contact inside a running engine. The aim is to modify the system as little as possible and to be as close as possible to real operating conditions.

Measurements are also often needed to quantify the input parameters for computer simulations. In addition, conducting numerical and experimental investigations in parallel, may help one to understand the physics of the contact and improve both the prediction and the experimental device. In this study, two distinct ball on plate rigs where used to quantify the Diamond-Like Carbon (DLC) coating friction and wear in several lubricants. Then, one ball on plate rig is partially modified to evaluate the friction force of a reciprocating line contact using a roller on plate set-up. Several operating conditions and roller geometries are tested. The measured friction results are in the end used to verify the computer-based prediction accuracy. In parallel, a specific Piston-Ring / Cylinder-Liner (PRCL) test-rig relying on real piston-rings, cylinder-liner and lubrication conditions, is optimised to measure the friction losses of the complete piston ring pack.

In this chapter, the design, functioning principle and experimental method related to each rig are detailed. Specimen testing results for coated and uncoated lubricated contacts are discussed. In addition, a short historical review of DLC tribology and PRCL measurements is supplied.

3.2 State of the Art

3.2.1 DLC Tribology

Historically, the first carbon film was created by Schmellenmeier in 1953 [96] but Aisenberg and Chabot are considered as the pioneers of this technology because of their comprehensive studies in the 1970s [97, 98]. After two decades of production and chemical characterisation, the mechanical and tribological properties of DLC coatings were studied during the 1990s, for example with the study of DLC on the cutting edge of steel blades [99]. Since the interest in DLC tribology gained momentum, according to Donnet and Erdemir, authors of the well-known book “Tribology of Diamond-Like Carbon Films: Fundamentals and Applications” [29], DLC films are considered as one of the most important tribological coatings in many fields.

DLC coating tribological properties may vary a great deal depending on the DLC type, the contact operating conditions and environment. Donnet and Erdemir [29] reported friction values in a range of 0.001 to 0.7 for a variety of DLC films. They also observed a similar wide range in wear behaviour. According to them, such a large disparity in friction and wear properties of DLC coatings arises from a complex combination of intrinsic (coating-specific factors) and extrinsic (test-condition-specific) factors. The degree of sp^2 versus sp^3 bondings, the relative amount of hydrogen and/or

alloying elements are the main intrinsic factors. Whereas, chemical, physical and mechanical interactions between the rubbing surfaces are the fundamental extrinsic factors affecting DLC tribological performance, with the physical roughness being of the first order [98]. The friction performance and different mechanisms controlling the tribological interaction of DLC films is discussed and clearly summarized by Ronkainen and Holmberg in [11] and their conclusions are shown in Figure 3.1.

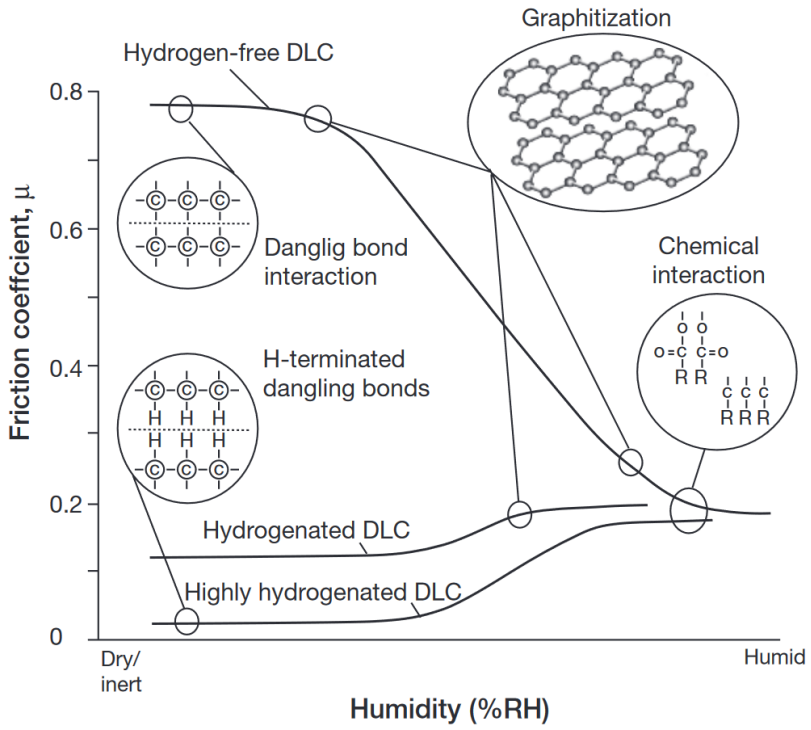

Figure 3.1: Schematic of the friction performance of DLC coatings as a function of relative humidity and mechanics controlling the tribological performance [11]

The tribological interaction of lubricated DLC is even more complex. Despite the high number of published papers dealing with DLC-lubricant compatibility, it is still difficult to select a specific lubricant facing a DLC film without testing. In 2008, Kahlin et al. [100] reviewed a range of published systematic studies to analyse the boundary lubrication of self-mated DLC coatings. They concluded that the hydrogen content in DLC films plays a crucial role in the tribological performance under lubricated conditions, as self-mated a-C:H contact shows lower wear and friction for oil containing a large amount of polar and unsaturated molecules.

DLC coatings are more and more used on different IC engine parts [31, 101]. DLC compatibility with fully-formulated engine oils and especially with additives has therefore become a popular research topic. Several tribological research teams, for example in [102–105], worked to characterise the tribological performance of different

DLCs lubricated with engine oils. They all reported some build up of tribo-layers on the DLC surfaces. However, Equey et al. [106] highlighted the weak adhesion of those tribofilms on DLC surfaces compared to steel. Recently, Ueda et al. [105] suggested that an important factor in the formation of Anti-Wear (AW) tribo-layers on non-ferrous surfaces is the presence and concentration of metal atoms or ions at the surface. This makes sense since oil additives have been developed for years to interact with ferrous surfaces. For self-mated DLC contacts, the grow and impact of the tribo-layer is small compared to steel contacts. However, for a DLC coated surface rubbing against a steel surface, additives may play a key role in the tribological interaction, especially by forming a tribo-layer on the steel counterpart. De Feo et al. [107] showed the effective performance of the MoDTC Friction-Modifier (FM) additive on reducing the friction coefficient (roughly 50% of reduction, excepted for Si-doped DLC) compared to the additive-free base oil for a number of DLC coatings rubbing against steel. But they observed a loss in MoDTC performance with ageing oil. In addition, they noticed dramatic wear on silicon and oxygen doped DLC coatings. In their latest study [108], they analysed in detail this drastic DLC wear induced by MoDTC lubrication and observed some molybdenum carbide on the steel counterpart. Nevertheless, because of the tribo-layer low hardness and the small size of the third-body particles in the contact, they concluded on a chemical wear mechanism. Masuko et al. [109] also observed some progressive chemical wear of DLC coatings lubricated with oil containing MoDTC. However, they suggested that the formation of molybdenum oxide (MoO_3) might have a role on the chemical wear of hydrogenated DLC. On the contrary, they reported no wear acceleration action of MoDTC on hydrogen-free DLC. Currently, it is not clear in the literature on which element of the MoDTC FM additive breakdown is responsible of the DLC coating chemical wear.

DLC films offer the hope to reach the super-lubricity regime outside the walls of a laboratory. Even if extremely low friction coefficients have been measured by several tribological research teams [110–114], the super-lubricity sliding regime is only reachable for certain types of DLC films and under some restrictive test and environmental conditions [115]. For example, the coupling of self-mating ta-C coatings with glycerol may, under specific test conditions lead to friction coefficient below 0.01 [112]. Not only intrinsic and extrinsic sources of friction have to be effectively eliminated, but also they have to remain absent all along the sliding process. This combination of factors generating low friction are far from the usual conditions of most industrial contacts. In addition, the super-lubricity friction coefficient reported by several authors are often linked to a progressive polishing of the surface roughness which may change the lubrication regime from boundary to mixed.

The main future interest of DLC films, especially for the automotive industry, is its compatibility and good tribological performance with water [116], organic lubricants/additives (as glycerol) [101] and green-lubricants (as castor oil) [117, 118]. Also, DLC coating capability to replace sulphur and phosphorous compounds from engine oils

without compromising long-term engine durability and performance is of key interest for future sustainable goals. DLC coating technologies may for example help hydrogen combustion engines to become reliable in real driving conditions.

To conclude, M.I. De Barros Bouchet's and J.M. Martin's statement back in 2007 is today still meaningful: "Whether a carbon-based material is used in a drive-train system or another application, the lubricant must be adapted to ensure the formation of necessary lubricant films and the adequate lubrication of components." [101], therefore experimental testing for each combination of DLC-lubricant is still needed.

3.2.2 PRCL Measurement

Experimental investigation methods to understand the tribological mechanisms of the PRCL contact are numerous and have improved for several decades. Two main parameters related to the PRCL tribology are commonly investigated: oil film thickness and frictional losses. The following section is mainly based on I. Sherrington's review entitled "Measurement techniques for piston-ring tribology" [119].

3.2.2.1 Film Thickness Measurement

The film thickness in-between the ring and the liner is the principal parameter evaluated by computer-based models. Therefore, oil film thickness data is useful to compare predictions with measurements. Multiple measurement techniques have become well established to quantify the piston-ring film thickness and they all fall into three groups: electrical methods, optical methods and acoustic methods [119].

- **Capacitance, inductance and resistive methods** are based on the measurement of changes of electrical parameters related to the film thickness. For each, the sensors are relatively small and are often custom made by investigators. Sensors can be both mounted in the piston-ring or in the cylinder wall.
  The capacitance technique involves the formation of the equivalent of a miniature parallel capacitor between the sensor and the opposite surface.
  The inductance technique relies on the variation of the inductance of a circuit element caused by the proximity of a magnetic field (i.e. ferrous part).
  The resistive method is the more convenient approach which was the first applied to the piston-ring film thickness measurement in the 1940s. First, the piston-ring is electrically insulated, it is then connected to a small DC voltage and finally the change in film thickness is quantified by the measurement of the bridge circuit resistance.
  These methods have the benefits to be relatively non-invasive and easy to install and the handling of the electrical output is relatively straightforward. However, in practice, the sensor calibration, sensor sensitivity to the surroundings and interferences due to asperity contact or tribo-layer formation are huge limitations that make these methods relatively difficult to use. In addition, these methods are more difficult to

use with electrical and magnetic insulating coatings such as DLC films. Examples of the use of these methods for the measuring of the piston-ring oil film thickness can be found in [120–122].

- **Ultrasound method** is the most recent technology to measure oil film thickness. Using a piezoelectric sensor emitting and receiving ultrasounds, the aim of this method is to determine the reflection coefficient or time-delay of the ultrasonic wave on the lubricant layer, in a similar manner to that used for non-destructive testing. Several models and types of pulse mode exist and are adapted to different configurations.
  This method allows the measurement of the film thickness in many IC engine contacts such as journal bearings, ball/roller bearings and the piston-assembly [123] and can be used for coated surfaces. However, for thin coated layers such as DLC films, a complex four-layered ultrasonic model has to be considered including overlapping problematical echoes. Mills et al. [124, 125] did for example study the lubrication of the piston skirt and ring on a fired IC engine using acoustic methods.

- **Laser-Induced Fluorescence (LIF) method** was establish in the 1970s with the discovery that the fluorescence of oils in ultra-violet light is dependent on the oil film thickness. Nowadays, this method has become convenient to analyse the piston-lubrication using cylinder windows or optical fibres as well as specific dyes and blue light to gain in optical precision.
  The main limits of this method are; the significant amount of specific equipment and operator knowledge needed, the oil fluorescence decreases in time, the inclusion of combustion products and the non-linearity of oil fluorescence with temperature. However, the LIF method offers a large and direct visualisation of the contact lubrication which considerably helped to understand the oil transport around and in the piston assembly. Additionally, this method allows for some estimation of the thickness of lubricant outside as well as inside the contact. For example, in 2007 Przesmitzki and Tian [126] studied the oil transport through the ring pack using the LIF method.

The principal drawback of these film thickness measurement methods is that it is almost impossible to obtain a continuous measurement of the film thickness along the piston stroke.

3.2.2.2 Friction Measurement

Whereas it is difficult to obtain a detailed film thickness measurement all along the piston stroke, continuous friction measurement on a motored or fired engine is less difficult. Nevertheless, measuring the instantaneous piston-ring friction tends to require more invasive engine modifications than for film thickness measurements. Commonly, two forms of engine modifications exist: the floating liner method and the indicated mean effective pressure (IMEP) method [119].

- **Floating liner method** is a direct technique allowing for a straight measurement of the instantaneous friction forces of the piston acting against the liner. For this purpose, small clearances are machined between the cylinder liner and the crankcase allowing the cylinder to move freely in the axial direction but is constrained in the radial direction. The liner is then connected to the crankcase by mean of several force sensors typically located at the bottom of the liner to avoid effects due to the high-temperature of the combustion chamber. This equipment measures the friction force of the piston skirt and ring pack rubbing against the liner. The main interest of this system is to measure the friction forces for real operating conditions, including combustion and high pressures.
  Therefore, the combustion chamber has to be sealed but a direct contact in between the floating liner and the cylinder head would bypass the force transducers and compromise the measurement. No ideal solution exists, nevertheless two techniques have been developed over time; the use of hydrostatic bearings and the use of force balancing seals. The hydrostatic bearings offer a high rigidity in the radial direction, allow axial motion and form a seal preventing any gas leakage. In spite of this, it requires extensive engine modifications. The force balancing seal technique offers an easier alternative using a well designed seal balancing the gas force acting on the top of the liner with the gas forces acting on other parts.
  Since the floating liner method requires extensive modification of the engine, they are commonly designed from scratch to be test-benches instead of being modified real engines. Principally single cylinder engines, they suffer from vibration instability at medium to high rotational speeds. Last but not least, it is hardly possible to separate the contribution to friction force from the piston skirt and the piston rings. Making precise investigations in each element friction relatively complex. Recent examples of the use of floating liner arrangements can be found in [76, 127, 128].

- **IMEP method** is an indirect measuring technique. On one hand, strain gauges are mounted on the connecting rod to measure the forces acting on the piston. On the other hand, accurate measurements of the cylinder pressure, engine speed and crank position allows one to theoretical compute the forces expected on the connecting rod. The difference in the computed and measured forces in the connecting rod is ascribed to friction.
  This method as two principal drawbacks. First, small errors in the measurement or calculated data may lead to significant errors in the estimated friction. Second, the strain gauges set-up and linkage to route the signal away from the connecting rod is technical and sensitive. However, compared to the floating liner method, the IMEP method requires less extensive modifications of the engine and allows to measure the piston friction for highly representative operating conditions [129, 130].

In addition, other methods exist. For example, the flywheel torque can be measured and converted to a pressure i.e. Brake Mean Effective Pressure (BMEP) and be compared to the Indicated Mean Effective Pressure (IMEP) computed from the in-cylinder pressure. The difference between the IMEP and BMEP is referred to the Friction Mean Effective

Pressure (FMEP) which is the value of friction losses from the combustion process to the flywheel, including the piston-assembly, the con-rod, the crankshaft and the valve-train friction. The Morse, Wilans line and the deceleration test method are also often use in industrial context to quantify the engine friction, but in a comparative way. These methods are indeed, contrary to the two previous ones, not adapted to a detailed study of the PRCL lubrication.

3.3 Ball on Plate

Tribological ball on plate testing is a simplified configuration using representative materials, surface roughness, contact pressures, speeds and lubricants. They allow a rapid investigation of the friction and wear of a lubricated tribo-pair under controlled operating conditions. Two different ball on plate test-rigs are used in this study; the High Frequency Reciprocating Rig (HFRR) commercialised by PCS-Instruments and the home-build ARTEMIS reciprocating test-rig.

3.3.1 HFRR

The High Frequency Reciprocating Rig (HFRR) commercialised by PCS-Instruments is a microprocessor-controlled reciprocating friction and wear test system, which provides a fast, repeatable assessment of the performance of fuels and lubricants. It is particularly suitable for wear testing of relatively poor lubricants such as diesel fuels and for boundary friction measurements of engine oils and greases[1].
An electromagnetic vibrator, powered with a sinusoidal electrical signal, drives the upper specimen (the ball) into a back and forth sliding motion. The electrical signal frequency defines the sliding speed as the signal amplitude defines the stroke length, which is rigorously controlled using a feedback loop. The lower specimen (the disc) is clamped into a small lubricant reservoir such that the contact is totally submerged. The reservoir is mounted onto a heating block and by mean of a control loop with a thermocouple the lubricant temperature can be precisely set. A horizontal force sensor, located in between the reservoir and the frame measures the tangential friction forces of the moving ball on the fixed disc. The normal contact load is applied to the upper specimen by hanging several masses below it. In addition, the film thickness is qualitatively estimated by measuring the electrical resistance of the gap between the ball and the disc. Figure 3.2 shows a picture and a schematic of the test-rig.

Standard PCS-Instruments ball and plate specimens are used. The upper specimen is a 6 mm diameter ball of ANSI E-52100 steel, with a Rockwell hardness of 58-66 HRC (ISO 6508) and a surface finish of $R_a \leq 0.05$ µm. The lower specimen is a 10 mm in diameter

[1] From the PCS-Instruments website: https://pcs-instruments.com/product/hfrr-high-frequency-reciprocating-rig/

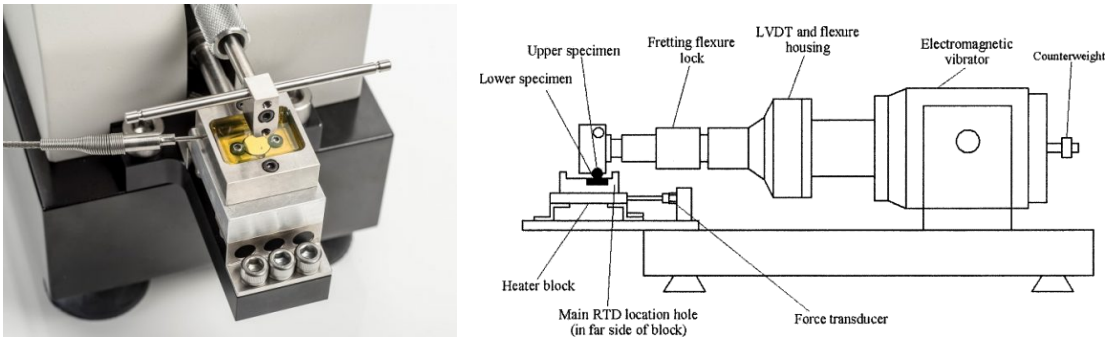

(a) Picture from www.pcs-instruments.com

(b) Schematic from [131]

Figure 3.2: HFRR test-rig

disc of ANSI E-52100 steel, machined from annealed rod, with a Vickers hardness 30 of 190 - 210 (ISO 6507/1). It is turned, lapped and polished to a surface finish of $R_a \leq 0.02$ µm. A 2.1 µm thick a-C:H film (with roughly 20% of hydrogen) is deposited on both specimens using the PECVD technique. The coated specimen roughness parameters are given in Table 3.1. DLC coated specimens are polished using sandpaper before testing to remove high asperity peaks created during the deposition process which may severely scratch the counter part.

[µm]	Steel ball	DLC ball	Steel disc	DLC disc
Sq	0.022	0.036	0.005	0.004
Sa	0.016	0.026	0.004	0.003

Table 3.1: HFRR specimen roughness parameters (ISO 25178)

Specimens and lubricant reservoir are cleaned before each test by placing them successively five minutes into an ethyl acetate and heptane ultrasonic bath. The test conditions are severe; in the boundary lubrication regime, to quickly identify the different wear mechanisms and friction behaviour. Therefore, the contact pressure is deliberately set to a high value compared to PRCL contacts. However, testing speeds are relatively low. In terms of PV ratios (pressure times velocity ratio) these tests are in the same order of magnitude as typical PRCL PV ratios (excepted for the combustion stroke). Testing operating conditions are detailed in Table 3.2 and tested engine oils denominations as well as specifications are given in Table 3.3.

3.3.2 ARTEMIS

The ARTEMIS rig is a home-build linear-reciprocating friction and wear test system. Contrary to the HFRR rig, it is the lower specimen, mounted on a rail, that moves in a reciprocating manner by means of a crank mechanism driven by an electric motor. The radius of the crank can be adapted to vary the stroke length and contact speed. The test

Parameter	Value
Load	200 g - $p_{hertz} = 0.5$ GPa
Frequency	20 Hz - $u_{max} = 40$ mm/s
Stoke length	1 mm
Temperature	$20 - 40 - 60 - 80 - 100 - 120\,^{\circ}$C
Duration	20 min per temperature step
Lubrication	Fully flooded

Table 3.2: HFRR test operating condition.

Denomination	Brand	Grade	Detail
Evo. 900 SXR	ELF	5W-30	Basic engine oil with AW
RN-Tech Elite	ELF	5W-30	Recent low-SAPS oil
Quartz Ineo First	TOTAL	0W-30	Advanced engine oil with AW & FM
Mobil1 Racing oil	Mobil1	0W-30	Advanced engine oil with AW & FM
Glycerol (G7893)	Sigma-Aldrich	-	ACS reagent $\geq 99.5\%$
Castor oil	-	-	-

Table 3.3: Lubricant specification.

rig design allows one to use a variety of upper specimen holders offering the possibility to test other configurations than only ball on plate as pin on plate or roller on plate. The upper specimen holder is attached to the bench frame by means of a thin steel plate (rigid in the horizontal direction but flexible in the vertical direction to avoid any additional loads) and a force sensor. The contact load is applied on the top of the upper specimen. Figure 3.3 shows pictures of the rig.

The upper specimen is a 10 mm diameter roller bearing ball of 100C6 steel, with a Rockwell hardness of 59 HRC. The lower specimen is a 25 mm in diameter disc of M2 steel, with a Rockwell hardness of 62.5 HRC. A 2.1 µm thick a-C:H film (roughly 20% of hydrogen) is deposited on both specimens using the PECVD technique. Measured specimen roughness parameters are detailed in Table 3.4. All DLC coated specimens are polished using sandpaper before testing and specimens are cleaned using solvents and a microwave bath as described in Section 3.3.1. Table 3.5 gives the testing operating conditions. Tests were performed in the ELF Evolution 900 SXR 5W-30, the ELF RN-Tech Elite 5W-30 and the TOTAL Quartz Ineo First 0W-30 engine oils (see Table 3.3).

[µm]	Steel ball	DLC ball	Steel disc	DLC disc
Sq	0.042	0.050	0.002	0.006
Sa	0.027	0.034	0.001	0.005

Table 3.4: ARTEMIS specimen roughness parameters (ISO 25178)

Parameter	Value
Load	$510g$ - $p_{hertz} = 0.49GPa$
Speed	$u_{max} = 40mm/s$ and $u_{mean} = 28mm/s$
Stoke length	$10mm$
Temperature [$^{\circ}C$]	$55 - 110$
Time-step	$60min$ per temperature
Lubrication	Fully flooded

Table 3.5: ARTEMIS test operating condition.

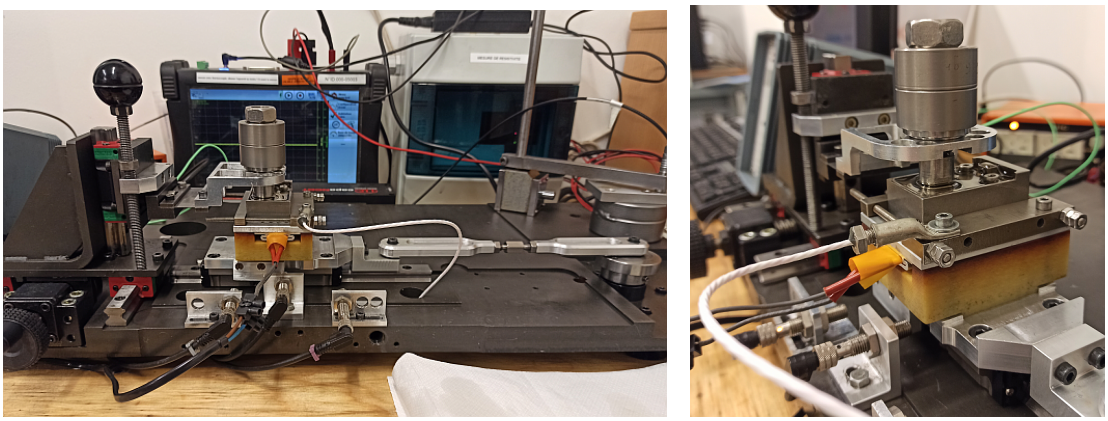

Figure 3.3: ARTEMIS test-rig.

3.3.3 Results

The aim of these studies was to investigate using an easy and controlled way the tribological performance of the a-C:H coating intended to the PRCL contact. DLC-DLC, DLC-steel and steel-steel tribo-pairs are tested for several lubricants (basic / advanced fully formulated engine oils, pure glycerol, castor oil and water). All the tests were carried out in the boundary to mixed lubrication regime by keeping the λ ratio below 0.5 (with the λ ratio defined as $\lambda = h_0/\sigma_q$ with h_0 computed using Moes and Venner minimum film thickness formula [43, 132] and σ_q the specimens composite root mean square roughness). Also, the ARTEMIS test-rig offers the possibility to visualize in real time the instantaneous friction force as a function of time as shown in Figure 3.4. This allows one to control that the contact stays in the boundary lubrication regime during the testing. Tables 3.6 and 3.7 give a detailed summary of these investigations (given at the section end). Wear observations are performed using a microscope and a white light interferometer.

Tests have been carried out on two similar rigs and under similar test conditions. The main difference between the two methodologies is the mechanical properties of the samples. Even if the mechanical properties of the DLC coatings are rigorously the same, the HFRR steel substrate is almost four times softer ($\approx$ 15 HRC - ISO 18265) than the

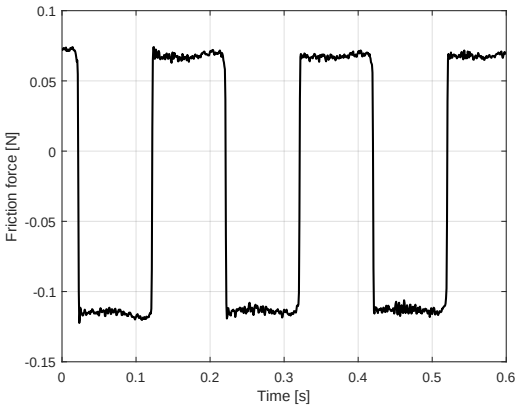

Figure 3.4: ARTEMIS instantaneous friction measurement, the squared signal is typical from the boundary lubrication regime.

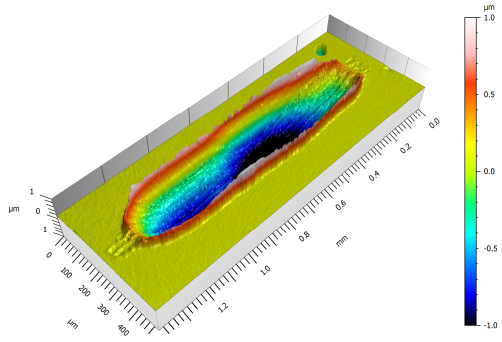

Figure 3.5: HFRR disc wear scar topography measured by interferometry, highlighting the material plastic flow from inside to outside of the wear scar.

ARTEMIS specimens (62.5 HRC). This difference in hardness explains the shift in friction and wear behaviour between the two rigs presented in Table 3.6 and 3.7. In general, deep and wide wear scars are observed on the HFRR disc specimens as no wear is observed on the ARTEMIS discs as suggested by the profile measurements across the wear scars in Figure 3.8. Not only the HFRR disc specimens hardness is low, the yield strength of the ANSI E-52100 ($\approx 500 - 800$ MPa) is also relatively low and is similar to the test initial contact pressure of ≈ 500 MPa. Hence, the uncoated HFRR discs are plastically deformed during the test and 3D wear observation suggests that some plastic flow occurs during the rubbing process (see Figure 3.5). Also, some deep wear "scratches" are observed on some of the HFRR DLC coated discs. It is supposed that the soft steel substrate may also deform plastically beneath the thin coating due to locally high contact pressures generated by the presence of particles (wear debris or silica). Because the coated film is thin (≈ 2 µm) it follows the substrate deformation. Therefore, and due to the difference in hardness between the coating and the substrate, some cracks may appear in the hard-coating and some delamination of the film was observed. Such a ruin was not observed on the hard ARTEMIS disc specimens. Last but not least, the "pushing" plastic deformation of the HFRR tests may explain the systematic higher measured friction coefficient for the HFRR tests than for the ARTEMIS tests. As some plastic deformation of the disc occurs while rubbing the ball on the plate, the measured friction is composed of both the interface (fluid and asperity) shear stress and the force needed to plastically deform the metal (pushing). On the contrary, the ARTEMIS configuration is more likely to only measure the friction arising from the shearing of the contact interface.
However, the following comparable conclusions for both test-rigs can be stated:

- For all tests including at least one steel counterpart, large tribofilm patches are observed inside the steel wear scar (see Figure 3.6(a)). The tribofilm thickness depends on the lubricant type, lubricant temperature and counterpart material. On the

contrary, only small tribofilm patches are observed on the DLC coating (see Figure 3.6(b)) and adhesion of these patches is relatively weak as the tribo-layer is easily wiped-off while the surfaces are cleaned for optical analysis,

- Almost no wear (some slight polishing, see Figure 3.6(b)) is observed for DLC-DLC tribo-pairs in all lubricants. However, for non-filtered lubricants (here with a 8 µm porosity filter) and for the soft HFRR discs some third-body abrasion can be observed,

- Tribo-chemical wear of the DLC coating, as reported in [108, 109], is observed for some DLC-steel configurations lubricated with oils containing MoDTC FM additives. The wear process is smooth and the hard-coating is progressively worn-out, slowly revealing the steel substrate. Figure 3.7 illustrates the smooth tribo-chemical wear of a HFRR DLC coated ball specimen rubbed against a steel plate lubricated with the Total Quartz Ineo First engine oil. Also, coating delamination for DLC-steel configurations was observed but is not attributed to tribo-chemical wear but to an excessive plastic deformation of the soft steel substrate (only observed for HFRR tests),

- Friction wise, a 15% to 20% friction reduction is measured for a DLC-DLC tribo-pair compared to a steel-steel tribo-pair lubricated with an oil free from FM additives,

- For oils containing MoDTC FM additives, steel-steel tribo-pairs highlight lower friction than a DLC-DLC configuration. The fully-developed tribofilm on each steel surface composed of both AW additives and MoS_2 (dissolution of the MoDTC FM additives) has a relatively low shear stress. However, as shown in [107], MoDTC low-friction capabilities is strongly deteriorated for ageing oils as, on the contrary, time as no effect on DLC coatings friction performance,

- For tests with pure-glycerol and castor oil, no super-lubricity was observed. Super-lubricity is commonly obtained for hydrogen-free DLC coatings. Here, the tested coating is an a-C:H containing at least 20% of hydrogen,

- The DLC-DLC tribo-pair shows good tribological properties when lubricated with water. After four hours of testing in purified water the friction coefficient stabilised at 0.06 (see Figure 3.9). The surfaces of both specimens were polished during the test from a $S_q = 10$ nm to $S_q = 1$ nm, which leads to a λratio change from 0.06 to 0.6. According to the experimental and numerical work of Zhu et al. [133], for a λratio of 0.6 a considerable portion of load ($> 15\%$) is carried by the lubricant film, typical of the mixed lubrication regime which may explains a low friction coefficient. Furthermore, the gentle polishing of both surfaces may have created a conforming roughness pattern along the sliding direction, allowing the generation of a thin lubricant full film which separates the surfaces and thus induces a low friction (low water viscosity).

For a homogeneous 50-50 oil-water mixture (ELF Evolution 900 SXR and purified water) the friction coefficient (0.126 - see Figure 3.9) after four hours of testing is in the same order of magnitude of the test with pure oil (0.137 - see Figure 3.9). Wear is similar for both tests. However, larger and thicker AW tribofilm patches are developed on the DLC surface for the 50-50 oil-water mixture than for the pure oil configuration.

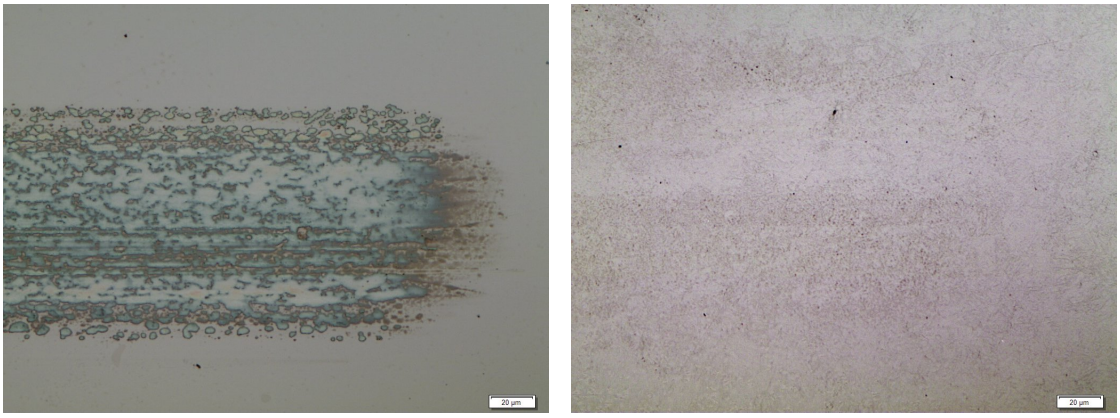

(a) Steel - Steel (b) DLC - DLC

Figure 3.6: Disc wear scar in ELF Evolution 900 SXR.

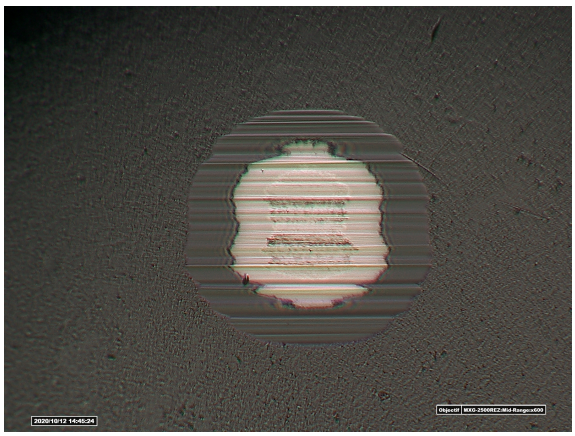

Figure 3.7: Chemical wear on a DLC coated ball specimen, the central light part is the revealed steel substrate.

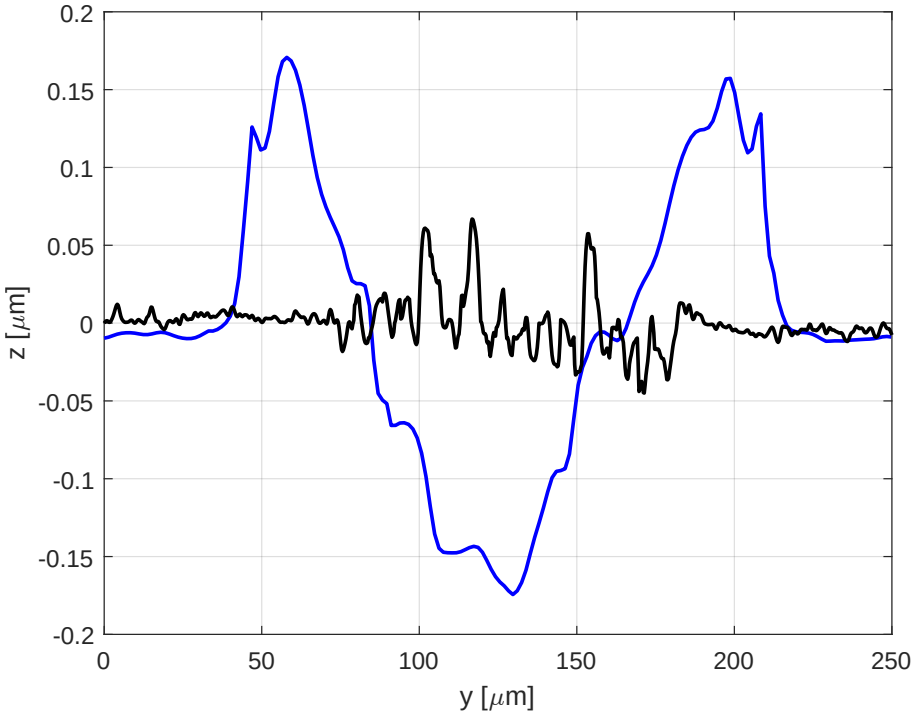

Figure 3.8: Central wear profile measurement perpendicular to the sliding direction (blue solid line: HFRR - black solid line: ARTEMIS).

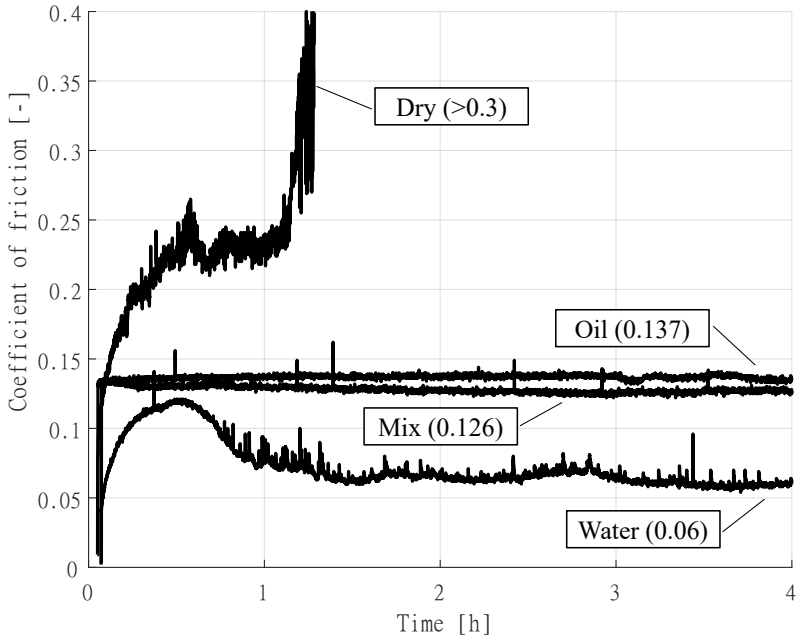

Figure 3.9: a-C:H DLC coating friction performance lubricated with water (freq. = 20 Hz, stroke = 1 mm, temp. = 40°C, $P_{Hertz} = 500$ MPa).

Ball	Disc	Lubricant	Rig	CoF	Wear detail
Steel	Steel	Evo. 900 SXR	HFRR	0.150	-[1]
Steel	Steel	Evo. 900 SXR	ARTEMIS	0.125	Large AW patches on ball and disc
DLC	DLC	Evo. 900 SXR	HFRR	0.122	-[1]
DLC	DLC	Evo. 900 SXR	ARTEMIS	0.105	No observable wear
DLC	Steel	Evo. 900 SXR	ARTEMIS	0.125	No wear on ball, large AW pacthes on disc
Steel	Steel	RN-Tech Elite	HFRR	0.174	-[1]
Steel	Steel	RN-Tech Elite	ARTEMIS	0.125	Small AW patches on ball and disc
DLC	DLC	RN-Tech Elite	HFRR	0.150	-[1]
DLC	DLC	RN-Tech Elite	ARTEMIS	0.103	Almost no polishing on ball
DLC	Steel	RN-Tech Elite	ARTEMIS	0.132	Small AW patches on disc
Steel	Steel	Quartz Ineo first	HFRR	0.115	-[1]
Steel	Steel	Quartz Ineo first	ARTEMIS	0.043	Small AW & FM patches on ball and disc
DLC	DLC	Quartz Ineo first	HFRR	0.120	-[1]
DLC	DLC	Quartz Ineo first	ARTEMIS	0.070	Almost no polishing on ball
DLC	Steel	Quartz Ineo first	HFRR	0.087	-[1]
DLC	Steel	Quartz Ineo first	ARTEMIS	0.052	Polishing & small cracks $\perp$ to sliding direction on ball, tiny AW & FM patches on disc
Steel	DLC	Quartz Ineo first	HFRR	0.097	-[1]
Steel	DLC	Quartz Ineo first	ARTEMIS	0.070	Abrasive wear on ball and disc
Steel	Steel	Mobil 1 Racing	HFRR	0.123	-[1]
DLC	DLC	Mobil 1 Racing	HFRR	0.086	-[1]
DLC	Steel	Mobil 1 Racing	HFRR	0.121	-[1]
Steel	DLC	Mobil 1 Racing	HFRR	0.094	-[1]
DLC	DLC	Glycerol	HFRR	0.129	-[1]
DLC	Steel	Glycerol	HFRR	0.109	-[1]
DLC	DLC	Castor oil	HFRR	0.080	-[1]
DLC	Steel	Castor oil	HFRR	0.064	-[1]

Table 3.6: Ball on plate tribological results (for 55-60 $^{\circ}C$).

[1] HFRR tests have not been stopped in between every temperature steps. Thus, wear scars were not observed at the end of the 60°C temperature step.

Ball	Disc	Lubricant	Rig	CoF	Wear detail
Steel	Steel	Evo. 900 SXR	HFRR	0.177	AW on ball, disc plastic def. (depth≈ 0.15µm)
Steel	Steel	Evo. 900 SXR	ARTEMIS	0.115	AW on ball & large/thick on disc (thick≈ 0.10 µm)
DLC	DLC	Evo. 900 SXR	HFRR	0.130	Disc substrate plastic def.
DLC	DLC	Evo. 900 SXR	ARTEMIS	0.109	Slight ball polishing
DLC	Steel	Evo. 900 SXR	ARTEMIS	0.121	AW on disc
Steel	Steel	RN-Tech Elite	HFRR	0.175	AW on ball, deep disc plastic def. (depth> 1.0 µm)
Steel	Steel	RN-Tech Elite	ARTEMIS	0.129	AW on ball & disc (thick≈ 0.07 µm)
DLC	DLC	RN-Tech Elite	HFRR	0.155	Ball & disc slight polishing
DLC	DLC	RN-Tech Elite	ARTEMIS	0.096	Ball slight polishing
DLC	Steel	RN-Tech Elite	ARTEMIS	0.134	AW on disc
Steel	Steel	Quartz Ineo first	HFRR	0.065	Abrasive wear on ball, disc plastic def. (depth≈ 0.1µm)
Steel	Steel	Quartz Ineo first	ARTEMIS	0.037	AW & FM on disc (thick≈ 0.06 µm)
DLC	DLC	Quartz Ineo first	HFRR	0.100	Ball slight polishing
DLC	DLC	Quartz Ineo first	ARTEMIS	0.065	Ball slight polishing
DLC	Steel	Quartz Ineo first	HFRR	0.105	DLC complete removal by chemical wear (figure 3.7), AW & FM on disc
DLC	Steel	Quartz Ineo first	ARTEMIS	0.041	Ball slight polishing, tiny AW & FM on disc
Steel	DLC	Quartz Ineo first	HFRR	0.094	Abrasive wear on ball, disc coating partial delamination
Steel	DLC	Quartz Ineo first	ARTEMIS	0.063	Abrasive wear on ball, disc coating partial delamination
Steel	Steel	Mobil 1 Racing	HFRR	0.086	Tiny AW & FM on ball, disc plastic def. (depth≈ 0.2µm)
DLC	DLC	Mobil 1 Racing	HFRR	0.085	No observable wear
DLC	Steel	Mobil 1 Racing	HFRR	0.124	Chemical wear on ball, fully developed AW & FM on disc
Steel	DLC	Mobil 1 Racing	HFRR	0.114	Abrasive wear on ball, disc coating partial delamination
DLC	DLC	Glycerol	HFRR	0.190	Ball & disc slight polishing
DLC	Steel	Glycerol	HFRR	0.154	Slight abrasion wear on disc
DLC	DLC	Castor oil	HFRR	0.078	No observable wear
DLC	Steel	Castor oil	HFRR	0.052	Slight abrasion wear on disc

Table 3.7: Ball on plate tribological results (for 100-110 °C).

3.4 Roller on Plate

In order to compare the computer-based predictions with experimental data, the previously described ARTEMIS test-rig (see Section 3.3.2) is modified. To reproduce a theoretical line contact, a roller on plate configuration is selected.

The roller specimen is taken from a roller bearing, it has a 20 mm length and a 7 mm radius. It is fixed onto the new upper specimen holder by means of two semi-spherical arms and a pressure screw. The new upper specimen holder is divided into two parts, the lowest part (which holds the roller) is linked to the second by means of two thin metallic sheets. These plates are relatively flexible to bending loads along the x direction, allowing the roller to lay flat onto the plate and thus neglects the potential miss alignment. However, those sheets are rigid along the y axis (sliding direction) and along the z axis (normal load direction) to fully transmit the contact forces. The second part of the holder is connected to the force transducer by means of a thin plate which can be deformed to precisely align the contact height with the force sensor axis.
The normal contact load is provided by means of a rigid bar placed onto the upper specimen holder to which masses are added on each side of the rig. Figure 3.10 shows a picture of the roller on plate test-rig configuration.

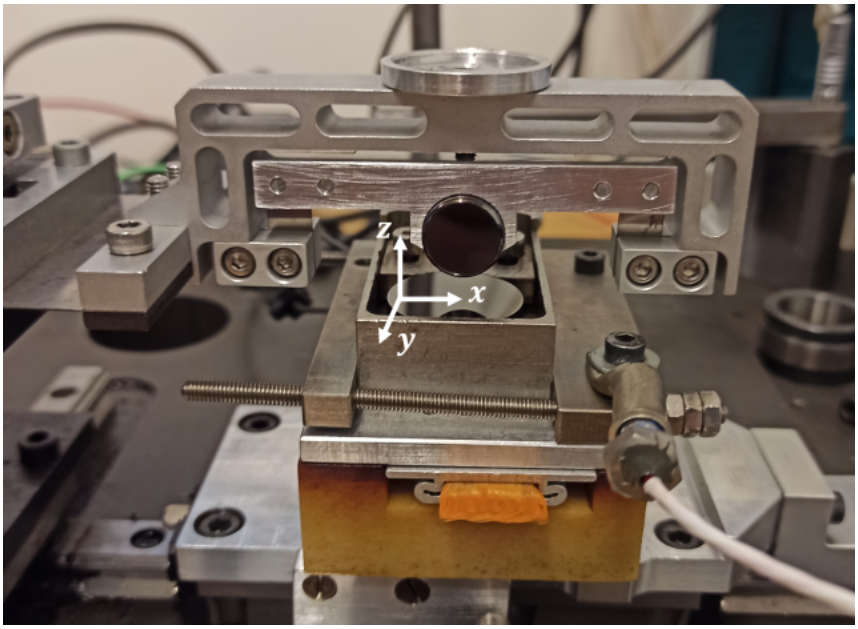

Figure 3.10: ARTEMIS rig roller on plate configuration.

The plate specimen are the same DLC coated discs used for the ball on plate testing described in Section 3.3.2. Steel roller specimens are polished using a vibratory finishing industrial process to promote the DLC coating adherence and to get as close as possible to the theoretical model assumptions (detailed in Section 2.3). Thus, the final coated

roller roughness parameters are: $S_a = 0.011$ µm and $S_q = 0.014$ µm.
In addition, some of the roller specimens are machined in order to mimic a limited piston ring geometry and study the geometrical starvation effect. Using a wire Electrical Discharge Machine (EDM), a 0.5 mm wide slider with an unchanged face radius and roughness is produced. Figure 3.11 shows a measurement of the slider profile. The rollers are machined after the surface finishing process in order not to alter the slider parabolic shape. All specimen are DLC coated for testing. Figure 3.12 shows the roller specimen after each modification process.

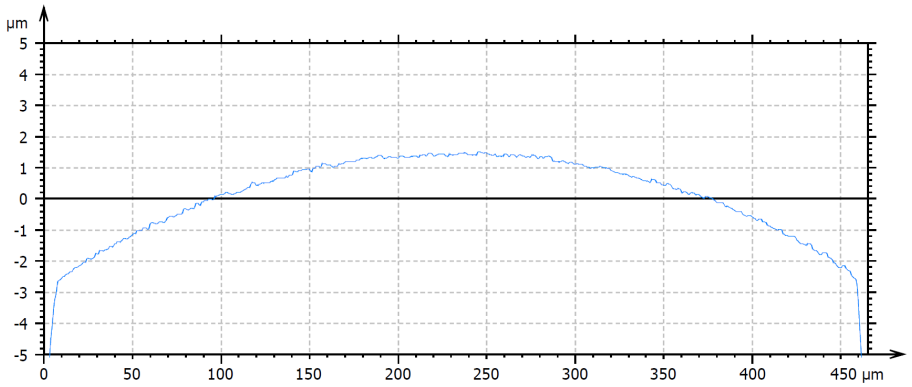

Figure 3.11: 0.5*mm* wide slider profile.

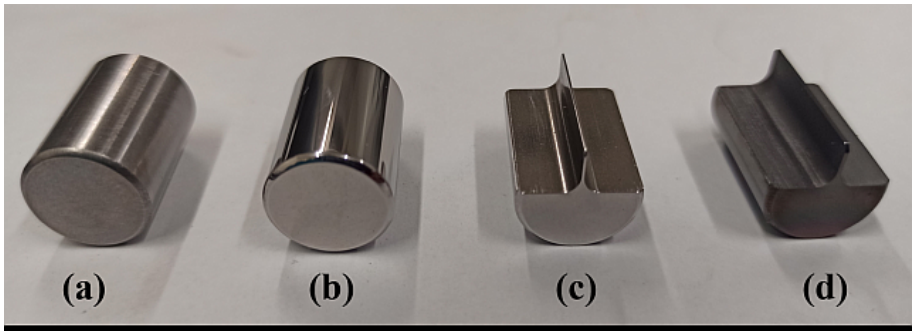

Figure 3.12: Different roller specimen: (a) original (b) polished (c) 0.5 mm wide slider (d) DLC coated slider.

One of the main difficulties of these experiments is the correct rotational alignment of the slider profile onto the plate around the x axis. First, the slider is aligned visually. Then, it is "dynamically" aligned while the test-rig is running. Therefore, the contact is loaded and lubricated. While the slider is sliding against the plate, the roller angle (around the x axis) is changed by varying the height of the specimen/frame linkage. This is accurately done by means of a precision screw-nut system. Correct alignment of the roller on the plate is reached when the friction is low (assuming viscous friction) and when the friction signal is symmetrical for a back and forth displacement (assuming the roller profile to be

symmetrical). Alignment error is computed by comparing the friction forces for similar dynamic conditions (i.e. acceleration and deceleration phases). Figure 3.13 shows the alignment accuracy for a 0.5 mm slider, for low and high test speeds the alignment error is below five percent.

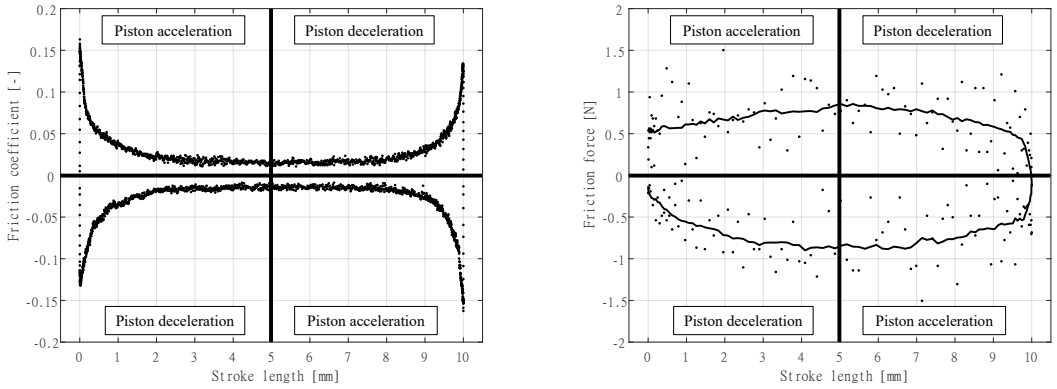

(a) $u_{mean} = 10$ mm/s (b) $u_{mean} = 150$ mm/s

Figure 3.13: Slider alignment validation (solid line: moving average). Alignment error is below 5 %.

To reduce the measurement noise on the friction force signal, the signal is averaged over several cycles (at least over 5 cycles for low speeds and over 50 cycles for high speeds). Figure 3.14 shows an example of the averaged measured friction force at mid-speed. Detailed results and comparisons with the computer-based predictions are discussed in Chapter 4.

3.5 Piston-Ring / Cylinder-Liner

A floating liner test-rig is used to experimentally study the tribological performance of the DLC coated PRCL contact. Compared to the previously described specimen test-rigs, it allows the testing of real engine parts (piston and piston rings) for real engine speeds. Figure 3.15 shows a picture and a kinematic scheme of the test-rig.

On the top of the rig, a crankshaft with two crank-pins is driven by an electric motor. The rotational movement of the crankshaft is converted into an alternative linear movement by means of two long connecting rods attached to two carts. A piston is rigidly linked to the bottom of one cart (no piston pin) as the second cart operates as a counterweight. Both carts are linearly guided onto two columns by mean of two ball bushings. In order to measure the piston ring friction alone, the engine original piston is slightly modified. The piston skirt is totally removed and the piston external diameter is reduced by 1 mm. Pressure screws are also added into the top-ring groove giving the

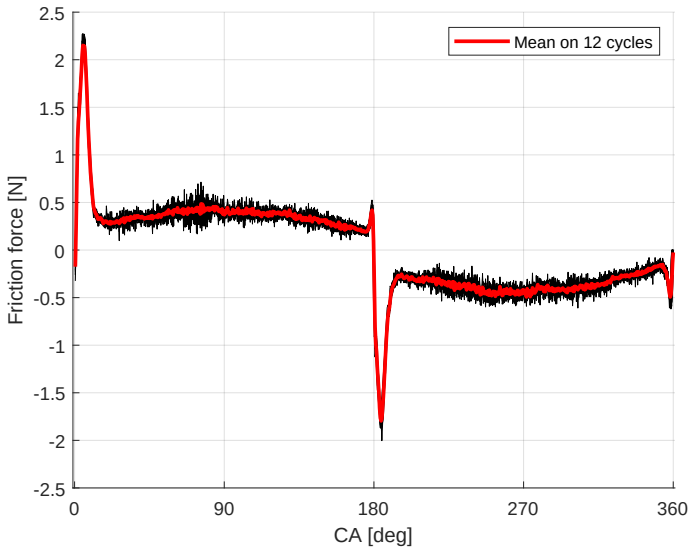

Figure 3.14: Averaged friction force on 12 cycles for $u_{mean} = 30$ mm/s, $w = 24.4$ N, 10W-60 oil at 21°C.

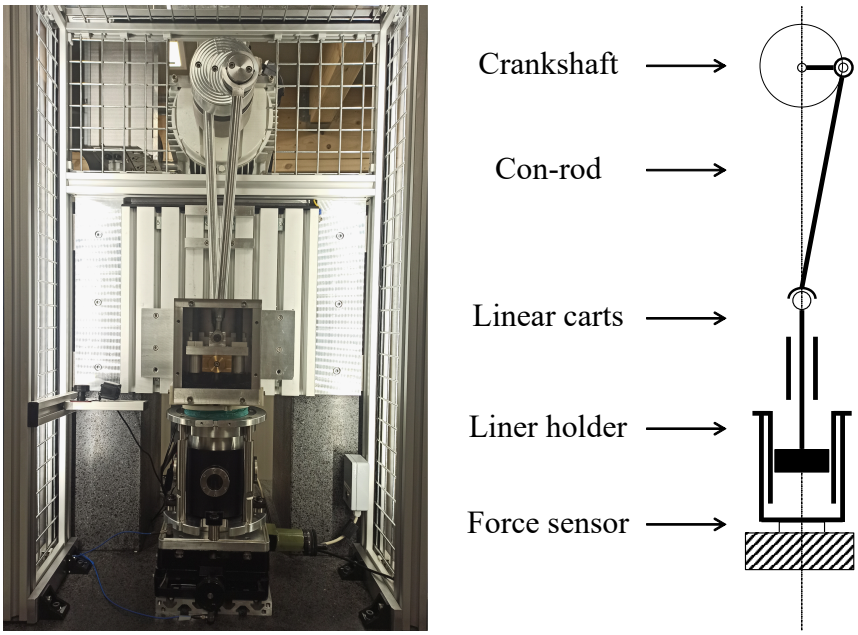

Figure 3.15: PRCL floating liner test-rig.

possibility to add some additional contact pressure in order to mimic the combustion pressure acting behind the ring.
At the other end, the engine liner is assembled into a liner holder itself mounted onto a single force transducer centred onto the piston axis. The liner is not standard and is machined to the required specifications. The piezoelectric force sensor is located on the piston axial axis in order to accurately measure the piston rings friction. An external

thermally controlled lubricant reservoir supplies by means of two pumps a continuous lubricant flow on the outer surface of the liner (liner temperature regulation) and on the inner surface of the liner (PRCL contact lubrication) by means of a nozzle located at the bottom end of the liner. The piston adjustment/centring into the liner is precisely verified before every test using control-parts. In addition to the possibility to test real engine parts, the main test-rig benefit is the possibility to rapidly change the test specimen. It takes approximatively 30 minutes to disassemble, change parts and reassemble the rig.

However, as most floating liner engines, the test rig suffers from vibrational instabilities above 400 RPM. Figure 3.16 shows raw friction measurements at a 100, 500 and 1000 RPM.

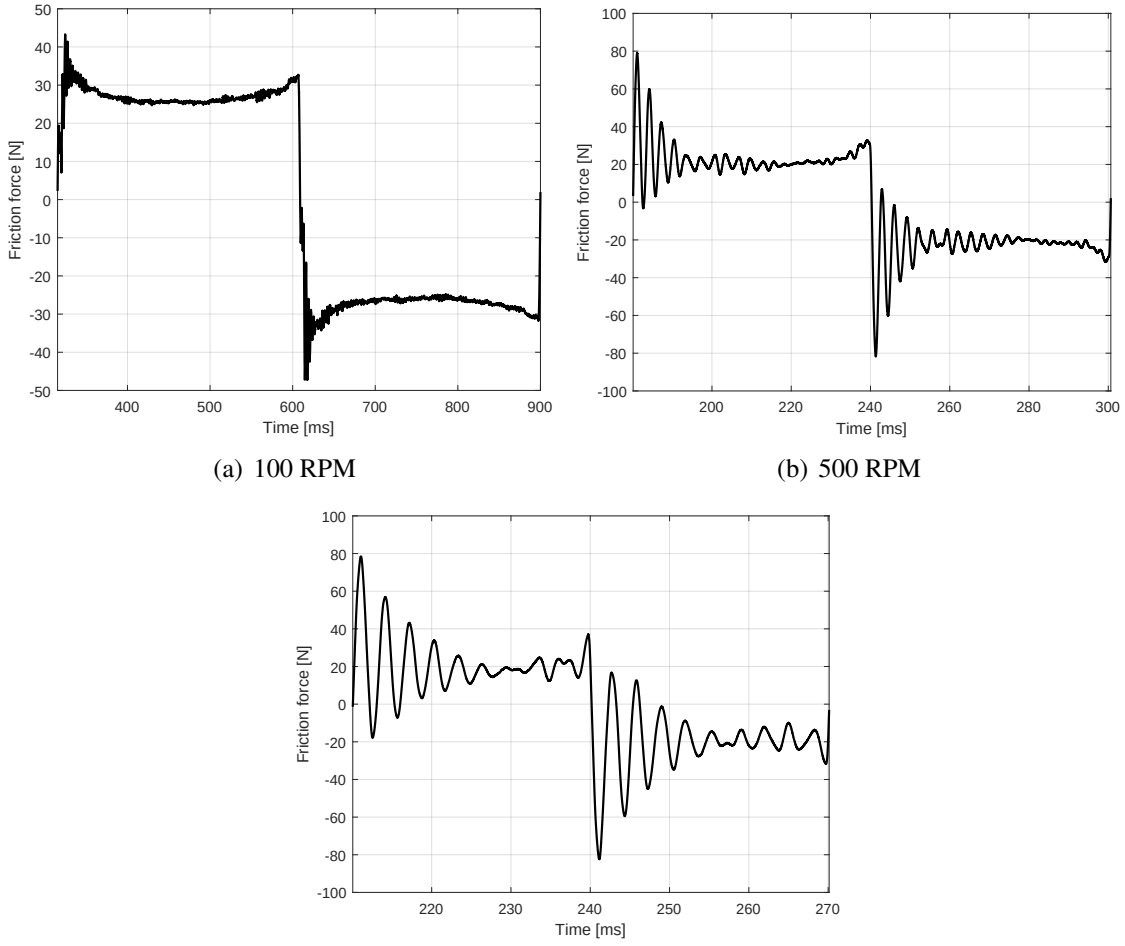

(a) 100 RPM

(b) 500 RPM

(c) 1000 RPM

Figure 3.16: Floating liner friction measurement.

The friction signal oscillations in Figure 3.17 suggest the presence of a flexible element in the system. Figure 3.18 shows the corresponding frequency distribution of the

signal “noise” (computed by discrete Fast Fourrier Transform - DFFT) and highlights the existence of a problematic frequency around 300 Hz .

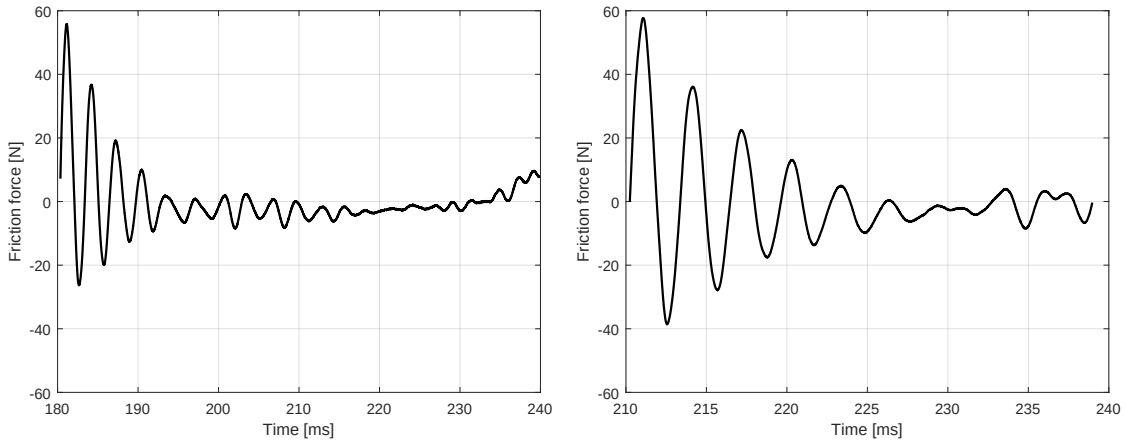

(a) 500 RPM (b) 1000 RPM

Figure 3.17: Friction signal oscillation.

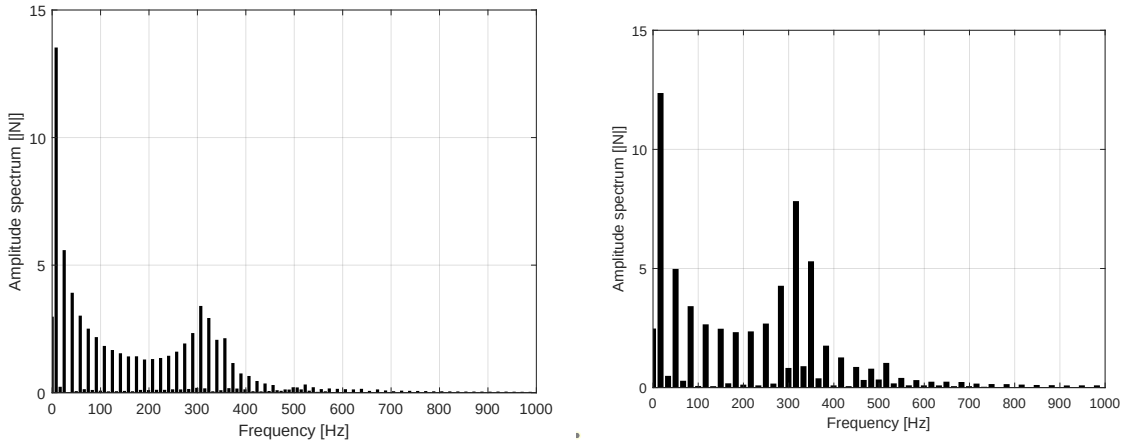

(a) 500 RPM (b) 1000 RPM

Figure 3.18: Friction signal oscillation frequency distribution.

To detect the flexible part of the rig oscillating at 300 Hz, vibrational investigations have been carried out using several accelerometers and an instrumented hammer. Thereby, to improve the test-rig stability at high-speed the initial aluminium frame has been changed for a heavy concrete block. Also, the cart linear guides were changed from linear journal bearings to ball bushings to minimise the transmitted energy from the moving parts to the frame. These changes reduced significantly the global vibration of the rig, allowing us to carry on the investigations.
The frequency response of each test-rig part was measured using an accelerometer and by

shocking it with an instrumented hammer. By dividing the system vibration (accelerometer measurement in [m/s^2]) with the injected force in the system (hammer shock measurement in [N]) one can compute the inertance (or transfer function) of the system which describes the natural vibrational behaviour of it. Figure 3.19 shows the liner-holder inertance spectrum. The liner-holder has four natural frequencies at 60 Hz, 175 Hz, 300 Hz and 400 Hz. The natural frequencies at 60 Hz and 175 Hz were identified as lateral displacement modes which are both soften ones the test-rig is completely assembled. The measured natural frequency at 300 Hz is consistent with the signal oscillations frequency highlighted in Figure 3.18. In contrary, the 400 Hz natural frequency is non-existent in Figure 3.18 and is thus not considered as problematic despite its amplitude in Figure 3.19.

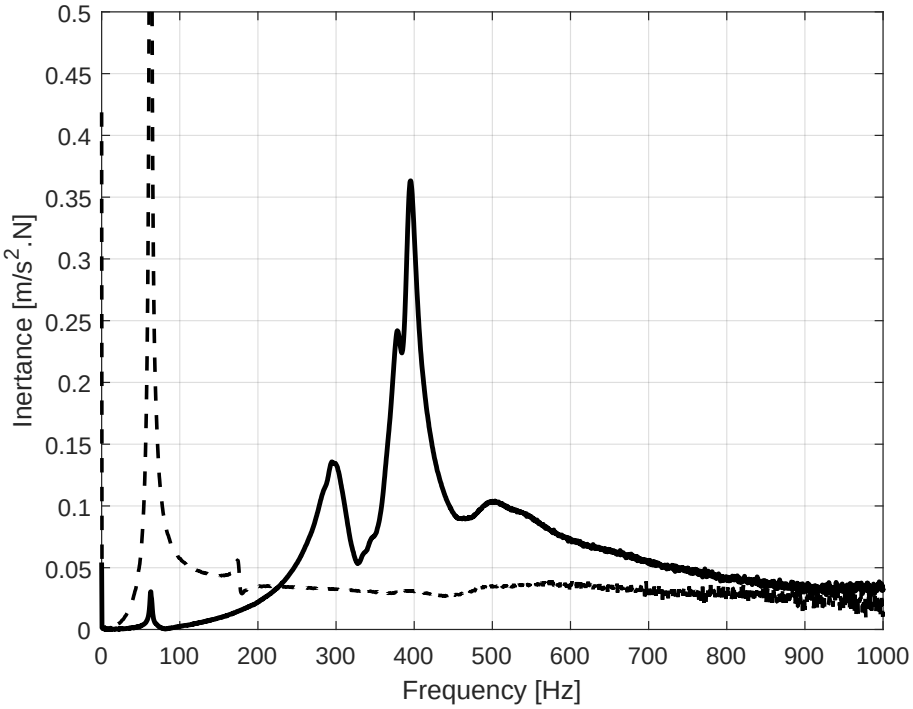

Figure 3.19: Liner holder lateral (dotted line) and vertical (solid line) inertance measurement.

Furthermore, a 3D modal analysis of the liner-holder system has been carried out using *Ansys Mechanical*. Figure 3.20 shows the model mesh constituted of more than 12E4 nodes and 62E3 linear tetrahedron elements. All mechanicals connections and contacts are assumed infinitely rigid. Table 3.8 gives the modal analysis results obtained after a model convergence study. Because of the infinitely rigid assumptions, the computer-based model is significantly stiffer than the real liner-holder, thus the computed natural frequencies are roughly higher. Thereby, and by analysing the different mode displacements we can state that: the computed modes 1 and 2 at 110 Hz and 111 Hz correspond to the measured natural frequency at 60 Hz, mode 3 at 300 Hz corresponds to the measured natural frequency at 175 Hz and mode 4 corresponds to the measured natural frequency at 300 Hz. Figure 3.21 shows the liner-holder displacement for the

first vertical mode (mode 4) corresponding to the problematic frequency. For this mode, both the bottom plate fins and the four long columns are bending in phase generating an important vertical displacement of the liner. This displacement is responsible of the large amplitude oscillation presented in Figure 3.17. Based on the numerical modal analysis, solutions to rigidify the liner-holder have been proposed and are currently being budgeted.
In addition, according to [134] the rig is not dynamically balanced. This unbalance participates to the rig vibration instabilities, especially at the dead centres where the inertia forces change in direction.

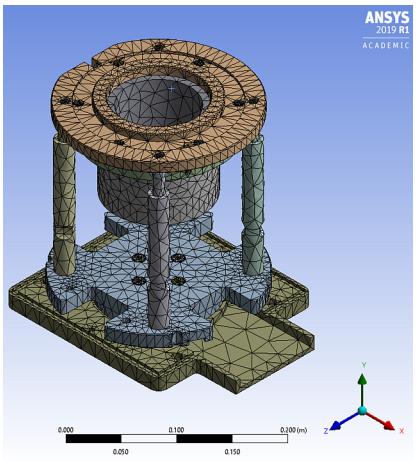

Figure 3.20: Liner-holder modal analysis mesh.

Mode	Frequency [Hz]
1	110
2	111
3	306
4	565
5	595
6	602

Table 3.8: Liner-holder modal analysis results.

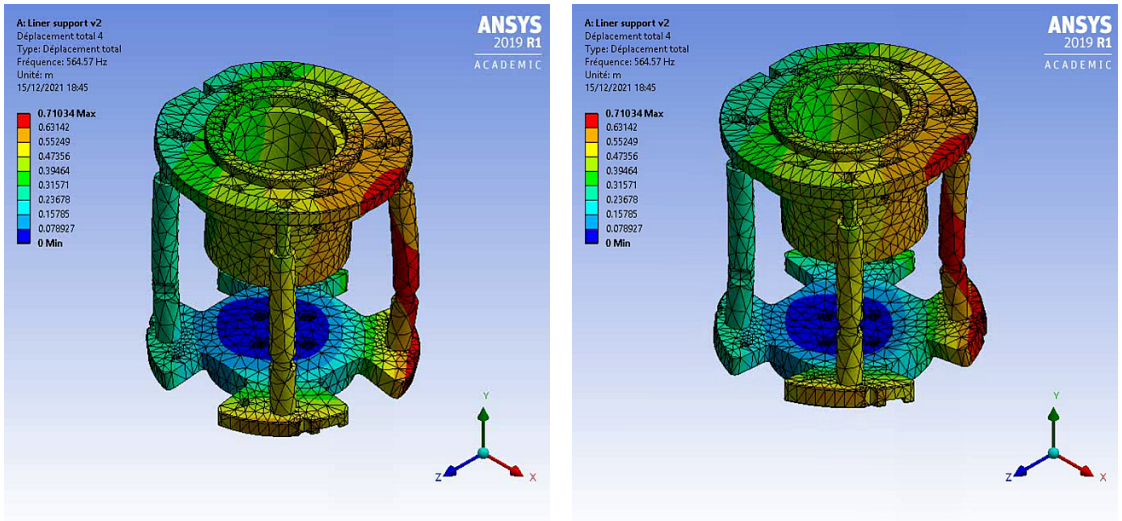

Figure 3.21: Liner-holder total displacement for mode 4 at 564 Hz (first vertical mode)

In order to tackle the rig vibrational instability, the following strategy is established. Based on the IVR Reynolds equation, one can state that load, speed, radius of curvature and lubricant viscosity are the four contact parameters determining the oil film thickness and the viscous friction [43,132]. This analysis is valid for both the steady-state and time-dependent theory as well as for fully-flooded conditions (see Appendix C). Assuming load to be constant, the oil film thickness is proportional to the contact speed times the oil viscosity ($h \propto u_m \eta$). In this way and by ignoring the inertia effects, a high-speed / low-viscosity contact is similar to a low-speed / high-viscosity. One can thus mimic high-speed operating conditions without suffering from the test-rig vibration instabilities. This method is used on the PRCL test-rig to improve the signal to noise ratio. For example, the contact viscous variables for a mean speed of $u_m = 2$ [m/s] at 100°C in a 5W-30 grade oil are theoretically similar to those for a contact mean speed of $u_m = 0.2$ [m/s] at 50°C lubricated with a 10W-60 grade oil.
In addition, the friction signal is post-processed using a low-pass filter with a cut-off frequency $f_c = 250$ Hz and is averaged at least over ten cycles to improve once more the signal to noise ratio. Figure 3.22 shows some examples of post-processed friction measurements. Measurement results and comparison with predictions are discussed in Chapter 5.

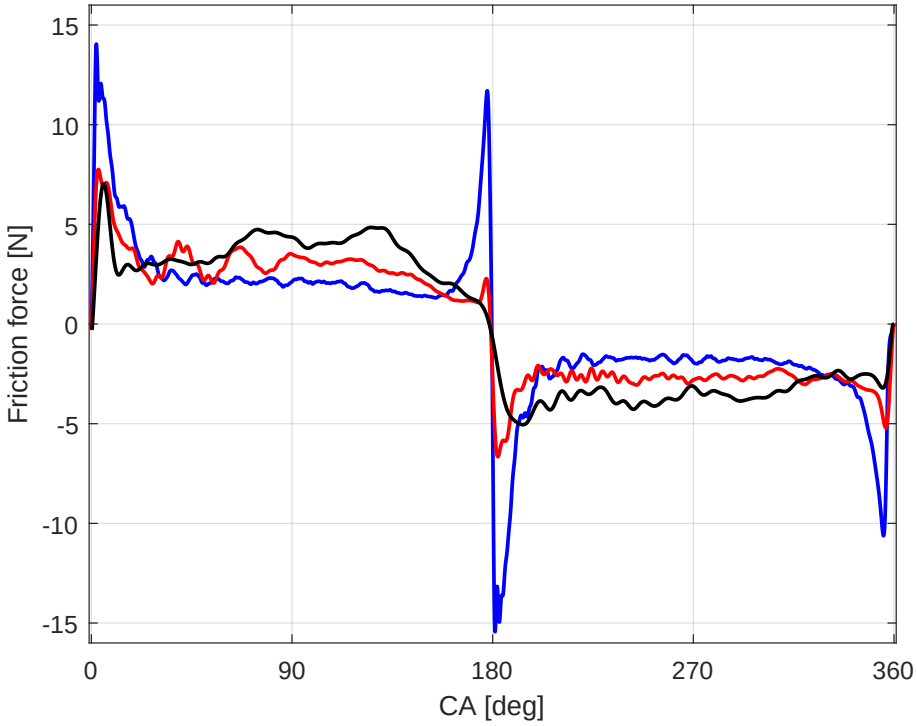

Figure 3.22: Post-processed floating liner friction measurement at 100 RPM (blue), 200 RPM (red) and 400 RPM (black) for a compression ring and a 10W-60 oil at 50°C.

3.6 Conclusion

In this chapter, the experimental rigs and methods used in this work are described. First, the coating tribological performance under boundary lubrication conditions are assessed by means of two reciprocating ball on plate test-rigs. Thereby, the following trends where observed:

- Almost no tribofilm is observed on the DLC coated parts. On the contrary, large and thick tribofilm patches are obtained on the steel surfaces for every fully-formulated engine oil tested,
- Generally the DLC coated parts show no wear, with only some slight polishing of the roughness tops. However, tribo-chemical wear of the DLC is noticed when it is tested against a steel surface in fully formulated engine oils containing MoDTC FM additives,
- A 15% to 20% friction reduction is measured for a DLC coated contact compared to an uncoated contact in fully formulated engine oils without FM additives. For oils containing FM additives, the DLC coating shows no reduction in friction,
- No super-lubricity is obtained with glycerol and castor oil. However, the DLC coating has shown a good tribological performance lubricated with water. No wear and a 0.06 friction coefficient are obtained after a four hour testing period.

Secondly, a line-contact friction measurement method is developed in order to evaluate the model accuracy. Therefore, a mirror-like polished, DLC coated roller is rubbed against a plate for controlled speeds, loads and lubricant temperatures/viscosities. In addition, some rollers are machined to mimic the finite width of a piston-ring and thus test geometrical starvation. This method allows for an accurate assessment of the line-contact friction all along the stroke, for all lubrication regimes and for starved conditions. Hence, it is a useful tool to assess the model relevance, investigated in Chapter 4.

Finally, the floating-liner test-rig used to experimentally study the PRCL contact is described. It allows the testing of real engine parts such as the piston and the piston-rings for typical engine speeds and lubrication conditions. The piston motion is driven by an electric motor and thus the test-rig is easy to use and to assemble/disassemble. However, this test-rig presents two main limitations. First, the lack of the combustion phase, which has a direct influence on the ring lubrication. This limitation is inherent to the test-rig design and was performed in order to keep the contact simple for a first approach. Secondly, the test-rig presents a vibrational instability which pollutes the friction force signal for engine speeds above 400 RPM. By means of a vibrational investigation, the liner-holder natural frequency have been identified as problematic. Solutions to rigidify the part have been designed using a numerical modal analysis and upgraded components will be installed in the near-future. Nevertheless, according to the fact that the oil film thickness

is proportional to the viscosity$\times$velocity product, a strategy to mimic high speed / low viscosity operating conditions using low speed / high viscosity parameters is introduced. Thereby, the tribological performance of a DLC coated compression ring is investigated in Chapter 5.

Chapter 4

Model Validation

Contents

4.1 Introduction

Predictions from the model described in Chapter 2 are compared to numerical and experimental solutions in order to test its predictive performance. First, the hydrodynamic predictions are compared to a P-θ solution computed using finite difference (where P is the pressure and θ the void ratio). Then, predictions are compared to roller on plate friction measurements. Consequently, the line-contact model is upgraded to account for the roller macro-geometry. The original and upgraded model accuracy is discussed for each lubrication regime (boundary, mixed and full-film) and for fully-flooded/starved lubrication conditions.

4.2 Model Input

Table 4.1 lists the calculation domain input.

Name	Notation	Detail
First crank-angle	CA_{first}	Calculation domain first crank-angle step in [deg]
Last crank-angle	CA_{last}	Calculation domain last crank-angle step in [deg]
Crank-angle step	dCA	Nominal crank-angle step in [deg]
Max. refining level	lvl_{max}	Maximum time-step refining level [-]

Table 4.1: Calculation domain input.

The domain input can be chosen freely, however it is recommended to choose a CA_{first} at mid-stroke to minimise the transient term drift due to the steady-state initialisation. From the crankshaft angular input and from the engine rotational speed given in Table 4.2, the calculation time-step is defined as:

$$\delta_t = \frac{1}{6}\frac{dCA}{RPM} \tag{4.1}$$

Table 4.2 regroups the model engine input, from which the piston position and speed are computed.

Name	Notation	Detail
Stroke length	$s = 2e$	in [m]
Con-rod length	c	in [m]
Bore diameter	b	in [m]
Engine RPM	RPM	Engine rotational speed in [revolutions per minutes]
TDC temperature	$temp_{TDC}$	Liner Top-Dead-Center temperature in [$^{\circ}C$]
BDC temperature	$temp_{BDC}$	Liner Bottom-Dead-Center temperature in [$^{\circ}C$]
In-cylinder pressure	P_{gas}	In-cylinder pressure measurement data in [Pa]

Table 4.2: Engine input.

Based on the TDC and BDC liner temperatures, the temperature distribution along the stroke is interpolated in a linear or in a quadratic manner. A measured temperature/stroke-position data can also be used and be curve-fitted using the *Matlab spline* function. For instance, the in-cylinder pressure is curve-fitted using measured pressure values as a function of the crank-angle.

Table 4.3 details the code lubricant input. ν_1, ν_2, $temp_1$, $temp_2$, $temp_3$ and ρ are obtained from the lubricant data sheet and are used to compute the lubricant viscosity change with temperature (using the ASTM viscosity/temperature equation defined in Section 2.4). In order to be used in the model, the lubricant kinematic viscosity is multiplied by the lubricant density to obtain the lubricant dynamic viscosity. The density is corrected according to the temperature using ASTM D 1250-04 and IP 200/04 tools.

Measured viscosity/temperature data can also be used and be curve-fitted using the Matlab *spline* function. The lubricant shear-thinning effect is not accounted for. h_{in} is defined as the initial lubricant film thickness available on the liner and is fixed by the user since it is rather difficult to measure. h_{in} is mostly chosen to be large in order to model the fully-flooded lubrication conditions when the piston moves from TDC to BDC (for the closest ring to the crankcase).

Name	Notation	Detail
Viscosity n°1	ν_1	Lubricant kinematic viscosity at $temp_1$ in [$m^2\ s^{-1}$]
Viscosity n°2	ν_2	Lubricant kinematic viscosity at $temp_2$ in [$m^2\ s^{-1}$]
Density	ρ	Lubricant density at $temp_3$ in [$kg\ m^{-3}$]
Temperature n°1	$temp_1$	Lubricant temperature at ν_1 measurement in [° C]
Temperature n°2	$temp_2$	Lubricant temperature at ν_2 measurement in [° C]
Temperature n°3	$temp_3$	Lubricant temperature at ρ measurement [° C]
Initial film thickness	h_{in}	Lubricant initially available on the liner in [m]

Table 4.3: Lubricant input.

The ring geometry is defined using a discontinuous piecewise function. It is mostly described using three parts, two high parts which correspond to the piston sides and a centred part which corresponds to the ring face. The ring face is generally approximated by a parabolic symmetric profile, the ring width and the ring radius being the main geometrical parameters. However, asymmetric ring shapes can also be implemented by dividing the central part in two, each having a different radius of curvature. Also, a measured ring profile can be curve-fitted and be used as input of the calculation, as long as the primitives given in Equations 2.16-2.18, 2.22-2.24, 2.26, 2.35 and 2.36 defined in Chapter 2 can be formally integrated twice by the Matlab symbolic toolbox.
In order to compute the ring contact pressure, the user has to provide the ring pre-tension. If this ring parameter is unknown, the ring contact pressure can be computed using the following approximation [135, 136]:

$$p_{ring} = \frac{gEI_r}{3\pi\ell(b/2)^4} \tag{4.2}$$

with the ring cross section defined as $I_r = \ell d^3/12$, g the ring end gap prior to fitting, E the ring Young modulus, ℓ the ring width, b the bore diameter and d the ring height.

The final model input is related to the solid-to-solid contact. The "load-distance" data computed from the measured surface topography (see Section 2.6) is curve-fitted using the Matlab *spline* or *pchip* functions in order to be used in the solver. In addition, the boundary friction coefficient is given, based on friction measurements detailed in Section 3.3.

4.3 Model Output

The model main output are listed below:

- h_0 **the lubricant minimum film thickness in *meters*:** describes the minimum gap in between the ring and the liner. It can be computed in an absolute or a relative manner (compared to the surface roughness),
- f **the contact friction force in *Newtons*:** is equal to the sum of the hydrodynamic f_{hydro} and the asperity contact f_{asp} friction force,
- P_w **the contact power loss in *Watts*:** is equal to speed times the friction force,
- $\bar{E}$ **the energy loss in *Watt-seconds*:** is defined as the integral of the power loss over time,
- w_h/w_{tot} **and** w_{asp}/w_{tot} **ratios:** are respectively the ratio of load carried by the fluid and the asperity contact. These parameters indicate on the contact lubrication regime. For w_{asp}/w_{tot} values close to 1 (i.e. w_h/w_{tot} values close to 0), the contact is in the boundary lubrication regime as the normal load is mainly carried by the solid-to-solid contact. For w_h/w_{tot} values close to 1 (i.e. w_{asp}/w_{tot} values close to 0), the contact is in the full-film lubrication regime, the fluid carries completely the normal load, no solid asperities are in contact, theoretically no wear occurs and the friction is caused by the shearing of the fluid. In between these values, the contact is in the mixed lubrication regime for which the normal load is carried by both the fluid and the solid-to-solid contact, this lubrication regime highlight an interesting minimum friction value.

The model output is mainly described as function of the crankshaft angle CA, the time t or the piston position x.

4.4 Numerical Validation

In order to control the model hydrodynamic part accuracy, predicted viscous variables such as the film thickness h_0, the viscous friction f_{hydro} and the meniscus positions x_a and x_b are compared to a numerical integration solution. For this purpose, the 2D iso-viscous-rigid, steady-state solver described in [137] is extended to a time-dependent, line-contact problem at imposed load. Based on the P-θ theory and using the Fischer-Burmeister equation to model cavitation, it yields to the film thickness prediction solving the discrete load-balance equation and de discrete Reynolds equation obtained by finite differences.

The following operating conditions are applied to both calculation methods. The ring geometry is defined as a finite parabolic shape:

$$\begin{cases} h = h_{side} + h_0 + \frac{x_l^2}{2r} & \text{for} \quad x < -x_l \,\&\, x > x_l \\ h = h_0 + \frac{x^2}{2r} & \text{for} \quad -x_l \leq x \leq x_l \end{cases} \tag{4.3}$$

h_{side} is set such as $h_{side} >> h_0$ in order that the side geometry does not influence the results.

Two different contact frequencies (i.e. speeds) with a significantly different transient behaviour are studied. Table 4.4 regroups the contact parameters as Table 4.5 lists the dimensionless parameters used for both models.

Parameter	Value	
u_m	$\frac{1}{2}u_{max}\cos(2\pi f_r t)$	[m/s]
u_{max}	10	[m/s]
f_r	25 - 250	[Hz]
w_1	100	[N/m]
h_{side}	1	[mm]
r	1	[cm]
x_l	0.5	[mm]
h_{in}	5	[µm]
η_0	$1E-2$	[Pa.s]

Table 4.4: Contact parameters.

Parameter	Value	
x_r	1	[mm]
h_r	1	[µm]
$\bar{u}_m$	1	[m/s]
t_r	1	[ms]
p_r	120	[MPa]
f_r	120	[N/m]

Table 4.5: Dimensionless parameters.

Figures 4.1 to 4.4 present the dimensionless results for both the fully numerical method (circles) and the semi-analytical solver (solid blue line). All output variables are plotted as a function of the dimensionless piston abscissa X along the stroke, with $X = 0$ the mid-stroke position and minimum/maximum values of X the dead-centres. The dimensionless minimum film thickness H_0 and the viscous friction coefficient curve interpretation are relatively explicit. Arrows indicate the time-evolution of the variables. X_{right} and X_{left} are variables specific to the fully numerical solution and their interpretation is more complex. Since the piston ring has a back and forth motion along the liner, the contact inlet and outlet are successively on one side and the other of the piston ring. Therefore, X_{left} describes the meniscus position on the left-hand side of the ring as X_{right} describes the right-hand side meniscus position. In this way, when the ring moves to the right (i.e. positive speeds) X_{right} stands for the inlet meniscus position (i.e. X_a for the semi-analytical model) as X_{left} stands for outlet meniscus position (i.e. X_b). The opposite is true for the ring moving to the left (i.e. negative speeds).

The first noticeable result of Figure 4.1 is the non zero film thickness at the piston reversal position because of the transient (squeeze) term. Due to the damping effect induced by the transient term, H_0 reaches its minimum value slightly later than the speed (black dotted line). Also because of this damping effect, the H_0 increase is delayed which leads to a lubricant accumulation in the inlet area (i.e. X_{left} rapidly increases for $5 < X < 6$ in figure 4.3(a)). This extra lubricant then leads to an overshoot of the film thickness (for $2 < X < 5$ in figure 4.1(a)). Once this extra volume of lubricant is fully

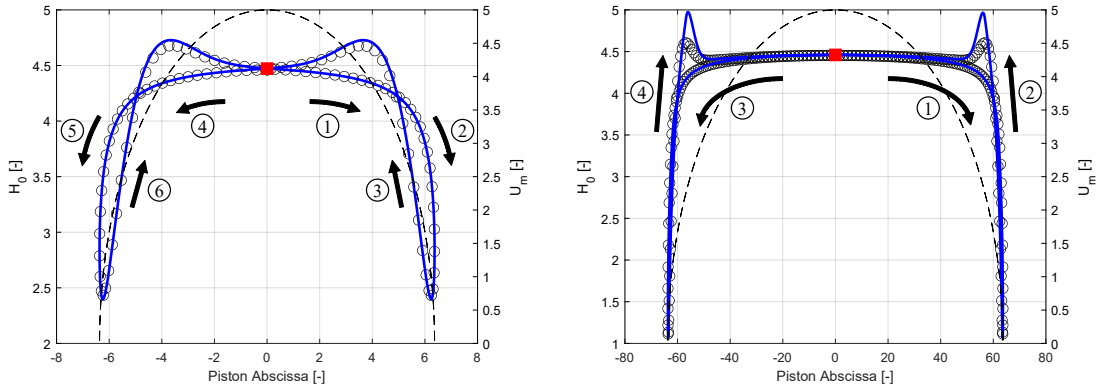

(a) 250 Hz (b) 25 Hz

Figure 4.1: Dimensionless minimum film thickness H_0 (see Appendix B) as a function of the piston abscissa X (circles: fully numerical - blue solid line: semi-analytical - black dotted line: dimensionless mean speed).

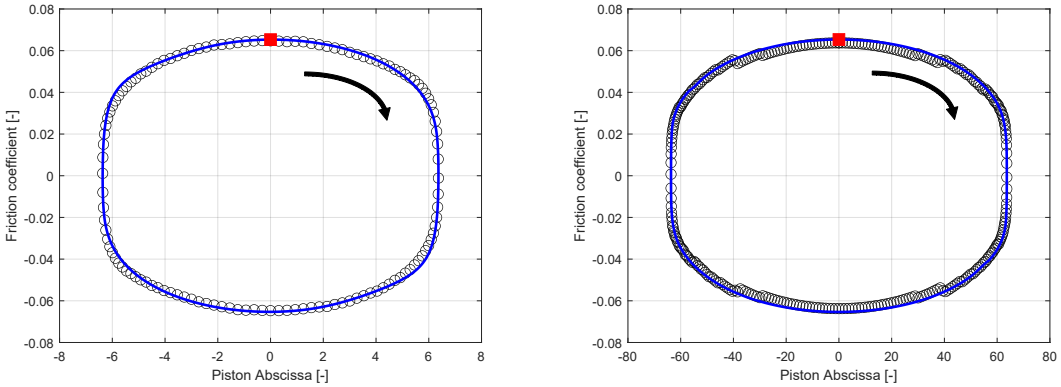

(a) 250 Hz (b) 25 Hz

Figure 4.2: Viscous friction coefficient as a function of the piston abscissa X (circles: fully numerical - blue solid line: semi-analytical).

consumed, H_0 returns to its quasi steady-state value at mid-stroke which is consistent with the initial lubricant film thickness available on the liner H_{in}. This analysis confirms the correct modelling of the starvation and oil transport physics in the semi-analytical model. In addition, both fully numerical and semi-analytical values of H_0 and friction coefficient are in good agreement as shown by the small relative errors presented in Tables 4.6 and 4.7.

In Figures 4.3 and 4.4 the X_{right} and X_{left} results show as slight deviation between both models, especially at the reversal positions and for the contact outlet meniscus position. This difference is expected since the right hand side of the outlet flow conservation

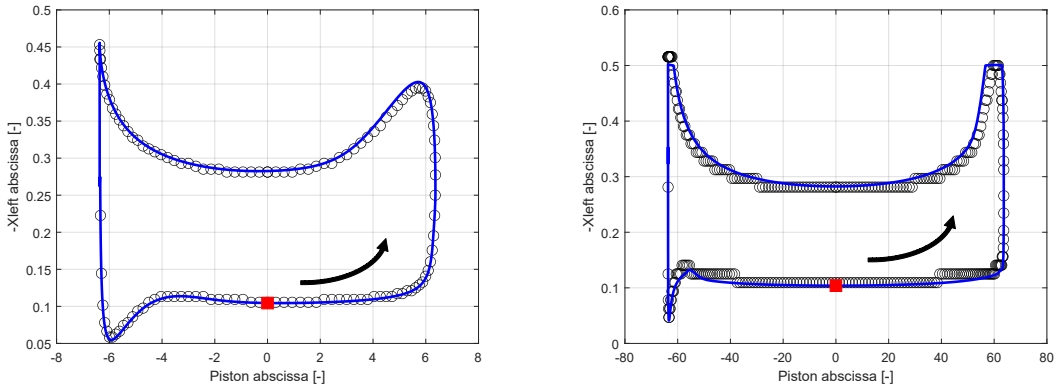

(a) 250 Hz (b) 25 Hz

Figure 4.3: Left meniscus position as a function of the piston abscissa X (circle marker: fully numerical - blue solid line: semi-analytical).

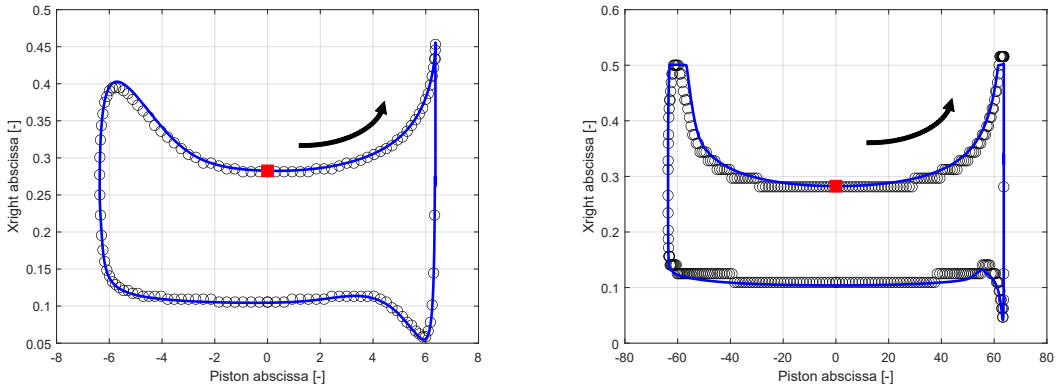

(a) 250 Hz (b) 25 Hz

Figure 4.4: Right meniscus position as a function of the piston abscissa X (circles: fully numerical - blue solid line: semi-analytical).

equation is an approximation (Equation 2.29 in Section 2.5). Also, the finite difference method relies on a fine spatial grid allowing for a more precise prediction of the flow imbalance. However, this approximation has a negligible impact on the main output variables H_0 and f.

In addition, the steady-state fully flooded and starved solutions have also been validated using the analytical expressions given in [56, 57].

The main benefit of the semi-analytical solver is that it needs only a single discrete time grid δ_t whereas the fully numerical method needs a spatial δ_x and a time δ_t discrete grid. Consequently, the semi-analytical solver needs fewer calculation steps to predict

Variable	Numerical		Semi-analytical		Difference [%]	
[-]	250 Hz	25 Hz	250 Hz	25 Hz	250 Hz	25 Hz
H_0	4.4727	4.4545	4.4737	4.4604	0.02	0.13
CoF	0.0649	0.0638	0.0653	0.0653	0.62	2.50

Table 4.6: Full numerical and semi-analytical results at mid-stroke.

Variable	Numerical		Semi-analytical		Difference [%]	
[-]	250 Hz	25 Hz	250 Hz	25 Hz	250 Hz	25 Hz
H_0	2.4316	1.1068	2.3978	1.0744	1.39	2.92
CoF	0.0011	0.0063	0.0012	0.0058	6.18	7.40

Table 4.7: Full numerical and semi-analytical results at TDC.

the transient film thickness. It also relies only on continuous mathematics expressions (excepted for the right hand side of the outlet flow conservation equation and for the transient term). In addition, only one convergence study of the time-step size is performed for the semi-analytical solver against two for the fully numerical method (spatial- and time-wise). Apart from the formal calculation, for a 250 Hz contact frequency, the computation times for each method are similar ($\approx$ 30 seconds on a laptop computer) for a semi-analytical δ_t four times smaller than the fully numerical one. It should be noted that for calculation stability issues, the semi-analytical time-step as to be small compared to the fully numerical method. Nevertheless, the Matlab native *fsolve* function used to solve the system of non-linear equations is not yet optimised and improved calculation stability as well as shorter computation times might be reached by some fine-tuning.

4.5 Experimental Validation

In order to control the code accuracy in predicting boundary and mixed lubrication friction, the model results are compared to friction measurements. Therefore, roller on plate friction measurements are performed for simplified and controlled operating conditions ahead of the complex PRCL contact. The transient and starvation features of the model are investigated.

4.5.1 Experimental Set-up

Roller on plate friction measurements are performed on the ARTEMIS test-rig described in Section 3.4 in order to approximate as much as possible the theoretical line-contact. Two different roller specimen are tested; an original roller from a cylindrical roller bearing named in this document “full roller” and a machined roller with a slider width equal to 0.5 mm, called the “0.5 mm slider”. The main goal of the 0.5 mm slider compared to the full roller is to study the geometrical starvation influence on friction.

All specimen are polished and DLC coated to get as close as possible to the model assumptions and the future conditions in engine applications. The specimen detailed specifications can be found in Section 3.4.
In addition, all roller on plate pairs are run-in before testing. The run-in process is a 60 minute sliding at a 24.4 N normal load (leading to a maximum Hertz pressure of 82 MPa) and for a low sliding speed equal to 5 mm/s. The run-in process is controlled by monitoring the mean friction on each back and forth cycle and by comparing the instantaneous friction curve after several cycles (see Figure 4.5).

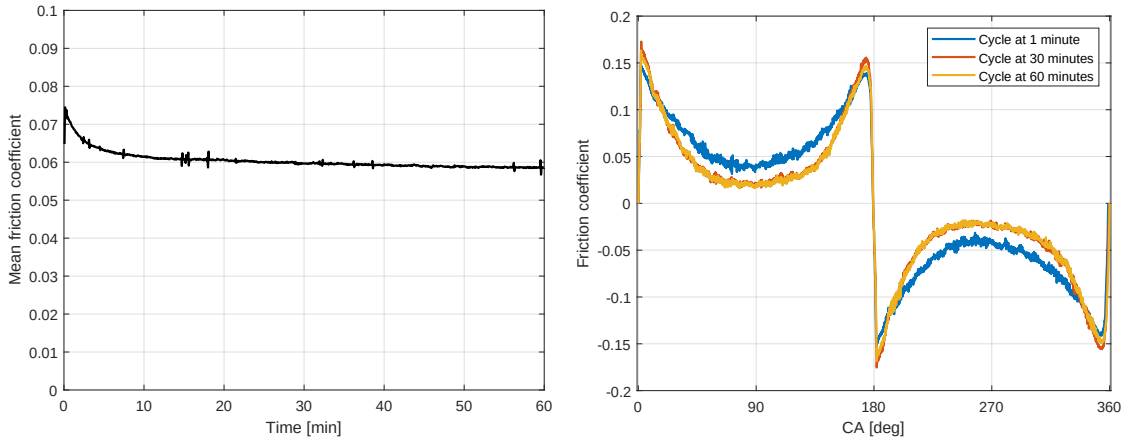

(a) Mean.

(b) Instantaneous (for run-in first, mid and last cycle).

Figure 4.5: Run-in friction coefficient monitoring.

Table 4.8 lists the different test operating conditions. A wide range of speeds is tested in order to study the contact friction in all three lubrication regimes (boundary, mixed and full-film). The contact load is intentionally large in order to minimise the influence of a potential additional load due to the test-rig design. Thereby, the load uncertainty is estimated as ± 1 N. In terms of PV ratios (pressure times speed ratio) these tests are of the same order of magnitude as typical PRCL PV ratios (1 to 10 MPa $\times$ m/s ignoring the combustion stroke). Because of a crowning of approximately 1 mm on each extremity of the roller, the contact length is slightly smaller than the complete length of the roller.

In order to widen the validation process, two different lubricants are tested: a 10W-60 grade fully formulated engine oil and a vegetable glycerine liquid composed of 99.5% glycerol. Intentionally, the selected lubricants have a high viscosity at room temperature in order to easily reach the full-film lubrication regime for relatively low speeds, to avoid test-rig vibrational instability and to mimic the viscosity times speed product at mid-stroke of a real engine. The computed viscosities are based on the lubricant datasheets (kinematic viscosities at 40°C and 100°C) and the ASTM viscosity-temperature formula defined in Section 2.4. In addition, viscosity measurements are performed for the

Parameter	Value
Theoretical contact length	18 mm
Normal force	24.4 & 10.7 N
Max. Hertz pressure	82 & 54 MPa
Stroke length	10 mm
Rotational speed	15 – 30 – 60 – 90 – 150 – 225 – 300 – 450 RPM
Linear mean speed	5 – 10 – 20 – 30 – 50 – 75 – 100 – 150 mm/s

Table 4.8: Test operating conditions.

10W-60 grade engine oil over a temperature range of 10°C to 100°C, using a tuning fork vibro-viscometer (A&D SV-10). The lubricant viscosity as a function of the temperature is given in Figure 4.6.

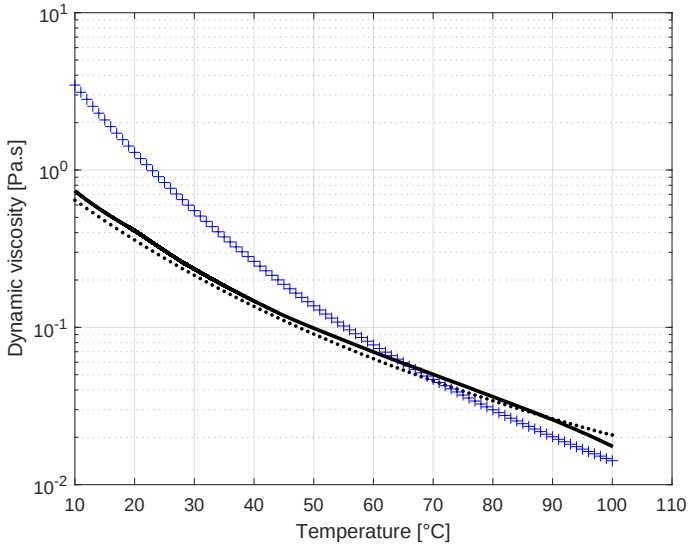

Figure 4.6: Lubricants dynamic viscosities (black points: theoretical 10W-60 grade oil - black line: measured 10W-60 grade oil - blue plus signs: theoretical 99.5% glycerol).

Friction tests are performed at room temperature ($\approx$ 19°C to 20°C). At 20°C the measured viscosity of the 10W-60 engine oil is roughly 10% higher than the theoretical viscosity. Since the theoretical viscosity formula is computed using the data-sheet lubricant viscosities at 40°C and 100°C, it is reasonably accurate in between these temperature boundaries but is relatively inaccurate outside those temperatures, especially for low temperatures. Therefore, the oil measured viscosity value will be retained in further calculations.

However, a rapid viscosity decrease over time is observed for the glycerol lubricant. For operating speeds in the full-film lubrication regime ($>$ 150 RPM) a significant decrease in the mean friction coefficient is observed after 10 minutes of testing. After 60

minutes a 30% decrease in the mean friction coefficient is measured. Glycerol is a hydrophilic liquid with a strong water-absorbing capacity and its viscosity is directly linked to the fraction of water by volume of fluid. Figure 4.7 shows the glycerine liquid viscosity variation as a function of the water/glycerol ratio at 20°C. For a ratio equal to 0, the liquid viscosity is high ($\approx$ 1.3 Pa.s) as for a ratio equal to 0.2 the liquid viscosity is divided by a factor of ten. During the friction test, the glycerol liquid may absorb the room humidity resulting into a significant decrease in viscosity and an unexpected change in operating conditions. To avoid as much as possible this undesired phenomenon, tests involving glycerol as lubricant were shortened in order to last less than 10 minutes. In addition a lubricant replacement was undertaken every 10 minutes.

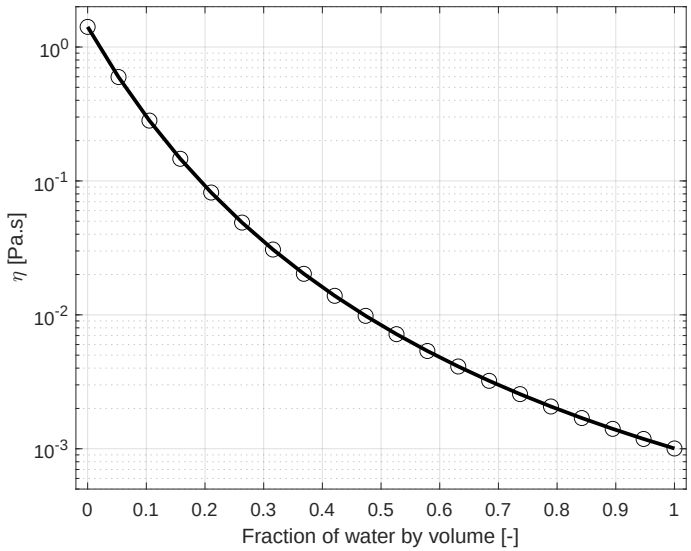

Figure 4.7: Glycerine fluid viscosity as a function of the water/glycerol ratio at 20°C (from www.met.reading.ac.uk).

With a relative uncertainty of ± 1°C on the room temperature, the lubricant viscosity for the 10W-60 engine oil is 0.41 ± 0.02 Pa.s (measured value) and for the glycerol is 1.3 ± 0.12 Pa.s (theoretical value).

In order to reduce the measurement signal to noise ratio, all friction signals are averaged over several back and forth cycles with respect to the stroke position. No low-pass or band-width frequency filter is applied in order not to alter the signal, especially the reversal friction peaks.

All tested samples are analysed after testing. The wear scar dimensions (width, length, discontinuity) are measured using a microscope. The roughness change inside the wear scar is studied using both confocal and interferometry methods.

Figure 4.8 gives an example of the test reproducibility at low and high speeds as Table 5.5 regroups the mean friction value over a full back and forth cycle for all tested speeds.

Tests with assembly 1 and 2 were performed on two different days with a complete disassembling of the test-rig in between. A difference in friction below 5 % is observed (excepted for the 15 RPM configuration) with a decreasing difference for increasing speeds. Repeatability is assessed by computing the cycle-to-cycle friction deviation (over 10 to 50 cycles depending on the speed). Figure 4.9 gives an example of the test repeatability at low and high speeds and highlights a relatively constant and random signal noise along the stroke. Table 5.5 also lists assembly 2 friction mean standard deviation. Results show a good assessment of the friction periodicity as the standard deviation is below 10 % for low speeds. For speeds above 150 RPM, the standard deviation increases due to the test-rig vibration instability, however the mean standard deviation stays below 20 %. Figure 4.9 gives an example of the scattered measurement at high speed.

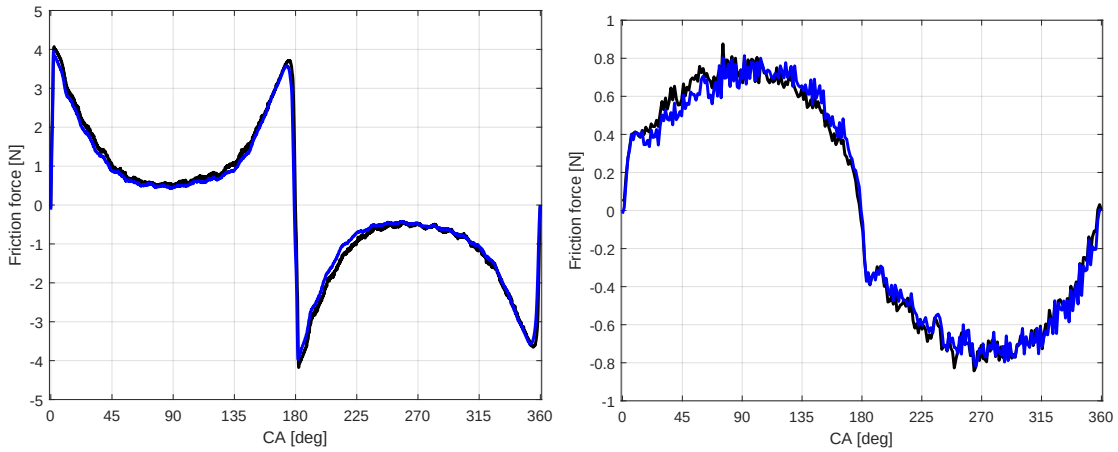

(a) 15 RPM (b) 150 RPM

Figure 4.8: Experiments reproducibility (black: assembly 1 - blue: assembly 2).

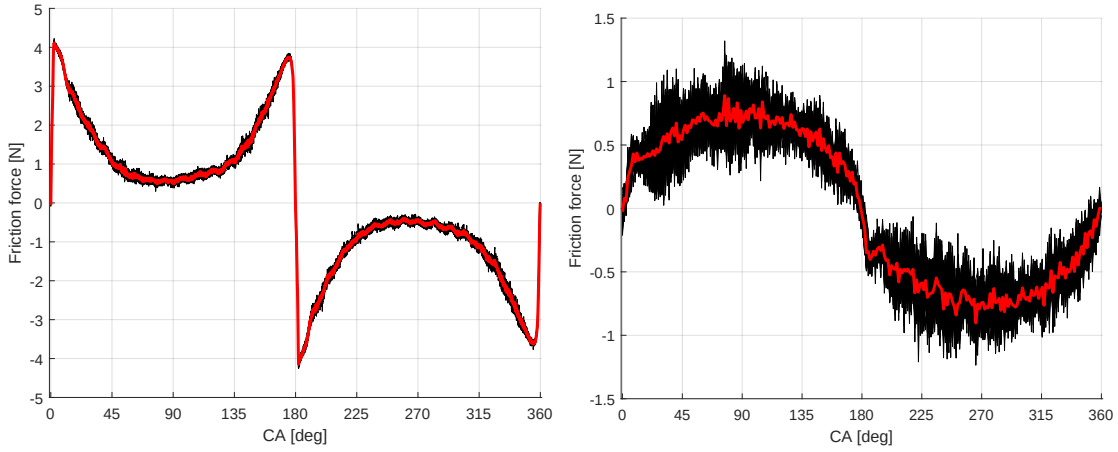

(a) 15 RPM (b) 150 RPM

Figure 4.9: Experiments repeatability (red line stands for the mean value).

Speed [RPM]	15	30	60	150	225	300	450
Mean friction Ass. 1 [N]	1.38	0.79	0.51	0.41	0.44	0.49	0.55
Mean friction Ass. 2 [N]	1.49	0.83	0.52	0.40	0.43	0.48	0.56
Difference [%]	8.00	4.48	2.04	1.83	2.04	1.01	1.05
Mean STD Ass. 2 [N]	0.06	0.05	0.04	0.05	0.06	0.09	0.12
Mean STD Ass. 2 [%]	4.02	6.21	7.83	13.33	14.71	18.56	20.95

Table 4.9: Test reproducibility and repeatability analysis.

4.5.2 Model Input

The roller geometry is defined as a parabolic profile using Equation 4.3 with $r = 7$ mm. The difference between the full roller and the finite slider is implemented by varying the parabolic profile width. For the full roller $x_l = r$ and for slider $x_l = 0.25$ mm. The roller sides height is set to $h_{side} = 5$ mm.

The model kinematics parameters are measured on the test-rig; the crankshaft radius is $e = 5$ mm and the con-rod length is $c = 200$ mm. The contact normal load is computed by dividing the applied normal force by the theoretical contact length. For a 24.4 N normal force the normal load is $w_{tot} = 1356$ N/m and for 10.7 N is $w_{tot} = 595$ N/m (with a 18 mm contact length).

The lubricant viscosity is assumed to be constant along the stroke and is equal to the viscosity values detailed in Section 4.5.1. However, in order to improve the prediction to measurement fit, the lubricant viscosity value is set such as the friction prediction at high speeds ($\geq$ 300 RPM) matches with the friction measurements (see Figure 4.10). For the 10W-60 engine oil, the best fit is found for a viscosity value $\eta = 0.50$ Pa.s which is 18% higher than the measured viscosity $\eta = 0.41$ Pa.s.
The relatively high contact pressure ($p_{hertz} = 82$ MPa) leads to an increase in the lubricant viscosity due to the piezo-viscous effect. According to the Barus viscosity-pressure relationship [43, 138], a viscosity increase by a factor of 5 is predicted on the contact central line. This may lead to an higher mean viscosity value in the contact compared to the ambient fluid viscosity and may explain the higher viscosity needed in the predictions in order to fit the measurements. In addition, no shear-thinning of the engine oil is assumed. Lubrication conditions are assumed fully-flooded (i.e. $h_{in} >> h_0$) to correspond to the test lubrication conditions depicted in Figure 4.11.

Topography measurements are performed by interferometry on both the roller and plate wear scars in order to measure the micro-geometry after the run-in process. A robust Gaussian filter (ISO 16610-71) with a 80 µm cut-off is used on the roller topography patch (280×280 µm^2) in order to remove the sample macro-geometry. Then, according to the small wear scar width (≈ 50 µm wide) a 35×35 µm^2 topography patch is extracted. On the other end, the measured topography of the plate is corrected by subtracting a de-

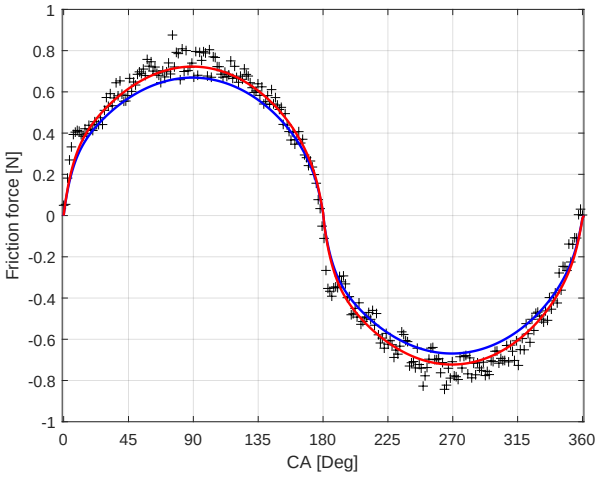

Figure 4.10: Model viscosity fit on measurement (plus signs: measurement - blue line: $\eta = 0.41$ Pa.s - red line: $\eta = 0.50$ Pa.s).

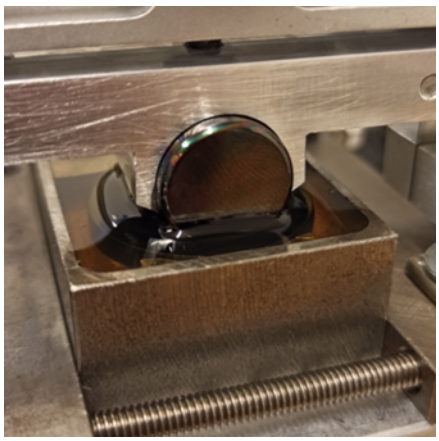

Figure 4.11: Measurement lubrication condition.

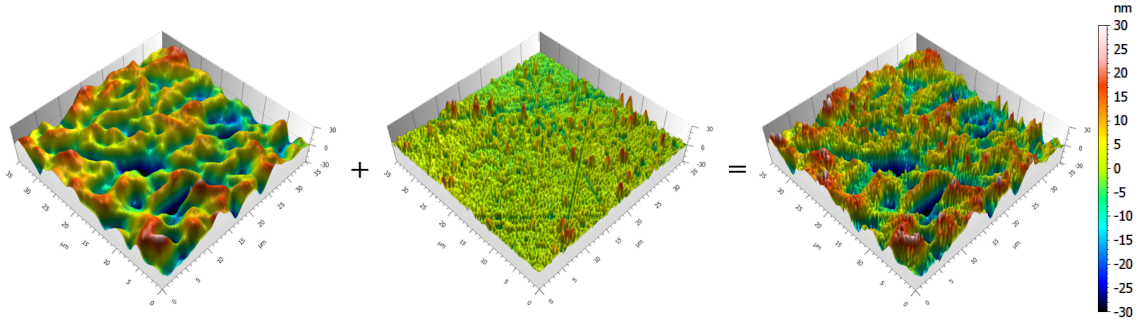

Figure 4.12: Surface 3D measured topography (left: roller - mid: plate - right: equivalent surface).

gree five polynomial. Figure 4.12 gives the 3D topographies of the roller and the plate and Table 4.10 regroups the corresponding roughness parameters. From these measurements, an equivalent roughness is defined as $h_{tot}(x,y) = h_{roller}(x,y) + h_{disc}(x,y)$. The roughness parameters of the equivalent surface are also given in Table 4.10.

A contact mechanics calculation is performed on the equivalent roughness in order to obtain the surface "pressure-distance" data presented in Figure 4.13. This data is then converted to a line-contact "load-distance" curve by a discrete calculation on the roller profile. Figure 4.14 gives the "load-distance" curve for the DLC coated roller/plate dry contact.

The second input parameter of the solid-to-solid contact model is the boundary friction coefficient value μ_{bound}. DLC coated ball on plate friction measurements in the boundary lubrication regime are performed (as described in Section 3.3) in order to quantify this value. Lubricated with the 10W-60 engine oil, a constant boundary friction

coefficient value of 0.161 is measured. In addition, the roller on plate measurements at low speeds (< 30 RPM) in figure 4.15 highlight a maximum friction coefficient of 0.165 at the dead-centres. Thereby, a boundary friction coefficient value equal to 0.16 is used in the following calculations.

All calculations are performed for at least three complete back and forth cycles (1080°CA) in order to minimise the transient term initialisation instability. Friction predictions from the last cycle are analysed in the following. A maximum crank angle step $dCA = 1$ degree as well as a refining level $lvl_{max} = 2$ are fixed, leading to a minimum crank angle step $dCA = 0.25$ degree. Depending on the rotational speed, the time-step varies from $\delta_t = 11$ ms to $\delta_t = 0.28$ ms. Computation times are within 90 to 250 seconds depending on the contact speed. All calculations are performed on a laptop computer.

[nm]	Roller	Plate	Equiv.
Sq	10.1	3.49	10.7
Sa	8.05	2.41	8.42
Ssk	−0.645	0.960	−0.528
Sku	3.36	8.30	3.34
Sp	24.6	25.9	39.8
Sv	42.1	16.4	42.3
Sz	66.7	42.3	82.1

Table 4.10: Surface roughness parameters (ISO 25178).

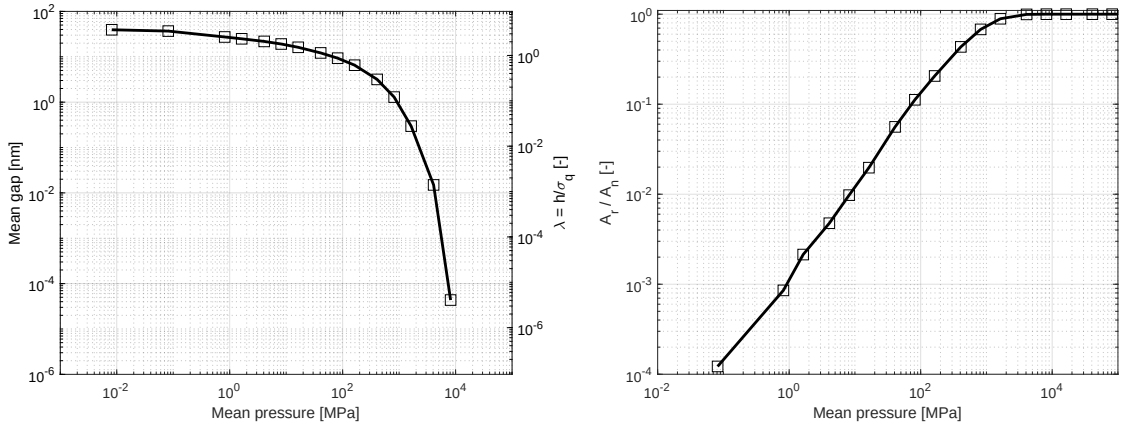

(a) Mean gap.

(b) Real contact area ratio.

Figure 4.13: Contact mechanics calculation output.

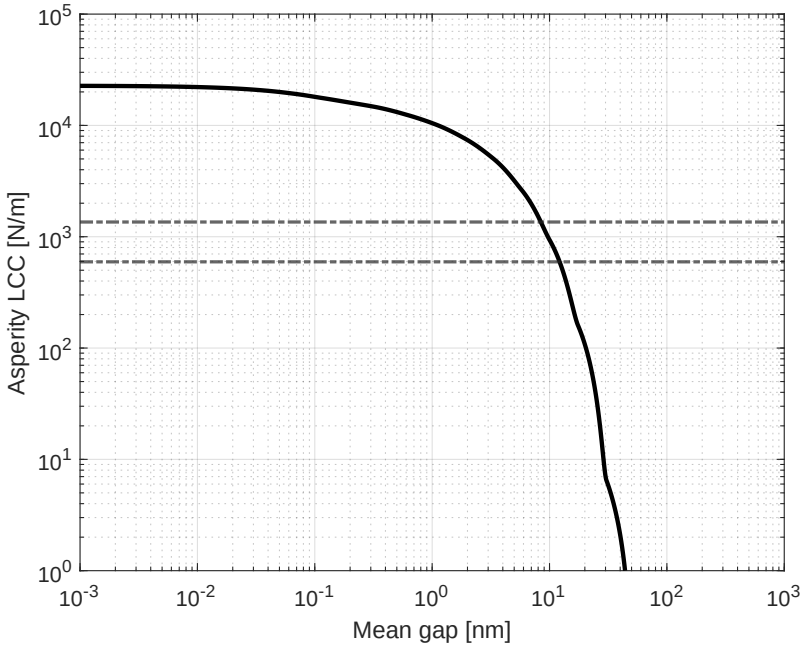

Figure 4.14: "Load-distance" curve for the DLC coated roller/plate dry contact (the dotted lines represents the contact normal loads at 24.4 N and 10.7 N).

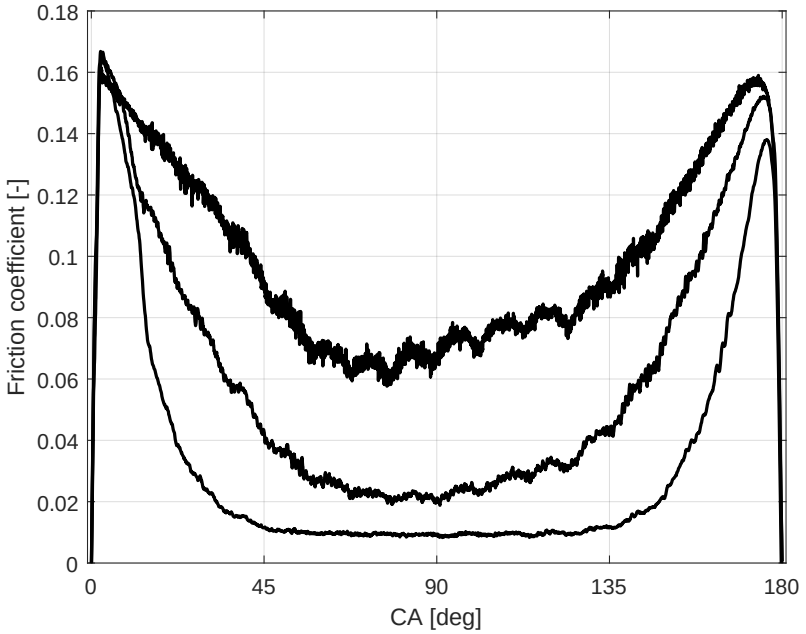

Figure 4.15: Roller on plate low speed friction measurements (from top to bottom: 7.5, 15 and 30 RPM).

4.5.3 Micro-geometry / Roughness Results

The following analysis is focusing on the predictions of the full roller friction for a 10W-60 grade engine oil and a 24.4 N normal load as these test conditions ensure minimal unknowns of the input parameters. Nevertheless, 10.7 N and glycerol friction results have been used in the validation process and yield to the same conclusions.

Figures 4.16 and 4.17 present the film thickness predictions, friction predictions and the measured frictions for four different mean speeds. The model results are drawn as solid lines, the blue color stands for $\eta_0 = 0.41$ Pa.s and the red color stands for $\eta_0 = 0.50$ Pa.s. The dotted black line stands for the Moes & Venner steady-state iso-viscous-rigid prediction (for $\eta_0 = 0.50$ Pa.s) and is used as a reference. The plus sign markers represent the friction measurements.

In figures 4.16(a), 4.16(c), 4.17(a) and 4.17(c) the film thickness is always different from zero, even at zero speed locations 0°CA, 180°CA and 360°CA (i.e. dead-centres). This is because of the transient (squeeze) effect and has already been discussed in Section 4.4. In addition, the transient term induces a time (i.e. position) shift (proportional to speed) of the predicted film thickness compared to the Moes & Venner steady-state solution. In figure 4.17(a) and 4.17(c) the film thickness difference between the two mean speeds ($u_{mean} = 50$ mm/s and $u_{mean} = 100$ mm/s) is proportional to the change in speed which is representative of the full-film lubrication regime. This observation is also true at the dead-centres. In figure 4.16(a) and for both viscosity values the film thickness at the dead-centres is $h_0(u_m = 0) \approx 8.7$ nm similar to the surface roughness arithmetical-mean-height (Sa). A change in the film thickness curve slope is observed for both predicted curves at $h_0 \approx 16$ nm which corresponds to a stroke position of roughly ±20°CA from the dead-centres. This change is an indicator on the transition from the full-film lubrication regime to the mixed regime where a fraction of the normal load is carried by the solid-to-solid contact. Figure 4.18(b) shows the ratio of normal load carried by the asperity contact as a function of $\lambda = h_0/Sa$. For $\lambda < 1$ the load is completely carried by the solid-to-solid contact. For $1 < \lambda < 2$ the ratio of load carried by the asperity contact decreases quickly and linearly from a 100% to 13%. Then, for $\lambda > 2$ the proportion of load carried by the asperities slowly drops to zero at $\lambda > 3.5$. For $\lambda = 3$, mostly known as the lower boundary of the full-film lubrication regime, approximately 2.5 % of the normal load is carried by the solid-to-solid contact.

In Figure 4.17(d), measurement data is scattered due to the test-rig vibration instabilities. However measurement general trend is readable and friction prediction for $\eta_0 = 0.50$ Pa.s exhibits an excellent fit. Similarly, Figure 4.17(b) shows a good prediction to measurement agreement for ±45°CA from mid-stroke positions (for $h_0 > 30$ nm). According to Figure 4.18(b), the contact operates in the full-film lubrication regime for film thicknesses larger than 30 nm. These results confirm the Section 4.4 conclusions and validate experimentally the hydrodynamic model theory.
In figure 4.16(b), the predicted friction peaks at the dead-centres are consistent with the

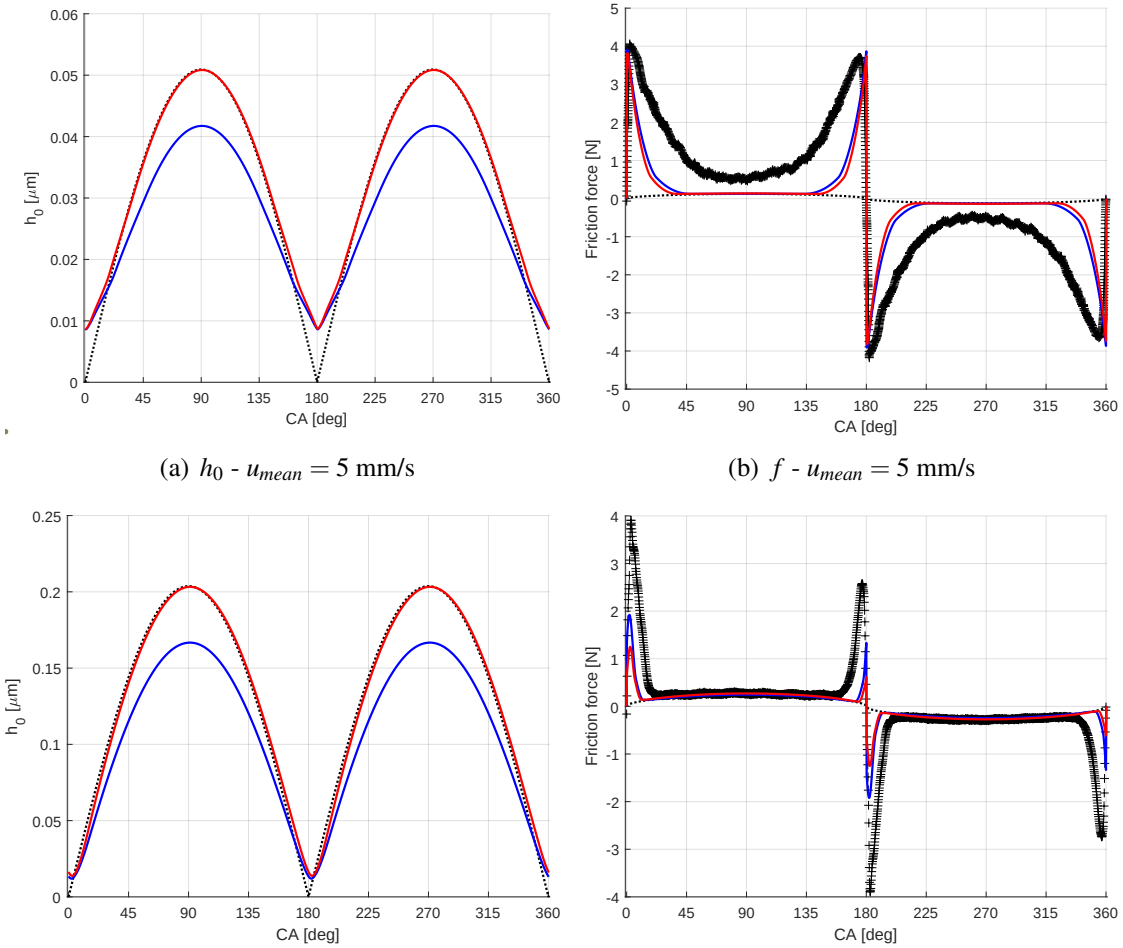

(a) h_0 - $u_{mean} = 5$ mm/s

(b) f - $u_{mean} = 5$ mm/s

(c) h_0 - $u_{mean} = 20$ mm/s

(d) f - $u_{mean} = 20$ mm/s

Figure 4.16: Roller on plate friction prediction vs. friction measurement (blue line: $\eta_0 = 0.41$ Pa.s - red line: $\eta_0 = 0.50$ Pa.s - black dotted line: Moes & Venner solution - plus signs: measurement).

measured friction. According to figure 4.18(a), 93 % of the normal load is carried by the asperities at the dead-centres which is characteristic from the boundary lubrication regime. Also, Figure 4.15 highlights a tiny change in the measured friction values at the dead-centres for three different operating speeds, also characteristic from the boundary lubrication regime. Thus, the model is representative at the dead-centre locations.

However, the computed friction does not fit the measurements towards the mid-stroke. Figure 4.19 gives a detailed view of Figure 4.16(b) friction prediction with some precisions related to the following analysis. In Figure 4.19 a rapid decrease in the friction prediction is observed between marker 0 and 1 (respectively 5 and 45°CA). At marker 1, the mixed lubrication model results (red color) reach the theoretical, full-film, Moes & Venner viscous friction value (dotted black line) meaning that the normal load is fully

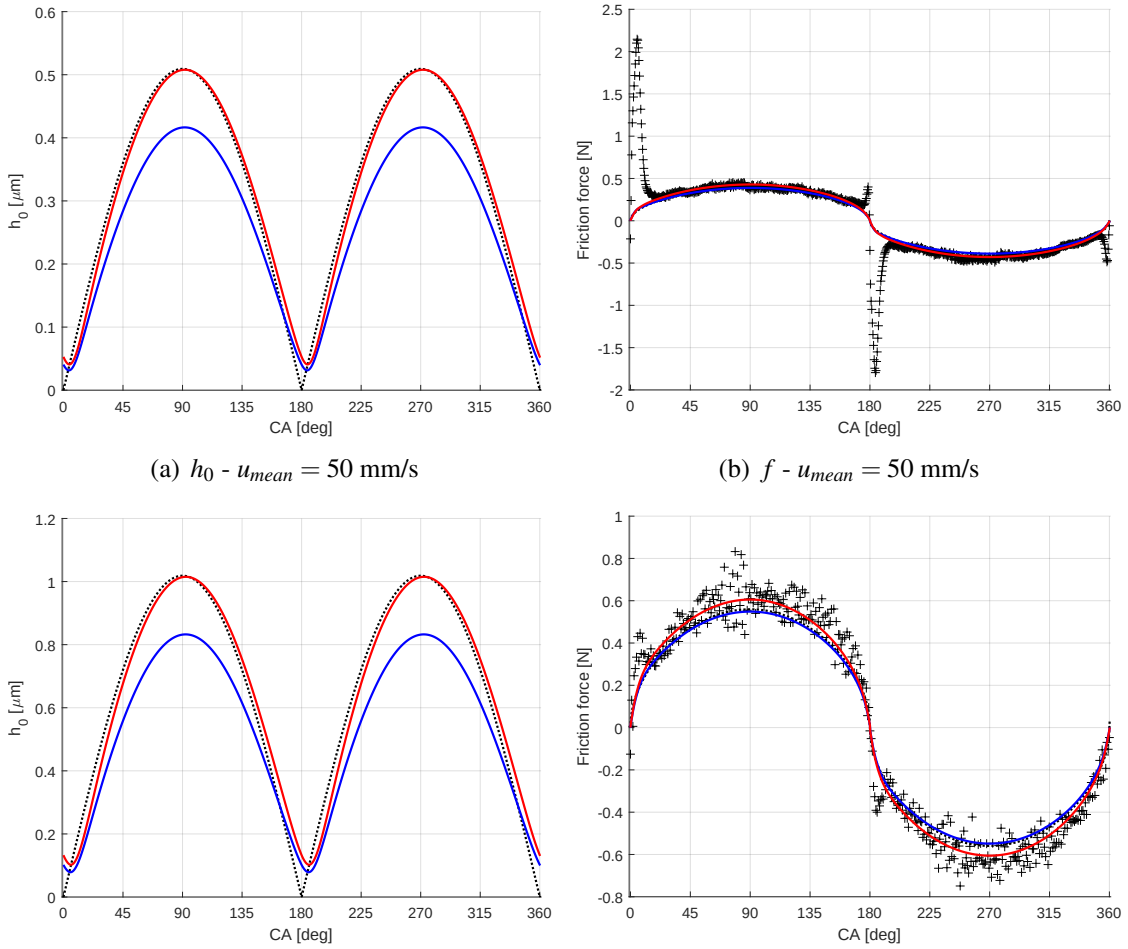

(a) h_0 - $u_{mean} = 50$ mm/s

(b) f - $u_{mean} = 50$ mm/s

(c) h_0 - $u_{mean} = 100$ mm/s

(d) f - $u_{mean} = 100$ mm/s

Figure 4.17: Roller on plate friction prediction vs. friction measurement (blue line: $\eta_0 = 0.41$ Pa.s - red line: $\eta_0 = 0.50$ Pa.s - black dotted line: Moes & Venner solution - plus signs: measurement).

carried by the fluid as confirmed in Figure 4.18(a). On the other hand, the measured friction continuously decreases from marker 0 to marker 2 at mid-stroke (i.e. maximum speed) where it reaches a minimum value four times higher than the predicted friction value. The measured friction evolution suggests the contact to be in the mixed lubrication regime for the entire stroke as the friction decreases with increasing speed (from marker 0 to 2). On the contrary, the computed solution highlights an incorrect faster transition from the mixed to the full-film lubrication regime (from marker 0 to 1). This difference suggests an incorrect prediction of the LCC balance (w_h/w_{asp}).

An asymmetry in the friction signal peaks (measured and predicted) is observed for increasing operating speeds. This “hysteresis” effect has previously been reported by Hess and Poom [139] as well as by Taylor [67]. It is due to the transient term that slightly

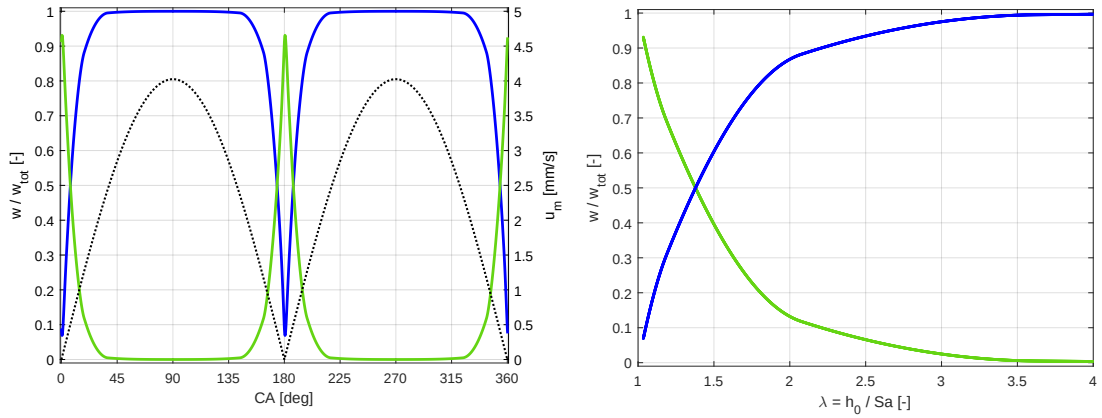

(a) (b)

Figure 4.18: Predicted LCC hydrodynamic (blue) and asperity (green) ratio as a function of (a) the crank angle ($u_{mean} = 5$ mm/s - dotted black line: u_m) - (b) the ratio $\lambda = h_0/Sa$.

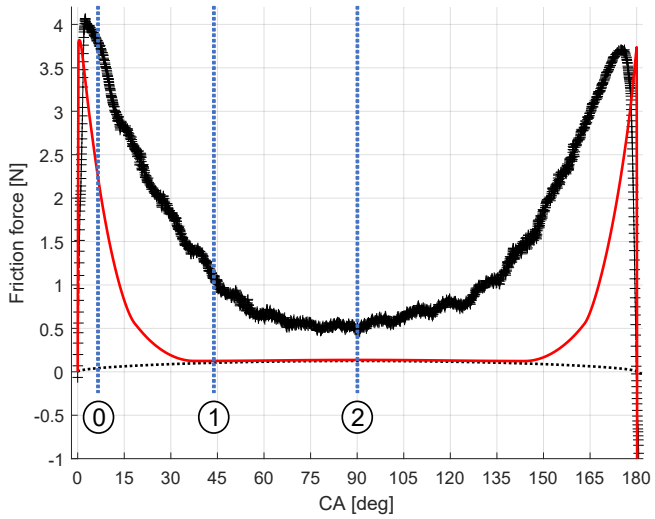

Figure 4.19: Roller on plate friction prediction vs. measurement for $u_{mean} = 5$ mm/s (red: mixed-lubrication prediction - dotted black: Moes & Venner solution - plus sign markers: measurement).

shifts the minimum film thickness a few CA degrees after the dead-centre, resulting in an asymmetric friction peak.

The LCC balance between the hydrodynamic and solid-solid part of the contact is directly related to the ratio $\lambda = h_0/Sa$ as described in Figure 4.18(b). In the λ ratio, the film thickness h_0 is proportional to $\eta_0 u_m w_{tot}^{-1}$ (for a fully-flooded, IVR contact) and Sa is the roughness arithmetic-mean-height. To improve the prediction to measurement fitting, one has to decrease the λ ratio by either decreasing h_0 (i.e. decrease η_0, u_m and w_{tot} are

fixed) or by increasing the roughness amplitude. A decrease in the viscosity value will affect the full-film lubrication regime which has been proven to be accurately predicted. An increase by a factor 2.5 of the roughness amplitude shows in Figure 4.20 an excellent prediction to measurement agreement despite the fact that this solution is not consistent with the topography measurements.

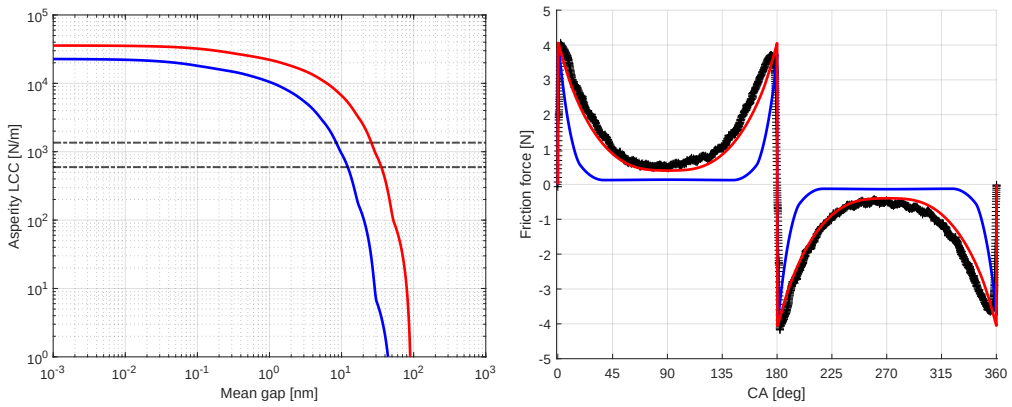

(a) Load-distance data (b) Friction force

Figure 4.20: Results for an amplified roughness by a factor 2.5 (blue line: original - red line: amplified - black dashed lines: normal load - black plus signs: measurement).

Observations of the roller wear scar after testing highlighted an unexpected discontinuous wear scar shown in Figure 4.21(a). An additional profile measurement along the roller length (see Figure 4.21(b)) using a stylus profilometer shows that the roller has a non-negligible macro-geometry (i.e. undulation) with a peak-to-peak amplitude of roughly 400 nm ($\approx 40 \times Sq$). According to the amplitude of the roller macro-geometry along its length, the previous predictions relying only on the roller micro-geometry/roughness are irrelevant. In order to correctly predict the contact friction, the roller macro-geometry has to be accounted for.

A solution with a physical meaning (compared to the multiplication of the roughness amplitude) would be to measure the topography of several patches along the roller wear scar and compute the contact mechanics for each patch defined using absolute height coordinates in order to account for the roller undulation. By averaging the data, an approximation of the macro-geometry "load-distance" data can be computed. However, this solution has two main drawbacks. First, the measurements and calculations for a large number of topography patches is time-consuming. Secondly, this methodology does not account for the influence of the macro-geometry on the hydrodynamic LCC. Yet, for undulation amplitudes (i.e. grooves) in the order of the film thickness Noutary et al. [69] showed that the hydrodynamic LCC carrying capacity can be strongly altered. Therefore, one has to account for the macro-geometry influence on both the hydrodynamic and the solid-to-solid contact parts of the model.

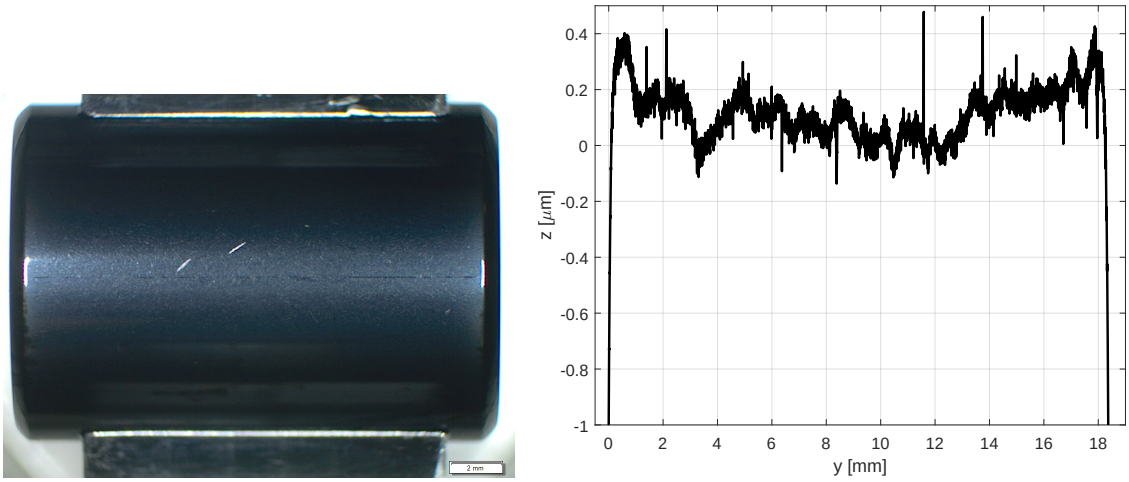

(a) (b)

Figure 4.21: Roller wear scar investigations (a) microscope picture (the central discontinuous dark line highlights the discontinuous wear scar) - (b) raw wear profile.

4.5.4 Macro-geometry / Undulation Results

The goal is to develop a simple method that accounts for the influence of the roller macro-geometry on both the hydrodynamic and the asperity LCC within the developed line-contact, mixed lubrication model.

The first step is to correctly quantify the roller run-in macro-geometry. Figure 4.21(b) gives the profile measured along a random generatrix of the roller and is not representative of the worn-out macro-geometry. Yet, according to the tactile profilometer precision it is almost impossible to measure the roller profile along its entire length inside the 50 µm wide wear scar. This measurement might be possible using a high-precision optical measurement device but the stitching process may introduce some topography artefacts. To tackle this difficulty, a numerical 3D parabolic rough roller is generated using the measured profile undulation. Therefore, the measured profile given in Figure 4.21(b) is first filtered in order to consider only the macro-geometry (i.e. undulation) in the calculation and not the micro-geometry which is already accounted for in the contact mechanics calculation. Then, the virtual roller is generated by revolution of the filtered profile according to a radius $r = 7$ mm. The numerically generated 3D roller is relatively representative of the real roller geometry since the undulation along the roller length are prevailing due mainly to the roller manufacturing process.
Afterwards, a contact mechanics calculation is performed on the numerical roller in order to obtain its elastically deformed geometry. The large scale contact mechanics computation (domain size: $19.1\text{mm} \times 0.12\text{mm}$, approximately 6 million nodes) is

performed using the Multi-Grid method [10] and is performed on a computer with extended memory. The computed deformed geometry for a 24.4 N normal load is shown in Figure 4.22(a) and is assumed to be the run-in macro-geometry of the roller (sum of the elastic deformation and the sliding wear). The computed roller deformed geometry is coherent with the wear observation shown in Figure 4.21(a). Figure 4.22(b) highlights a deformed macro-geometry with a "plateaux and groove" shape which is substantially different from a theoretical line-contact. Approximately 50 % of the profile can be described as "plateaux" as the other half is composed of relatively deep grooves.

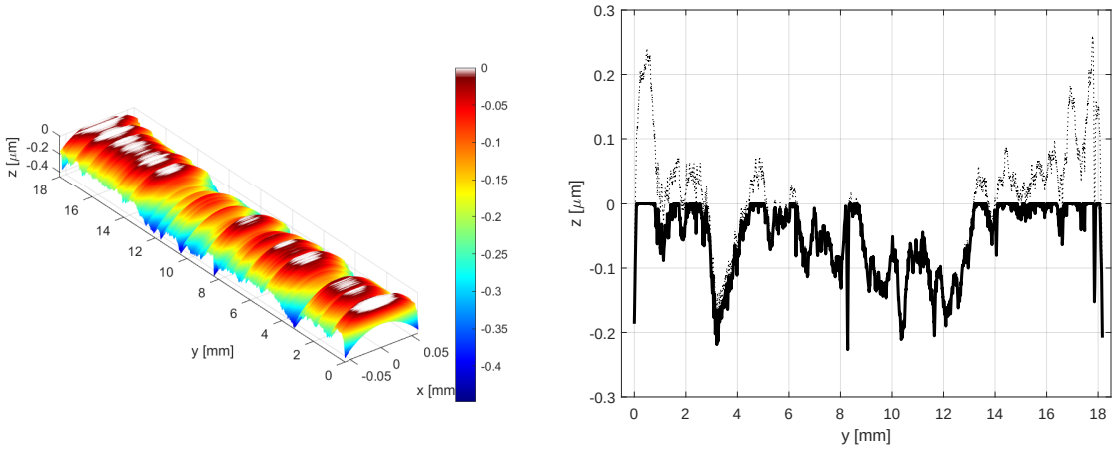

(a) 3D deformed geometry (the white areas highlight the contacting zones).

(b) 2D center line $x = 0$ deformation (the dotted line indicates the original profile).

Figure 4.22: Computed roller deformed macro-geometry for a 24.4 N normal force.

For the viscous part of the model, the idea is to generate two correction hydrodynamic coefficients based on the macro-geometry, in order to weight the theoretical line-contact viscous LCC and friction. Therefore, the following assumption is used: the pressure gradient along the y axis (i.e. roller length) is negligible compared to the pressure gradient along the x axis (sliding direction); $\partial p_h/\partial x >> \partial p_h/\partial y$. From this assumption, the roller profile (along the y axis) can be approximated by a succession of independent parabolic slices i defined at a certain height h_i. From the Reynolds equation analysis detailed in Appendix C, one can state that the hydrodynamic LCC of a line-contact is inversely proportional to the minimum film thickness: $w_h \propto h_0^{-1}$. Thereby, an approximation of the hydrodynamic LCC of the deformed roller geometry can be evaluated as:

$$\bar{w}_h = \frac{1}{n}\sum_{i=1}^{n}(h_i + h_0)^{-1} \tag{4.4}$$

with the "plateaux" height as reference for h_0. Then, the correction coefficient α_w which describes the loss in hydrodynamic LCC due to the macro-geometry is computed as:

$$\alpha_w = \frac{\bar{w}_h}{w_h} \tag{4.5}$$

with $w_h = h_0^{-1}$. The same methodology is applied to compute the correction coefficient α_f which describes the loss in viscous friction due to the macro-geometry, assuming $f_{hydro} \propto h_0^{-1/2}$ (see Appendix C). Figure 4.24(a) gives the coefficient values as a function of the film thickness h_0 for the deformed roller profile shown in Figure 4.22(b).

The coherence of the $\partial p/\partial x >> \partial p/\partial y$ assumption as well as the veracity of the α coefficients is checked using a P-Θ numerical solution [137] (also used and described in Section 4.4). Figure 4.23 shows, for several h_0 values, the computed hydrodynamic pressure distribution generated by the sliding of the deformed roller macro-geometry given in Figure 4.22(a). Please note that pressure is made dimensionless with respect to h_0 and thus the pressure results are not directly comparable. However, the different pressure shapes give an interesting insight on the macro-geometry influence. For h_0 values significantly larger than the grooves depth (Figure 4.23(a)), the pressure distribution is similar to the theoretical smooth solution. The grooves have a small influence and the α coefficient values are equal to 1. For h_0 values in the same order of the grooves depth , the pressure distribution is highly altered and presents high pressurised zones at the "plateaux" and almost no pressure in the grooves. For example, a 65% reduction in the generated LCC is predicted for $h_0 = 3E1$ nm.
The global trend is presented in Figure 4.24(a) where the solid and dashed lines represent respectively the LCC and friction analytical results whereas the markers represents the corresponding numerical results. The analytical and numerical results are in good agreement with a relative difference below 12% for $h_0 \geq 10$ nm. This confirms the consistency of the analytical theory.

Then, the line-contact solver is slightly modified in order to include the macro-geometry α weighting coefficients. The LCC coefficient α_w is added to the load balance equation as follows:

$$w_{hydro}\,\alpha_w + w_{asp} = w_{tot} \tag{4.6}$$

Similarly, the viscous friction is weighted by implementing the coefficient α_f:

$$f = f_{hydro}\,\alpha_f + f_{asp} \tag{4.7}$$

Both α correction coefficients are, during the solver iterating process, interpolated from the data presented in figure 4.24(a). This method allows for a quick solution of the line-contact lubrication problem while accounting for the sample macro-geometry.
Because the original line-contact model is time-dependent, the fluid LCC is generated by the sliding and the squeeze effect. Yet, the α_w LCC correction coefficient does not include the influence of the grooves on the squeeze part of the LCC. According to the Reynold equation analysis (Appendix C) for a pure impact operating condition, the hydrodynamic LCC is proportional to $w_{h_{impact}} \propto h_0^{-4/5}$. As a first approach, this term is neglected in the current analysis.

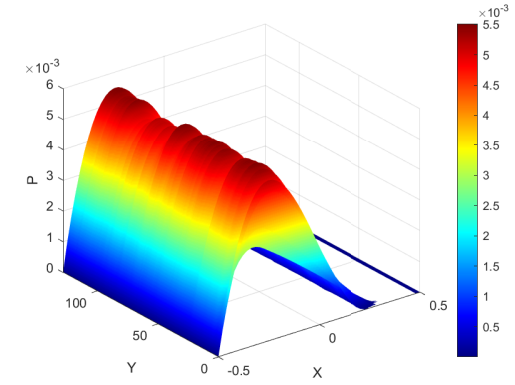

(a) $h_0 = 3E3$ (nm) - 3D view

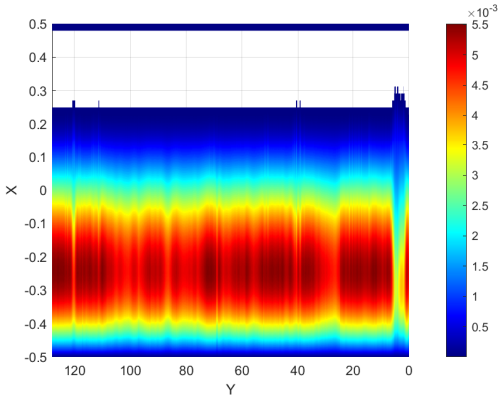

(b) $h_0 = 3E3$ (nm) - Top view

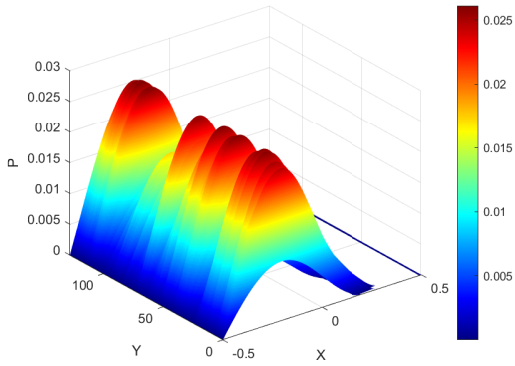

(c) $h_0 = 3E2$ (nm) - 3D view

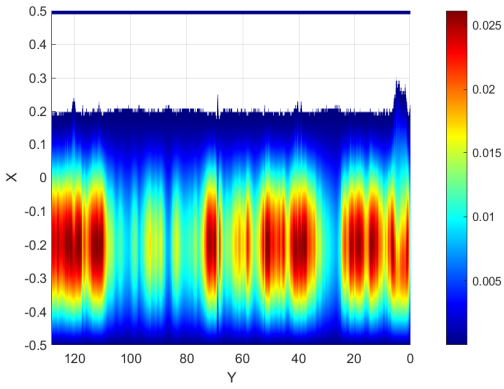

(d) $h_0 = 3E2$ (nm) - Top view

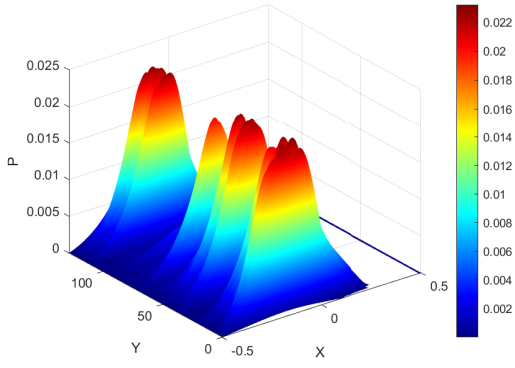

(e) $h_0 = 3E1$ (nm) - 3D view

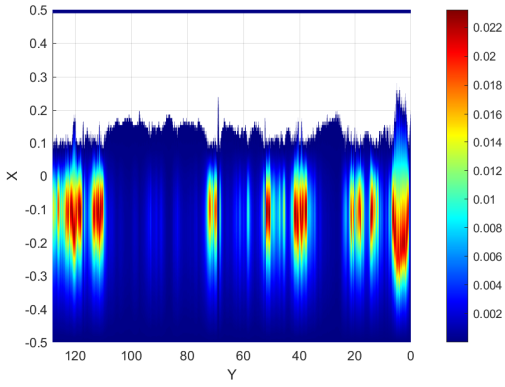

(f) $h_0 = 3E1$ (nm) - Top view

Figure 4.23: Numerically computed dimensionless hydrodynamic pressure distribution accounting for the measured roller macro-geometry.

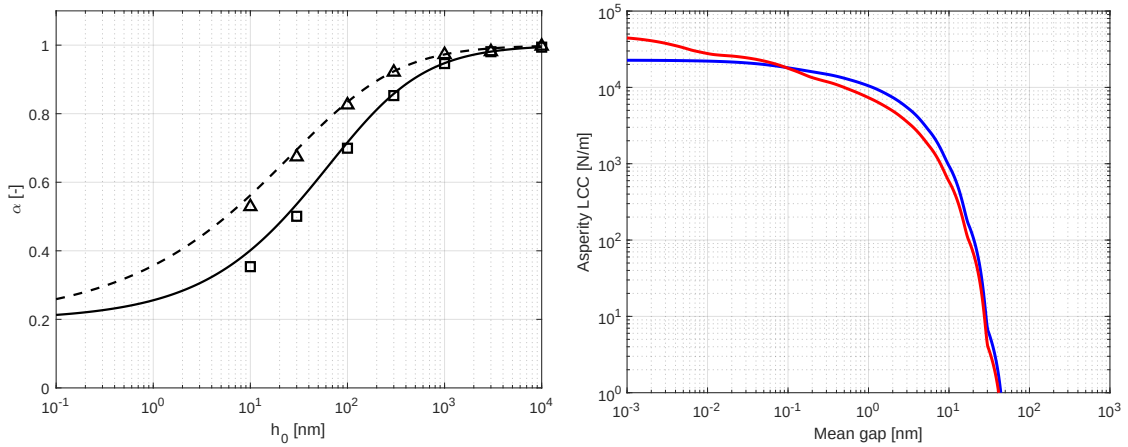

(a) α hydrodynamic correction coefficients (solid line: α_w - dashed line: α_f - markers: numerical results).

(b) "load-distance" data (red: macro-geometry - blue: micro-geometry).

Figure 4.24: Upgraded input parameters accounting for the roller macro-geometry.

The deformed geometry given in figure 4.22(a) also has a significant influence on the solid-to-solid contact. Figure 4.25 highlights the difference in contact area between the theoretical line-contact model (dotted lines) and the real macro-geometry (black zones). In order to upgrade the existing solid-to-solid part of the line-contact model, the roughness "pressure distance" data given in Figure 4.13 is applied to each roller element of the 3D deformed macro-geometry. In this way, a new macro-geometry "load-distance" curve is computed based on the following equation:

$$w_{asp}^{macro} = \frac{1}{L}\Delta x \Delta y \sum_{i=1}^{n}\sum_{j=1}^{m} p_{asp}^{micro}(h_0 + h_{ij}) \tag{4.8}$$

with L the roller length, Δx and Δy the element size, p_{asp}^{micro} the dry mean contact pressure for the micro-geometry interpolated from the data given in Figure 4.13. The "plateaux" height is fixed as reference for h_0 and h_i is the element i height. Figure 4.24(b) compares the original micro-geometry/roughness "load-distance" curve (blue line) to the upgraded macro-geometry "load-distance" curve. Data for the deformed macro-geometry is slightly shifted to lower mean gap values mostly because the real contact area is equal to a third of the theoretical Hertz line-contact area (see Figure 4.25). Thus, taking into account the macro-geometry, the mean gap has to be narrower in order to carry the same load.

Similarly to Section 4.5.3, the following analysis is focusing on the predictions of the full roller friction for a 10W-60 grade engine oil and for a 24.4 N normal load. Figure 4.26 presents the film thickness and friction predictions for both models (with and without macro-geometry) as well as the measured frictions for three different mean speeds. Prediction results are drawn as solid lines, the blue color stands for the original

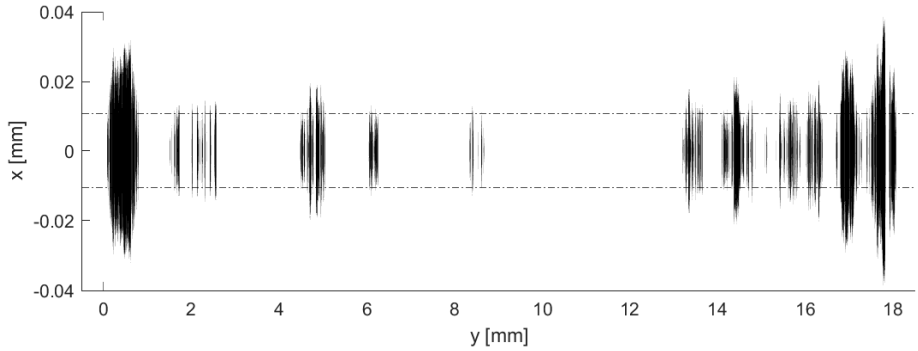

Figure 4.25: Real computed contact area (dashed lines depict the theoretical Hertz line-contact area).

micro-geometry/roughness predictions and the red color stands for the upgraded macro-geometry/undulation predictions. The dotted black line stands for the Moes & Venner, steady-state, iso-viscous-rigid prediction and is used as a reference. Plus signs represent the friction measurements.
For increasing mean speeds (Figures 4.26(a) to 4.26(e)) the film thickness difference between the two calculation methods is decreasing. This is coherent with the macro-geometry implementation, for increasing h_0 values, the α correction coefficients tend to 1 and thus the solution tends to the smooth result. In other words, for a film thickness significantly larger than the groove depth ($h_0/amp > 5$ with $amp = 0.1$ µm) the macro-geometry has no influence on the hydrodynamic LCC. On the opposite, for low speeds the predicted h_0 accounting for the macro-geometry is significantly lower than for the micro-geometry prediction. In Figure 4.26(a) a lower film thickness is even observed in the boundary lubrication regime (i.e. at the dead-centres).
As expected for large h_0/amp values, the friction in figures 4.26(d) and 4.26(f) shows an excellent prediction to measurement fit. In figure 4.26(b) the macro-geometry friction predictions highlight a slower decrease from dead-centre towards the mid-stroke. In Figure 4.26(d) a substantial higher friction peak is computed at the dead-centres being more consistent with the friction measurements.
Generally, accounting for the roller deformed macro-geometry by implementing the α correction coefficients in the line-contact solver has substantially improved the friction prediction to measurement fit. However, the friction force in the mixed lubrication regime is still slightly underestimated. Two modelling approximations might explain this difference. First, the computed deformed macro-geometry might not be exactly representative of the real run-in roller geometry. Secondly, the roller computed deformed macro-geometry is assumed fixed once loaded/unloaded. Yet, the macro-geometry elastic deformation following the unloading of the surface might generate a substantial proportion of solid-to-solid friction throughout the mid-stroke.

In order to account for the real roller run-in macro-geometry shape and macro-

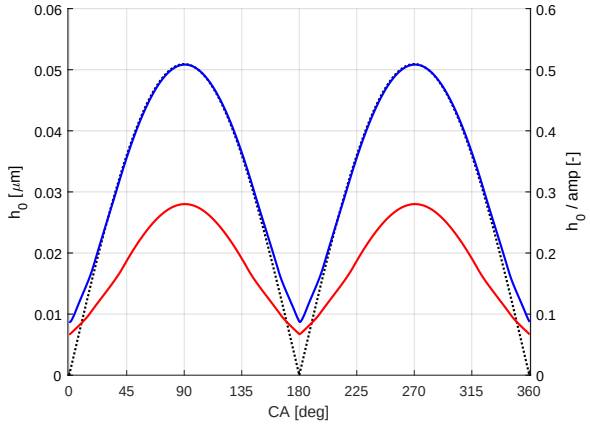

(a) h_0 - $u_{mean} = 5$ mm/s

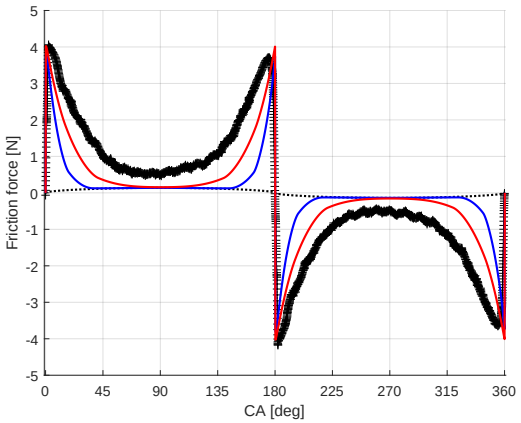

(b) f - $u_{mean} = 5$ mm/s

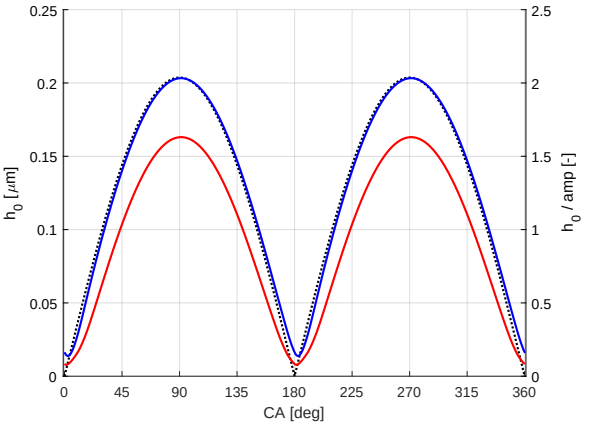

(c) h_0 - $u_{mean} = 20$ mm/s

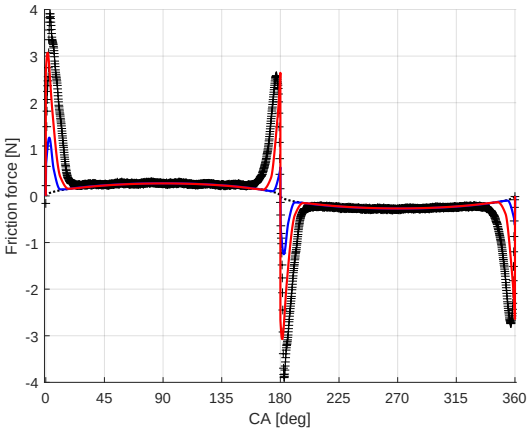

(d) f - $u_{mean} = 20$ mm/s

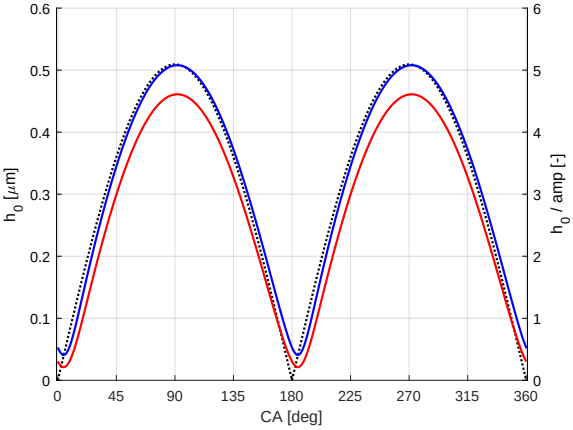

(e) h_0 - $u_{mean} = 50$ mm/s

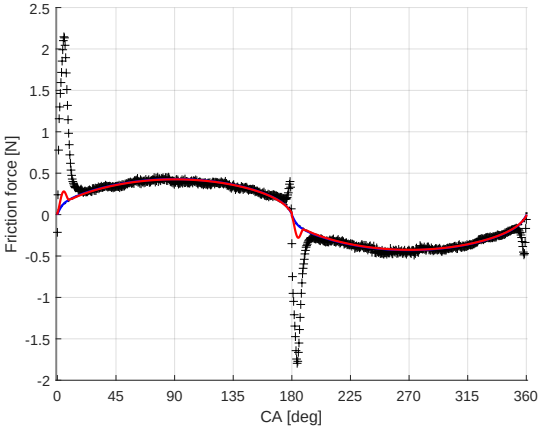

(f) f - $u_{mean} = 50$ mm/s

Figure 4.26: Roller on plate friction prediction vs. friction measurement (blue: micro-geometry - red: macro-geometry - black dotted line: Moes & Venner solution - plus signs: measurement).

geometry elastic deformation, one has to first precisely measure the roller 3D topography in the wear scar along the complete roller length (19 mm $\times$0.1 mm). Then, perform a contact mechanics calculation on the entirety of the topography patch in order to obtain the "load-distance" data for the real roller geometry. Both the topography measurement and the contact mechanics calculation on such a large size surface are rather complex and time-consuming, both aspects being outside the scope of the present work.

Besides, even the upgraded model is unable to predict the friction peaks for high mean speeds at the reversal locations (Figure 4.26(f)). These friction peaks might be due to a localised lack of lubricant on the few CA degrees just after the roller velocity change in direction. For high speeds, the lubricant might not have the time to flow back on the track and thus the contact is supplied by a tiny amount of lubricant left on the track from the previous passage. Actual predictions do not account for starvation as the lubrication condition is made fully-flooded for every crank angle step as in the experimental set-up used.
Figure 4.27 shows the film thickness and friction prediction accounting for lack of oil starvation for $u_{mean} = 50$ mm/s. For this calculation, the contact inlet film thickness is equal to the outlet film thickness from the previous passage. Calculations were performed on only one back and forth cycle. A lower film thickness is observed all along the stroke leading to a higher friction at the dead-centres (i.e. in the mixed lubrication regime) and a lower friction at mid-stroke (i.e. full film lubrication regime). However, the friction increase at the dead-centres due to the lubricant starvation is not sufficient to fit the measurements. Deep investigations of the test-rig have shown a relatively irregular rotational speed of the electric motor leading to an unsteady linear speed. Also, the plays in the test-rig roller bearings may have a substantial influence on the contact lubrication condition compared to the theoretical operating conditions. Hence, additional investigation have to be carried on both the experimental and numerical part to understand these differences.

4.5.5 0.5 mm slider

In order to test the model accuracy in predicting the friction of a geometrically starved contact, the model results are compared to friction measurements performed on the 0.5 mm slider. The actual analysis is focusing on the 10W-60 grade engine oil and the 24.4 N normal load. The previously described methodology to account for the roller deformed macro-geometry is used. Figure 4.28 shows the 0.5 mm slider computed deformed macro-geometry which is substantially different compared to the full roller one studied previously. The 0.5 mm slider spots a "barrel" shape macro geometry (typical from the roller manufacturing process) with a maximum amplitude in the centre of roughly 0.6 µm. Figures 4.29 gives the "load-distance" data and the α correction coefficients related to the slider macro-geometry.

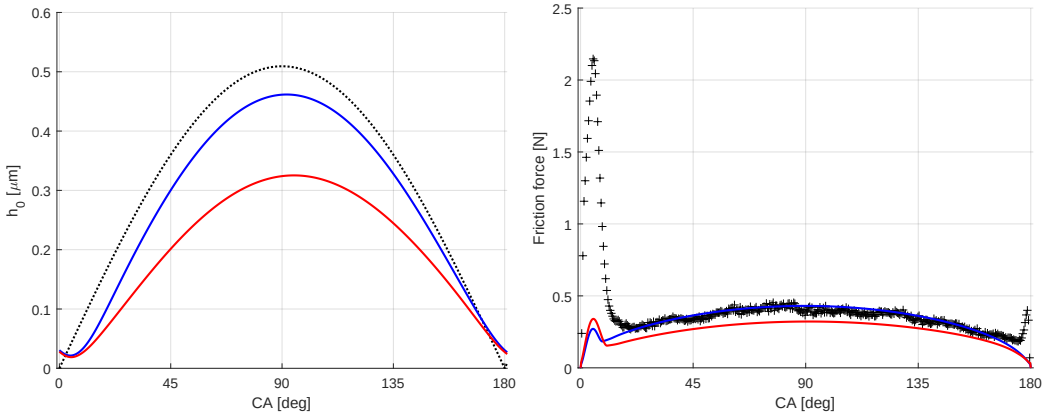

(a) h_0 - $u_{mean} = 50$ mm/s (b) f - $u_{mean} = 50$ mm/s

Figure 4.27: Starved roller on plate friction prediction vs. friction measurement (blue: fully-flooded - red: starved - black dotted line: Moes & Venner solution - plus signs: measurement).

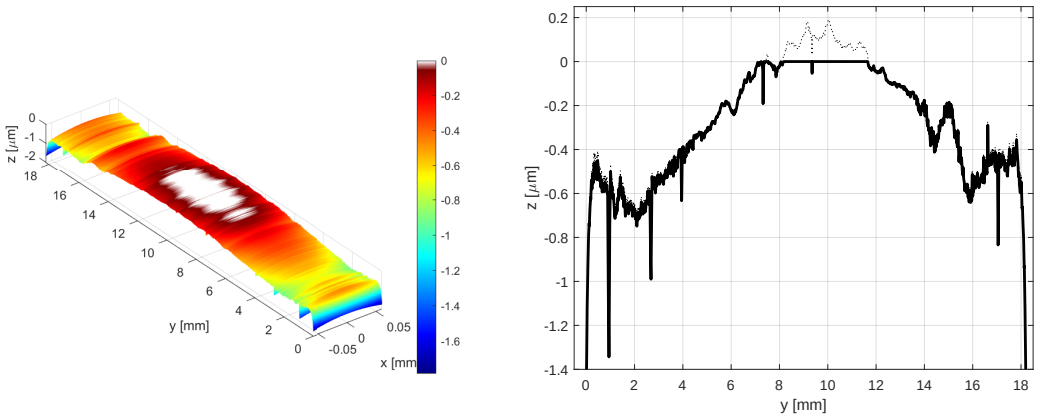

(a) 3D deformed geometry (white areas stand for contacting zones). (b) 2D center line $x = 0$ deformation (the dotted line indicates the original profile).

Figure 4.28: Computed 0.5 mm slider deformed macro-geometry for a 24.4 N normal force.

Figures 4.30 and 4.31 show the slider film thickness and friction predictions for both models (with and without macro-geometry) as well as the measured frictions for four different mean speeds. The prediction results are drawn as solid lines, the blue color stands for the micro-geometry/roughness results and the red color stands for the macro-geometry/undulation predictions. The dotted black line indicates the Moes & Venner, steady-state, iso-viscous-rigid prediction and is used as a reference. Plus signs represent the friction measurements.

In figures 4.30 and 4.31, the predicted minimum film thickness at mid-stroke (i.e.

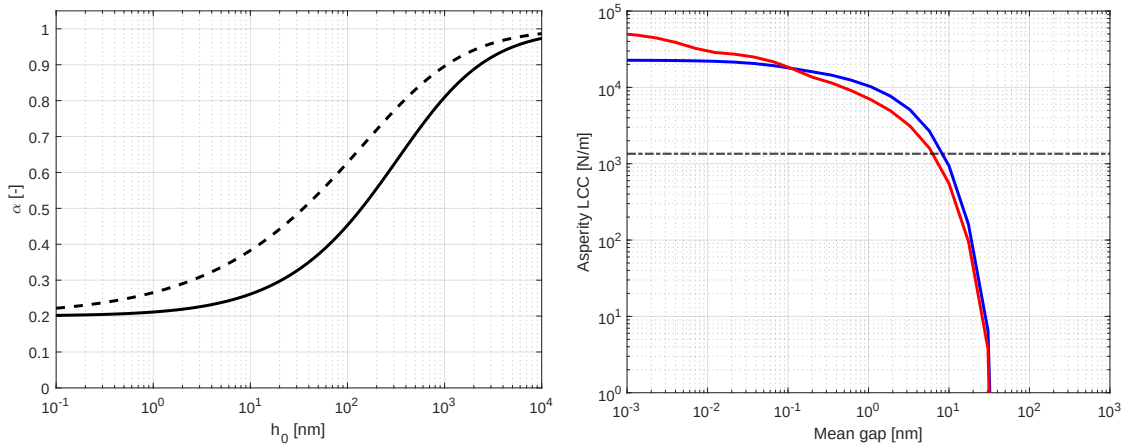

(a) α hydrodynamic correction coefficients (solid line: α_w - dashed line: α_f).

(b) "Load-distance" data (red: macro-geometry, blue: micro-geometry).

Figure 4.29: 0.5 mm slider input.

maximum speed) is systematically lower than the Moes & Venner fully-flooded solution. This is because of the geometrical starvation effect which limits the hydrodynamic pressure domain and thus induces a lower film thickness to satisfy the load balance. This effect is more important as the contact speed increases. Differences in predicted film thickness between the original and macro-geometry upgraded model are similar to the full roller case, discussed in Section 4.5.4.

Friction wise, the modelling of a finite slider geometry allows for an excellent prediction/measurement fit at high speeds compared to the fully-flooded Moes & Venner solution (Figure 4.31(d)). For low speeds, using the macro-geometry correction, the predicted friction is consistent with the measurements. In figure 4.30(b), the macro-geometry computed friction fits accurately to the measurement. The mixed lubrication friction decrease from dead-centre towards mid-stroke is well predicted. In Figures 4.30(d) and 4.31(b), the friction peaks at the dead-centres are also precisely evaluated by the upgraded macro-geometry model. These results suggest an improved estimation of the mixed lubrication regime.

Generally, the macro-geometry friction prediction to measurement fit is excellent over the full range of operating speeds. In comparison to the full roller case, the computed slider deformed macro-geometry is probably more representative of the real run-in slider geometry. This can be explained by the less complex slider "barrel-shape" compared to the full roller wave-like geometry.

Figure 4.32 compares the film thickness and friction predictions for a full roller (red) and a 0.5 mm slider (blue) in order to highlight the code ability in predicting geometrical starvation along with the latest "macro-geometry" upgrade. Therefore, the "barrel-shape"

deformed geometry given in Figure 4.28 is applied to both roller profiles.
At low speeds (i.e. $u_{mean} = 20$ mm/s) the film thickness and friction predictions for both roller profiles are relatively similar. At higher test-rig speeds, the 0.5 mm slider presents a significantly thinner film thickness at the mid-stroke as well as a lower friction force. In Figure 4.32(f), the 0.5 mm slider friction highlights an excellent prediction to measurement fit compared to the full roller which significantly overestimates the friction force. These differences are due to the geometrical starvation. Compared to the full roller geometry, the 0.5 mm slider presents a limited width resulting in a shorter pressurised zone and a thinner film thickness. These results show the importance in modelling geometrical starvation since it has a significant influence on the friction prediction.

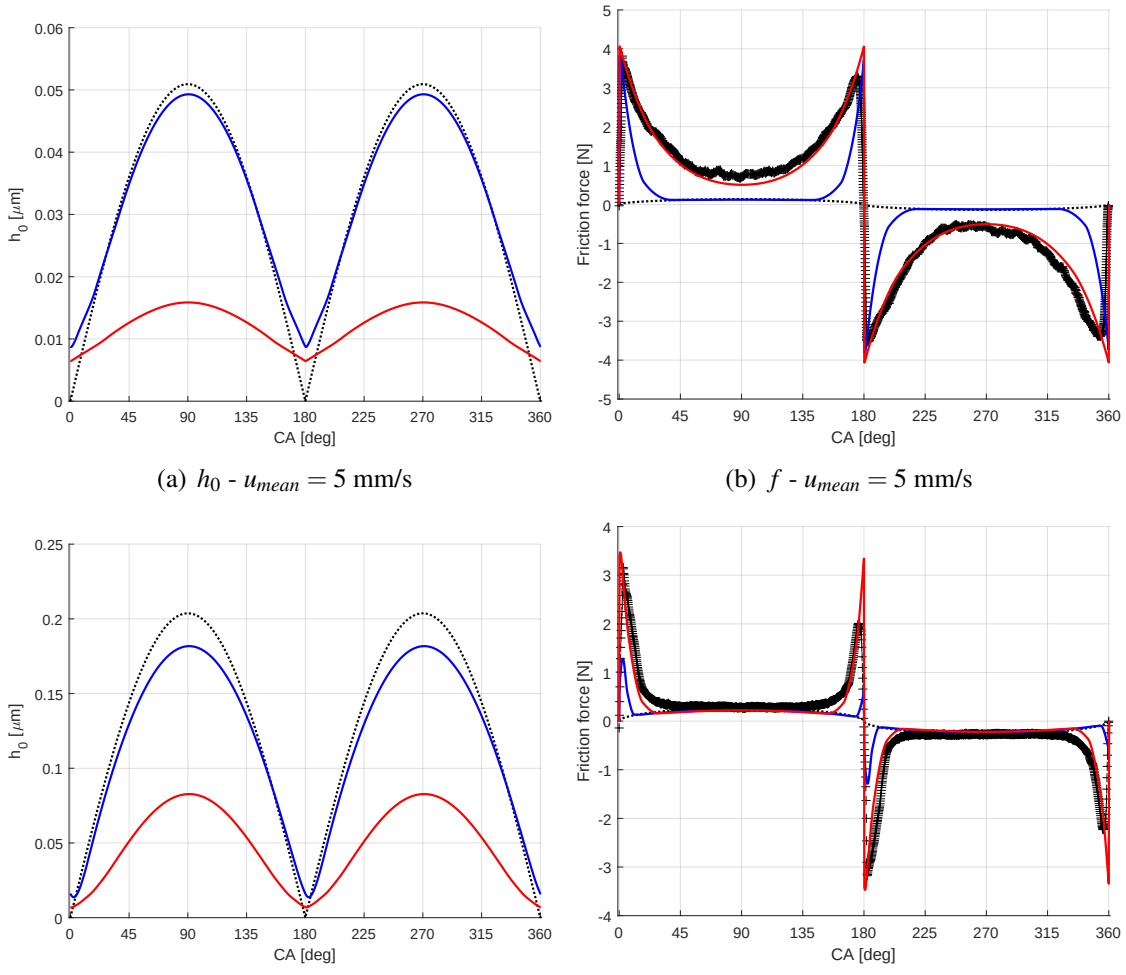

(a) h_0 - $u_{mean} = 5$ mm/s

(b) f - $u_{mean} = 5$ mm/s

(c) h_0 - $u_{mean} = 20$ mm/s

(d) f - $u_{mean} = 20$ mm/s

Figure 4.30: Slider on plate friction prediction vs. friction measurement (blue: micro-geometry - red: macro-geometry - black dotted line: Moes & Venner solution - plus signs: measurement).

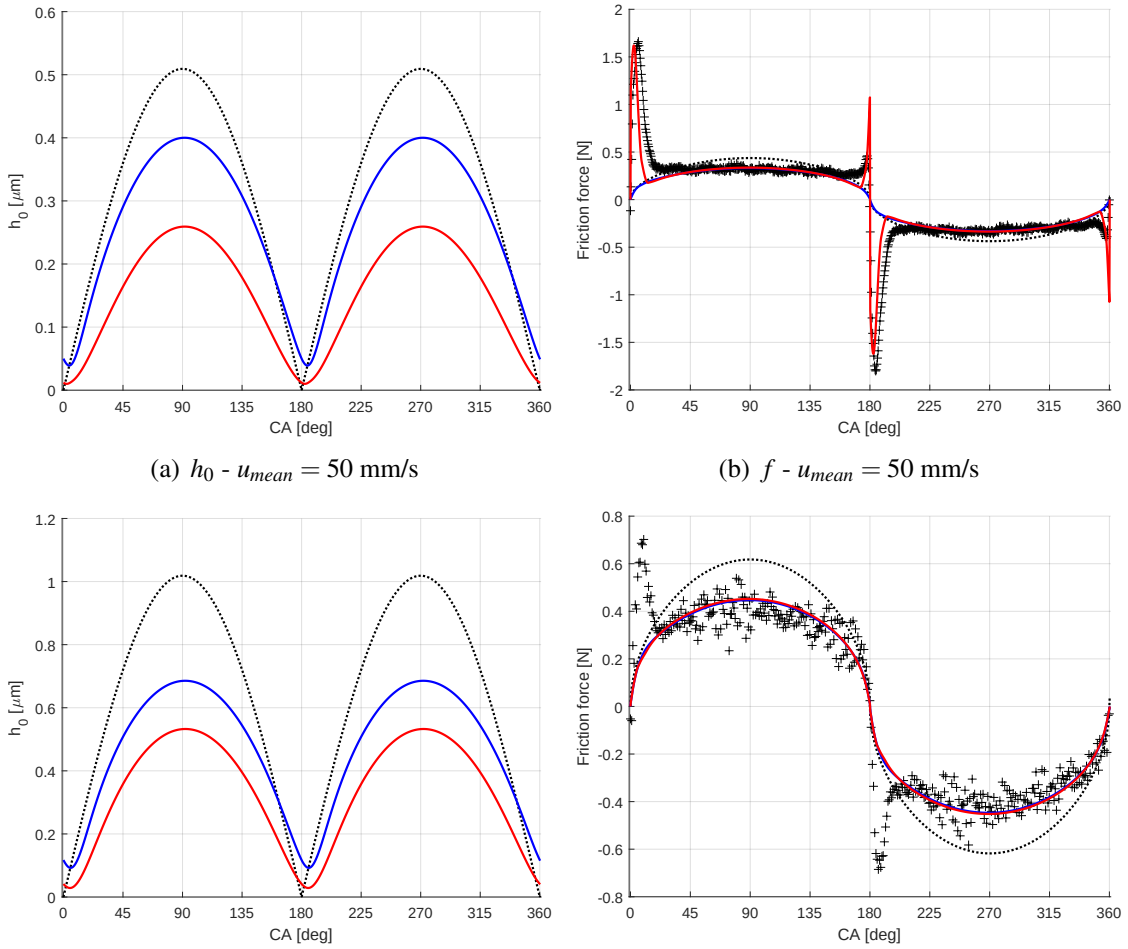

(a) h_0 - $u_{mean} = 50$ mm/s

(b) f - $u_{mean} = 50$ mm/s

(c) h_0 - $u_{mean} = 100$ mm/s

(d) f - $u_{mean} = 100$ mm/s

Figure 4.31: Slider on plate friction prediction vs. friction measurement (blue: micro-geometry - red: macro-geometry - black dotted line: Moes & Venner solution - plus signs: measurement).

The analysis in this section confirms the model ability to predict geometrical starvation and validates the relevance of the latest model upgrade which includes the "macro-geometry" effect. Moreover, using the same input the friction for low sliding speeds can be predicted. Figure 4.33 shows the predicted friction force for five test-rig speeds: u_{mean} =0.5, 1, 2, 5, 10 mm/s. These results are coherent with the measurements shown in Figure 4.15. For decreasing speeds, the friction increases and tends to a square signal typical from the boundary lubrication regime (as given in Figure 3.4 for a ball on plate test). These results highlight once more the ability of the model to predict the three different lubrication regimes with only a few input deterministic parameters.

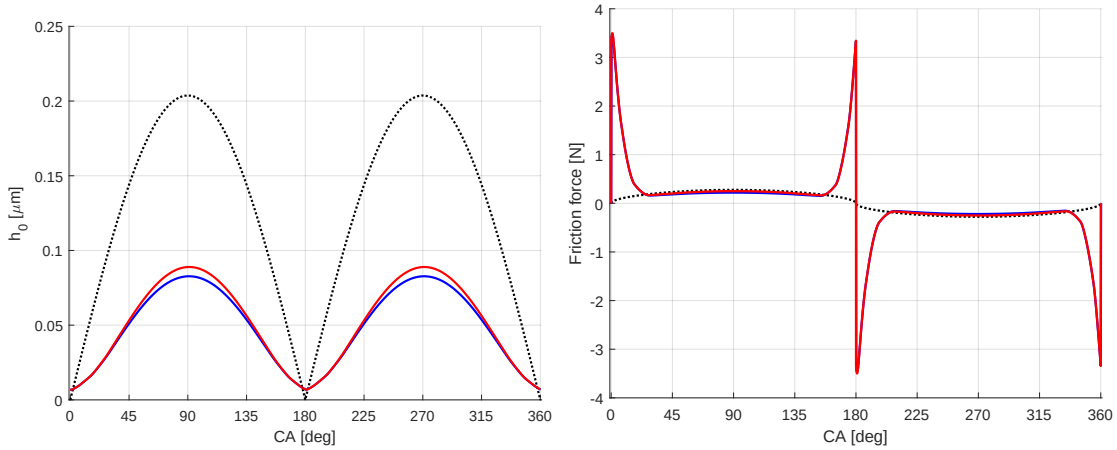

(a) h_0 - $u_{mean} = 20$ mm/s (b) f - $u_{mean} = 20$ mm/s

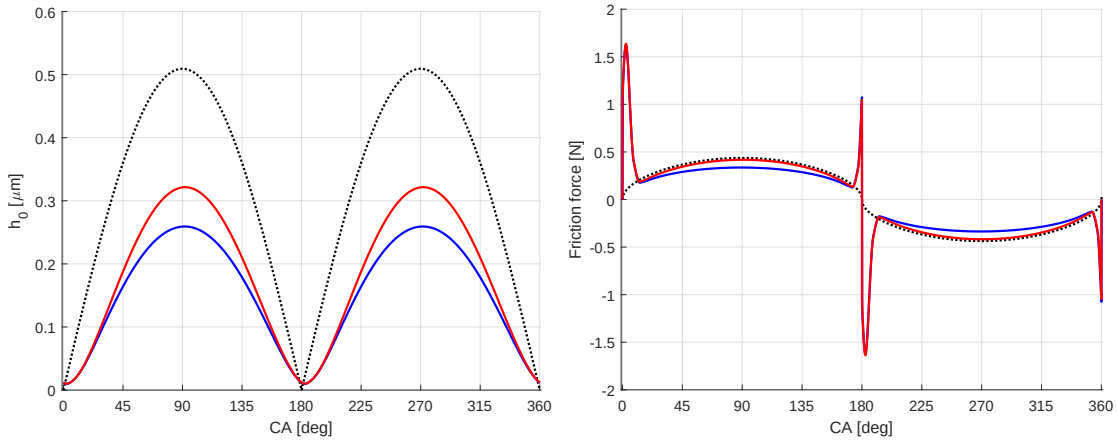

(c) h_0 - $u_{mean} = 50$ mm/s (d) f - $u_{mean} = 50$ mm/s

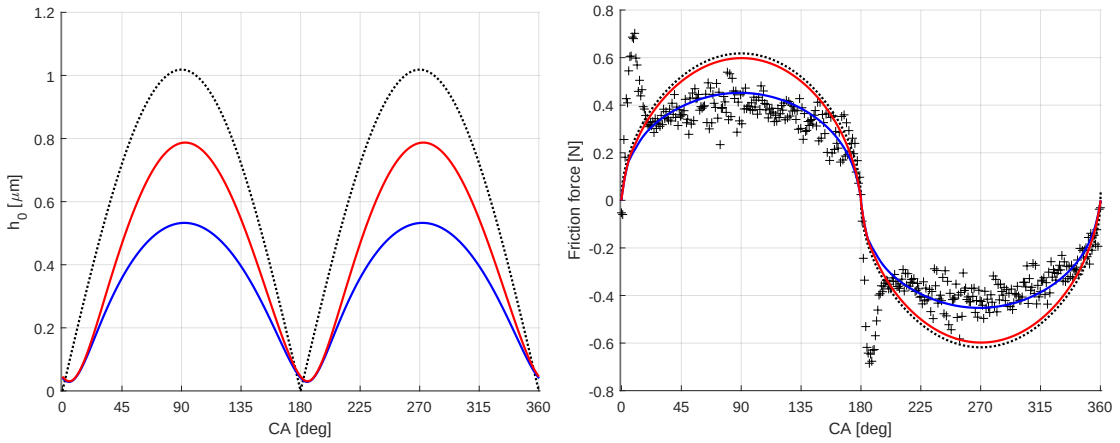

(e) h_0 - $u_{mean} = 100$ mm/s (f) f - $u_{mean} = 100$ mm/s

Figure 4.32: Film thickness h_0 and friction f predictions for a full roller (red) and a 0.5 mm slider (blue - black dotted line: Moes & Venner solution - plus signs: measurement).

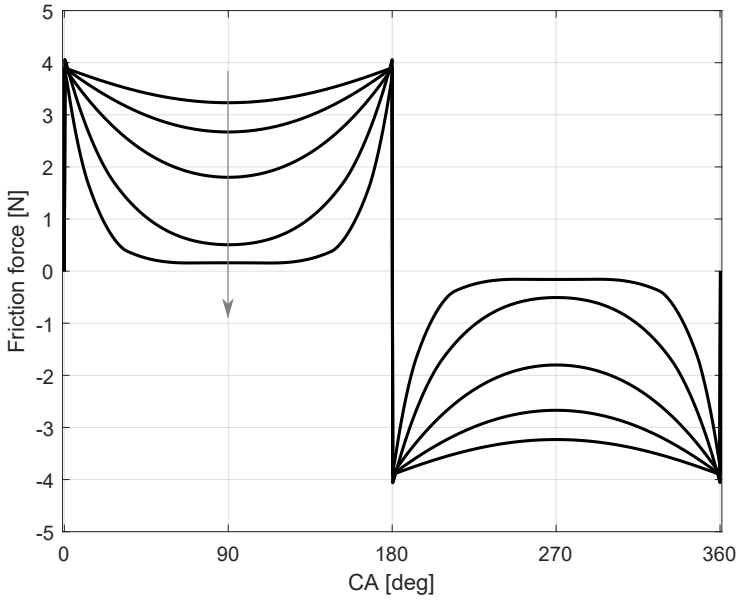

Figure 4.33: Predicted friction at low speed for a 0.5 mm slider, the arrow indicates the increasing speeds (from top to bottom: u_{mean} =0.5, 1, 2, 5, 10 mm/s).

4.5.6 Power loss

The power loss is a major point of interest in the PRCL study as it describes the effective energy loss due to friction. The power loss in Watt is define as:

$$P_w = f \times u \tag{4.9}$$

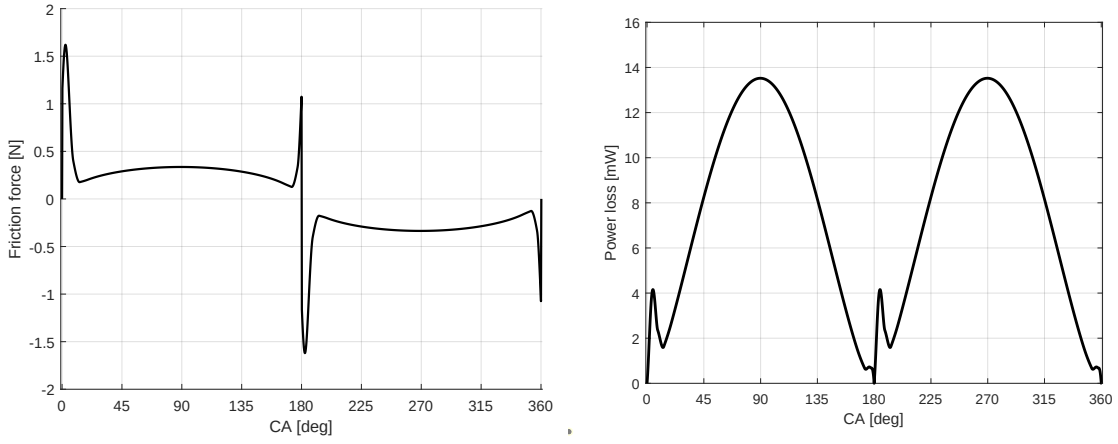

(a) Friction prediction.

(b) Power loss prediction.

Figure 4.34: Friction and power loss prediction for a 0.5 mm slider and $u_{mean} = 50$ mm/s.

Mean speed [mm/s]	5	10	20	30	50	75	100	150
Measured [mJ]	20.8	8.8	6.2	6.6	7.8	9.6	11.2	13.2
Predicted [mJ]	8.8	4.8	5.2	6.0	7.6	9.4	10.8	13.2
Relat. Diff. [%]	58.0	45.7	17.6	7.8	3.2	2.6	3.4	0.6

Table 4.11: Full roller power loss results.

Mean speed [mm/s]	5	10	20	30	50	75	100	150
Measured [mJ]	22.4	10.8	7.0	6.4	6.6	7.2	7.6	8.6
Predicted [mJ]	19.6	6.6	4.8	5.2	6.2	8.2	9.8	11.2
Relat. diff. [%]	12.8	38.1	31.1	19.7	6.7	2.2	5.4	13.1

Table 4.12: 0.5 mm slider power loss results.

By integrating the power loss over time for a full back and forth motion, one obtains a unique value that describes the mean contact energy loss per unit time due to friction:

$$\bar{E} = \int_0^{t_{360}} P_w \, dt \quad \text{with} \quad t_{360} = 60/RPM \tag{4.10}$$

Figure 4.34 gives an example of the predicted friction force and power loss for one configuration. One can notice that the higher power loss value (at mid-stroke) is computed for the lowest friction force value in the full-film lubrication regime. Also, the high friction forces at the dead-centres generate a relatively low power loss due to the low speed of the piston at theses positions. Figures 4.35(c) and 4.35(d) show for $u_{mean} = 50$ mm/s and for both geometries the predicted power loss (red solid line) compared to the measured power loss (black plus signs). For both geometries, the predicted power loss is relatively consistent with the measured values except at the dead-centres. It is noticeable that the 0.5 mm slider shows a lower power loss over the stroke than the full roller, except at the dead-centres for which the values are similar. On the contrary, Figures 4.35(a) and 4.35(b) show for $u_{mean} = 5$ mm/s a relatively bad predictions to measurements fit. Tables 4.11 and 4.12 regroup for each geometry and for every mean speed the predicted and measured mean energy loss by time unit. In order to estimate the model accuracy, a relative difference between the predicted and measured value is computed. Measured and predicted power losses listed in Tables 4.11 and 4.12 show the existence of an optimum speed for which the contact energy loss is minimum (i.e. transition from the mixed to full-film lubrication regime). For the full roller configuration, the minimum power loss is obtained at $u_{mean} = 20$ mm/s as for the 0.5 mm slider this minimum is reached at $u_{mean} = 30$ mm/s. Above this optimum speed, the contact power loss increases linearly with speed (typical from the full-film lubrication regime) with a factor 0.0266 for the full roller and 0.0103 for the 0.5 mm slider especially because of the geometrical starvation effect. The power loss prediction is relatively bad for low speeds (relative difference > 30 %) as the contact is mainly in the mixed lubrication regime. However, for mean speeds above $u_{mean} = 50$ mm/s the relative difference between the measurement and the prediction is mostly below 5 %.

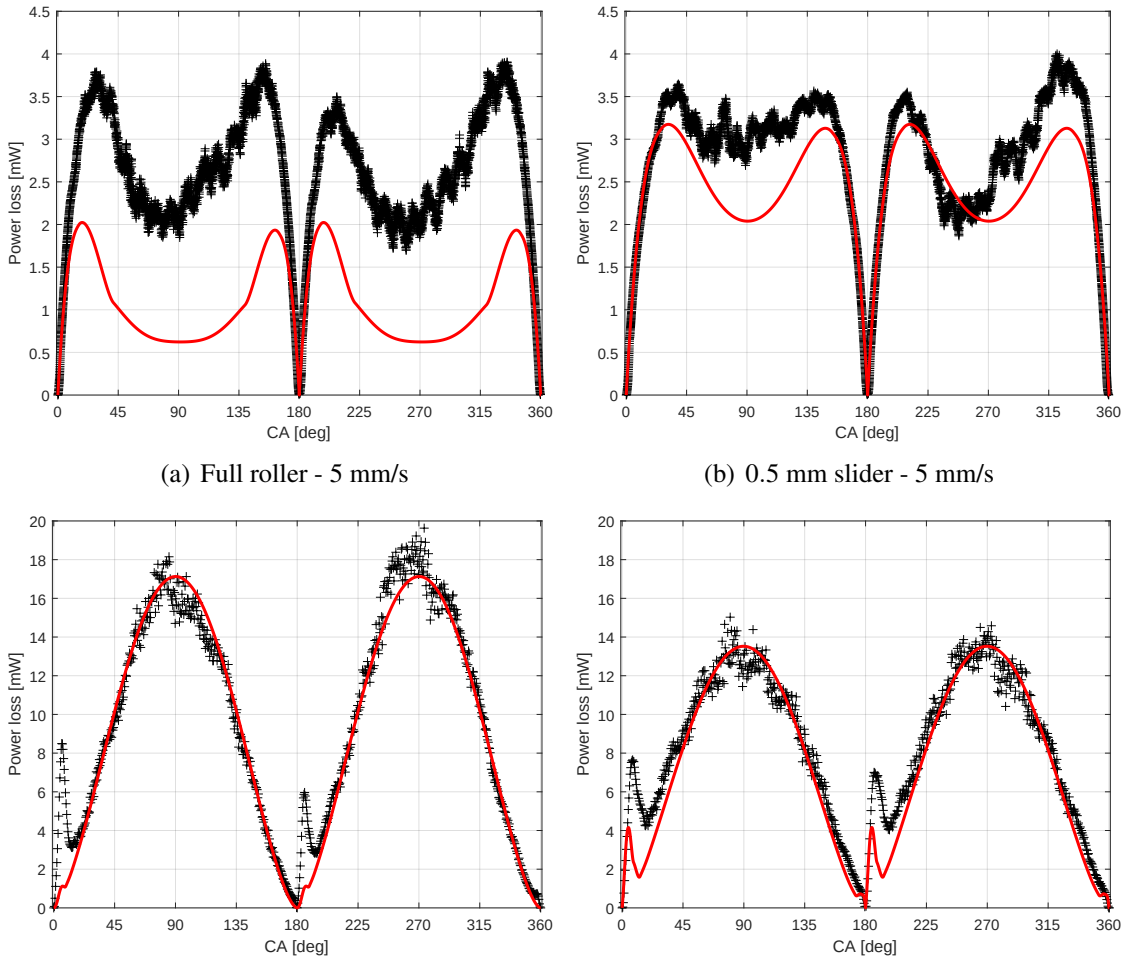

(a) Full roller - 5 mm/s

(b) 0.5 mm slider - 5 mm/s

(c) Full roller - 50 mm/s

(d) 0.5 mm slider - 50 mm/s

Figure 4.35: Power loss prediction (red line) and measurement (plus signs).

4.6 Convergence and Computing Time

The previous operating conditions for the 0.5 mm slider at $u_{mean} = 50$ mm/s are used to illustrates the model time discretisation error and convergence order. The system of non-linear equations is solved using the Levenberg-Marquardt algorithm of the Matlab *fsolve* function with a function tolerance value equal to $10E-12$. Tables 4.14 and 4.13 regroup the values of the film thickness and friction force at respectively 180°CA (i.e. dead-centre) and 270°CA (i.e. mid-stroke) for various values of the angle step dCA (i.e. time step δ_t).

Table 4.13 presents the model convergence in the full-film lubrication regime and for a relatively small transient effect. On the contrary, table 4.14 presents the model convergence in the mixed lubrication regime and for an important transient effect.
For both configurations, film thickness and friction results converge towards a value, which is the solution of the continuous problem. In addition, the relative change in the

variable values (h_0 as well as f) is divided by a factor of ≈ 2, each time the crank angle step (i.e. the time step) is divided by 2. Thus, the accuracy of the numerical scheme is order 1, as demonstrated by Biboulet et al. [9] for the pure hydrodynamic solver.
From Tables 4.14 and 4.13, it can be observed that at a given time step δ_t the results at mid-stroke are more precise than the results at the dead-centre. This is because the time-step has a direct influence on the transient term $v = \partial h/\partial t \approx (h_0^{(k)} - h_0^{k-1})/\delta_t$, which is dominant at the dead-centre and minimal at mid-stroke. It is mainly for this reason that the time-step refining method is introduced (see Section 2.10). It allows for a constant level of precision along the time domain without having to compromise the computing time. For example, a calculation with a discretisation error close to 1 % can be performed with an initial $dCA = 1$ and a refined $dCA = 0.125$ within 160 seconds which is 1.7 times faster than the same calculation with a fixed $dCA = 0.125$. All calculation were performed on a laptop computer.

dCA [deg]	δ_t [ms]	h_0 [nm]	Change [%]	f [N]	Change [%]
1.0	1.11	259.134	-	0.335942	-
0.5	0.56	259.171	0.0144	0.335934	0.0023
0.25	0.28	259.190	0.0072	0.335930	0.0012
0.125	0.14	259.199	0.0036	0.335928	0.0006

Table 4.13: Convergence analysis at mid-stroke.

dCA [deg]	δ_t [ms]	h_0 [nm]	Change [%]	f [N]	Change [%]	Comp. time [s]
1.0	1.11	12.231	-	1.00	-	29.5
0.5	0.56	12.032	1.623	1.05	4.601	68.2
0.25	0.28	11.931	0.840	1.07	2.285	135.2
0.125	0.14	11.880	0.428	1.08	1.140	275.2

Table 4.14: Convergence analysis at dead-centre.

Also, the addition of the solid-to-solid contact theory upon the existing hydrodynamic solver has increased the calculation stability and has aided the code to converge more rapidly for small film thickness values. This is mostly because the solid-to-solid contact stiffness is higher than the fluid stiffness since the contact stiffness $\partial w/\partial h$ appears in the solver Jacobian.

Formal calculations are performed ahead of the transient iterating solver using the Matlab symbolic calculation toolbox. The solver analytical integrals and equations are mostly computed within 30 seconds. The computation time for the "load-distance" data is strongly related to the topography sizes (i.e. number of points). For a surface with 4096×4096 points the calculations where performed within two hours on a laptop computer, the limit being the computer memory (i.e. RAM). To this, one has to add the time needed to measure the surface topography and to post-process it.

4.7 Conclusion

In this chapter the prediction relevance as well as the code efficiency is investigated. First, the hydrodynamic predictions from the semi-analytical solver are compared to a fully numerical P-Θ solution. Both solutions are in excellent agreement whereas the semi-analytical solver needs fewer calculation steps. Secondly, the model results are compared to line-contact friction measurements with similar pressure to velocity ratios as for a PRCL contact. Thereby, it has been shown that the model is unable to accurately predict the solid-to-solid contact accounting only for the sample micro-geometry. Indeed, the high amplitude macro-geometry/undulation of the roller has a non-negligible impact on the contact hydrodynamic load carrying capacity. Therefore, the model is upgraded using analytical correction coefficients evaluated using the deformed roller geometry. As a result, the predicted friction force is in good agreement with the measurements and the calculation time is unchanged. Finally, based on the experiments, an efficient semi-analytical method to predict the time-dependent, starved, line-contact friction accounting for a measured topography and the sample macro-geometry is demonstrated. For a sufficiently smooth contact with a negligible macro-geometry, the initial version of the code might provide a sufficiently accurate prediction.

Chapter 5

Results

Contents

5.1 Introduction

This chapter is dedicated to the experimental friction results obtained using the PRCL test-rig described in Chapter 3. The analysis is focusing on the lubrication of the compression ring. Different configurations of Diamond-like Carbon (DLC) coated or uncoated liner and ring are tested for a variety of rotational speeds. The coating benefits on the Piston-Ring / Cylinder-Liner (PRCL) contact are discussed. In addition, the measurements of the ring profile and ring/liner roughness are used as input for the mixed lubrication model. Predictions are compared to the experimental results, differences and adjustments are discussed. From the floating liner configuration, examples of the abilities of the developed code are presented such as the optimisation of the compression ring geometry.

5.2 Compression Ring Experimental Results

As detailed in Section 3.5 describing the PRCL test-rig, a standard piston engine is modified in order to study only the ring friction. Therefore, the piston skirt is completely removed and the piston outer diameter is machined in order to remove 1 mm. In addition, the test-rig specific design allows for a quick change of the tested ring and liner, giving the possibility to test a variety of ring/liner configurations. Considering the test-rig instabilities (investigated in Section 3.5) the measurements were performed for relatively low engine speeds. However, based on the strategy detailed in Section 3.5, a high-viscosity engine oil (10W-60 grade Mobil 1) was used in order to mimic the piston ring lubrication for higher engine speeds with a lower viscosity engine oil, a 5W-30 grade for example. The main difference being the oil additives in each engine oil. As a reminder, the contact oil film thickness is mainly driven by the velocity$\times$viscosity product. Table 5.1 lists the test and target engine speeds for each engine oil. All tests are carried out for a controlled liner temperature of 50°C.

Parameter	Test	Target
Engine oil	10W-60 grade	5W-30 grade
Liner/oil temperature	50°C	100°C
Dynamic viscosity	$\eta_{test} = 90.6$ mPa.s	$\eta_{target} = 9.0$ mPa.s
Engine speed	100 RPM	1000 RPM
	150 RPM	1500 RPM
	200 RPM	2000 RPM
	400 RPM	4000 RPM

Table 5.1: Test and target experimental parameters.

Table 5.2 regroups the test-rig kinematic parameters.

Parameter	Value
Bore	80.08 mm
Stroke	60.0 mm
Con-rod	485 mm

Table 5.2: Test-rig kinematic parameters.

In this document, the analysis focuses only on the compression ring friction, although complete ring pack friction measurements have also been performed. For a first approach and in order to confirm the test-rig accuracy, the compression ring offers a simple symmetrical parabola face which provides a relatively straightforward lubrication behaviour. The tested compression rings were purchased from the GOETZE ENGINE company with the following reference: 2.0mm 001 CR P GOE13. Figure 5.1 provides some pictures of the cylinder and ring samples.

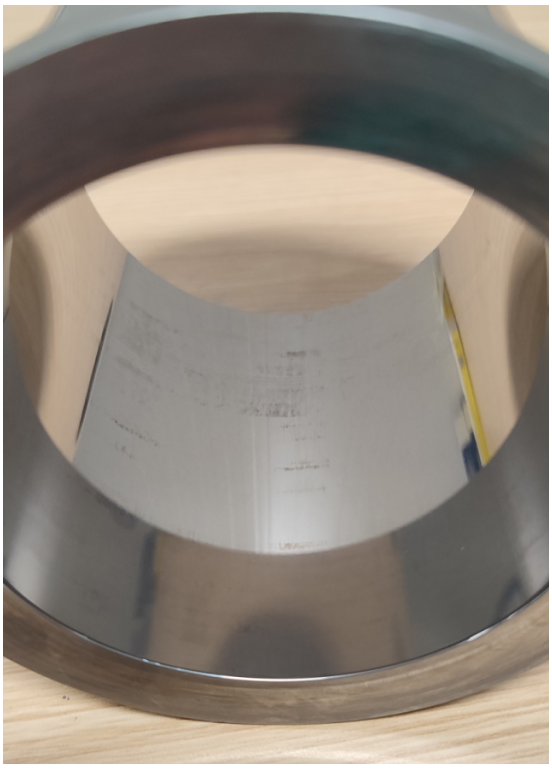

(a) Steel mirror-like liner

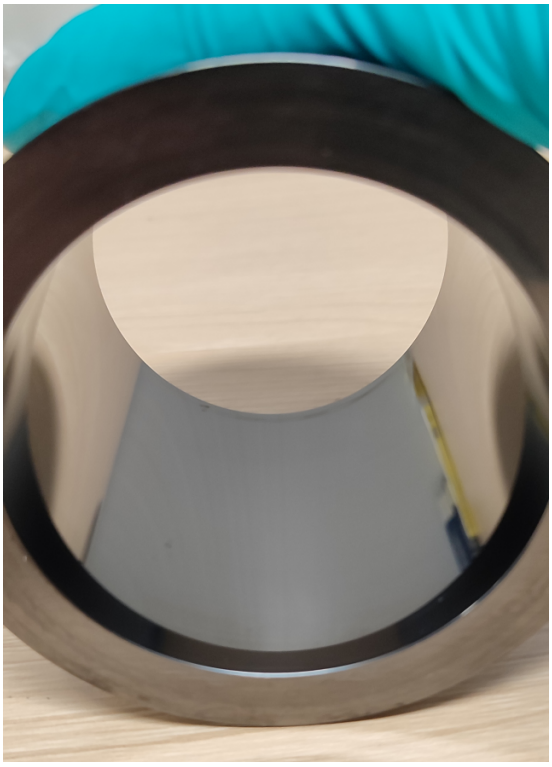

(b) DLC coated mirror-like liner

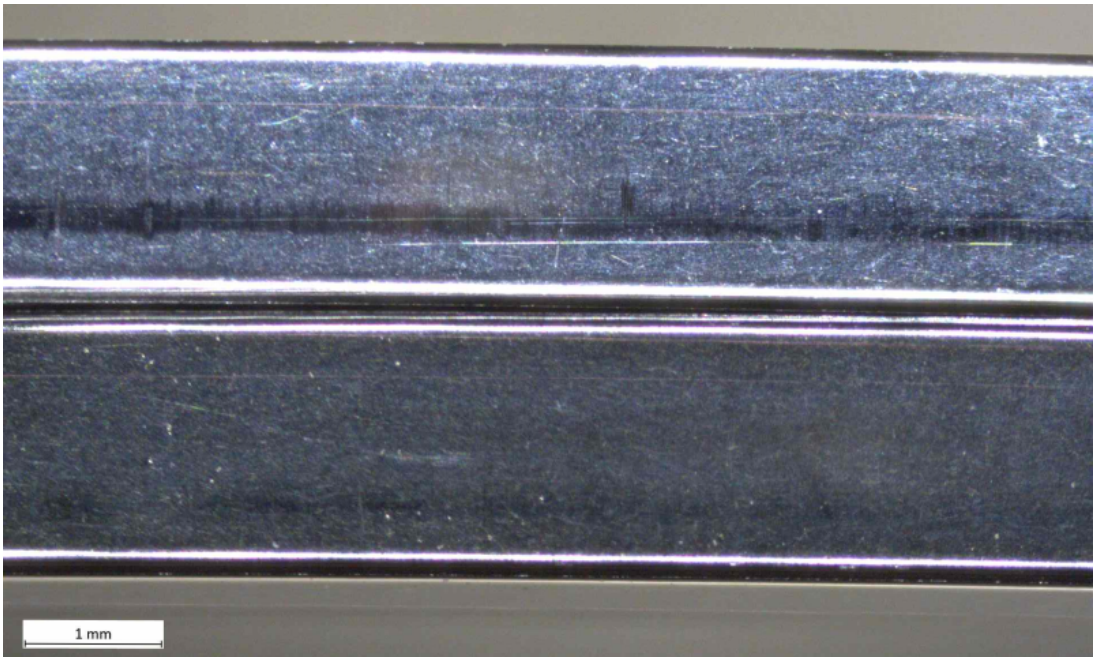

(c) Uncoated (top) and DLC coated (bottom) compression ring

Figure 5.1: Pictures of the liners and ring samples.

All rings were first polished using a vibratory finishing industrial process and some were subsequently DLC coated (2 µm thick a-C:H with ≈ 20 % hydrogen) using a PECVD process. The cylinder samples were machined from a steel block to the desired bore dimension and were polished to a mirror-like, non-textured aspect using a honing process and a diamond suspension/paste. This surface finish is necessary for a good adherence of the coating on the liner. Then, a similar DLC coating is applied on the polished liner surface of one of the cylinders. In order to primarily study the DLC coating tribological benefits and to match with the model assumptions, the uncoated liner is polished to the same surface finish. Please note that this differs from the standard cross-hatch liner texture. Tables 5.3 and 5.4 provide the measured roughness parameters of each tested sample.

[nm]	Steel liner	DLC liner
Ra	17.8	15.7
Rq	23.4	22.1
Rz	129.35	119.5
Rk	57.8	48.9
Rpk	22.1	27.9
Rvk	34.4	30.8

Table 5.3: Liner roughness parameters (tactile profilometer ISO 4287 & 13565).

[nm]	Uncoated ring	DLC coated ring
Ra	13.9	14.9
Rq	19.1	19.8
Rz	142.0	140.0
Rk	17.5	14.9
Rpk	36.8	31.1
Rvk	40.0	47.0

Table 5.4: Ring roughness parameters (inside wear scar - confocal ISO 4287 & 13565).

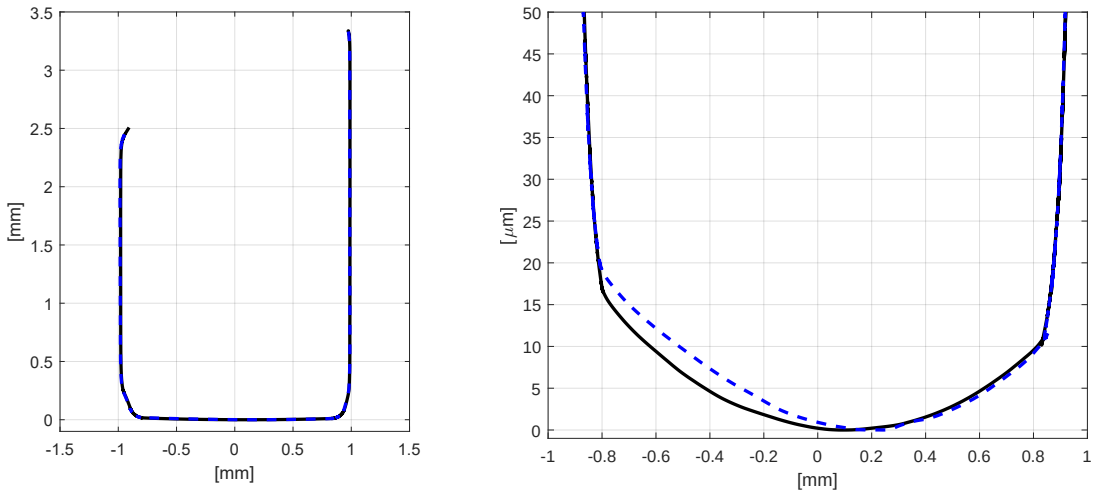

(a) Complete ring

(b) Zoom on the ring faces

Figure 5.2: Compression ring profiles (black: uncoated - dotted blue: DLC coated).

Figure 5.2 gives the measured DLC coated and uncoated ring's profile using a Coordinate-Measuring Machine (CMM). The rings parabolic-like central part are slightly different. The uncoated ring profile has a tiny asymmetry with a minimum gap located at roughly 0.096 mm from the center as the DLC coated ring is more asymmetric with a minimum gap located at roughly 0.18 mm from the centre. Also, the DLC coated ring presents a 20% smaller ring radius equal to 22 mm versus 26 mm for the uncoated ring. These differences are either due to a manufacturing dispersal or due to the erratic vibratory finishing process. Nevertheless, these differences in the ring faces may lead to different lubrication behaviours as detailed in the following analysis.
From the previously described liner and compression ring samples, three different tribological pairs are tested: uncoated ring and liner, DLC coated ring against uncoated liner and DLC coated ring and liner. All tribo-pairs are run-in before testing. The run-in consists in a two hours V cycle process with an initial engine speed of 500 RPM and a minimum speed of 100 RPM at a constant 100°C liner/oil temperature. Afterwards, a five minute test is performed at each engine speed and the PRCL friction force is recorded during the last thirty seconds. For all tests, a continuous engine oil flow is sprayed on to the liner below the piston.

The measured friction signal is filtered using a Butterworth low-pass filter of order 6 with a cut-off frequency $f_c = 250$ Hz. The signal is then averaged over several back and forth cycles with respect to the piston position. Figure 5.3 shows the benefit of the signal filtering and averaging for a 200 RPM engine speed. The measurement repeatability is assessed by computing the cycle-to-cycle friction deviation, listed for each engine speed in Table 5.5. The experimental reproducibility is evaluated by comparing the friction force of two assemblies. Assembly 1 and assembly 2 are made up of the same samples (a top and second uncoated piston ring and an uncoated liner) but a complete disassembly of the test-rig is performed between the two measurements. Table 5.5 regroups the mean friction value and difference over a full back and forth cycle for all tested speeds and for both assemblies. On one hand, the cycle-to-cycle repeatability of the measurements is relatively bad with an STD= 20% for low engine speed and STD= 10% for high engine speed. But, on the other hand, the experimental exhibits a good reproducibility with an error below 5% which means that the signal post-treatment is relatively representative of the reality.

Engine speed	100 RPM	150 RPM	200 RPM	400 RPM
Mean friction Ass. 1 [N]	4.41	4.36	4.51	5.22
Mean friction Ass. 2 [N]	4.38	4.14	4.66	5.21
Difference [%]	0.79	5.01	3.36	0.20
Mean friction Ass. 3 [N]	1.56	1.60	1.78	2.33
Mean STD Ass. 3 [N]	0.30	0.28	0.25	0.23
Mean STD Ass. 3 [%]	19.3	17.6	14.1	9.8

Table 5.5: Test reproducibility and repeatability analysis.

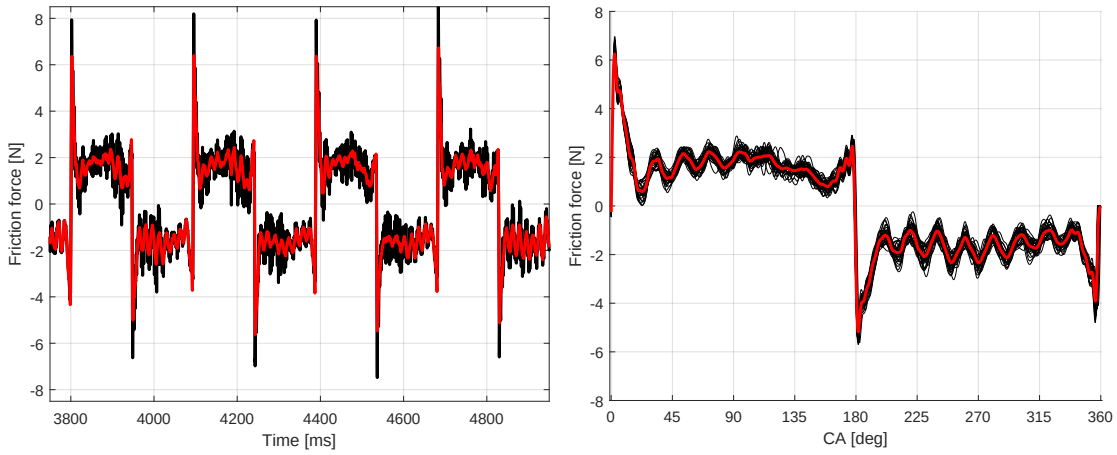

(a) Filtering (b) Averaging

Figure 5.3: Signal post-processing for a Steel-Steel configuration and for a 200 RPM engine speed (black: raw data - red: post-treated data).

Figure 5.4 presents the post-treated friction force results for each engine speed over a full cycle (from TDC 0°CA, to BDC 180°CA, to TDC 360°CA). The black curve stands for the uncoated ring and liner configuration, the grey curve for the DLC coated ring against the uncoated liner and the blue curve for the DLC coated ring and liner configuration.

In Figure 5.4, both tribo-pairs with a DLC coated ring systematically exhibit a higher friction force at the mid-stroke positions (i.e. 90°CA and 270°CA) compared to the tribo-pair with an uncoated ring. Concluded from the increasing friction force with increasing piston speed, the contact is in the full-film lubrication regime at mid-stroke and for all four engine speeds. Thus, the friction difference observed towards mid-stroke is mostly due to the ring geometry outlined in Figure 5.2. According to the theoretical Moes & Venner film thickness equation, a smaller radius of curvature generates a thinner film thickness which for a constant speed, load, and viscosity, leads to a higher viscous friction. As the DLC coated ring has a smaller radius of curvature compared to the uncoated ring, it is thus logical that configurations made up of a the DLC coated ring exhibit a higher friction at mid-stroke. For this reason, the friction difference at mid-stroke must not be attributed to the DLC coating.
For an unexplained reason, the tribo-pair with a DLC coated ring rubbing against the uncoated liner exhibits systematically a higher friction spike at the dead-centres, except for the 2000 RPM engine speed. Therefore, these results will be ignored in the following analysis. In addition, for the measurements at 4000 RPM, the friction spikes at the TDC position are probably due to the test-rig vibrational instability as the friction spikes of the uncoated and DLC coated configurations are rigorously the same, which is not the case for all other tested speeds. Therefore, this data will also be ignored in the following analysis.

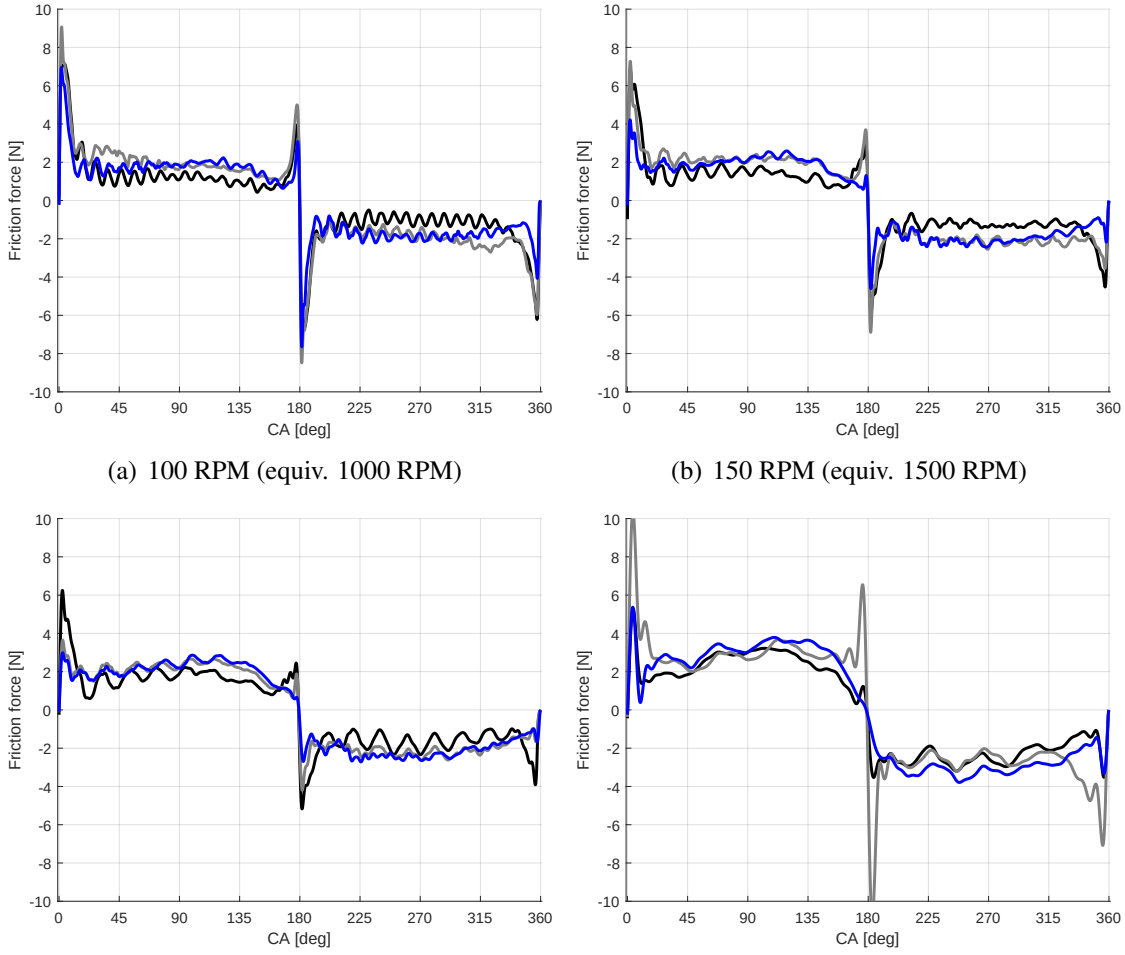

(a) 100 RPM (equiv. 1000 RPM)

(b) 150 RPM (equiv. 1500 RPM)

(c) 200 RPM (equiv. 2000 RPM)

(d) 400 RPM (equiv. 4000 RPM)

Figure 5.4: Compression ring friction measurement for a 10W-60 grade Mobil 1 oil at 50°C (equiv. 5W-30 grade at 100°C - black: uncoated ring and liner - grey: DLC coated ring against uncoated liner - blue: DLC coated ring and liner).

For all tested speeds (ignoring the friction at the TDC location for 4000 RPM), a lower friction spike at both the TDC and the BDC is observed for the completely DLC coated configuration. For engine speeds above 1500 RPM, the friction spike just before the BDC position is almost vanished. According to the increasing friction force for decreasing speeds towards the dead-centres, the contact is in the mixed to boundary lubrication regime and a substantial part of the contact load is carried by some solid-to-solid interaction between the surface roughness. As both coated and uncoated rings and liners present a similar micro-geometry (see Tables 5.3 and 5.4) the dissimilarity in friction in the boundary lubrication regime is mainly driven by the difference in the boundary friction coefficient. Using the methods described in Section 3.3, a boundary friction coefficient of 0.18 was measured for a Steel/Steel tribo-pair and a friction coefficient of 0.16 (11 % reduction) was measured for a DLC/DLC contact lubricated with the tested engine oil at 50°C.

Focusing on the maximum friction force value at the dead-centres, on average a 40 % friction reduction (with a 20 % standard deviation) is observed for the DLC coated ring and liner configuration compared to the uncoated set-up. This benefit is substantially larger than the 11 % reduction expected because of the lower boundary friction coefficient of the DLC coating. It is most likely that the difference in geometry of the uncoated and coated ring (detailed in the previous paragraph) has a major impact on the ring lubrication at the TDC and BDC.

In order to mimic the additional load generated by the combustion gases on the back of the ring, eight spring pressure screws are mounted inside the piston and generate an additional force that pushes the compression ring against the liner. This additional force is assumed to be equally distributed over the bore circumference and is evaluated by means of the Hooke's law at 32.4 N for each screw. Leading to an equivalent additional load of 1030 N/m corresponding to five times the original ring load and being representative of an in-cylinder pressure of 10.3 bar. Figure 5.5 gives the friction results with the additional load.

Compared to the friction results given in Figure 5.4, the measured signal for a highly loaded compression ring in Figure 5.5 show less vibrational instability. The high ring load generates a solid support of the liner against the piston which stiffens the whole measurement system. For this configuration, the friction results for the DLC coated ring against the steel liner configuration seem coherent.
In Figure 5.5, for speeds lower than 4000 RPM, the uncoated tribo-pair exhibits a constant maximum friction force at the TDC location approximately equal to 39 N which is typical from the boundary lubrication regime. At the dead-centres, the DLC ring / uncoated liner configuration presents systematically a lower friction force than the completely uncoated set-up. Similarly, the fully DLC coated tribo-pair shows an even lower friction force spike. This trend is amplified for increasing engine speeds as shown in Figure 5.6. Table 5.6 regroups the benefits of the DLC coating on the PRCL friction.

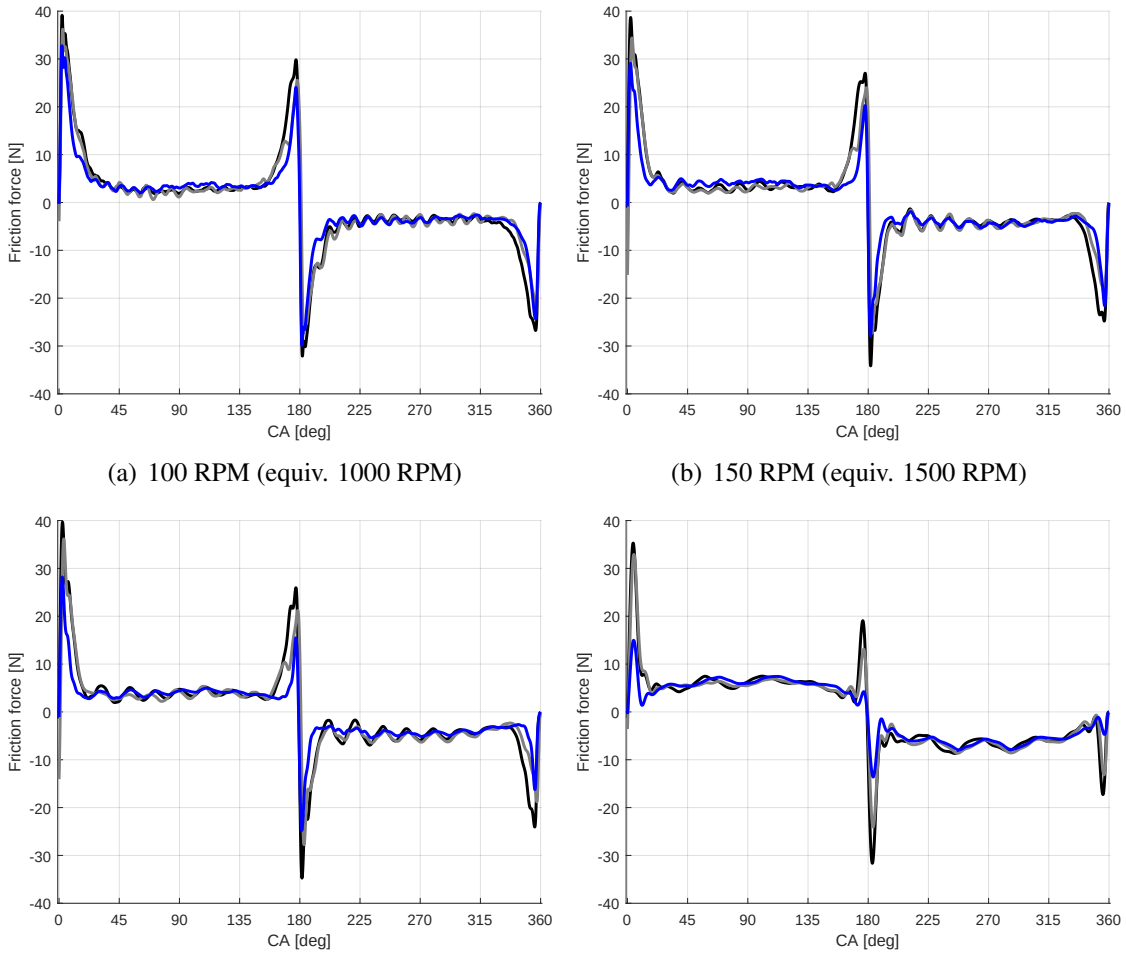

(a) 100 RPM (equiv. 1000 RPM)

(b) 150 RPM (equiv. 1500 RPM)

(c) 200 RPM (equiv. 2000 RPM)

(d) 400 RPM (equiv. 4000 RPM)

Figure 5.5: Compression ring friction measurement with additional load for a 10W-60 grade Mobil 1 oil at 50°C (equiv. 5W-30 grade at 100°C - black: uncoated ring and liner - grey: DLC coated ring against uncoated liner - blue: DLC coated ring and liner).

The DLC coated / uncoated liner configuration exhibits a 10% to 20% reduction in friction while the complete DLC coated set-up yields a 10% to 30% reduction in friction (4000 RPM values are ignored because of the test-rig vibrational instability). In addition, for all tested speeds a narrower friction force spike is observed for the complete DLC coated tribo-pair compared to the two other configurations.

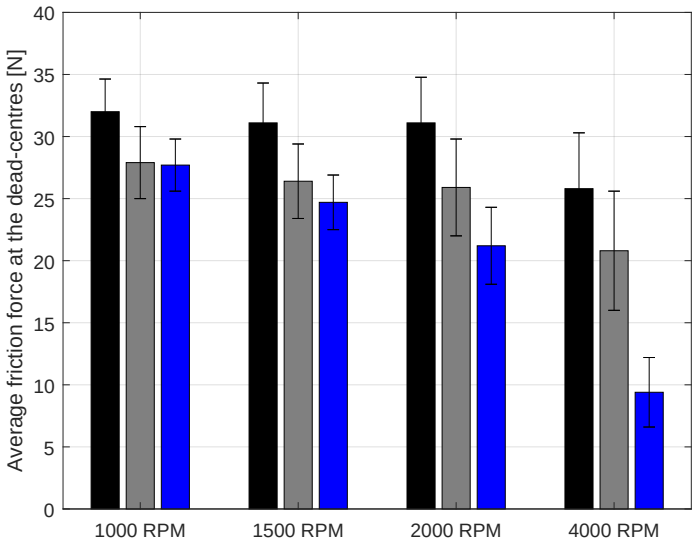

Figure 5.6: Measured average friction force at the dead-centres, errorbars indicate the standard deviation (black: uncoated ring and liner - gray: DLC coated ring against steel liner - blue: DLC coated ring and liner).

Configuration	1000 RPM	1500 RPM	2000 RPM	4000 RPM
DLC ring / Steel liner	12.7 %	15.1 %	16.9 %	19.3 %
DLC ring / DLC liner	13.2 %	20.7 %	31.9 %	63.7 %

Table 5.6: DLC coating friction reduction at the dead-centres for the additional load.

Figure 5.7 details the computed Friction Mean Effective Pressure (FMEP) for all tested configurations. The FMEP value is computed using the following equation:

$$FMEP = \frac{\int_0^{360} P_w \, \mathrm{d}CA}{V_d \, \Omega} \tag{5.1}$$

with $P_w = f \times u$ the contact power loss integrated over a complete back and forth movement, V_d the displaced volume and Ω the engine rotational speed in [deg/s].

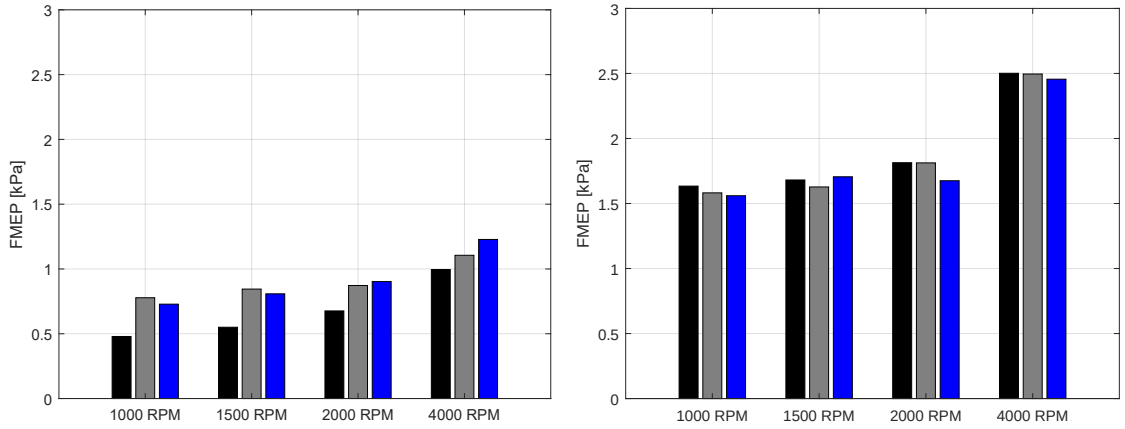

(a) Original tension force.

(b) Additional tension force.

Figure 5.7: Measured FMEP (black: uncoated ring and liner - gray: DLC coated ring against steel liner - blue: DLC coated ring and liner).

For the measurements with the original ring load, the FMEP results displayed in Figure 5.7(a) show a contradictory tendency with lower FMEP values for the uncoated configuration than for the DLC coated set-up. This is because for low loads, the proportion of viscous friction on a cycle is high compared to the asperity friction. Moreover, the DLC coated ring has a geometry generating more viscous friction, it thus leads to a higher FMEP value. For these reasons, FMEP results in Figure 5.7(a) are not an indication of the DLC benefits.
However, the measurement results mimicking the effect of the combustion pressure on the ring load exhibit a high proportion of mixed to boundary lubrication regime on a cycle. Therefore, the DLC coating benefits can be identified for high load configuration. In this way, a 5% reduction in FMEP is measured for the completely DLC coated set-up compared to the uncoated tribo-pair.

Another well known tribological benefit of the DLC film is its hardness and resistance to wear. Figure 5.8 shows microscope pictures of both uncoated and DLC coated tested compression rings, the dark zones highlight the wear scars.
Both rings have been run-in using the same process, have been tested for the same amount of time, for the same operating conditions and against each liner (uncoated and DLC coated). In Figure 5.8, the DLC coated compression ring (bottom pictures) exhibits for each studied location a 85% smaller wear scar area. On the uncoated compression ring the wear scar can be easily identified and is large (roughly 0.4 mm) while it is barely visible on the DLC coated ring. In the same way, no wear is observed on the DLC coated liner as small marks can be seen on the uncoated liner surface (see Figure 5.1). Moreover, for both rings the wear scar is discontinuous along the circumference, which suggests a relatively important ring and liner out of roundness.

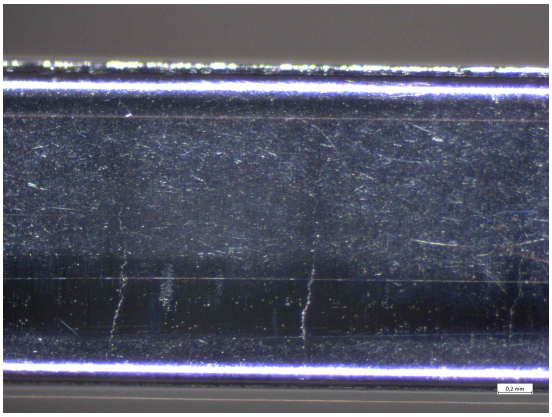

(a) Uncoated ring - back location

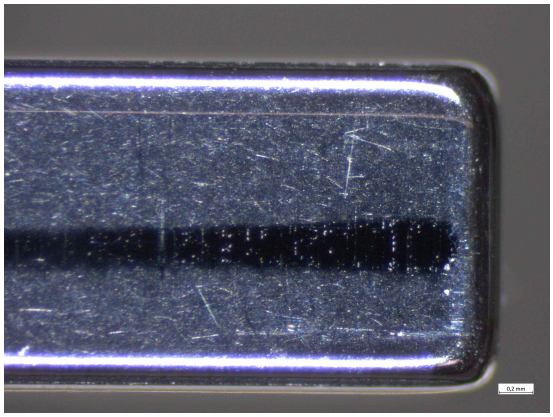

(b) Uncoated ring - gap location

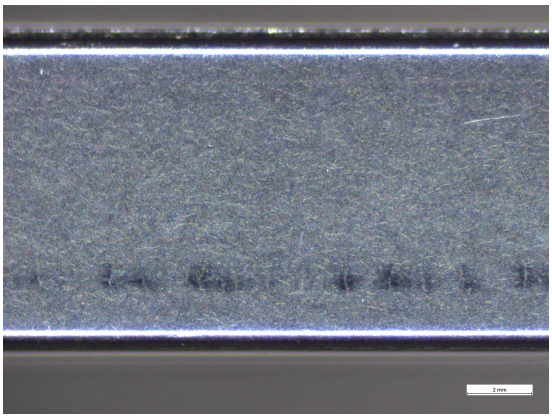

(c) DLC coated ring - back location

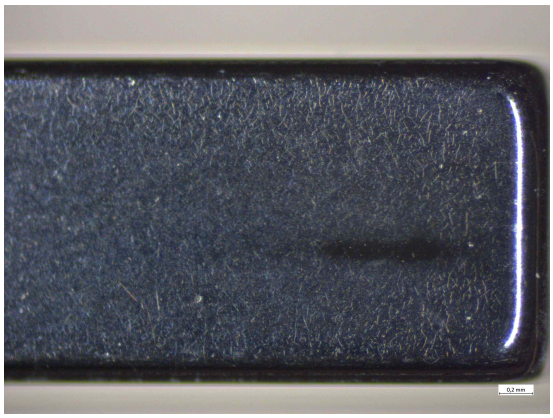

(d) DLC coated ring - gap location

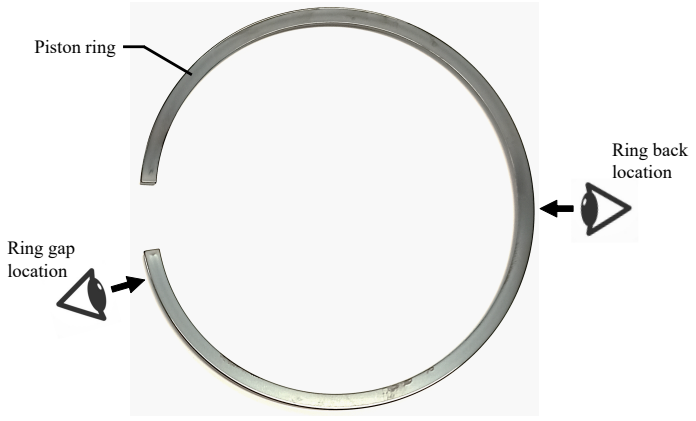

(e) Observation location

Figure 5.8: Microscope pictures of both tested compression rings, the dark zones highlight the wear scars.

5.3 Compression Ring Numerical Results

In the model, the rings are defined using a piecewise function detailed in Equation 5.2. The two high sides represent the piston flanks with $h_{side} = 5$ mm. The central part is described as a shifted parabolic profile with for the uncoated ring $x_s = 0.096$ mm, $r = 26$ mm and for the DLC coated ring $x_s = 0.18$ mm and $r = 22$ mm. Figure 5.9(a) compares the numerical ring profiles (solid lines) to the measured ring profiles (circles). Figure 5.9(b) gives the "pressure-distance" data computed using the contact mechanics methodology described in Chapter 2. The solid contact data is computed for each tribo-pair (uncoated and DLC coated) using an equivalent topography generated by summing the corresponding ring and liner measured 3D topographies. Figure 5.10 shows a 3D representation of the equivalent rough surfaces. Table 5.7 regroups the surface roughness parameters.

$$\begin{cases} h = h_{side} & \text{for} \quad x < -x_l \,\&\, x > x_l \\ h = h_0 + \frac{(x-x_s)^2}{2r} & \text{for} \quad -x_l \leq x \leq x_l \end{cases} \tag{5.2}$$

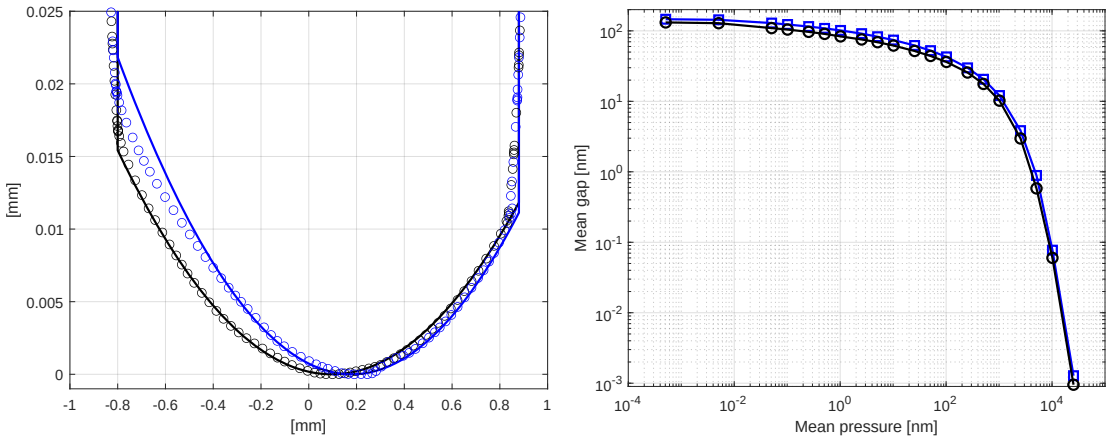

(a) Ring profiles (circles: measurement - solid lines: fitted).

(b) "Pressure-distance" contact mechanics results.

Figure 5.9: Model input (blue: DLC coated - black: uncoated).

The data in Table 5.7 and the 3D topographies in Figure 5.10 present two surfaces with a similar micro-geometry. Therefore, the contact mechanics results for both tribo-pairs (given in Figure 5.9(b)) are relatively close.

The calculations are performed for the target oil viscosity ($\eta_{target} = 9.0$ mPa.s - 5W-30 grade at 100°C) and speeds given in Table 5.1. From Equation 4.2 in Chapter 4 the compression ring load is estimated at $w_{tot} = 867$ N/m. However, viscous friction predictions are overestimated for this ring load value and are not consistent with the measurements. Therefore, the contact normal load is fitted on the experimental results

at high engine speeds (i.e. 4000 RPM) to a $w_{tot} = 200$ N/m value and is used in all the following predictions. The lubrication conditions are assumed fully flooded (i.e $h_{in} >> h_0$) according to the experimental lubrication conditions. The boundary friction coefficient is set at $\mu_{bound} = 0.18$ according to the ball on plate friction measurement results.

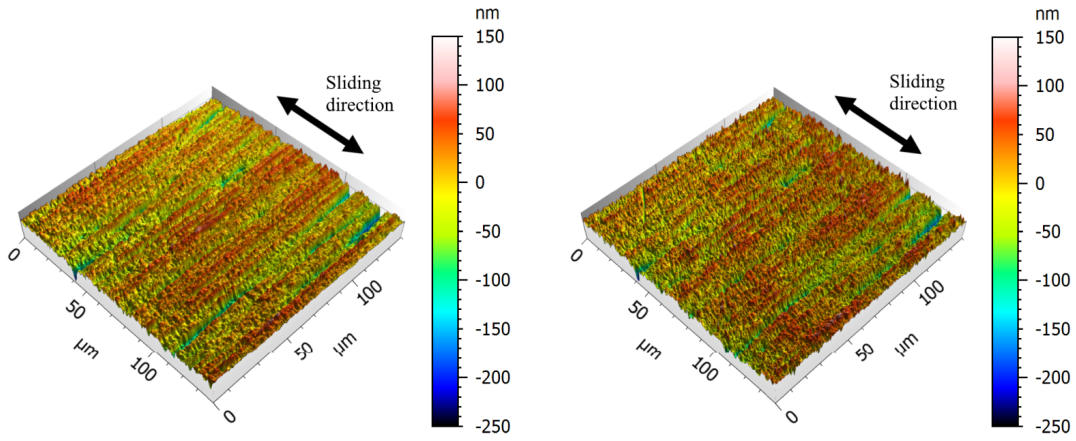

(a) Uncoated ring and liner equivalent topography.

(b) DLC coated ring and liner equivalent topography.

Figure 5.10: Generated equivalent topographies used in the contact mechanics calculations.

[nm]	Uncoated	DLC coated
Sq	36.0	36.3
Sa	27.1	27.8
Ssk	−1.06	−0.756
Sku	5.44	4.64
Sp	132	147
Sv	236	252
Sz	368	398

Table 5.7: Equivalent surfaces roughness parameters (ISO 25178).

Figure 5.11 compares the friction prediction to the experimental results from Section 5.2 for the completely uncoated configuration at a 1000 RPM engine speed. In Figure 5.11(a), the prediction exhibits a relatively good fit around the mid-stroke position in the full-film lubrication regime. Close to the dead-centres, no friction spikes are predicted, however the experiments show mixed to boundary friction. This error in predicting the solid-to-solid contact has already been observed and discussed for the

roller on plate set-up in Chapter 4. It is mainly due to the samples macro-geometry, here the ring and liner out of roundness. In order to fit the predictions to the measured friction spikes at the dead-centres, the "pressure-distance" data (see Figure 5.9(b)) can be multiplied by a factor 12.5 with respect to the gap. These results are presented in Figure 5.11(b). This artificial amplification of the contact mechanics data may correspond physically to an amplification of the roughness amplitude. Thereby, the contact load is completely carried by the solid-to-solid interaction at a gap distance of 1 µm compared to 69 nm for the original "pressure-distance" data. For increasing engine speeds, the friction predictions according to the 12.5 multiplication factor are not consistent with the measurements and a larger multiplication factor on the mixed to boundary friction is needed. Figure 5.12 gives the predicted film thickness and friction compared to the experimental results for all tested engine speeds, for a 12.5 multiplication factor on the "pressure-distance" data (in blue) and for a higher multiplication factor (in dotted red).

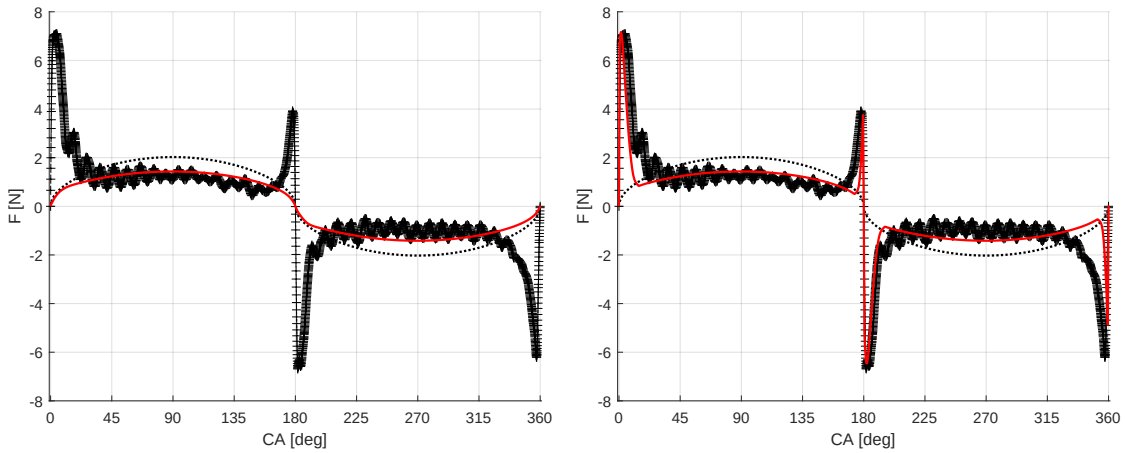

(a) Original "load-distance" data.

(b) Fitted "load-distance" data.

Figure 5.11: Friction prediction vs. experimental results for an uncoated configuration at 1000 RPM engine speed (red solid line: predictions - dotted black line: Moes & Venner solution - plus signs: experimental friction).

Friction prediction in Figures 5.12(d), 5.13(b) and 5.13(d) are obtained with a multiplication factor on the "load-distance" data of respectively 18, 24 and 36. These results are in excellent agreement with the friction measurements. Nonetheless, this fitting relying on an artificial increase of the roughness amplitude with increasing engine speeds is not physical. As discussed in Chapter 4, the macro-geometry of the samples might have a huge impact on the contact lubrication behaviour. For a significant macro-geometry amplitude, the hydrodynamic load-carrying capacity of the ring can be strongly altered, leading to a thinner film thickness and thus more solid-to-solid contact. Figure 5.14 gives an example of the measured rings and liners circularity/roundness using a CMM machine. For the ring circularity measurements, the rings were set to their in-cylinder diameter by closing the ring gap and were clamped in this position.

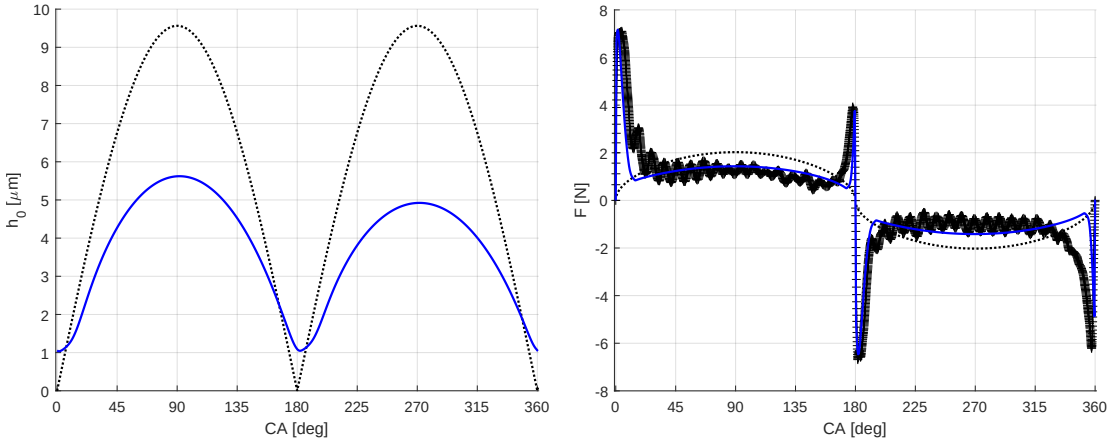

(a) h_0 - 1000 RPM

(b) f - 1000 RPM

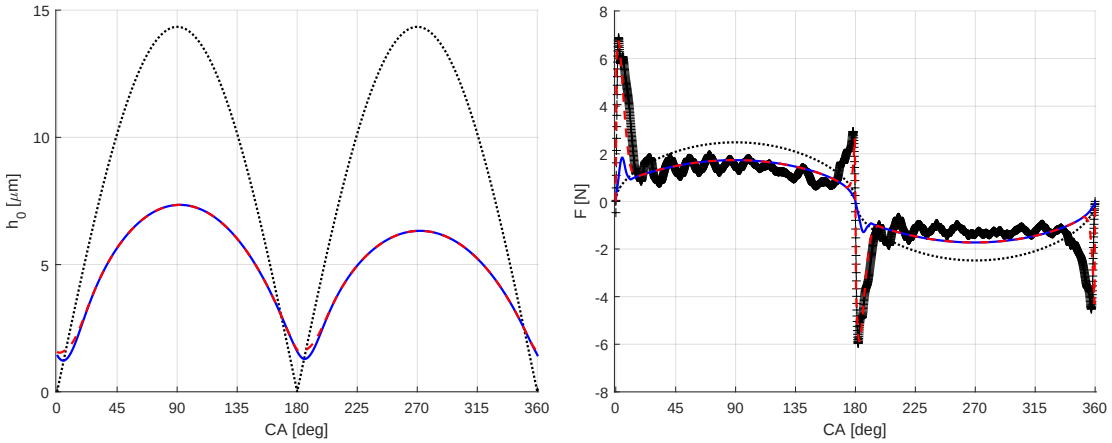

(c) h_0 - 1500 RPM

(d) f - 1500 RPM

Figure 5.12: Friction prediction vs. experimental results for an uncoated configuration and different "load-distance" data multiplication factors (blue solid line: predictions for a 12.5 multiplication factor - red dotted liner: prediction for a higher multiplication factor - dotted black line: Moes & Venner solution - plus signs: experimental friction).

The liners exhibit a maximum bore distortion of 3.9 µm for the uncoated liner and 3.6 µm for the DLC coated liner. The compression rings highlight a stronger out of roundness with a maximum amplitude of 7.5 µm for the uncoated ring and 11.8 µm for the DLC coated ring. In comparison with the film thickness predicted in Figures 5.12 and 5.13, the contact undulation is 1.2 to 15 times larger than the film thickness predicted at the dead-centres and equals to 0.3 to 2.8 times the film thickness predicted at the mid-stroke. For this reason, the results provided by the model accounting only for the micro-geometry of the samples might be limited and a similar strategy as the one applied to the roller on plate contact in Chapter 4 has to be implemented. This task is however more complex because the ring and liner out of roundness and the relative

angular position of the ring in the cylinder are either unknown or difficult to measure. This has yet not been investigated but will be part of future research.

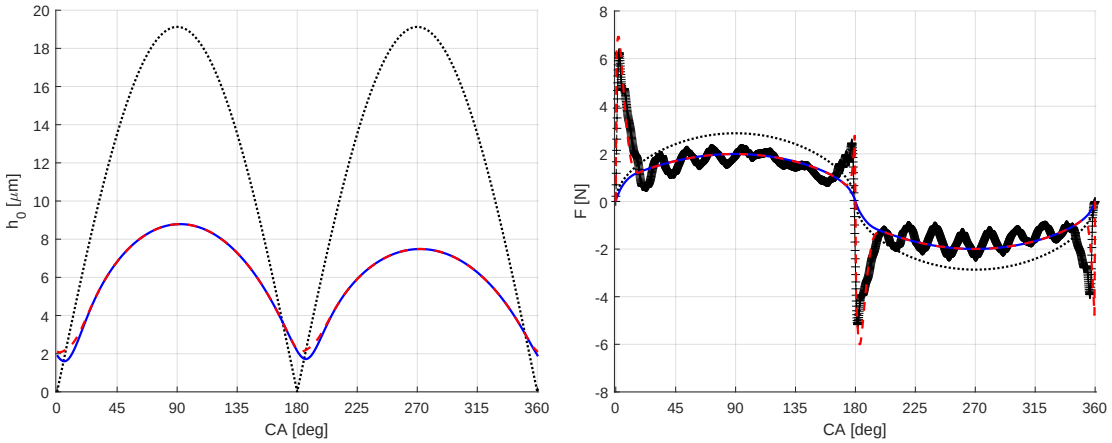

(a) h_0 - 2000 RPM

(b) f - 2000 RPM

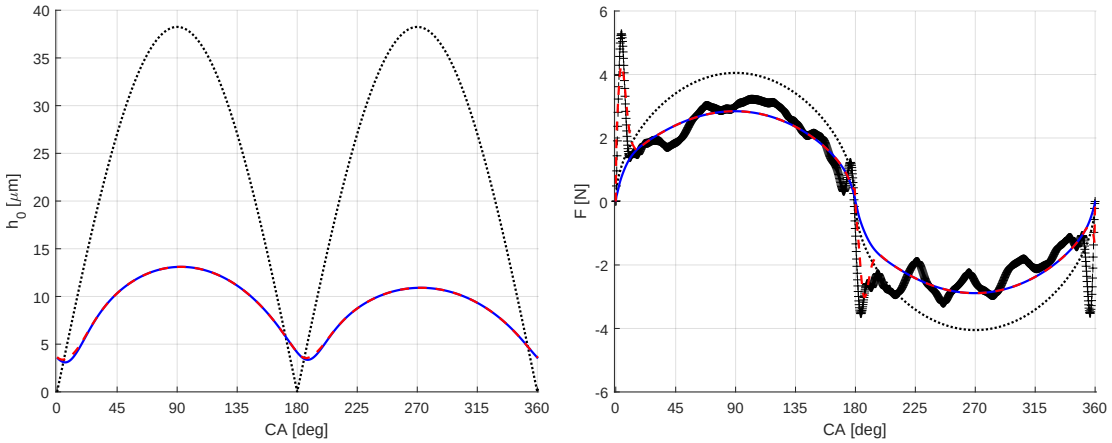

(c) h_0 - 4000 RPM

(d) f - 4000 RPM

Figure 5.13: Friction prediction vs. experimental results for an uncoated configuration and different "load-distance" data multiplication factors (blue solid line: predictions for a 12.5 multiplication factor - red dotted liner: prediction for a higher multiplication factor - dotted black line: Moes & Venner solution - plus signs: experimental friction).

Consequently, with the current mixed lubrication model accounting for only the micro-geometry it is impossible to accurately reproduce the experimental operating conditions and results because of the ring and liner macro-geometry / distortion. Therefore, the model has to be first upgraded in order to account for the non uniform loading of the ring by using for example a curve beam finite element model as developed by Baelden and Tian [140, 141].

However, by assuming the ring geometry, the operating conditions, the contact

mechanics data and the ring-liner conformability identical, the only difference between the DLC coated and uncoated contact is the lower boundary friction coefficient provided by the DLC film. Thereby, the DLC benefits are easily predictable and thus to some extend, the code can be used to estimate the DLC coating benefit in reducing the power loss for a full engine cycle. Nevertheless, it is also possible to use the time-dependent, mixed lubrication model in order to predict the best ring parameters to minimise the power losses. The following section presents some examples of this possibility.

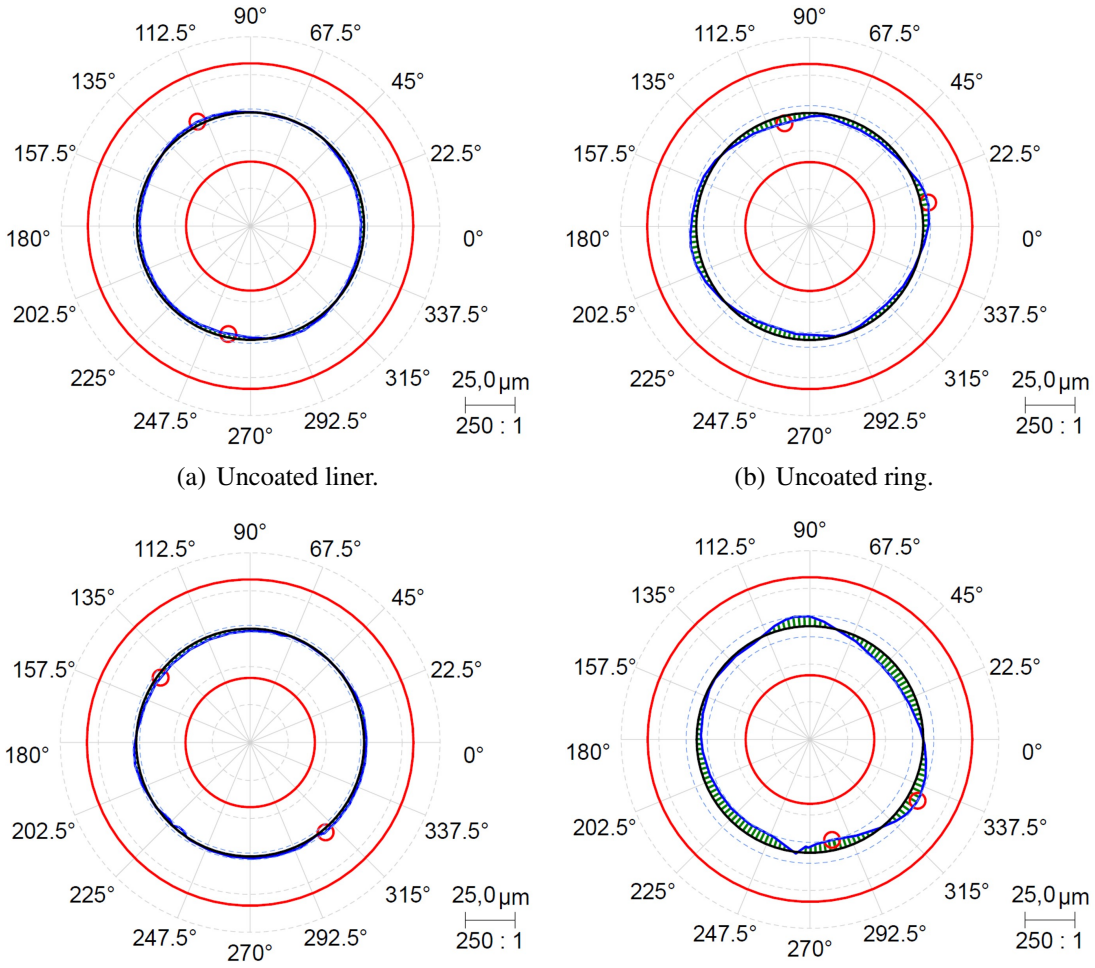

(a) Uncoated liner.

(b) Uncoated ring.

(c) DLC coated liner.

(d) DLC coated ring.

Figure 5.14: Out of roundness measurement.

5.4 Compression Ring Friction Optimisation: an Example

In this section, the developed mixed lubrication model is used in order to predict the optimised compression ring parameters to minimise the contact power losses. Two main ring parameters are studied, the ring profile radius of curvature and the ring face width. The operating conditions, ring load, "pressure-distance" data and multiplication factor are based on the previously fitted uncoated PRCL contact in Section 5.3 and the engine speed is set to 1000 RPM. The boundary friction coefficient is set to $\mu_{bound} = 0.18$ for the uncoated configuration and to $\mu_{bound} = 0.16$ for the DLC coated contact according to the ball on plate friction measurements. The ring profile is defined as a symmetrical parabola using Equation 5.2 with $x_s = 0$ and $h_{side} = 5$ mm. In order to predict the friction reduction for realistic operating conditions, the in-cylinder combustion gas pressure is added to the original ring load using Equation 2.4 in Chapter 2. Figure 5.15 gives P_{gas} as a function of the crankshaft angle, measured on the AVL single-cylinder floating liner engine for a 100°C, a 6 bar BMEP and a 1000 RPM engine speed. For each tribo-pair (DLC coated and uncoated), the PRCL contact FMEP is computed on a full engine cycle (intake, compression, combustion and exhaust strokes) according to:

$$FMEP = \frac{\int_{-360}^{360} P_w \, \mathrm{d}CA}{2 V_d \, \Omega} \tag{5.3}$$

The ring parameter is optimised when the FMEP reaches a minimum. Wear and oil consumptions are outside of the scope of this study. The results presented in this section can be seen as a demonstration of the model possibilities.

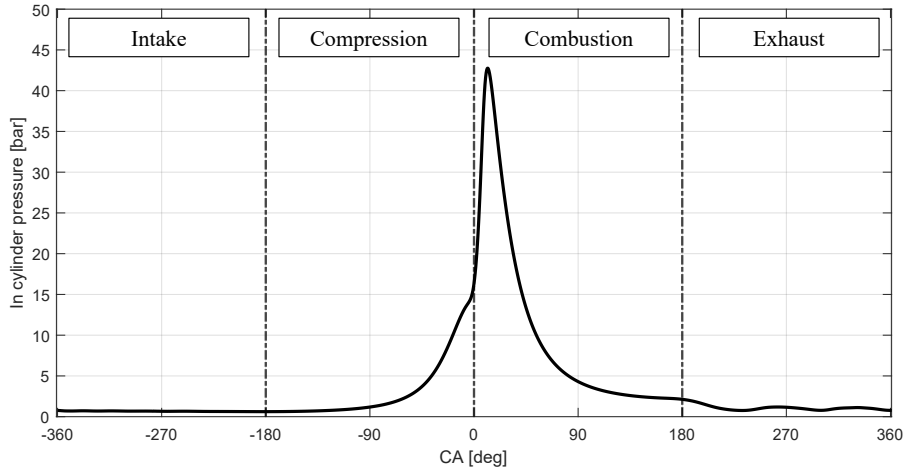

Figure 5.15: In-cylinder combustion gas pressure measured in the AVL single-cylinder floating liner engine for a 100°C, a 6 bar BMEP and a 1000 RPM engine speed.

5.4.1 Ring Radius

This section presents the ring radius optimisation for a finite, 2 mm wide, symmetrical, parabolic ring profile. Figure 5.16 gives the predicted FMEP for a variety of ring radii r from 1 mm to 1 m, with (a) and without (b) combustion and for both boundary friction coefficients ($\mu_{bound} = 0.18$ in black and $\mu_{bound} = 0.16$ in blue). Please note that the horizontal scale is not linear for readability issues as well, the vertical scale in Figure 5.16(b) is three times larger than the vertical scale in Figure 5.16(a).

In Figure 5.16, both FMEP curves have a shape similar to the Stribeck curve. By analogy with the Stribeck curve, the contact shows boundary to mixed lubrication for small ring radius values and exhibit full-film lubrication regime for large ring radius values. Taking into account the combustion pressure acting on the back of the ring, the FMEP curves in Figure 5.16(b) present a longer transition to the full-film lubrication regime according to increasing radius values. Both FMEP results in Figure 5.16 display a minimum but not for the same radius of curvature. Without combustion, the FMEP minimum value 0.52 kPa is obtained for a ring radius $r = 40$ mm as with combustion, the FMEP minimum value equals to 1.29 kPa is predicted for a ring radius five time larger, $r = 200$ mm. However, both minima are obtained at the transition between the mixed to full-film lubrication regime.

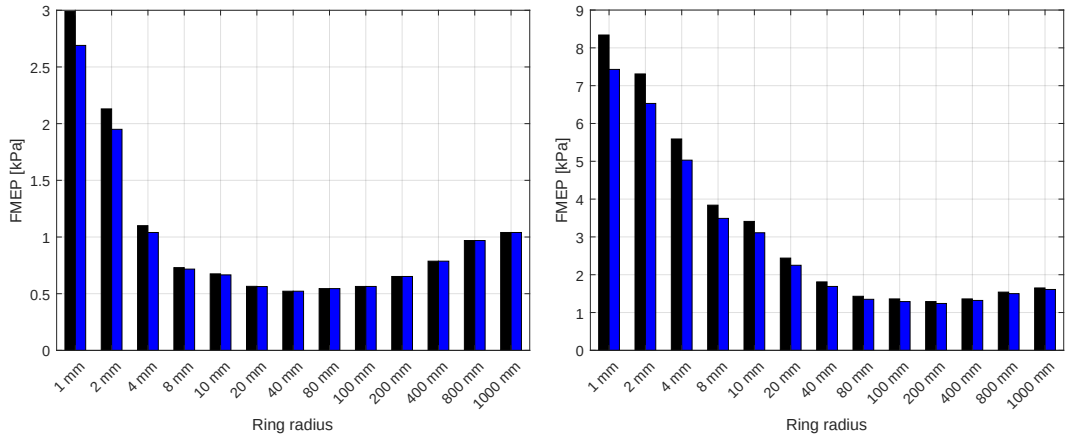

(a) Without P_{gas}. (b) With P_{gas}.

Figure 5.16: Predicted FMEP aver a full engine cycle as a function of the ring radius.

Figure 5.18 gives an insight of the predicted friction forces and power losses, with combustion pressure and for three ring radii: 1 mm (black), 200 mm (the optimum - red) and 1 m (blue). In Figure 5.18(a), the black curve ($r = 1$ mm) friction prediction is high all along the four strokes and exhibits the highest friction force during the combustion (≈ 200 N). Figure 5.17(a) presents the mean minimum film thickness (computed on an engine cycle) as a function of the ring radius. Small ring radii ($r < 10$ mm) lead to a thin film thickness and thus to a higher proportion of solid-to-solid contact and friction.

Figure 5.17(b) shows the proportion of FMEP generated by the viscous or asperity friction, for small ring radii, high FMEP is mainly induced by the solid-to-solid contact.

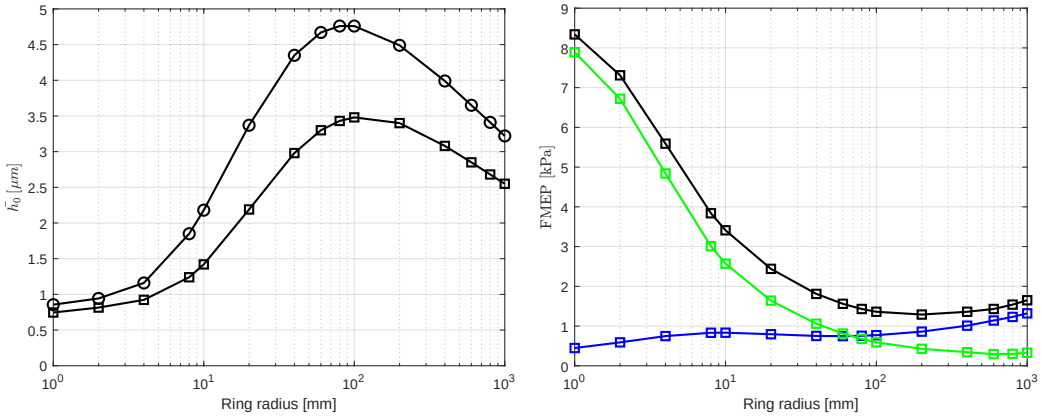

(a) Mean minimum film thickness (circles: without combustion - squares: with combustion)

(b) Viscous (blue), asperity (green) and total (black) FMEP with combustion

Figure 5.17: Piston ring radius optimisation.

In Figure 5.18 the difference in friction/power between the blue curve ($r = 200$ mm) and the red curve ($r = 1$ m) is more subtle. Even if the red curve presents a higher friction and power loss at the combustion, it generates all along the four strokes a lower viscous friction due to a thicker film thickness as shown in Figure 5.17(a). On the opposite, the blue curve presents a higher viscous friction and power loss along the strokes because of a thinner film thickness due to the geometrical starvation which is prevailing for larger ring radii ($r > 100$ mm) as demonstrated by Biboulet et al. [57]. Therefore, to minimise the FMEP value one aims for the thickest film thickness resulting in a lower viscous and asperity friction as provided by the ring radius $r = 200$ mm. In other words, the red curve present the best viscous to asperity power loss balance over the four strokes. However, it is noticeable that large ring radii (i.e. "flatter" rings) provide a greater oil film thickness when the squeeze motion is dominant (i.e. at the dead-centres) as shown by Taylor [67]. In this study this results in a lower proportion of solid-to-solid contact during the combustion process.

Ring radius r [mm]	1	4	10	20	40	100	400	1000
Without P_{gas} [%]	10.0	4.8	1.3	0.4	0.0	0.0	0.0	0.0
With P_{gas} [%]	11.0	10.0	8.8	7.8	6.8	5.0	2.9	2.3

Table 5.8: FMEP reduction due to the DLC coating.

Table 5.8 presents the DLC coating benefit by comparing the predicted FMEPs for the DLC coated and uncoated configurations. The highest benefit (11 %) is observed

for small radius values corresponding to the case with a maximum of boundary to mixed lubrication friction. This value is consistent with the difference between the two boundary friction coefficients. The DLC coating benefit is decreasing with increasing ring radii as the contact moves from the mixed to full-film lubrication and thus no more contact occurs. Without combustion, for ring radii larger than $r = 20$ mm the DLC coating exhibits no more FMEP reduction. Taking into account the combustion pressure in the calculation, a 2 % to 5 % FMEP reduction is observed with the DLC coating that helps to reduce the power losses during the combustion.

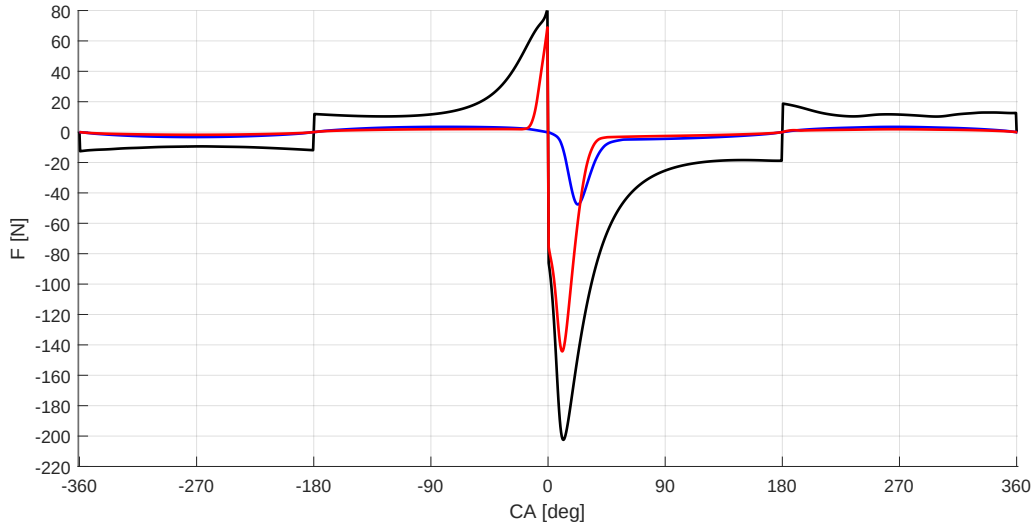

(a) Friction force - f

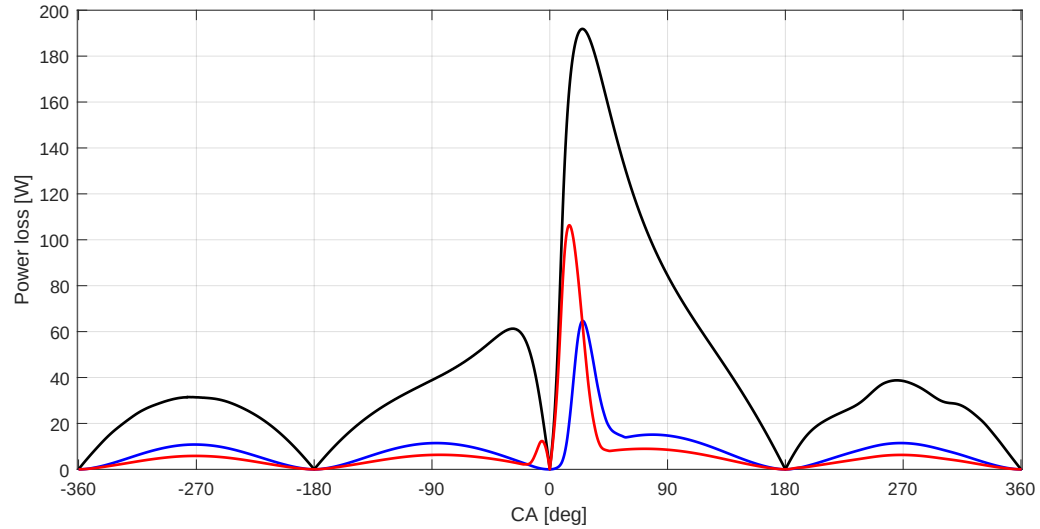

(b) Power loss - P

Figure 5.18: Predicted friction force and power loss accounting for the combustion pressure for three ring radii: 1 mm in black, 200 mm in red and 1 m in blue.

5.4.2 Ring Width

Similarly to the previous section, the ring width is optimised for a finite, symmetrical, parabolic ring profile with a radius of curvature $r = 50$ mm. Figure 5.19 regroups the predicted FMEP for a variety of ring width ℓ from 0.25 mm to 12 mm, with (a) and without (b) combustion and for both boundary friction coefficients ($\mu_{bound} = 0.18$ in black and $\mu_{bound} = 0.16$ in blue). Please note that the horizontal scale is not linear for readability issues as well, the vertical scale in Figure 5.19(b) is 4 times larger than the vertical scale in Figure 5.19(a).

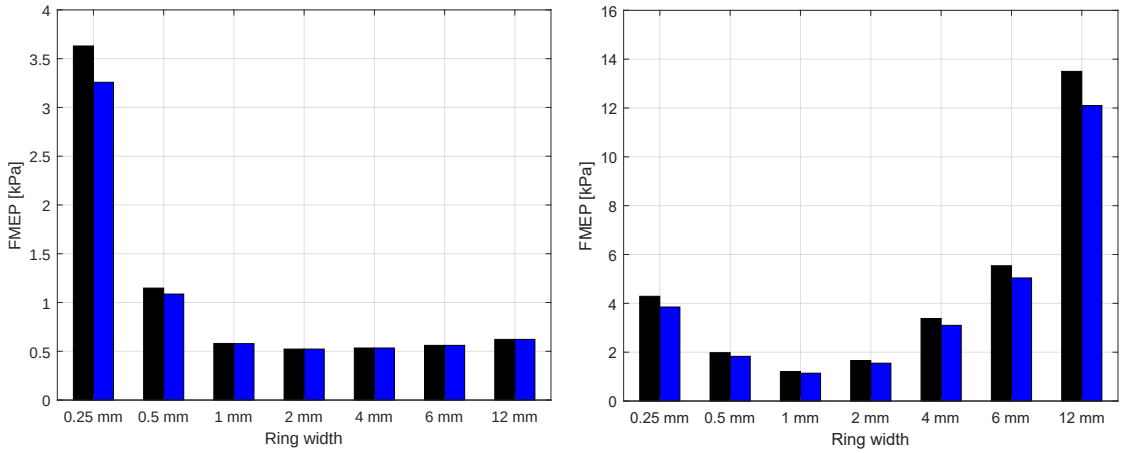

(a) Without P_{gas}.

(b) With P_{gas}.

Figure 5.19: Predicted FMEP over a full engine cycle as a function of the ring width.

In the same way as in Figure 5.16, the curves in Figure 5.19 have a shape similar to the Stribeck curve. Generally, for thin rings a high FMEP value is estimated while for large rings a substantially lower FMEP value is predicted. However, taking into account the combustion pressure in the calculations leads to an exponential increase of the FMEP prediction for increasing ring widths which is atypical. A minimum FMEP value of 0.52 kPa is reached for $\ell = 2$ mm without combustion as with combustion the minimum FMEP value of 1.21 kPa is obtained for $\ell = 1$ mm.

Figure 5.20 gives an insight of the predicted friction forces and power losses taking into account the combustion pressure and for three different ring widths: 0.25 mm (black), 1 mm (the optimum - red) and 2 mm (blue).
In Figure 5.20(a), ignoring the combustion stroke, the black curve ($\ell = 0.25$ mm) presents a high friction compared to the other curves. This is because for a small ℓ the ring experiences huge geometrical starvation and the hydrodynamic pressure generating zone is limited to the small ring width. As a consequence, the generated oil film is thin and the contact is mainly in the mixed to boundary lubrication regime. On the opposite, the blue and red curves are relatively similar and exhibit a low friction force along the strokes. The red curve ($\ell = 1$ mm) shows a bit more solid friction at the dead-centres

compared to the blue curve ($\ell = 2$ mm).
During the combustion, the three curves are inverted for the friction forces as well as for the power losses. The blue curve ($\ell = 2$ mm) which exhibits the lowest friction outside of the combustion stroke, presents during the combustion the highest friction spike and power loss. On the opposite, roughly no additional friction and power loss is predicted for the black curve ($\ell = 0.25$ mm). As the combustion pressure acts on the back of the ring, pushing it harder against the liner, the thicker the ring, the larger the pressure acting area and the higher the resulting contacting load. Therefore, a thicker ring generates more friction during the combustion process because the contact load is larger compared to a thin ring. However, a thin ring experiences more geometrical starvation resulting into a thinner film thickness and thus a high proportion of mixed to boundary friction. In this way, the red curve ($\ell = 1$ mm) shows an excellent viscous to asperity friction balance and results in the lowest FMEP value.

Ring width ℓ [mm]	0.25	0.5	1	2	4	6	12
Without P_{gas} [%]	10.2	5.3	0.4	0.0	0.0	0.0	0.0
With P_{gas} [%]	10.4	7.7	5.1	6.4	8.2	9.1	10.2

Table 5.9: FMEP reduction due to the DLC coating.

Table 5.9 presents the DLC coating benefit by comparing the predicted FMEPs for the DLC coated and uncoated configurations. Similarly as for the ring radius analysis, the highest benefits (10 %) are observed when the contact is mostly in the mixed to boundary lubrication regime, thus for thin rings or for thick rings with combustion pressure. Considering the optimum ring width $\ell = 1$ mm, a 5 % reduction in FMEP can be achieved by depositing a DLC coating on both the ring and the liner.

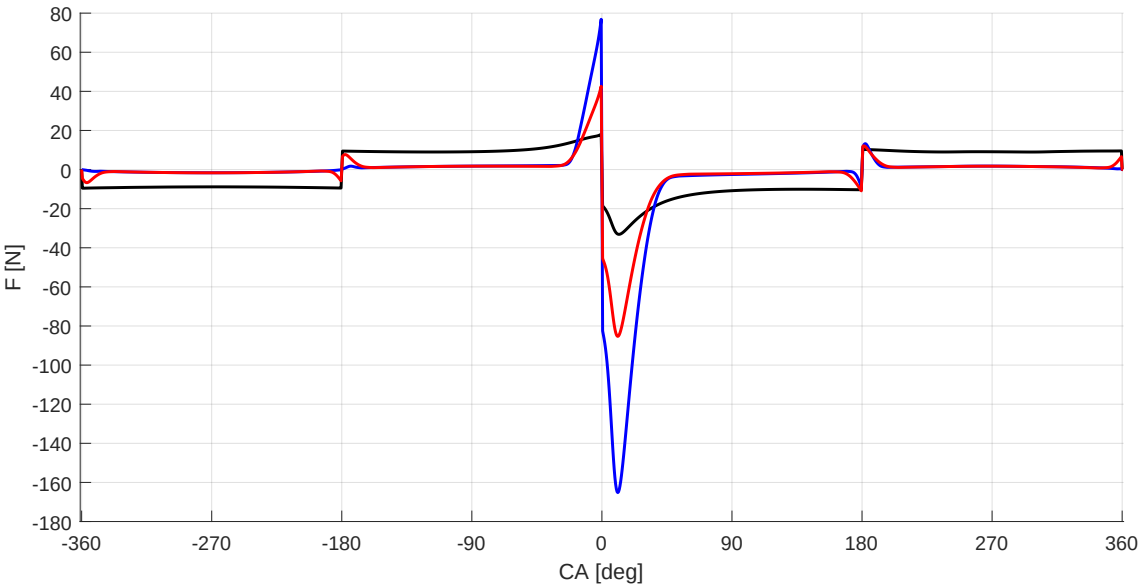

(a) Friction force

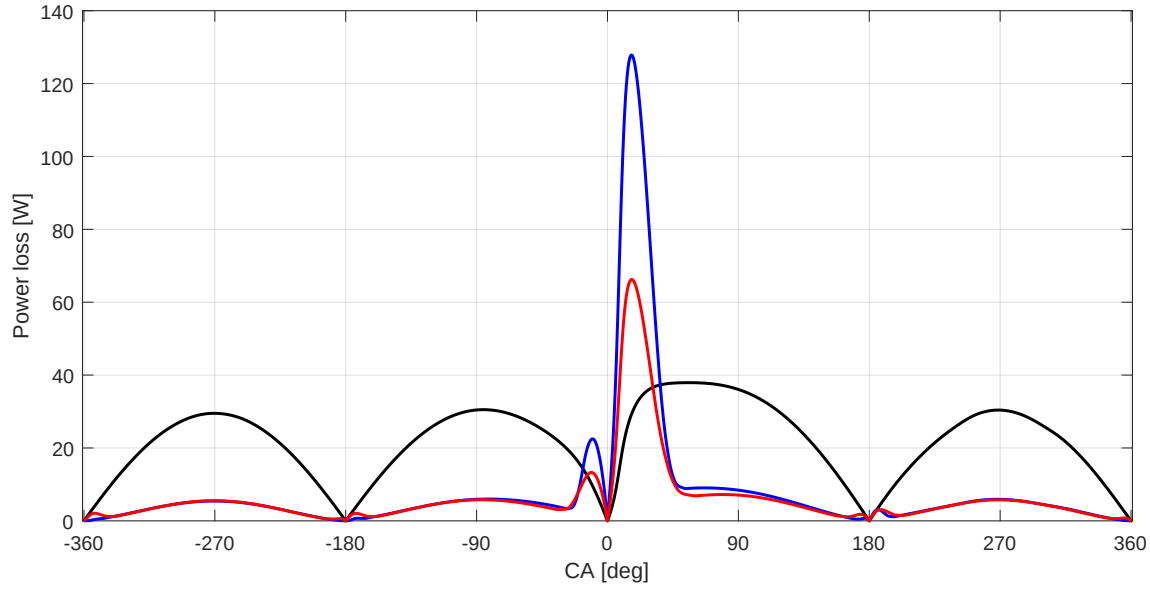

(b) Power loss

Figure 5.20: Predicted friction force and power loss accounting for the combustion pressure for three ring width: 0.25 mm in black, 1 mm in red and 2 mm in blue.

5.4.3 Discussion

Using the newly developed time-dependent, mixed lubrication model, optimum ring parameters such as the radius and face width have been identified. On average, a 50% reduction in FMEP can be achieved (up to 70% for the optimum ring width) by selecting the most favourable ring geometrical parameters. Furthermore, the deposition of a DLC coating on both the ring and the liner surfaces (generating a lower boundary friction coefficient) leads to an additional 2% to 5% reduction in the FMEP value.
The ring geometrical parameters have a direct influence on the film thickness generation and thus on the viscous and asperity friction. Therefore, optimising these parameters offers a large gain because a perfect balance between the two friction sources can be achieved. On the opposite and according to the steel and DLC liner similar surface finish, the DLC coating exhibits a reduction in friction losses only when solid-to-solid contact occurs. It is thus mainly beneficial at the dead-centres and during the combustion phase. It is notable that the minimum FMEP value is systematically reached at the transition between the mixed and full-film lubrication regime.
In practice, the DLC coating benefits should be compared to the tribological performances of a standard honed Gray Cast Iron liner. Thereby, the change in roughness and the smoothing of the texture may have a greater influence on the PRCL lubrication than the DLC coating benefits observed in the previous study. This comparison can be achieved by using as input of the model the pressure-distance data of a standard cross-hatch textured liner. However, the influence of the texture on the rings hydrodynamic LCC would not be considered.

Nevertheless, this study is no more than an overview of the code possibilities and many more calculations are needed in order to define the ring optimum parameters. For this purpose, the previous study has to be extended to a variety of engine speeds, combustion pressures, oil temperatures and for a complete ring pack in order to define the most favourable ring parameters for operating conditions representative of a real engine. With this in mind and according to the code relative simplicity, the code extension to predict the friction of a complete ring pack with a varying oil viscosity along the stroke seems to be easy to implement. Nevertheless, the current version of the line-contact model, assuming no macro-geometry of the samples, does not provide a correct prediction of the boundary to mixed lubrication friction (see Section 5.3). An analytical solution such as implemented in Chapter 4 or an extended 2D model has to be developed in order to account for the macro-geometry influence on the ring load carrying capacity. These improvements have to be implemented before carrying out further optimisation studies.

Furthermore, this study only focuses on the compression ring friction and power loss reduction, without taking into account the oil consumptions and the tribo-pair wear, which are also directly linked to the contact minimum film thickness. These topics may also be considered as future improvements of the code.

5.5 Conclusion

In this chapter the tribological performance of a DLC coating compression ring is experimentally and numerically investigated. Also, the efficiency of both methods is analysed.

According to the experimental results, the DLC coating exhibit a friction reduction in the mixed to boundary lubrication regime because of its lower boundary friction coefficient. Thereby, the DLC coated ring-liner configuration presents a 10% to 30% friction reduction at the dead-centres compared to an uncoated contact. In the full-film lubrication regime, occurring along more than 50% of the stroke, the DLC coating shows no friction reduction and the observed differences are related to a geometrical dissimilarity between the tested rings. For a complete engine cycle, a 5% reduction in the FMEP is observed for the DLC coated configuration. In addition, the DLC film shows an excellent protective capacity as roughly no wear is observed on the ring and liner compared to the uncoated samples. However, in view of the substantial differences between the coated and uncoated samples (ring geometry and ring/liner out of roundness) it is necessary to repeat these measurements with more samples in order to confirm, or not, the observed trends.

Numerically, the measured ring face geometry, ring and liner topographies as well as the test-rig operating conditions are implemented in the code. Once more, the code results compared to the friction measurements show that the sample macro-geometry, here the ring and liner out of roundness, has a huge influence on the contact lubrication. Indeed, no solid-to-solid friction is predicted and an artificially amplified roughness has to be implemented in order to fit the measurements. It appears that, similar to the roller on plate case, the ring/liner distortion leads to an heterogeneous loading that cannot be accurately predicted using a 1D model and a unique “small” micro-geometry topography measurement. Nevertheless, it is demonstrated that, once the model parameters are tuned to obtain a good prediction/measurement fit, the new code allows for a rapid evaluation of optimised ring parameters to minimise friction. As a result, a 50% friction reduction can be achieved by selecting the most favourable ring radius and width. According to the model simplicity and rapidity, this strategy can be extended to other contact parameters and operating conditions.

Chapter 6

Conclusion and Perspective

Contents

6.1 Conclusion

The world's developed countries, forced by the climate emergency and the recent geopolitical issues, are slowly exiting the fossil-fuel era and are seeking for more sustainable energies. The automotive industry is mainly relying on the electrical technology to deal with the local emission limitations. However, today this technology is not mature enough to overcome the worldwide freight transport challenges and Internal Combustion (IC) engines will probably be used for a few more years. Therefore, improving their efficiency, sustainability and reliability is still of main interest. Recently, the use of surface coatings such as Diamond-Like Carbon has become recurrent in order to improve the tribological performance of some IC engine parts. Its application to the Piston-Ring / Cylinder-Liner (PRCL) contact, on both the rings and liner, has not been widely studied yet. Nonetheless, this technical solution seems promising to reduce both the contact wear and friction. Evaluating these benefits is the main objective of this work. Therefore, experimental and numerical methods are developed in order to obtain a deep complementary understanding of the contact.

For the numerical part, a *Matlab* code relying on a semi-analytical, line-contact, mixed lubrication solver is developed. The model hydrodynamic part is based on the integration of the iso-viscous rigid Reynolds equation and on two inlet/outlet mass-conserving equations. The model asperity part is based on a so called "load-distance" curve describing the dry gap between the deformed roughness for a given load range. Contrary to stochastic theories, this method relies on deterministic contact mechanics results using measured surface topographies. In the end, a relatively simple and fast

solver for the time-dependent, mixed line-contact is presented. It accounts for oil starvation (geometrical or by lack of lubricant), oil transport as well as measured surface topographies. The main limitations of this numerical method being the need of specific tools for both the measurement and the contact mechanics calculation of the surface roughness.
Using a fully numerical P-Θ solution, the hydrodynamic results of the new code were validated. In addition, roller on plate friction measurements were performed in order to test the mixed model reliability. Comparison with the friction measurement have shown that the roller macro-geometry/undulation has a non-negligible influence on the contact lubrication and should be taken into account. This task is achieved by implementing analytical correction coefficients evaluated using the Reynolds equation dimensionless analysis and the deformed roller macro-geometry. Finally, the extended model predictions are in good agreement with the measurements and accurate prediction of geometrical starvation as well as solid-to-solid friction is obtained. Nevertheless, these predictions were performed using the computed deformed roller geometry which requires the entire contact surface topography measurement as well as a high performance numerical contact mechanics tool.

For the experimental part, a floating liner PRCL test-rig is improved. It allows the testing of real engine pistons and piston-rings, the liner is not standard and is machined to the required specifications. The piston motion is driven by an electric motor and lubrication conditions are typical of a car engine. It is designed to study the PRCL contact friction and wear for a variety of operating conditions (speed, load, viscosity, geometry, ...) but without combustion in order to offer a first and relatively easy understanding of the contact lubrication. However, as many existing floating-liner rigs, it presents a significant vibrational instability which highly pollutes the signal. A vibrational investigation using both vibration measurements and modal numerical simulation is performed. Thereby, the rig liner-holder flexibility is identified as being the main cause. Solutions to rigidify this part are proposed and a dynamic balance of the rig will be performed in the near-future. In addition, a strategy to mimic high speed / low viscosity operating conditions using low speed / high viscosity parameters is introduced by means of the theoretical Reynolds equation analysis. This strategy provides the opportunity to use the PRCL test-rig mimicking typical engine speeds.

Using both the developed experimental and numerical methods, the tribological performance of a DLC coated compression ring against a mirror-like DLC coated liner is investigated. Thereby, the efficiency and relevance of each method is questioned.
Experimentally, the DLC coating exhibits a friction reduction in the mixed to boundary lubrication regime, when solid-to-solid contact occurs, because of its lower boundary friction coefficient. Compared to an uncoated mirror-like contact, the DLC presents a 10% to 30% friction reduction at the dead-centres which leads to a 5% reduction in FMEP over a full engine cycle. In addition, the DLC coating has shown an excellent protective capacity as roughly no wear is observed on both the ring and liner. However,

regarding the sample differences (ring geometry and ring/liner distortion) it is necessary to repeat these tests for several ring/liner specimens in order to confirm, or not, the observed trends.
Numerically, the friction prediction/measurement comparison shows that the sample macro-geometry, here the ring/liner distortion, has a huge influence on the contact lubrication. However, regarding the ring/liner distortion complexity it is impossible to analytically extend the model as it is performed for the roller on plate configuration. Nevertheless, by tuning the model parameters to fit the friction measurements, one can use the developed code to perform an optimisation of the ring. As an example, the ring optimum radius and width are computed in order to minimise the friction losses. A FMEP reduction up to 50% can be achieved by selecting the most favourable ring geometries. Taking advantage of the model simplicity and rapidity, this strategy can be extended to other contact parameters and operating conditions.

In order to evaluate tribological benefits of the DLC coating only, this work compares the friction losses of a DLC coated PRCL contact to an uncoated configuration with a similar surface finish (mirror-like). In practice, the mirror-like DLC coated solution will replace a typical grey cast iron liner with a cross-hatched honing texture. According to the change in roughness and texture, the DLC coating benefits might be greater.

Generally, it was shown that the DLC coating (here an a-C:H) applied to all parts of the PRCL contact, may lead to a substantial reduction in friction when solid-to-solid contact occurs, especially during the combustion phase. An FMEP reduction up to 5% has been observed which may lead to a substantial reduction in the engine energy consumption. Moreover, the DLC coating has shown very good protective capabilities for a variety of lubricants. This improvement in the contact reliability may permit an increase in the combustion pressure as well as a global reduction of the contact film thickness i.e. reduction in viscous losses leading to more efficient engines. In the end, the DLC compatibility with water (low friction and wear) makes it a promising solution for hydrogen fuelled IC engines.

6.2 Perspective

In this study, experimental and numerical methods are developed in order to analyse the DLC coated PRCL lubrication. Nevertheless, both methods can be improved. This section lists some possible future work based on the previous conclusions, it is a non-exhaustive list.

First, the model can be extended to a complete ring pack friction prediction. Therefore, all equations have to be evaluated for each ring geometry. Also, each ring should see the amount of oil left on the liner by the preceding ring. Consequently, a blow-by model could be implemented. It will have an influence on each ring load as well as on

the hydrodynamic pressure boundary conditions. Moreover, an efficient way to account for the ring/liner distortion should be investigated. A solution would be to compute the ring/liner conformity using an FEM method. From these results, the ring could be divided into several parts, all having a specific linear load. Then the current solver could be used to compute each ring part linear friction and the complete ring friction will be averaged. Considering all these upgrades, it would then be interesting to reproduce the Section 5.4 optimisation for a full scope of engine operating conditions.

Secondly, further improvements on the floating-liner test-rig signal to noise ratio have to be made. Therefore, the liner-holder has to be redesigned to be stiffer. Furthermore, a dynamic balancing of the rig has to be carried out. Consequently, the measurements performed in Section 5.2 have to be repeated for several rings in order to reduce the measurement uncertainty. Then, the experimental method could be extended to test a complete ring pack. Additionally, the testing of a typical grey cast iron cross-hatched honed liner may provide some interesting results on the DLC benefits.

Finally, the DLC coated PRCL should be tested using a fired engine in order to asses its efficiency and reliability. With the aim of applying this solution to hydrogen fuelled internal combustion engines, it might be interesting to study the DLC coating tribological performance lubricated with an oil/hydrogen-combustion-residue mixture.

Bibliography

[1] H. Ritchie, M. Roser, and P. Rosado, "CO_2 and greenhouse gas emissions," Our World in Data, 2020. https://ourworldindata.org/co2-and-other-greenhouse-gas-emissions.

[2] K. Holmberg, P. Andersson, and A. Erdemir, "Global energy consumption due to friction in passenger cars," Tribology International, vol. 47, pp. 221–234, 2012.

[3] S. C. Tung and M. L. McMillan, "Automotive tribology overview of current advances and challenges for the future," Tribology International, vol. 37, pp. 517–536, 2004.

[4] J. B. Heywood, Internal Combustion Engine Fundamentals. Mechanical Engineering, MC Graw-Hill, 1988.

[5] M.-P. Noutary, A robust Reynolds solver for textured surfaces in the piston ring cylinder liner contact. PhD thesis, Mechanical Engineering, INSA-Lyon, Lyon, France, 2017.

[6] J. Robertson, "Diamond-like amorphous carbon," Materials Science and Engineering: R: Reports, vol. 37, no. 4, pp. 129–281, 2002.

[7] D. Dowson, "Piston assemblies; background and lubrication analysis," in Engine Tribology (C. M. Taylor, ed.), no. 26 in Tribology series, pp. 213–240, Elsevier, 1993.

[8] B. Persson, "Contact mechanics for randomly rough surfaces," Surface Science Reports, vol. 61, pp. 201–227, 2006.

[9] N. Biboulet and A. A. Lubrecht, "Semi-analytical prediction of starved line contacts considering oil transport," Tribology Letters, vol. 70, 2022.

[10] P. Sainsot and A. A. Lubrecht, "Efficient solution of the dry contact of rough surfaces: a comparison of fast fourier transform and multigrid methods," Proceedings of the Institution of Mechanical Engineers, Part J: Journal of Engineering Tribology, vol. 225, no. 6, pp. 441–448, 2011.

[11] H. Ronkainen and K. Holmberg, "Environmental and thermal effects on the tribological performance of DLC coatings," in Tribology of Diamond-Like Carbon Films: Fundamentals and Applications (C. Donnet and A. Erdemir, eds.), pp. 155–200, Springer US, 2008.

[12] L. Wang-Erlandsson, A. Tobian, R. J. van der Ent, and et al., "A planetary boundary for green water," Nature Reviews Earth & Environment, vol. 3, pp. 380–392, 2022.

[13] L. Persson, B. M. C. Almroth, C. D. Collins, and et al., "Outside the safe operating space of the planetary boundary for novel entities," Environmental Science & Technology, vol. 56, no. 3, pp. 1510–1521, 2022.

[14] J. Rockström, W. Steffen, K. Noone, and et al., "Planetary boundaries: Exploring the safe operating space for humanity," Ecology and Society, vol. 14, no. 2, 2009.

[15] W. Steffen, K. Richardson, J. Rockström, and et al., "Planetary boundaries: Guiding human development on a changing planet," Science, vol. 347, no. 6223, 2015.

[16] J. Rockström, W. Steffen, K. Noone, and et al., "A safe operating space for humanity," Nature, vol. 461, pp. 472–475, 2009.

[17] H. O. Pörtner, D. C. Roberts, M. Tignor, and et al., "IPCC, 2022: Climate change 2022: Impacts, adaptation, and vulnerability. contribution of working group II to the sixth assessment report of the intergovernmental panel on climate change," tech. rep., Cambridge University Press, 2022.

[18] C. W. Team, R. K. Pachauri, and L. A. Meyer, "IPCC, 2014: Climate change 2014: Synthesis report. contribution of working groups I, II and III to the fifth assessment report of the intergovernmental panel on climate change," tech. rep., IPCC, Geneva, Switzerland, 2014.

[19] P. Friedlingstein, M. W. Jones, M. O'Sullivan, and et al., "Global carbon budget 2021," Earth System Science Data, vol. 14, no. 4, pp. 1917–2005, 2022.

[20] R. Andrew and G. Peters, "The global carbon project's fossil CO2 emissions dataset," figshare, 2021. preprint.

[21] IEA, "Global EV Outlook 2020," tech. rep., IEA, Paris, 2020. https://www.iea.org/reports/global-ev-outlook-2020.

[22] H. Ritchie, M. Roser, and P. Rosado, "Energy," Our World in Data, 2020. https://ourworldindata.org/energy.

[23] C. Taylor, Engine Tribology. No. 26 in Tribology Series, Elsevier, 1993.

[24] E. Willis, "Surface finish in relation to cylinder liners," Wear, vol. 109, no. 1, pp. 351–366, 1986.

[25] H. Bouassida, Lubricated piston ring cylinder liner contact: Influence of the liner microgeometry. PhD thesis, Mechanical Engineering, INSA-Lyon, Lyon, France, 2014.

[26] W. Ma, N. Biboulet, and A. Lubrecht, "Cross-hatched groove influence on the load carrying capacity of parallel surfaces with random roughness," Tribology International, vol. 153, 2021.

[27] E. Tomanik, F. Profito, B. Sheets, and R. Souza, "Combined lubricant-surface system approach for potential passenger car CO_2 reduction on piston-ring-cylinder bore assembly," Tribology International, vol. 149, 2020.

[28] B. L. Ruddy, D. Dowson, and P. N. Economou, "A review of studies of piston ring lubrication," in Proceedings of 9th Leeds-Lyon symposium on tribology, pp. 109–121, 1982.

[29] C. Donnet and A. Erdemir, Tribology of diamond-like carbon films: fundamentals and applications. Springer Science & Business Media, 2007.

[30] T. Kruelle, F. Kaulfuss, V. Weihnacht, F. Hofmann, and F. Kirsten, "Amorphous carbon coatings with different metal and nonmetal dopants: Influence of cathode modification on laser-arc evaporation and film deposition," Coatings, vol. 12, no. 2, 2022.

[31] M. Kano, "Diamond-like carbon coating applied to automotive engine components," Tribology Online, vol. 9, no. 3, pp. 135–142, 2014.

[32] O. Sato, M. Takiguchi, A. Takayuki, Y. Seki, K. Fujimura, and Y. Tateishi, "Improvement of piston lubrication in a diesel engine by means of cylinder surface roughness," in SAE 2004 World Congress & Exhibition, SAE International, 2004.

[33] E. D. Rejowski, P. Mordente Sr, M. F. Pillis, and T. Casserly, "Application of DLC coating in cylinder liners for friction reduction," in SAE 2012 World Congress & Exhibition, p. 11, 2012.

[34] W. Koszela, P. Pawlus, R. Reizer, and T. Liskiewicz, "The combined effect of surface texturing and DLC coating on the functional properties of internal combustion engines," Tribology International, vol. 127, pp. 470–477, 2018.

[35] N. Dolatabadi, M. Forder, N. Morris, R. Rahmani, H. Rahnejat, and S. Howell-Smith, "Influence of advanced cylinder coatings on vehicular fuel economy and emissions in piston compression ring conjunction," Applied Energy, vol. 259, 2020.

[36] H. Christensen, "A theory of mixed lubrication," Proceedings of the Institution of Mechanical Engineers, vol. 186, no. 1, pp. 421–430, 1972.

[37] A. O. Lebeck, J. L. Teale, and R. E. Pierce, "Hydrodynamic lubrication and wear in wavy contacting face seals," Journal of Lubrication Technology, vol. 100, no. 1, pp. 81–90, 1978.

[38] F. Sahlin, R. Larsson, A. Almqvist, P. M. Lugt, and P. Marklund, "A mixed lubrication model incorporating measured surface topography. part 1: Theory of flow factors," Proceedings of the Institution of Mechanical Engineers, Part J: Journal of Engineering Tribology, vol. 224, no. 4, pp. 335–351, 2010.

[39] F. Sahlin, R. Larsson, P. Marklund, A. Almqvist, and P. M. Lugt, "A mixed lubrication model incorporating measured surface topography. part 2: Roughness treatment, model validation, and simulation," Proceedings of the Institution of Mechanical Engineers, Part J: Journal of Engineering Tribology, vol. 224, no. 4, pp. 353–365, 2010.

[40] M. Söderfjäll, A. Almqvist, and R. Larsson, "A model for twin land oil control rings," Tribology International, vol. 95, pp. 475–482, 2016.

[41] K. S. Bastidas Moncayo, Experimental and analytical study of the mechanical friction losses in the piston-cylinder liner tribological pair in internal combustion engines (ICE). PhD thesis, Mechanical and Internal Combustion Engine department, Universitat Politècnica de València, València, Spain, 2021.

[42] O. Reynolds, "IV. on the theory of lubrication and its application to Mr. Beauchamp tower's. Experiments, including an experimental determination of the viscosity of olive oil," Philosophical Transactions of the Royal Society of London, vol. 177, pp. 157–234, 1886.

[43] A. A. Lubrecht, "An introduction to elastohydrodynamic lubrication," lecture notes, INSA de Lyon, France, 2018-2019 edition.

[44] R. A. Castelman, "A hydrodynamical theory of piston ring lubrication," Physics, vol. 7, no. 9, 1936.

[45] S. Furuhama, "A dynamic theory of piston-ring lubrication (1st report, calculation)," Bulletin of JSME, vol. 2, no. 7, pp. 423–428, 1959.

[46] D. Dowson, P. N. Economou, B. L. Ruddy, P. J. Strachan, and A. J. S. Baker, "Piston ring lubrication. part II. theoretical analysis of a single ring and a complete ring pack," Energie Conservation through Fluid-Film Lubrication Technology, A.S.M.E, pp. 23–52, 1973.

[47] B. L. Ruddy, D. Dowson, P. N. Economou, and A. J. S. Baker, "Piston-ring lubrication. part III. the influence of ring dynamics and ring twist," Energie Conservation through Fluid-Film Lubrication Technology, A.S.M.E, pp. 191–215, 1979.

[48] J. T. Sawicki and B. Yu, "Analytical solution of piston ring lubrication using mass conserving cavitation algorithm," Tribology Transactions, vol. 43, no. 4, pp. 587–594, 2000.

[49] V. D'Agostino and A. Senatore, "10 - fundamentals of lubrication and friction of piston ring contact," in Tribology and Dynamics of Engine and Powertrain: Fundamentals, applications and future trends (H. Rahnejat, ed.), Mechanical Engineering, pp. 343–386, Woodhead Publishing, 2010.

[50] M. S. M. Perera, S. Theodossiades, and H. Rahnejat, "Elasto-multi-body dynamics of internal combustion engines with tribological conjunctions," Proceedings of the Institution of Mechanical Engineers, Part K: Journal of Multi-body Dynamics, vol. 224, no. 3, pp. 261–277, 2010.

[51] N. Morris, R. Rahmani, H. Rahnejat, P. King, and B. Fitzsimons, "Tribology of piston compression ring conjunction under transient thermal mixed regime of lubrication," Tribology International, vol. 59, pp. 248–258, 2013.

[52] N. Patir and H. S. Cheng, "An average flow model for determining effects of three-dimensional roughness on partial hydrodynamic lubrication," Journal of Lubrication Technology, vol. 100, no. 1, pp. 12–17, 1978.

[53] J. A. Greenwood and J. H. Tripp, "The contact of two nominally flat rough surfaces," Proceedings of the Institution of Mechanical Engineers, vol. 185, no. 1, pp. 625–633, 1970.

[54] N. Morris, R. Rahmani, H. Rahnejat, P. King, and B. Fitzsimons, "Tribology of piston compression ring conjunction under transient thermal mixed regime of lubrication," Tribology International, vol. 59, pp. 248–258, 2013.

[55] M. Gore, R. Rahmani, H. Rahnejat, and P. King, "Assessment of friction from compression ring conjunction of a high-performance internal combustion engine: A combined numerical and experimental study," Proceedings of the Institution of Mechanical Engineers, Part C: Journal of Mechanical Engineering Science, vol. 230, no. 12, pp. 2073–2085, 2016.

[56] N. Biboulet, F. Colin, and A. Lubrecht, "Friction in starved hydrodynamically lubricated line contacts," Tribology International, vol. 58, pp. 1–6, 2013.

[57] N. Biboulet and A. A. Lubrecht, "Geometric starvation of a one-dimensional parabolic profile," Tribology Letters, vol. 61, pp. 1–5, 2016.

[58] N. Biboulet and A. Lubrecht, "Analytical solution for textured piston ring - cylinder liner contacts (1D analysis)," Tribology International, vol. 96, pp. 269–278, 2016.

[59] G. M. Hamilton and S. L. Moore, "Second paper: Comparison between measured and calculated thicknesses of the oil-film lubricating piston rings," Proceedings of the Institution of Mechanical Engineers, vol. 188, no. 1, pp. 262–268, 1974.

[60] G. K. Miltsios, D. J. Patterson, and T. C. Papanastasiou, "Solution of the lubrication problem and calculation of the friction force on the piston rings," Journal of Tribology, vol. 111, no. 4, pp. 635–641, 1989.

[61] M.-T. Ma, I. Sherrington, and E. H. Smith, "Implementation of an algorithm to model the starved lubrication of a piston ring in distorted bores: Prediction of oil flow and onset of gas blow-by," Proceedings of the Institution of Mechanical Engineers, Part J: Journal of Engineering Tribology, vol. 210, no. 1, pp. 29–44, 1996.

[62] A. Paydas and E. H. Smith, "A flow-continuity approach to the analysis of hydrodynamic journal bearings," Proceedings of the Institution of Mechanical Engineers, Part C: Mechanical Engineering Science, vol. 206, no. 1, pp. 57–69, 1992.

[63] H. G. Elrod, "A cavitation algorithm," Journal of Lubrication Technology, vol. 103, no. 3, pp. 350–354, 1981.

[64] K. Liu, Y. B. Xie, and C. L. Gui, "Two-dimensional lubrication study of the piston ring pack," Proceedings of the Institution of Mechanical Engineers, Part J: Journal of Engineering Tribology, vol. 212, no. 3, pp. 215–220, 1998.

[65] L. Liu and T. Tian, "Implementation and improvements of a flow continuity algorithm in modeling ring/liner lubrication," SAE Technical Paper, 2005.

[66] K. Wannatong, S. Chanchaona, and S. Sanitjai, "Simulation algorithm for piston ring dynamics," Simulation Modelling Practice and Theory, vol. 16, no. 1, pp. 127–146, 2008.

[67] R. Taylor, "Squeeze film lubrication in piston rings and reciprocating contacts," Proceedings of the Institution of Mechanical Engineers, Part J: Journal of Engineering Tribology, vol. 229, no. 8, pp. 977–988, 2015.

[68] N. Patir and H. S. Cheng, "Application of average flow model to lubrication between rough sliding surfaces," Journal of Lubrication Technology, vol. 101, no. 2, pp. 220–229, 1979.

[69] M.-P. Noutary, N. Biboulet, and A. Lubrecht, "A robust piston ring lubrication solver: Influence of liner groove shape, depth and density," Tribology International, vol. 100, pp. 35–40, 2016.

[70] R. E. Alcouffe, A. Brandt, J. E. Dendy, Jr., and J. W. Painter, "The multi-grid method for the diffusion equation with strongly discontinuous coefficients," SIAM Journal on Scientific and Statistical Computing, vol. 2, no. 4, pp. 430–454, 1981.

[71] Y. Li, H. Chen, and T. Tian, "A deterministic model for lubricant transport within complex geometry under sliding contact and its application in the interaction between the oil control ring and rough liner in internal combustion engines," in 2008

SAE International Powertrains, Fuels and Lubricants Congress, SAE International, jun 2008.

[72] H. Chen, Y. Li, and T. Tian, "A novel approach to model the lubrication and friction between the twin-land oil control ring and liner with consideration of micro structure of the liner surface finish in internal combustion engines," in 2008 SAE International Powertrains, Fuels and Lubricants Congress, SAE International, jun 2008.

[73] C. H, Modeling the lubrication of the piston ring pack in internal combustion engines using the deterministic method. PhD thesis, PhD Thesis, Mechanical Engineering, Massachusetts Institute of Technology, USA, 2011.

[74] L. Y, Developing an approach utilizing local deterministic analysis to predict the cycle friction of the piston ring-pack in internal combustion engines. PhD thesis, Master Thesis, Mechanical Engineering, Massachusetts Institute of Technology, USA, 2013.

[75] L. Y, Multiphase oil transport at complex micro geometry. PhD thesis, PhD Thesis, Mechanical Engineering, Massachusetts Institute of Technology, USA, 2011.

[76] Y. Liu, D. Kim, Z. Westerfield, Z. Meng, and T. Tian, "A comprehensive study of the effects of honing patterns on twin-land oil control rings friction using both a numerical model and a floating liner engine," Proceedings of the Institution of Mechanical Engineers, Part J: Journal of Engineering Tribology, vol. 233, no. 2, pp. 229–255, 2019.

[77] H. Hertz, "Uber die beruhrung fester elastischer korper (on the contact of elastic solids)," J Reine Angew Math, vol. 92, pp. 156–171, 1882.

[78] J. F. Archard and T. E. Allibone, "Elastic deformation and the laws of friction," Proceedings of the Royal Society of London. Series A. Mathematical and Physical Sciences, vol. 243, no. 1233, pp. 190–205, 1957.

[79] J. A. Greenwood and J. B. P. Williamson, "Contact of nominally flat surfaces," Proceedings of the Royal Society of London. Series A, Mathematical and Physical Sciences, vol. 295, no. 1442, pp. 300–319, 1966.

[80] T. T. A.W. Bush, R.D. Gibson, "The elastic contact of a rough surface," Wear, vol. 35, no. 1, pp. 87–111, 1975.

[81] B. N. J. Persson, "Theory of rubber friction and contact mechanics," The Journal of Chemical Physics, vol. 115, no. 8, pp. 3840–3861, 2001.

[82] B. N. J. Persson, F. Bucher, and B. Chiaia, "Elastic contact between randomly rough surfaces: Comparison of theory with numerical results," Phys. Rev. B, vol. 65, p. 184106, 2002.

[83] A. Fabre, S. Raynaud, and B. Brenier, "Effect of measurement conditions on three-dimensional roughness values, and development of measurement standard," Journal of Physics: Conference Series, vol. 311, no. 1, p. 012008, 2011.

[84] A. Brandt and A. Lubrecht, "Multilevel matrix multiplication and fast solution of integral equations," Journal of Computational Physics, vol. 90, no. 2, pp. 348–370, 1990.

[85] Y. Ju and T. N. Farris, "Spectral analysis of two-dimensional contact problems," Journal of Tribology, vol. 118, no. 2, pp. 320–328, 1996.

[86] H. M. Stanley and T. Kato, "An FFT-based method for rough surface contact," Journal of Tribology, vol. 119, no. 3, pp. 481–485, 1997.

[87] W.-Z. Wang, H. Wang, Y.-C. Liu, Y.-Z. Hu, and D. Zhu, "A comparative study of the methods for calculation of surface elastic deformation," Proceedings of the Institution of Mechanical Engineers, Part J: Journal of Engineering Tribology, vol. 217, no. 2, pp. 145–154, 2003.

[88] L. Frérot, G. Anciaux, V. Rey, S. Pham-Ba, and J.-F. Molinari, "Tamaas: a library for elastic-plastic contact of periodic rough surfaces," Journal of Open Source Software, vol. 5, no. 51, p. 2121, 2020.

[89] S. Yin, G. Costagliola, and J.-F. Molinari, "Investigation of contact clusters between rough surfaces," vol. 70, no. 4, p. 124, 2022.

[90] M. Bigerelle, F. Plouraboue, F. Robache, A. Jourani, and A. Fabre, "Mechanical integrity of 3d rough surfaces during contact," Coatings, vol. 10, no. 1, 2020.

[91] G. Costagliola, T. Brink, J. Richard, C. Leppin, A. Despois, and J.-F. Molinari, "A simple mechanistic model for friction of rough partially lubricated surfaces," vol. 69, no. 3, p. 93, 2021.

[92] G. G.-A. Fatjo, E. H. Smith, and I. Sherrington, "Piston-ring film thickness: Theory and experiment compared," Proceedings of the Institution of Mechanical Engineers, Part J: Journal of Engineering Tribology, vol. 232, no. 5, pp. 550–567, 2018.

[93] P. Carden, D. Bell, M. Priest, and D. Barrell, "Piston assembly friction losses: Comparison of measured and predicted data," SAE Technical Paper, p. 13, 2006.

[94] E. Selmani, C. Delprete, and A. Bisha, "Simulation of the cylinder bore distortion and effect on the sealing capacity of the ringpack," SN Appl. Sci., vol. 1, p. 314, 2019.

[95] G. W. Stachowiak, A. W. Batchelor, and G. B. Stachowiak, "9 - lubricant or process fluid analysis," in Experimental Methods in Tribology (D. Dowson, ed.), vol. 44 of Tribology Series, pp. 221–252, Elsevier, 2004.

[96] H. Schmellenmeier Experimentelle Technik der Physik, vol. 1, p. 49, 1953.

[97] S. Aisenberg and R. Chabot, "Ion-beam deposition of thin films of diamondlike carbon," Journal of Applied Physics, vol. 42, no. 7, pp. 2953–2958, 1971.

[98] A. Erdemir and C. Donnet, "Tribology of diamond-like carbon films: recent progress and future prospects," Journal of Applied Physics, vol. 39, no. 18, pp. 311–327, 2006.

[99] S. Aisenberg, "Properties and applications of diamondlike carbon films," Journal of Vacuum Science & Technology A, vol. 2, no. 2, pp. 369–371, 1984.

[100] M. Kalin, I. Velkavrh, J. Vižintin, and L. Ožbolt, "Review of boundary lubrication mechanisms of DLC coatings used in mechanical applications," Meccanica, vol. 43, no. 6, pp. 623–637, 2008.

[101] M. I. de Barros'Bouchet and J. M. Martin, "New trends in boundary lubrication of DLC coatings," in Tribology of Diamond-Like Carbon Films: Fundamentals and Applications (C. Donnet and A. Erdemir, eds.), pp. 591–619, Springer US, 2008.

[102] M. I. de Barros'Bouchet, J. M. Martin, T. Le-Mogne, and B. Vacher, "Boundary lubrication mechanisms of carbon coatings by MoDTC and ZDDP additives," Tribology International, vol. 38, no. 3, pp. 257–264, 2005.

[103] T. Haque, A. Morina, A. Neville, R. Kapadia, and S. Arrowsmith, "Effect of oil additives on the durability of hydrogenated DLC coating under boundary lubrication conditions," Wear, vol. 266, no. 1, pp. 147–157, 2009.

[104] C. Héau, C. Ould, and P. Maurin-Perrier, "Tribological behaviour analysis of hydrogenated and nonhydrogenated DLC lubricated by oils with and without additives," Lubrication Science, vol. 25, no. 4, pp. 275–285, 2013.

[105] M. Ueda, A. Kadiric, and H. Spikes, "ZDDP tribofilm formation on non-ferrous surfaces," Tribology Online, vol. 15, no. 5, pp. 318–331, 2020.

[106] S. Equey, S. Roos, U. Mueller, R. Hauert, N. D. Spencer, and R. Crockett, "Reactions of zinc-free anti-wear additives in DLC/DLC and steel/steel contacts," Tribology International, vol. 41, no. 11, pp. 1090–1096, 2008.

[107] M. De Feo, M. I. de Barros'Bouchet, C. Minfray, T. Le Mogne, F. Meunier, L. Yang, B. Thiebaut, and J. M. Martin, "MoDTC lubrication of DLC-involving contacts. Impact of MoDTC degradation," Wear, vol. 348-349, pp. 116–125, 2016.

[108] M. De Feo, M. I. de Barros'Bouchet, C. Minfray, C. Esnouf, T. Le Mogne, F. Meunier, L. Yang, B. Thiebaut, S. Pavan, and J. M. Martin, "Formation of interfacial molybdenum carbide for DLC lubricated by MoDTC: Origin of wear mechanism," Wear, vol. 370-371, pp. 17–28, 2017.

[109] M. Masuko, T. Ono, S. Aoki, A. Suzuki, and H. Ito, "Friction and wear characteristics of DLC coatings with different hydrogen content lubricated with several mo-containing compounds and their related compounds," Tribology International, vol. 82, pp. 350–357, 2015.

[110] M. Kano, Y. Yasuda, Y. Okamoto, Y. Mabuchi, T. Hamada, T. Ueno, J. Ye, S. Konishi, S. Takeshima, J. M. Martin, M. I. De Barros Bouchet, and T. L. Mognee, "Ultralow friction of DLC in presence of glycerol mono-oleate (GNO)," Tribology Letters, vol. 18, no. 2, pp. 245–251, 2005.

[111] L. Joly-Pottuz, C. Matta, M. I. de Barros'Bouchet, B. Vacher, J. M. Martin, and T. Sagawa, "Superlow friction of ta-c lubricated by glycerol: An electron energy loss spectroscopy study," Journal of Applied Physics, vol. 102, no. 6, p. 064912, 2007.

[112] M. I. de Barros'Bouchet, C. Matta, T. Le-Mogne, J. M. Martin, Q. Zhang, W. Goddard, M. Kano, Y. Mabuchi, and J. Ye, "Superlubricity mechanism of diamond-like carbon with glycerol. coupling of experimental and simulation studies," Journal of Physics: Conference Series, vol. 89, 2007.

[113] A. Erdemir and O. Eryilmaz, "Achieving superlubricity in DLC films by controlling bulk, surface, and tribochemistry," Friction, vol. 2, no. 2, pp. 140–155, 2014.

[114] G. Yu, Z. Gong, B. Jiang, D. Wang, C. Bai, and J. Zhang, "Superlubricity for hydrogenated diamond like carbon induced by thin MoS2 and DLC layer in moist air," Diamond and Related Materials, vol. 102, 2020.

[115] A. Erdemir, J. Fontaine, and C. Donnet, "An overview of superlubricity in diamond-like carbon films," in Tribology of Diamond-Like Carbon Films: Fundamentals and Applications (C. Donnet and A. Erdemir, eds.), pp. 237–262, Springer US, 2008.

[116] H. Ronkainen, S. Varjus, and K. Holmberg, "Tribological performance of different DLC coatings in water-lubricated conditions," Wear, vol. 249, no. 3, pp. 267–271, 2001.

[117] Y. Long, J. Galipaud, V. Weihnacht, S. Makowski, J. M. Martin, and M. de Barros'Bouchet, "Achieving superlubricity using selected tribo-pairs lubricated by castor oil and unsaturated fatty acids," Tribology International, vol. 169, 2022.

[118] Y. Long, Y. Wang, V. Weihnacht, S. Makowski, M. Kubo, J. M. Martin, and M.-I. de Barros'Bouchet, "Mechanism of superlubricity of a DLC/Si3N4 contact in presence of castor oil and other green lubricants," Friction, vol. 10, pp. 1693–1706, 2022.

[119] I. Sherrington, "Measurement techniques for piston-ring tribology," in Tribology and Dynamics of Engine and Powertrain (H. Rahnejat, ed.), pp. 387–425, Woodhead Publishing, 2010.

[120] J. S. Courtney-Pratt and G. K. Tudor, "An analysis of the lubrication between the piston rings and cylinder wall of a running engine," Proceedings of the Institution of Mechanical Engineers, vol. 155, no. 1, pp. 293–299, 1946.

[121] G. M. Hamilton and S. L. Moore, "First paper: Measurement of the oil-film thickness between the piston rings and liner of a small diesel engine," Proceedings of the Institution of Mechanical Engineers, vol. 188, no. 1, pp. 253–261, 1974.

[122] S. L. Moore and G. M. Hamilton, "The piston ring at top dead centre," Proceedings of the Institution of Mechanical Engineers, vol. 194, no. 1, pp. 373–381, 1980.

[123] P. Dou, Y. Jia, P. Zheng, T. Wu, M. Yu, T. Reddyhoff, and Z. Peng, "Review of ultrasonic-based technology for oil film thickness measurement in lubrication," Tribology International, vol. 165, 2022.

[124] R. Mills and R. Dwyer-Joyce, "Ultrasound for the non-invasive measurement of IC engine piston skirt lubricant films," Proceedings of the Institution of Mechanical Engineers, Part J: Journal of Engineering Tribology, vol. 228, no. 11, pp. 1330–1340, 2014.

[125] R. Mills, J. Vail, and R. Dwyer-Joyce, "Ultrasound for the non-invasive measurement of internal combustion engine piston ring oil films," Proceedings of the Institution of Mechanical Engineers, Part J: Journal of Engineering Tribology, vol. 229, no. 2, pp. 207–215, 2015.

[126] S. Przesmitzki and T. Tian, "Oil transport inside the power cylinder during transient load changes," SAE Transactions, vol. 116, pp. 652–667, 2007.

[127] M. Söderfjäll, H. M. Herbst, R. Larsson, and A. Almqvist, "Influence on friction from piston ring design, cylinder liner roughness and lubricant properties," Tribology International, vol. 116, pp. 272–284, 2017.

[128] V. Maciàn, B. Tormos, V. Bermúdez, and S. Bastidas, "Development of a floating liner test rig and lubrication model for the study of the piston compression ring friction force under fully flooded and starved lubrication," Tribology International, vol. 160, 2021.

[129] R. A. Mufti, M. Priest, and R. J. Chittenden, "Analysis of piston assembly friction using the indicated mean effective pressure experimental method to validate mathematical models," Proceedings of the Institution of Mechanical Engineers, Part D: Journal of Automobile Engineering, vol. 222, no. 8, pp. 1441–1457, 2008.

[130] C. Wen, X. Meng, Y. Xie, R. Liu, X. Kong, R. Li, Z. Liu, and C. Fang, "Online measurement of piston-assembly friction with wireless IMEP method under fired conditions and comparison with numerical analysis," Measurement, vol. 174, 2021.

[131] R. Kolm, I. C. Gebeshuber, E. Kenesey, A. Ecker, A. Pauschitz, W. S. M. Werner, and H. Störi, "Tribochemistry of mono molecular additive films on metal surfaces, investigated by XPS and HFRR," in Life Cycle Tribology (D. Dowson, M. Priest, G. Dalmaz, and A. A. Lubrecht, eds.), vol. 48 of Tribology and Interface Engineering Series, pp. 269–282, Elsevier, 2005.

[132] H. Moes, "Lubrication and beyond," lecture notes, University of Twente, Netherlands, 2000 edition.

[133] D. Zhu and Q. J. Wang, "On the λ ratio range of mixed lubrication," Proceedings of the Institution of Mechanical Engineers, Part J: Journal of Engineering Tribology, vol. 226, no. 12, pp. 1010–1022, 2012.

[134] E. Baron and J.-L. Ligier, "Acyclisme des moteurs thermiques - forces, couples et moments appliqués au moteur monocylindre," Techniques de l'Ingénieur, no. 1, 2017.

[135] J. Prescott, "The bending of thin rings," Auto. Engr., vol. 9, p. 295, 1919.

[136] A. B. Chik and H. Fessler, "Radial pressure exerted by piston rings," Journal of Strain Analysis, vol. 1, no. 2, pp. 165–171, 1966.

[137] N. Biboulet and A. Lubrecht, "Efficient solver implementation for reynolds equation with mass-conserving cavitation," Tribology International, vol. 118, pp. 295–300, 2018.

[138] C. Barus, "Isothermals, isopiestics and isometrics relative to viscosity," American Journal of Science, no. 266, pp. 87–96, 1893.

[139] D. P. Hess and A. Soom, "Friction at a lubricated line contact operating at oscillating sliding velocities," Journal of Tribology, vol. 112, no. 1, pp. 147–152, 1990.

[140] C. Baelden, A Multi-scale Model for Piston Ring Dynamics, Lubrication and Oil Transport in Internal Combustion Engines. PhD thesis, the Department of Mechanical Engineering, Massachusetts Institute of Technology, Cambridge, MA, 2014.

[141] C. Baelden and T. Tian, "A dual grid curved beam finite element model of piston rings for improved contact capabilities," SAE International Journal of Engines, vol. 7, no. 1, pp. 156–171, 2014.

Appendix A

Negligible Inertia Terms

Newton's second law applied to the piston ring reads:

$$\sum \vec{w} = m_l \vec{a} \qquad \Leftrightarrow \qquad \vec{w_{hydro}} + \vec{w_{asp}} + \vec{w_{tot}} = m_l \vec{a} \tag{A.1}$$

with m_l the ring linear mass and $\vec{a}$ the ring radial acceleration. As the acceleration is the second derivative of the position with respect to time, this can also be written as:

$$a = \frac{dv}{dt} = \frac{d^2h}{d^2t} = \frac{d^2h_0}{d^2t} \tag{A.2}$$

$$v^{(k-1/2)} = \frac{h_0^{(k)} - h_0^{(k-1)}}{\delta_t} \tag{A.3}$$

$$a^{(k-1)} = \frac{h_0^{(k)} - 2h_0^{(k-1)} + h_0^{(k-2)}}{\delta_t^2} \tag{A.4}$$

$$w_{hydro}^{(k-1/2)} + w_{asp}^{(k-1/2)} - w_{tot}^{(k-1/2)} = m_l \left(\frac{h_0^{(k)} - 2h_0^{(k-1)} + h_0^{(k-2)}}{\delta_t^2} \right) \tag{A.5}$$

In Equation A.5, the load terms w are of the order of 100 to 1000 [N/m] and the ring linear mass is of order of a tenth to half of a [kg/m]. The order of magnitude of the ring acceleration can be computed using the code result h_0 and Equation A.4. Figure A.1 gives the computed vertical height, speed and acceleration of a compression ring at a 4000 RPM engine speed.

For a relatively high engine speed, the piston ring vertical acceleration is mostly comprised between -3 and $+3$ [m/s^2] with some high acceleration values (17 [m/s^2]) at a few crank angle steps after the dead-centres. This means that the ring inertia term represents at maximum a tenth and mostly less than a hundredth of the contact load. Therefore, it can in a first approach be neglected. However, it has to be considered for an accurate evaluation of the transient film thickness at the dead-centres, where the ring inertia influence is maximum. For this reason it will be implemented in future work.

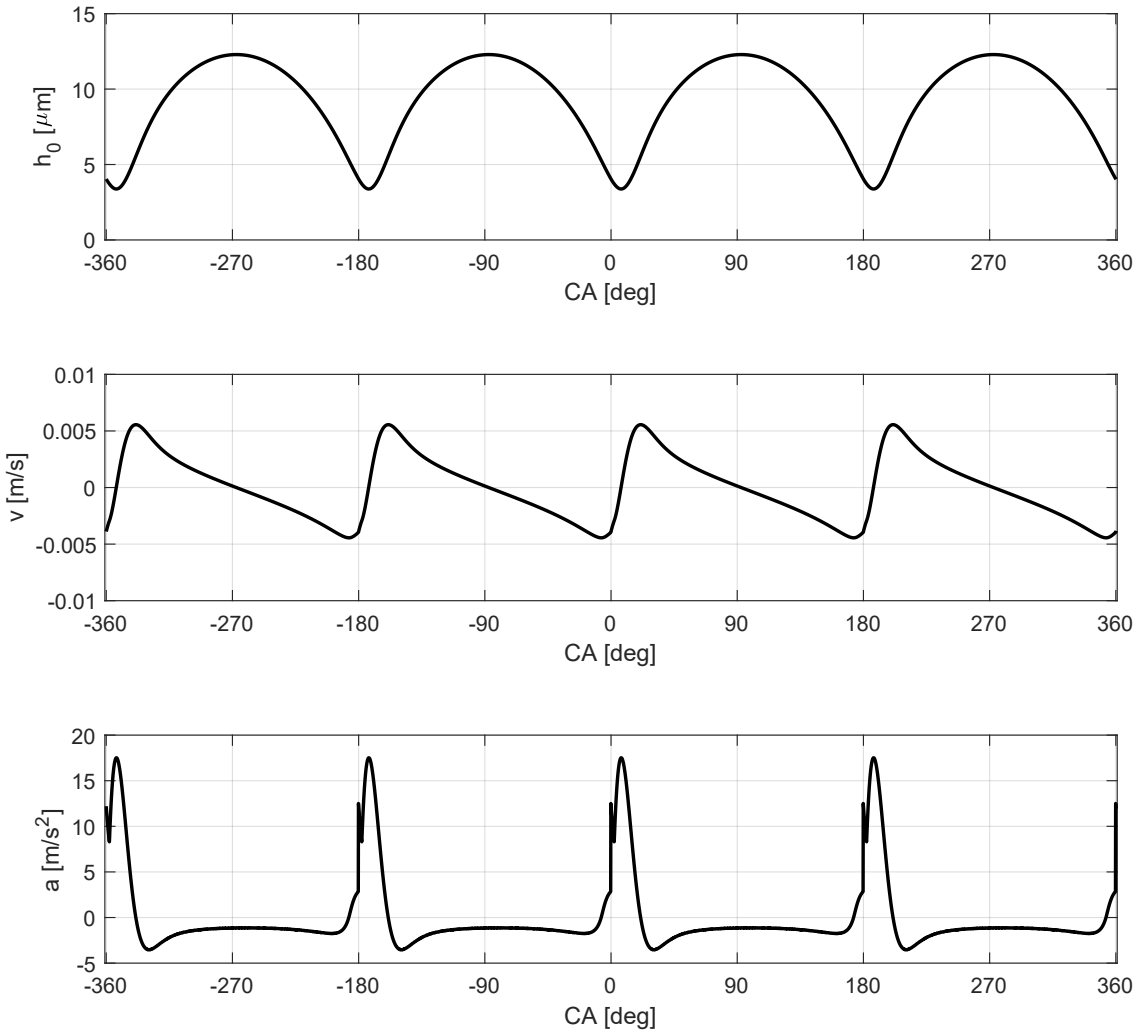

Figure A.1: Computed vertical position h_0, speed v and acceleration a of a compression ring at a 4000 RPM engine speed.

Appendix B

Dimensionless Equations

This appendix regroups the main model equations in their dimensionless form. The developed code relies on these dimensionless equations for both simplicity and to keep the variables close to 1 in order to avoid numerical difficulties.

First some dimensionless parameters are defined using the following convention: lower case for dimensional and upper case for dimensionless variables.

$$\begin{cases} h = h_r H \\ x = x_r X \\ u_m = \bar{u}_m U_m \\ \delta_t = t_r \Delta_t = \frac{x_r}{\bar{u}_m} \Delta_t \end{cases} \tag{B.1}$$

These definitions lead to:

$$\begin{cases} p_h = p_r P_h = \frac{12\eta \bar{u}_m x_r}{h_r^2} P_h = \frac{12\eta x_r^2}{t_r h_r^2} P_h \\ w_h = w_r W_h = p_r x_r W_h \\ f_{hydro} = w_r F_{hydro} \end{cases} \tag{B.2}$$

The reference parameters can be numerically fixed values chosen by the user in order to obtain a straightforward interpretation of the dimensionless quantities. This was done during this research with the following set of reference parameters:

$$\begin{cases} h_r = 1E-6[\text{m}] \\ x_r = 1E-3[\text{m}] \\ \bar{u}_m = 1[\text{m/s}] \\ t_r = 1E-3[\text{s}] \end{cases} \tag{B.3}$$

A proper way to make the reference parameters working for every operating conditions is to assign them to varying model variables such as the ring width, the ring radius of curvature, the piston maximum speed or the Moes & Venner film thickness solution. The following set of reference parameters is a suggestion that has not been tested so far:

$$\begin{cases} x_r = x_l \\ \bar{u}_m = max(u_m) \\ h_r = 4.9\frac{max(\eta)\bar{u}_m r}{min(w_{tot})} \\ t_r = \frac{x_r}{\bar{u}_m} \end{cases} \tag{B.4}$$

From the dimensionless parameters defined above, the following simplified dimensionless equations can be defined.

The dimensionless transient term reads:

$$V = \frac{H_0^{(k)} - H_0^{(k-1)}}{\Delta_t} \tag{B.5}$$

The dimensionless hydrodynamic pressure gradient reads:

$$U_m H - H^* + VX = 0 \tag{B.6}$$

The dimensionless hydrodynamic pressure and load carrying capacity are:

$$\tilde{P}_h = U_m I_1 - H^* I_2 + V I_3 \tag{B.7}$$

$$\tilde{W}_h = U_m J_1 - H^* J_2 + V J_3 \tag{B.8}$$

with the primitives I and J made dimensionless with respect to H and X.

The inlet flow balance equation reads:

$$\begin{aligned} &\Delta_t \left(2U_m H_{in} - H^{*(k-1)} - H^{*(k)}\right) \\ &+ \left(H_0^{(k)} - H_0^{(k-1)}\right)\left(X_a^{(k-1)} + X_a^{(k)}\right) \\ &= 2\left(I_H\left(X_a^{(k-1)}\right) - I_H\left(X_a^{(k)}\right) - \left(X_a^{(k-1)} - X_a^{(k)}\right) H_{in}\right) \end{aligned} \tag{B.9}$$

The outlet flow balance equation reads:

$$\begin{aligned} &\Delta_t \left(-2U_m \frac{I_H\left(X_b^{(k)}\right) - I_H\left(X_b^{(k-1)}\right)}{X_b^{(k)} - X_b^{(k-1)}} + H^{*(k-1)} + H^{*(k)}\right) \\ &- \left(H_0^{(k)} - H_0^{(k-1)}\right)\left(X_b^{(k-1)} + X_b^{(k)}\right) \\ &= 2\left(I_H\left(X_b^{(k)}\right) - I_H\left(X_b^{(k-1)}\right) - \left(X_b^{(k)} + X_b^{(k-1)}\right) H_0^{(k-1)}\right. \\ &\left. - Um\Delta_t\left(H_b^{(k)} - H_0^{(k)}\right)\right) \end{aligned} \tag{B.10}$$

The dimensionless amount of oil in the outlet is:

$$H_{out} = \frac{H^* - VX_b}{\tilde{U}} \tag{B.11}$$

The dimensionless hydrodynamic friction force reads:

$$\tilde{F}_{hydro} = \frac{h_r}{x_r}\left(\frac{2U_m}{3}I_4 - \frac{H^*}{2}I_2 + \frac{V}{2}I_5\right) \tag{B.12}$$

For a simple parabolic geometry, the height equation is:

$$H = H_0 + \frac{x_r^2}{rh_r}\frac{X^2}{2} \tag{B.13}$$

Appendix C

Reynolds Equation Analysis

This appendix regroups three detailed analysis of the Reynolds equation (based on Prof. Lubrecht work [43]) and details the Moes & Venner 1D solution used as a reference in this document (based on [132]). The first analysis of the Reynolds equation focuses on the pure sliding case, the second on the pure impact case and the third generalizes the problem to a geometry including a groove.

C.1 Dimensionless Reynolds Equation: Pure Sliding

The Reynolds equation and geometry are defined as:

$$\frac{\partial}{\partial x}\left(\frac{\rho h^3}{12\eta}\frac{\partial p}{\partial x}\right) - u_m\frac{\partial}{\partial x}(\rho h) - \frac{\partial}{\partial t}(\rho h) = 0 \tag{C.1}$$

$$h(x) = h_0 + \frac{x^2}{2R} \tag{C.2}$$

with ρ the lubricant density and R the reduced radius of curvature.

First, the geometry is simplified by introducing the dimensionless parameters: $H = h/h_0$ and $X = x/x_0$ (capitals are used for dimensionless variables). Which gives us:

$$H(X) = 1 + \frac{x_0^2 X^2}{2Rh_0} \tag{C.3}$$

To simplify the geometry equation, we choose $x_0 = \sqrt{h_0 R}$, which leads to the maximum simplification:

$$H(X) = 1 + \frac{X^2}{2} \tag{C.4}$$

Let us assume that ρ is constant and that the transient term is zero. Replacing H and X in the Reynolds equation leads to:

$$\frac{\partial}{x_0 \partial X}\left(\frac{h_0^3 H^3}{12\eta}\frac{\partial p}{x_0 \partial X}\right) - u_m \frac{h_0 \partial H}{x_0 \partial X} = 0 \tag{C.5}$$

Which, with some rewriting leads to:

$$\frac{\partial}{\partial X}\left(\frac{h_0^2 H^3}{12\eta u_m x_0}\frac{\partial p}{\partial X}\right) - \frac{\partial H}{\partial X} = 0 \tag{C.6}$$

We can define $P = p/p_0$ which leads to:

$$\frac{\partial}{\partial X}\left(\frac{h_0^2 H^3 p_0}{12\eta u_m x_0}\frac{\partial P}{\partial X}\right) - \frac{\partial H}{\partial X} = 0 \tag{C.7}$$

p_0 is the last reference parameter that can be freely chosen to simplify the equation. We chose p_0 as follow:

$$p_0 = \frac{12\eta u_m x_0}{h_0^2} = \frac{12\eta u_m \sqrt{h_0 R}}{h_0^2} = \frac{12\eta u_m \sqrt{R}}{h_0 \sqrt{h_0}} \tag{C.8}$$

Finally, the dimensionless steady-state Reynolds equation reads:

$$\frac{\partial}{\partial X}\left(H^3 \frac{\partial P}{\partial X}\right) - \frac{\partial H}{\partial X} = 0 \tag{C.9}$$

Re-introducing the transient term with $T = t/t_0$, we can chose $t_0 = x_0/u_m = \sqrt{Rh_0}/u_m$ which leads to a maximum simplification of the dimensionless transient Reynolds equation:

$$\frac{\partial}{\partial X}\left(H^3 \frac{\partial P}{\partial X}\right) - \frac{\partial H}{\partial X} - \frac{\partial H}{\partial T} = 0 \tag{C.10}$$

Thus, the pressure solution (stationary and transient) does not depend on any variable.

The load carrying capacity of the fluid is the integral of the pressure distribution over the contact area, for a line contact it reads:

$$w = \int_{-\infty}^{+\infty} p(x)\,\mathrm{d}x \tag{C.11}$$

Defining $W = w/w_0$, one finds $w_0 = 12\eta u_m/h_0$ and:

$$W = \int_{-\infty}^{+\infty} P(X)\,\mathrm{d}X \tag{C.12}$$

The friction force is the integral of the fluid shear stress over the contact area. For a pure sliding situation, one can approximate the shear stress by the Couette term which reads:

$$\tau = \frac{\partial u(z)}{\partial z} = \frac{2u_m \eta}{h} \tag{C.13}$$

The friction force (for the lower surface) is defined as:

$$f = \int_{-\infty}^{+\infty} \tau(x)\,\mathrm{d}x \tag{C.14}$$

Once more, defining $F = f/f_0$, one finds $f_0 = 2u_m\eta\sqrt{R}/\sqrt{h_0}$ and:

$$F = \int_{-\infty}^{+\infty} \frac{1}{H}\,\mathrm{d}X \tag{C.15}$$

From the dimensionless analysis of the Reynolds equation, for a pure sliding situation, the following relations are obtained:

$$\begin{cases} p_0 = \frac{12\eta u_m\sqrt{R}}{h_0\sqrt{h_0}} \rightarrow p \propto h_0^{-1.5} \\ w_0 = \frac{12\eta u_m}{h_0} \rightarrow w \propto h_0^{-1} \\ f_0 = \frac{2u_m\eta\sqrt{R}}{\sqrt{h_0}} \rightarrow f \propto h_0^{-0.5} \end{cases} \tag{C.16}$$

C.2 Dimensionless Reynolds Equation: Pure Impact

The Reynolds equation and geometry are defined as:

$$\frac{\partial}{\partial x}\left(\frac{\rho h^3}{12\eta}\frac{\partial p}{\partial x}\right) - \frac{\partial}{\partial t}(\rho h) = 0 \tag{C.17}$$

$$h(x) = h_0 + \frac{x^2}{2R} \tag{C.18}$$

The following parameters are introduced to simplify the Reynolds equation: $P = p/p_0$, $H = h/h_0$ and $X = x/x_0$. We assume ρ to be constant and the instantaneous vertical velocity v_0 as:

$$\frac{\partial h}{\partial t} = \frac{\partial h_0}{\partial t} = -v_0 \tag{C.19}$$

which yields:

$$\frac{\partial}{x_0\partial X}\left(\frac{p_0 h_0^3 H^3}{12\eta x_0}\frac{\partial P}{\partial X}\right) + v_0 = 0 \tag{C.20}$$

Defining $p_0 = 12\eta v_0 x_0^2/h_0^3$, the dimensionless Reynolds equation reduces to:

$$\frac{\partial}{\partial X}\left(H^3\frac{\partial P}{\partial X}\right) + 1 = 0 \tag{C.21}$$

and becomes unique.

In order to simplify the geometry equation, we chose $x_0 = \sqrt{h_0 R}$, with $H = h/h_0$ the dimensionless geometry equation becomes:

$$H(X) = 1 + \frac{X^2}{2} \tag{C.22}$$

The system of equations including the dimensionless Reynolds Equation C.21 and the dimensionless geometry Equation C.22 has a single and unique solution $P(X)$.

Integrating the dimensionless Reynolds equation once, we obtain:

$$\frac{\partial P}{\partial X} = -\frac{X}{H^3} + \frac{k_0}{H^3} \tag{C.23}$$

with k_0 being an integration constant. As the geometry is a symmetric function ($H(X) = H(-X)$), we want $P(X)$ to be a symmetric function as-well, therefore $k_0 = 0$ and:

$$\frac{\partial P}{\partial X} = -\frac{X}{H^3} \tag{C.24}$$

Integrating once more:

$$P(X) = \frac{1}{2H^2(X)} + k_1 \tag{C.25}$$

For $X = \pm\infty$ we want P to be zero, hence $k_1 = 0$ and:

$$P(X) = \frac{1}{2H^2(X)} \tag{C.26}$$

To obtain the dimensionless load per unit length W_ℓ, we integrate the pressure distribution:

$$W_\ell = \int_{-\infty}^{+\infty} P(X)\, dX = \int_{-\infty}^{+\infty} \frac{dX}{2(1+X^2/2)^2} \tag{C.27}$$

This integral has an analytical solution:

$$W_\ell = \frac{\pi\sqrt{2}}{4} \approx 1.11072073..... \tag{C.28}$$

Thus, the dimensional load carrying capacity has also an analytical solution which reads:

$$w_\ell = p_0 x_0 \frac{\pi\sqrt{2}}{4} = \frac{3\pi\eta v_0 \sqrt{2R^3}}{\sqrt{h_0^3}} \tag{C.29}$$

C.3 Impact LCC Decrease Due to a Groove: A Master Curve

The previous work can be generalised to a geometry including a groove in the y direction in order to study its influence on the load carrying capacity. Therefore, we will need a 2D dimensionless Reynolds equation. We can use the same dimensionless parameters as previously and expand the equation obtained so far:

$$\frac{\partial}{\partial X}\left(H^3\frac{\partial P}{\partial X}\right)+\frac{\partial}{\partial Y}\left(H^3\frac{\partial P}{\partial Y}\right)=-1 \tag{C.30}$$

With the new geometry defined as:

$$H(X,Y)=1+\frac{X^2}{2}+r_i \tag{C.31}$$

with r_i the groove geometry defined as:

$$r_i=\frac{amp}{h_0}\left(0.5+0.5\cos\left(\frac{2\pi y}{\lambda}\right)\right) \quad \text{for} \quad |y|<\lambda/2 \quad \text{else} \quad r_i=0 \tag{C.32}$$

and amp the groove depth amplitude and λ the groove wave length.

Defining the additional dimensionless parameters $Amp=amp/h_0$, $Y=y/\sqrt{h_0R}$ and $\Lambda=\lambda/\sqrt{h_0R}$ one obtains the following dimensionless geometry equation:

$$H(X,Y)=1+\frac{X^2}{2}+Amp\cos\left(\frac{2\pi Y}{\Lambda}\right) \tag{C.33}$$

For this situation, an analytical solution of the Reynolds equation no longer exists and numerical techniques are needed to solve the problem. A MultiGrid technique is used, Figure C.1 gives an example of the computed pressure distribution for a smooth case and with a groove.

The dimensionless load per unit length will depend on only two dimensionless parameters Amp and Λ. For $Amp=0$ the solution is trivial and is equal to the smooth case. In order to understand the influence of the groove dimensionless parameters Amp and Λ on the dimensionless load, we will study the load change compared to the smooth case:

$$\Delta W=\frac{W|_{groove}}{W|_{smooth}}=\frac{W|_{groove}}{\frac{pi\sqrt{2}}{4}}$$

with $W|_{groove}$ the load carried over the grooved zone.

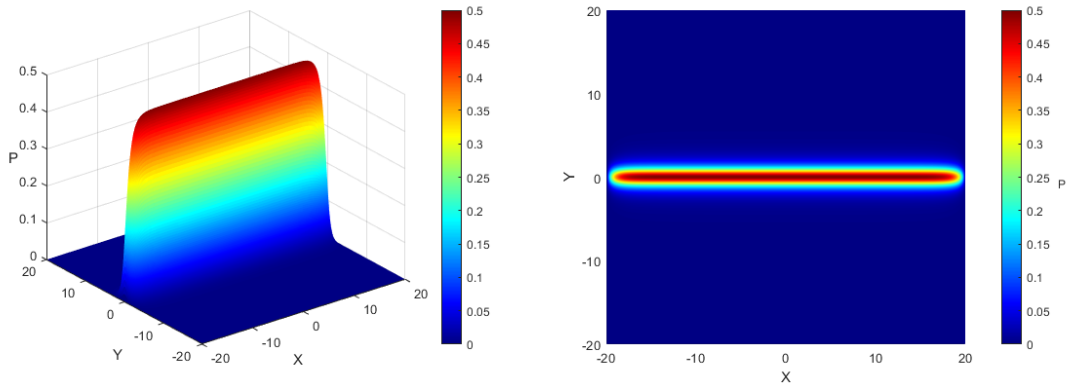

(a) 3D - Smooth

(b) 2D - Smooth

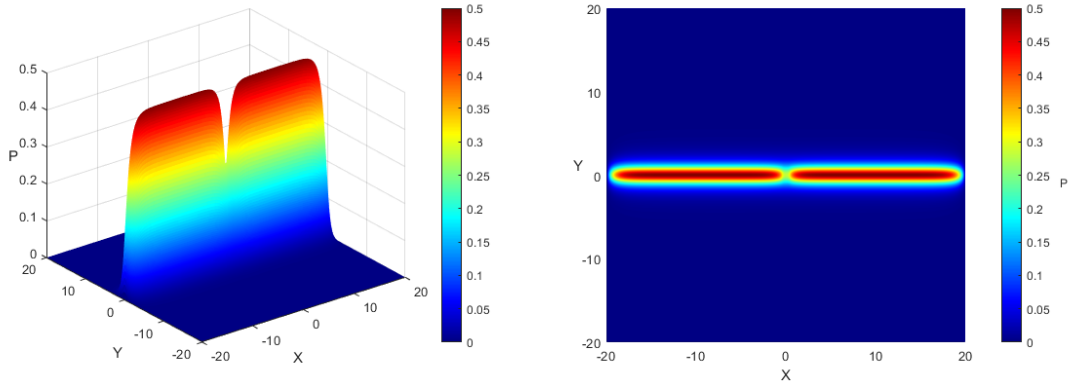

(c) 3D - Groove

(d) 2D - Groove

Figure C.1: Computed pressure distribution using a MultiGrid numerical technique for a smooth case and with a sinusoidal groove.

Figure C.2 shows the numerical results computed for a variety of dimensionless groove parameters Amp and Λ.

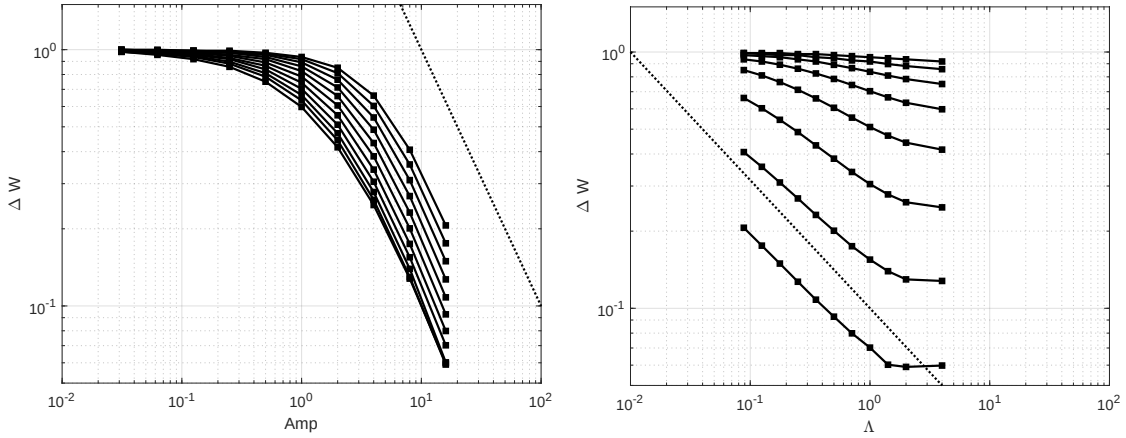

(a) For $\Lambda = 4, 2, \sqrt{2}, ..., 1/8\sqrt{2}$ (left to right). The dotted line represents the slope Amp^{-1}.

(b) For $Amp = 16, 8, 4, ..., 1/8$ (bottom to top). The dotted line represents the slope $\Lambda^{-1/2}$.

Figure C.2: Computed load carrying capacity as a function of the groove parameters (a) Amp and (b) Λ.

In Figure C.2(a) we notice that the contact load carrying capacity varies approximately as Amp^{-1}. In Figure C.2(b) the LCC varies approximately as $\Lambda^{-0.5}$. From these observations, it is possible to construct a dimensionless LCC master-curve. Figure C.3 shows the LCC results as a function of the master parameter $\kappa = Amp\sqrt{\Lambda}$, one obtain a single curve. Equation C.34 gives a rather good approximation and an excellent fit-to-complexity ratio of the master curve.

$$\Delta W \approx \frac{1}{(1+\kappa^2)^{(-1/2)}} \tag{C.34}$$

From this equation, one can rapidly estimate the decrease in LCC due to a groove compared to a smooth case for a pure impact case.

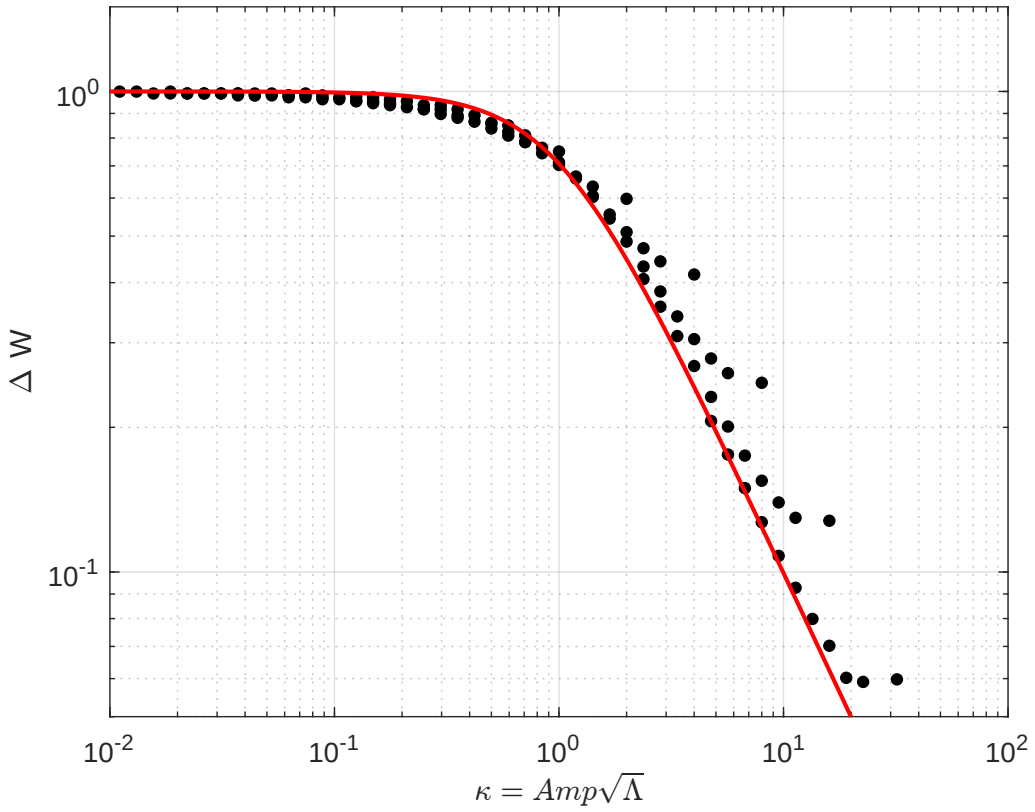

Figure C.3: Computed load carrying capacity as a function of κ (markers: calculation results - solid red line: curve fit).

C.4 Moes & Venner 1D Solution

To describe the Moes & Venner solution we first have to define the Dowson and Higginson dimensionless parameters. In the 1960's, Dowson and Higginson have computed a large number of minimum film thickness values for a variety of operating conditions. By means of a curve fit, they obtained from these results a film thickness equation. They introduced the following dimensionless parameters in order to reduce the number of parameters:

$$W_1 = \frac{w_1}{E'R} \tag{C.35}$$

$$U = \frac{\eta_0(u_1+u_2)}{E'R} \tag{C.36}$$

$$G = \alpha E' \tag{C.37}$$

$$H_m^D = h_m/R \tag{C.38}$$

where h_m is the minimum film thickness, R the reduced radius of curvature, E' the reduced elastic modulus, α the pressure viscosity index, w_1 the load per unit length, u_1 and u_2 the velocity of the lower/upper part. They obtained the following equation as the best curve fit of their results:

$$H_m^D = 0.985 G^{0.6} U^{0.7} W_1^{-0.13} \tag{C.39}$$

Later on, Moes & Venner developed an other set of dimensionless parameters, having the advantage of being smaller and allow for a graphical representation. They are formed by regrouping the Dowson and Higginson parameters and are defined as followed:

$$M_1 = \frac{W_1}{\sqrt{U}} \tag{C.40}$$

$$L = G\sqrt[4]{U} \tag{C.41}$$

$$H_m^M = \frac{h_m}{R\sqrt{U}} \tag{C.42}$$

The Moes & Venner minimum film thickness equation reads:

$$H_m^M = 1.56 L^{0.55} M_1^{-0.125} \tag{C.43}$$

From this equation, two asymptotic solutions exist. First, the rigid iso-viscous asymptote, when no elastic deformations occurs, and the viscosity is constant and equal to the ambient pressure value η_0. The parameter L is zero since $\alpha = 0$ and the minimum film thickness equation reads:

$$H_m^M = \frac{2.45}{M_1} \tag{C.44}$$

Second, the elastic isoviscous asymptote. The elastic deformation can no longer be neglected, but the viscosity remains at its ambient pressure value η_0 ($\alpha = 0$). For this asymptote the minimum film thickness equations reads:

$$H_m^M = \frac{2.05}{\sqrt[5]{M_1}} \tag{C.45}$$

In this document, the iso-viscous rigid (IVR) assumptions is selected to model the PRCL contact. Therefore, the Moes & Venner 1D IVR solution given in Equation C.44 is used as a reference. Using the dimensionless parameter definitions, one obtains the dimensional 1D IVR solution:

$$h_m = 2.45 \frac{R\eta_0 u}{w_1}$$

Using this document notation and the contact mean speed definition $u_m = (u_1 + u_2)/2$, the Moes & Venner dimensional solution reads:

$$h_0^{MV} = 4.9 \frac{\eta u_m r}{w} \tag{C.46}$$

FOLIO ADMINISTRATIF

THESE DE L'INSA LYON, MEMBRE DE L'UNIVERSITE DE LYON

NOM : Lubrecht DATE de SOUTENANCE : 17/04/2023

Prénoms : Thomas

TITRE :
Numerical and Experimental Analysis of the Tribological Performance of a Diamond-Like Carbon Coated Piston Ring Cylinder Liner Contact.

NATURE : Doctorat Numéro d'ordre : 2023ISAL0029

Ecole doctorale : ED 162 MEGA (Mécanique, Energétique, Génie Civil, Acoustique)
Spécialité : Génie Mécanique

RESUME :
Contraints par l'urgence climatique et les enjeux géopolitiques, les secteurs mondiaux de l'industrie et du transport initient une transition vers les énergies durables. L'industrie automobile mise sur les véhicules électriques pour satisfaire les normes locales d'émissions de polluants. Cependant, cette technologie est, en l'état, incapable de répondre aux challenges de la mondialisation. Pour cette raison, les moteurs à combustion interne seront probablement toujours utilisés au cours des prochaines années. Ainsi, améliorer leur efficacité, fiabilité et réduire leurs émissions de polluants est aujourd'hui plus que nécessaire. Les revêtements de surface, tel que le Diamond-Like Carbon (DLC), peuvent par leurs excellentes propriétés tribologiques améliorer le rendement et la durée de vie d'un moteur. La mise en œuvre de revêtement DLC sur toutes les pièces du contact primordial Segment-Piston-Chemise (SPC) a pour le moment peu été étudiée, mais semble cependant être une solution prometteuse. Afin d'évaluer la pertinence d'une telle solution, une étude expérimentale et numérique du contact SPC revêtu DLC est menée.
Dans ce but, un solveur semi-analytique transitoire pour la résolution de contact linéique, lubrifié mixte est développé. Contrairement aux habituelles théories stochastiques, cette méthode repose sur un calcul déterministe du contact entre rugosité à partir du relevé topographique de la surface. Afin de prendre en compte la macro-géométrie des pièces en contact, des coefficients correcteurs évalués analytiquement à partir de l'équation de Reynolds et de la macro-géométrie sont implémentés. Ainsi, le solveur permet l'estimation rapide des différentes forces de frottement du contact tout en considérant les phénomènes de sous-alimentation (géométrique ou par manque de lubrifiant) et de transport d'huile. Le solveur est validé expérimentalement et numériquement.
En parallèle, un moyen d'essai dit à « chemise-flottante » et équipé de vraies pièces moteur est amélioré. A la suite d'une étude expérimentale (mesures vibratoires) et numérique (analyses modales) du banc d'essai, certaines pièces sont modifiées afin d'obtenir un meilleur ratio signal sur bruit mesuré. En outre, une méthode permettant de reproduire des conditions d'essai à hautes vitesses tout en fonctionnant à basses vitesses est présentée.
Enfin, à partir des méthodes expérimentales et numériques, d'excellentes performances tribologiques sont observées pour le contact segment coupe-feu / chemise revêtu DLC. Une réduction significative du frottement ainsi qu'une excellente résistance à l'usure pour une variété de lubrifiants sont obtenues. Ces résultats sont prometteurs pour l'amélioration du rendement des moteurs à combustion interne futurs.

MOTS-CLÉS :
Moteur à Combustion Interne (MCI) – Segment Piston Chemise (SPC) – Diamond Like Carbon (DLC) – Lubrification mixte – Sous-alimentation – Chemise flottante.

Laboratoire de recherche : LaMCoS
Directeur de thèse : Professeur Antonius Adrianus Lubrecht
Président de jury : Professeur Jean-François Molinari

Composition du jury :

Molinari, J.-F.	Professor and lab. director, EPFL, Lausanne	Président
Tian, Tian	Senior Research Engineer, MIT, Boston	Rapporteur
Fabre, Agnès	Maître de Conférences HDR, ENSAM, Aix-en-Provence	Rapporteur
Dufils, Johnny	Docteur-ingénieur, IREIS (HEF groupe), Saint-Etienne	Encadrant
Biboulet, Nans	Maître de Conférences HDR, INSA-Lyon	Co-directeur de thèse
Lubrecht, A. A.	Professeur des Universités, INSA-Lyon	Directeur de thèse